At the Cutting Edge: Structural Analysis and Chemical Modification of the Edges of Mechanically Cleaved Graphene Nanoribbons

A thesis presented in partial fulfilment of the requirements for the degree of

Doctor of Philosophy in Nanoscience

at Massey University, Manawatū, New Zealand

Haidee Michaela Dykstra

2017

Abstract

The first decade of the new carbon nanomaterial graphene has been a time of great discovery and excitement as the exceptional properties of this material were uncovered and its promise for numerous applications realised. The unique properties of graphene, including its exceptional electronic structure, are now well-established, and investigations into how these properties can be manipulated and exploited are rapidly taking off. This research contributes to the emerging field by exploring the structure and chemistry of the edges of mechanically cleaved graphene nanoribbons; groundwork for the future development of edge-modified nanoribbons that could be used to form self-assembled graphene nanoribbon composite structures with potential for devices in solar energy conversion. For this purpose, a Raman microscope was built that enabled for various aspects of the structure of graphene nanoribbons to be probed, in particular the geometry and smoothness of the edges, which have important implications for the specific reactivity of the edge carbon atoms. Chemical approaches for the specific functionalisation of the edges of the nanoribbons were developed, involving reactions tailored to the reactive groups present at the edges, and these were found to be highly successful and selective.

Acknowledgements

I would like to thank my primary supervisor, A. Prof. Mark Waterland, for his extensive guidance, input, support and patience throughout the project, as well as my co-supervisors A. Prof. Gareth Rowlands and Prof. Simon Hall for their useful advice.

I would also like to thank Olaf Griewaldt from IFS Engineering Services for his assistance in the design and machining of microscope mounts; MMIC (Manawatu Microscopy and Imaging Centre) for the use of their microtome for cutting HOPG and TEM for imaging - in particular Jordan Taylor for all the hours she has put into this; Sergei Lebedkin from Karlsruhe Institute of Technology for his very helpful advice regarding optimisations of the microscope; Krishanthi Jayasundera for her advice and guidance for the nanoribbon edge chemistry; and Dominique Appadoo for his help with the Far-IR beamline at the Australian Synchrotron.

I would also like to thank Sam Brooke, Ewan Fisher and Ashley Way for their continued collaboration, advice and input throughout the project, in particular to Ewan Fisher for his invaluable assistance in developing methodologies for characterising graphene nanoribbon samples at the Far-IR beamline at the Australian Synchrotron.

Finally, I would like to thank my family, in particular my husband Liande Gao, for their continued support throughout the project.

Contents

List of Figures

List of Tables

List of Acronyms and Abbreviations

In order of appearance:

CVD	Chemical vapour deposition
GO	Graphene oxide
BZ	Brilluoin zone
QHE	Quantum Hall effect
FET	Field effect transistor
LED	Light-emitting diode
ITO	Indium Tin oxide
SAM	Self-assembled monolayer
DOS	Density of states
GNR	Graphene nanoribbon
CNT	Carbon nanotube
HOPG	Highly-oriented pyrolytic graphite
HNF	Holographic notch filter
VBG	Volume Bragg grating
VHG	Volume holographic filter
PTR	Photo-thermo-refractive
BNF	BragGrate^{TM} notch filter
BPF	BragGrate^{TM} bandpass filter
OD	Optical density
NA	Numerical aperture
OPSL	Optically pumped semiconductor laser
MFD	Mode field diameter
PM	Polarisation maintaining
PMMA	Poly(methyl) methacrylate
GNB	Graphite nanoblock
AFM	Atomic force microscopy
TEM	Transmission electron microscopy
IPA	Isopropanol
SDS	Sodium dodecylsulfate
CMC	Critical micelle concentration
THF	Tetrahydrofuran
r-GNR	Reduced GNR
4-ABA	4-aminobenzoic acid
EDC	1-Ethyl-3-(3-dimethylaminopropyl) carbodiimide
DMAP	4-Dimethylaminopyridine

DMSO	Dimethyl sulfoxide
f-GNR	functionalised GNR
SA	Sulfanilic acid
NHS	N-Hydroxysuccinimide
DMF	Dimethylformamide
FTIR	Fourier transform infrared
ATR	Attenuated total reflection
S:N	Signal-to-noise
HDFT	Heptadecafluoro-1-decanethiol
KK	Kramers-Kronig
SERS	Surface-enhanced Raman spectroscopy
CTAB	Cetyltrimethylammonium bromide
Agnp	Silver nanoparticle
PE	Polyethylene
XPS	X-ray photoelectron spectroscopy
TA	Terephthalic acid
TMA	Trimesic acid
BTB	Benzene 1,3,5-tribenzoic acid
EDA	Ethylenediamine
TFA	Trifluoroacetic acid
4-NA	4-nitroaniline
PDOS	Phonon density of states
iTO	In-plane transverse optical
iLO	In-plane longitudinal optical
DR	Double resonance
PAH	Polycyclic aromatic hydrocarbon
NMP	N-methyl-pyrrolidone
SDBS	Sodium dodecylbenzenesulfonate
BDE	Bond dissociation energy
OTS	Octadecyltrichlorosilane
hBN	Hexagonal Boron nitride
STM	Scanning tunnelling microscopy
TERS	Tip-enhanced Raman spectroscopy
AE	Activated ester
4-NBA	4-nitrobenzoic acid
RhB	Rhodamine B
SP	Sulfophenyl
NP	Nitrophenyl
SPR	Surface plasmon resonance

R6G	Rhodamine 6G
HATN	hexaazatriphenylene
TCNQ	7,7,8,8-tetracyanoquinodimethane
F4-TCNQ	2,3,5,6-tetrafluoro-7,7,8,8-tetracyanoquinodimethane

1 Introduction

1.1 The History of Graphene

Graphene, the two-dimensional carbon nanomaterial, quickly became a hot topic after it was first isolated in 2004 by Novoselov et al.[1], and interest in the unique properties of this material and its great promise for applications, including optical and electronic devices, has continued to grow ever since.[2–4] This remarkable material has been the subject of theoretical studies for sixty years, and for most of this time it was believed that the perfectly two-dimensional nature of graphene meant that it was thermodynamically too unstable to exist in a free state.[5] Thin films are known to have rapidly decreasing melting temperatures with decreasing thickness, which typically leads to instability and, as a result, decomposition when the layer thickness approaches dozens of atomic layers.[6,7] It is of no surprise then, that the first occurrence of free-standing graphene quickly led to a boom in interest and research on this material. The stability of graphene in its isolated single-layer state, despite the early theoretical predictions, has been explained with the argument that 3D warping effects and strong interatomic bonds can suppress thermal fluctuations that are anomalously large in 2D materials and would normally lead to the formation of defects or dislocations in the crystal lattice.[8,9]

Following its isolation in the single-layer state, a frenzy to uncover the unique electronic properties of graphene quickly ensued. One of the most monumental of these discoveries, namely the ambipolar electric field effect, was reported by Novoselov et al.[1] in the same paper announcing the first isolation of monolayer graphene. Other highly notable discoveries soon followed, including those of the unprecedented high carrier mobility[10,11], anomalous Quantum Hall effect[12] and Klein tunneling[13].

A large proportion of the early experimental studies on graphene also focused on simple and scalable methods for its production. Micromechanical cleavage, which was the method used for the first reported isolation of graphene by Novoselov et al.[1] and simply involves repeated peeling of graphene layers using sticky tape until single layer flakes are obtained, is an attractive method as it can provide high-quality crystals of graphene with dimensions up to 100 μm.[14] Key to the success of this approach was the effect of a 300 nm SiO_2 layer on Si wafer allowing for the observation of monolayer graphene under an optical microscope.[5] Without the discovery of this effect, it would have been exceedingly difficult to isolate single-layer graphene crystallites from the multitude of multilayer flakes produced via the micromechanical cleavage method. The micromechanical cleavage method for graphene production has some severe problems in terms of scalability, and other methods of production that could solve this problem soon followed. One such approach involves exfoliation of bulk graphite[15], often employing sonication[16,17] or intercalation[18–20] to separate atomic planes. This is an attractive and scalable approach due to the high availability and low cost of bulk graphite. Bottom-up approaches, such as

chemical synthesis[19,21–23], epitaxially growing graphene directly via chemical vapour deposition (CVD)[24,25] onto metal substrates or thermal decomposition on SiC[10,11,26], have also received considerable interest. An alternative approach is based on the reduction of graphene oxide (GO) to remove surface oxygen functional groups via chemical, thermal or electrochemical techniques.[27–29] However, the reduced GO materials produced via these methods are typically inferior in quality and electronic performance to pristine graphene, as it is usually not possible to completely remove all of the oxygen groups.[30]

1.2 The Properties and Applications of Graphene.

With its honey comb-like structure, graphene can conceptually be considered as the material from which other carbon nanostructures, such as carbon nanotubes and fullerenes, are formed.[30] The properties of this material are very different from its parent graphite. In particular, the unique band structure and zero band-gap of graphene make it a semiconductor with high electron mobility (as high as 15,000 $cm^2\ V^{-1}\ s^{-1}$).[5] Graphene is especially famous for its quasiparticle charge carriers, known as massless Dirac fermions, which have a Fermi velocity of $\sim 10^6\ ms^{-1}$ and arise as a result of electrons interacting with the periodic potential of the carbon lattice. Due to its exceptionally high crystal quality and continuous nature, charge carriers in graphene can travel great distances (an electron mean free path of over 1 μm has been reported[31]) through the carbon lattice without scattering.[1,5,12,32] Graphene has a honeycomb lattice structure with two equivalent sublattices, known as the A and B sublattices. Intersection of the energy bands associated with these sublattices at E=0 at the corners of the Brilluoin zone (BZ) results in a conical electronic dispersion around the point of intersection (the Dirac point). This linear dispersion (in 2 dimensions) near the Dirac point results in an ambipolar electric field effect, which allows for continuous tuning of charge carriers between electrons and holes in high concentrations (up to $10^{13}\ cm^{-2}$), upon shifting the position of the Fermi energy via the gate voltage.[1,12,14,32]

The Dirac-like Hamiltonian for the approximation of the quasiparticles in graphene at low energies is given by[5]:

$$\hat{H} = \hbar v_F \begin{pmatrix} 0 & k_x - ik_y \\ k_x + ik_y & 0 \end{pmatrix} = \hbar v_F \boldsymbol{\sigma} \cdot \mathbf{k} \tag{1}$$

Where v_F is the Fermi velocity, $\boldsymbol{\sigma}$ the 2D Pauli matrix and $\mathbf{k}$ the quasiparticle momentum (with components k_x and k_y). The 2×2 matrix is due to the two A and B sublattices, which gives rise to a new degree of freedom to account for their respective contributions. This is known as the pseudospin, which can be either parallel or antiparallel to k from the K-point, and is not related to the real electron spin. The two inequivalent reciprocal space

points K and K' at the BZ corners have opposite pseudospin, and are thus referred to as valley-isospin states.[30] Electrons and holes with opposite pseudospins travel in opposite directions and from different valleys. In bilayer graphene there are four states, due to the contribution of two pseudospins from each layer. The confinement of electrons in the 2D plane of graphene, often referred to as a two-dimensional electron gas[32], gives rise to unique phenomena such as Berry's phase and the anomalous quantum Hall effect (QHE).[12,33]

It is important to consider at what point multilayer graphene can be regarded as 3D instead of 2D. Bilayer graphene also behaves as a 2D material, and monolayer and bilayer graphene are both zero-bandgap semiconductors. For graphene with more than two layers, the electronic band structure becomes more complicated, with the appearance of charge carriers and overlap of the conduction and valence bands.[1,34] Approaching 10 layers, graphene moves towards the 3D limit and can be regarded as graphite, which has semi-metallic behaviour.[35]

The electronic properties of graphene are not its only outstanding feature, as this material also has unique optical, mechanical and thermal properties.[30] For example, a single graphene monolayer absorbs 2.3% of white light, allowing for it to be observed with optical microscopy. Graphene is also highly stable and able to withstand temperatures up to 250° C without degrading. It also exhibits a negative thermal expansion due to its 2D nature and out-of-plane phonons. It has very high in-plane thermal conductivity (up to 5 x 10^3 W/mK), making it an excellent dissipater of heat. Due to strong C-C bonding, graphene is both incredibly strong and very flexible, with a Young's modulus of 1 TPa and shear modulus $\sim$ 280 GPa. The large surface area and extensive π orbital network provide good capability for van der Waals interactions, giving it high adhesive strength ($0.2-0.38$ Jm^{-2} interlayer binding energy, 0.45 Jm^{-2} for monolayer binding to SiO_2). Graphene is also highly hydrophobic, with a strong water-repelling nature.

The use of silicon in electronics has become widely prevalent and has generated large growth in technological applications.[30] In addition, the continual miniaturisation of silicon electronic components, directed by Moore's law, has resulted in continual enhancement of computational performance. However, approaching the fundamental limits of miniaturisation in silicon technology, as determined by the physical properties of Si, will inevitably present obstacles for continued technological advancement. To solve these problems, new materials and breakthroughs are needed. One possible candidate for this is graphene, and the atomic thinness of this material could solve the problems in miniaturisation. Graphene has other advantages over Si for electronic devices, for example very high carrier mobility. Graphene-based electrodes hold promise for many applications, including FETs[36–38] (field effect transistors), solar cells[39–41], LEDs[42,43] (light emitting diodes), batteries[44,45], integrated circuits[46] , electrochemical sensors[47,48], etc.

The properties of graphene make it particularly well-suited for applications in pho-

tovoltaics.[49] ITO (Indium Tin Oxide) is conventionally used as the anode in solar cells, however the supply of Indium is dwindling, making it more and more expensive.[41] For this reason, graphene, which exists in abundance and can be produced large-scale and cost-effectively, could be a promising substitute for ITO thin films. A single layer of graphene has an intrinsic sheet resistance of ~ 6 kΩ, which is inferior to that of ITO ($10-20\ \Omega\ \mathrm{sq}^{-1}$).[50] However, layer-by-layer stacking and doping of graphene can significantly reduce the sheet resistance (down to $20\ \Omega\ \mathrm{sq}^{-1}$), although there is a trade-off with transparency when the thickness increases. Thus, there are some challenges that need to be overcome for the high performance of graphene-based solar cells to be realised. The large surface area of graphene presents a convenient means to tailor the carrier density, Fermi energy and work function of the material, enabling it to be used as either a cathode or anode. Graphene can also be used in organic, inorganic and dye-sensitised solar cells as transparent window electrodes.[50,51] Graphene is particularly useful in dye-sensitised solar cells, in which it can serve a large range of functions[52], from the electrode materials[51,53–56] (e.g. counter electrode/photoanode) to components such as the electrolyte[57,58] and photosensitiser[59–61]). Stacked graphene sheets also offer the possibility for inclusion of organic molecules between the layers. For example, insertion of a SAM (self-assembled monolayer) of 1-pyrenebutyric acid N-hydroxysuccinimide ester was found to improve the conductivity between graphene layers by acting as a molecular bridge and hole-dopant.[62]

1.3 Graphene Nanoribbons

The zero bandgap of pristine graphene poses a problem for its use in digital electronics requiring large on/off ratios.[2,63] To make graphene useful in many electronic applications, a bandgap is required. One way in which this can occur is by confinement of the graphene electronic wave-functions in the lateral dimension, for example in nanoribbons. Lateral confinement results in a modified electronic density of states (DOS), which can result in bandgap opening. For ribbons with small widths, the bandgap is theoretically predicted to be inversely proportional to the ribbon width.[64,65] For example, a ribbon of 10 nm width would have a bandgap of ~ 100 meV, and a ribbon of 1 nm width a bandgap of ~ 1 eV. In addition to the nanoribbon width, the edge geometry (see figure 1) also affects the electronic structure. According to tight-binding calculations[64,65], zigzag-edged nanoribbons are always metallic, regardless of width, while armchair-edged nanoribbons show a width-dependant gap, alternating between metallic and semiconducting. Additionally, zigzag ribbons have a flat band at zero energy in their electronic band structure, corresponding to states localised at the edges of the ribbon.[63] These edge states confer spin polarisation[66,67] and half-metallicity[68].

Graphene nanoribbons (GNRs) have been produced by a variety of different tech-

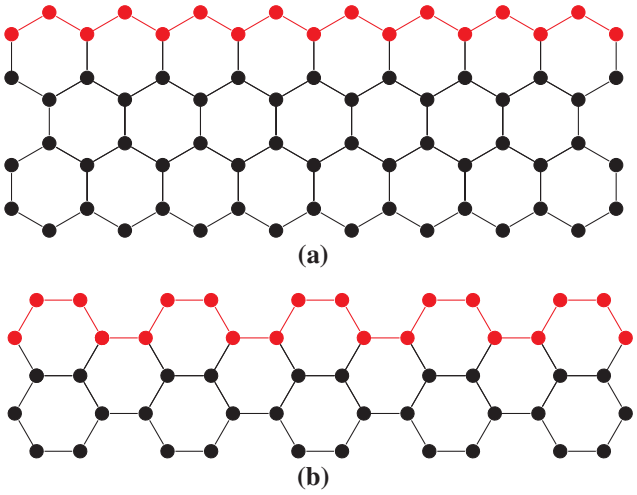

Figure 1: (a) Zigzag and (b) armchair GNRs.

niques, using both top-down and bottom-up approaches.[63] In the top-down approach, a graphene sheet or other graphene/graphite material is modified (e.g. by patterning) to give a nanographene with desired shape and size. A common example of this approach is lithographically patterning a mask onto a graphene sheet on a substrate, then etching the unmasked graphene with oxygen plasma until only the masked section remains.[69,70] This technique has been used to produce nanoribbons down to 10 nm width.[71,72] Another approach is to use chemical methods on graphitic or graphenic precursors to produce graphene nanoribbons dispersed in a solvent[73] or as a powder[74]. Another example is the unzipping of single-wall or multi-wall carbon nanotubes (CNTs) by oxidative cutting of the CNT wall upon treatment with a chemical agent, such as the oxidising reagent potassium permanganate in acid.[75,76] The widths of the ribbons produced by this method depend on the widths of the CNT precursors. Although most solution-based methods for unzipping CNTs give oxidised ribbons, it is also possible to use non-oxidative methods, for example laser-induced unzipping.[77] In this approach, a pulsed laser is used to irradiate CNTs dispersed in a solvent (DMF), resulting in the creation of defects, followed by defect migration and fragmentation. An additional example of the top-down approach is cutting of graphene with catalytic metal particles such as Fe or Ni.[78] In the bottom-up approach, GNRs are formed by the assembly and growth of monomeric precursors.[63] For example, employing synthetic chemistry techniques for the polymerisation of organic precursors, such as polyphenylene, to form ribbons with narrow widths.[22,79] Another example is CVD by reaction of hydrocarbons, such as ethylene or methane, onto a templated metallic catalyst, where the size and shape of the template dictates the nanoribbon dimensions.[80–82]

Few of these techniques can produce high-quality GNRs at high through-put and purity, and with uniform and controllable widths - factors which are all highly desirable. Recently, a novel method for GNR production has emerged, which combines all the de-

sirable factors in a simple, fast, scalable "nanotomy"-based method.[83] They key technique that distinguishes this method from numerous others is the use of mechanical force to effectively cleave graphene sheets. This involves cutting highly-oriented pyrolytic graphite (HOPG) with a diamond knife at controlled thickness to produce GNRs with corresponding widths. Using this technique, nanoribbons with widths ranging from $\sim$ 5 nm - 600 nm have been produced by Mohanty et al.[83]

1.4 The Chemistry of Graphene and Graphene Nanoribbons.

Precise control of the nanoribbon width and edge geometry at the atomic level is required to achieve the desired bandgaps and unique electronic properties of perfect zigzag and armchair graphene nanoribbons, which poses a challenge as it requires very elegant and precise methods of production. Bandgap tuning in graphene and graphene nanoribbons can, however, also be achieved by chemical functionalisation, which can be covalent or non-covalent.[2] Due to the two-dimensional nature of graphene, chemical doping of this material is limited to edge or surface interactions.[84] However, covalent modification of the graphene basal plane inevitably alters its exceptional electronic and optical properties, hence edge functionalisation, which preserves the pristine graphene electronic structure, is the more desirable strategy.

Though graphene is a chemically stable material with extensively delocalised π electrons, it can still undergo a large variety of chemical functionalisation reactions, including nucleophilic addition, cycloaddition, free radical addition, Friedel-Crafts acylation and Diels-Alder reactions.[85,86] Chemical functionalisation of graphene can be an effective tool to alter and control the electronic properties of the material. For example, electron-withdrawing or electron-donating functional groups can produce p- or n-doped graphene, respectively. Doping causes opening of the bandgap near the Fermi level, changing the metallic nature of graphene and making it a semiconductor. Functionalisation can also improve the solubility of graphene in aqueous or organic solvents. Graphene nanoribbons, which contain a higher proportion of the more chemically reactive edge atoms, are subject to an even wider range of chemical functionalisation strategies. Functionalisation of GNR edges can enable bandgap tuning, which is determined not only by the nature of the functional groups attached but also by the nature of the edge atoms (zigzag vs armchair).[87]

An important consideration for GNR edge functionalisation is whether selective edge functionalisation can be achieved without functionalisation of the basal plane. Edge functionalisations, in which a significantly larger proportion of functional groups have been attached to edge atoms compared to the basal plane, have been reported in the literature.[88–90] The selectivity in these cases is due to the graphene edge carbon atoms possessing a higher chemical reactivity than those of the basal plane, which are perfectly

bonded.[87] There are also reports of selectively functionalising graphite edges, followed by exfoliation to produce functionalised graphenes.[91–93] In these cases, the selectivity arises due the inability of the functionalising reagent to penetrate the graphite layers, due to the strong $\pi - \pi$ interactions between graphene planes, limiting basal plane functionalisation to the outer sheets.

The chirality of the graphene edge is another important factor to consider in functionalisation, as zigzag and armchair edges exhibit different chemical reactivities. Several computational studies investigating the nature of graphene zigzag and armchair edges and predictions about their different chemical reactivities have been reported in the literature.[87,94–96] Zigzag edge atoms possess unpaired π electrons, giving localised states at the edge which are not present in armchair edges.[87,96] The distribution of unpaired π electrons between the zigzag edge carbon atoms gives them partial radical character and hence unique chemical reactivity over armchair and basal plane carbon atoms. This could allow for good selectivity of zigzag edges for radical functionalisation reactions. Additionally, selective functionalisation of zigzag edges could arise due to sterical constraints. The formation energy for the attachment of functional groups to single carbon edge atoms is lower for zigzag edges than for armchair edges.[95] This is due to structural deformation of the armchair edge upon functionalisation due to steric hindrance between the functional group and the hydrogen atom attached to the neighbouring edge carbon atom. This structural deformation does not occur for zigzag edges. Likewise, there are certain types of functionalisation reactions that could be selective for armchair edges, e.g. the Diels-Alder reaction. Graphene has been shown to act as both diene and dienophile in Diels-Alder reactions.[86] However, computational studies have shown that the reaction energies for Diels-Alder functionalisation of the pristine graphene basal plane are unfavourable and require heating to proceed.[97] For armchair edges, however, the reaction energies are favourable for reaction with certain dienes/dienophiles and do not require heating. The large difference in reaction energies for armchair edge and basal plane functionalisation could allow for the development of highly selective Diels-Alder functionalisation strategies.

Tailoring the electronic properties of graphene and GNRs can also be achieved by non-covalent functionalisation, for example by adsorption of organic or inorganic molecules to the graphene basal plane to alter the electronic properties of the material via interaction with the sp^2 hybridised carbon atoms.[2] Investigations on doping graphene using organic molecules for charge-transfer have recently received growing interest.[84] Adsorption of aromatic molecules to the graphene basal plane allows for controllable doping of the material via charge-transfer, while largely preserving its high electron mobility. This idea can be extended to the production of layered graphene assemblies with intercalating aromatic molecules sandwiched between graphene sheets as doping agents for charge separation.

1.5 Raman Spectroscopy for Characterising Graphene Nanoribbons

Raman spectroscopy is an effective tool for the characterisation of graphene nanoribbons and is especially useful in probing the graphene edge structure. The Raman spectrum of graphene features three prominent bands, namely the G (1580 cm^{-1}), D (1350 cm^{-1}), and 2D (2700 cm^{-1}) bands. The G band arises from a first-order Raman scattering process, whereas the D and 2D bands both arise from second order processes.[98] The D band becomes particularly relevant at the graphene edge, as it is a disorder related band that only becomes active in the presence of defects.[99,100] In the absence of defects in the graphene basal plane, the D band will only be present at the edges, which act as defects. However, the nature of the graphene edge also determines the activity of the D band, which can only be activated by armchair edges. The D band cannot be activated by a perfect zigzag edge. The origin of this effect is discussed in detail in chapter 4. Additionally, the D band is known to be strongly dependent on the direction of linear polarisation of the laser excitation beam relative to the graphene edge direction, and is only activated for parallel polarisation.[101] Hence, polarised Raman spectroscopy is an effective tool for characterising the nature of graphene nanoribbon edges, namely, distinguishing between ribbons that have predominantly armchair edges from those with mostly zigzag edges.

Although the G band is due to a first-order scattering process and does not require defects for activation, it has been found that changes in the electronic states at the edges do modify the G band.[102] This manifests as a polarisation dependence of the G band at the graphene edges, with no polarisation dependence exhibited in the basal plane.[103] Opposite polarisation behaviour is observed for zigzag and armchair edges, with the G band being activated only at parallel incident polarisation for the armchair edge, and only at perpendicular incident polarisation for the zigzag edge. Thus, the G band can also be useful for distinguishing armchair from zigzag edges, and the different polarisation dependences of the G and D bands at the graphene edge can effectively provide a double test to allow for the unambiguous determination of the edge structure.

Raman spectroscopy can also be used to determine the number of graphene layers, by the low frequency mode that occurs at ~ 42 cm^{-1} in bulk graphite.[104] This is known as the shear mode, and involves atoms in adjacent graphene planes collectively moving in opposite directions. The frequency of the shear mode depends on the number of graphene layers and exhibits a shift to higher wavenumber with increasing number of layers. Hence, low-frequency Raman spectroscopy is a useful tool for identifying the number of layers in assemblies of graphene nanoribbons.

1.6 Project Scope, Aims and Outline

This project continues the exploration of the many exciting possibilities in the still-emerging field of graphene materials, with a focus on graphene nanoribbons. The motivation behind

this research was initially based on the underlying question: *using physical and/or chemical modifications, can the assembly of functional nanostructures from graphene nanoribbons and molecular materials be controlled?* The key idea to controlling the assembly was to selectively functionalise the nanoribbon edges with complementary (e.g. positively and negatively charged) groups so that interactions between the edges of nearby nanoribbons with different edge functionalities would direct the layer-by-layer assembly of individual ribbons. Intercalating molecules could also be introduced between the graphene layers to produce functional composites, utilising aromatic organic molecules with electron-accepting or -donating properties. In these composites, the adsorbing molecules could interact with the sp^2 hybridised carbon atoms of the graphene via van der Waals and $\pi - \pi$ interactions. There are several studies in the literature on the assembly of molecules on monolayer graphene sheets, but the use of GNRs in these types of studies is largely unexplored.[4,84,105] These GNR-based composites could have potential use in applications such as electronic devices, solar cells, energy storage and chemical sensing.

The nanotomy-based mechanical cleavage method for GNR production developed by Mohanty et al.[83] was utilised for the production of GNRs with uniform and controllable widths, and Raman microscopy was employed for characterisation of the as-produced and edge-modified ribbons. The development of successful strategies for selective edge functionalisation requires prior knowledge of various aspects of the nanoribbon structure, including the purity, size uniformity, level of defects, edge type (i.e. zigzag vs armchair) and edge smoothness (i.e. edges of predominantly one geometry vs disordered edges). Probing the graphene interlayer interactions is also important and useful for the characterisation of layered GNR composites. Raman spectroscopy, and in particular microscopy, is an ideal tool for characterising these aspects of the nanoribbon structure. However, this requires both polarised and low-frequency Raman capabilities, as well as the ability to achieve tight laser focus for characterising such small samples. Raman equipment was not readily available and within budget to meet these requirements, thus the first part of this project was to develop a Raman microscope for this purpose. This took up a substantial part of the research time, and was invaluable for moving forward with the rest of the experimental work on GNR production and edge-modification.

The initial project objectives for the production of edge-modified nanoribbons able to direct their own self-assembly for the formation of layered composite structures was quickly realised to be unrealistic, in large part due to the significant portion of time spent developing the Raman microscope. Additionally, the characterisation and edge-functionalisation of GNRs posed many experimental challenges, and the development of all the required experimental techniques proved to be time-consuming. For these reasons, the original scope of the project was modified to exclude the self-assembly stage, with the focus instead on obtaining edge-functionalised nanoribbons, an achievement that was in itself soon realised to be quite significant. Despite encountering many difficulties in

characterising these modified ribbons, due to the inherently low proportion of functionalised carbon atoms, a solid level of success was achieved, with substantial combined evidence for the selective modification of graphene nanoribbon edges. These results, and the procedures developed therein, pave the way for further tailoring and characterisation of nanoribbon edge functional groups, which could be used for the development of self-assembled composite structures in the future.

The remainder of this thesis is set out as follows: firstly, the journey in developing a Raman microscope with THz and polarised Raman capabilites is presented. This was almost the sole focus of the project in the first year, and chapter 2 outlines the process of design and development in detail, including the problems encountered along the way and how these were overcome. The experimental methods for the production, characterisation and functionalisation of GNRs are then given, followed by two chapters discussing the results of the characterisation (chapter 4) and edge-functionalisation (chapter 5) of the nanoribbons. Finally, the results and implications are summarised in chapter 6, and insights for future developments are given.

2 Design and Implementation of a Terahertz Raman Microscope

2.1 Introduction

This project requires that the edge structure of graphene nanoribbons be characterised prior to functionalisation, as knowledge of the edge smoothness and relative proportions of zigzag and armchair edges is a key factor in determining the functionalisation strategies to use. Raman spectroscopy is an ideal tool for the characterisation of graphene and graphite materials, as the absence of a band-gap results in resonance with all incidence wavelengths, allowing for both the physical and electronic structure to be probed.[102] As will be discussed in chapter 4, Raman spectroscopy can provide useful and important information on many aspects of the structure of graphene, including the level of defects, proportion of edges, edge structure (including smoothness and geometry) and graphene interlayer interactions. Raman spectroscopy is particularly powerful for probing the structure of GNRs, as the edges of GNRs show strongly polarisation-dependent and structure/geometry-dependent Raman behaviour. Additionally, Raman spectroscopy can also be used to determine the number of layers in assemblies of graphene nanoribbons, by the low-frequency shear mode. Thus, polarised and terahertz (THz) Raman capabilities can further extend the usefulness of Raman spectroscopy for the characterisation of GNRs. However, Raman instruments are typically suited for liquid or macroscopic solid samples and do not offer sufficient resolution to detect signals from sub-microscopic objects, hence Raman microscopy, which can offer resolution down to the diffraction limit, is required for characterising GNRs. These considerations present the need for a Raman microscope with capabilities for both polarised and low-frequency Raman studies. However, these features are highly specialised, particularly the latter, and most commercially available Raman microscopes are not equipped for even one, let alone both of these capabilities. Thus, the plan was to incorporate these features into a home-built Raman microscope, and the purpose of this chapter is to recount in detail the process undertaken to achieve this.

2.1.1 Basic Components of a Raman Spectrometer

There are four main components necessary for the observation of Raman scattering from a sample, namely: a source of monochromatic radiation, a set of optical components for illuminating the sample and collecting the scattered radiation, a system to disperse the scattered radiation into its frequency components and a device to detect the dispersed radiation. A simple Raman system is shown in figure 2. The monochromatic light source is typically a laser, which can provide high power and a narrow linewidth. The device for illuminating the sample and collecting the scattered photons contains a lens to focus

the laser onto the sample, and a second lens or set of lenses to collect the scattered radiation and focus it into the entrance slit of the spectrometer. The spectrometer contains a diffraction grating that disperses the radiation, which is then focused onto the detection device. This can be a photomultiplier or CCD camera. A notch filter to reject the Rayleigh-scattered light before it enters the spectrometer is also normally included in the Raman setup.

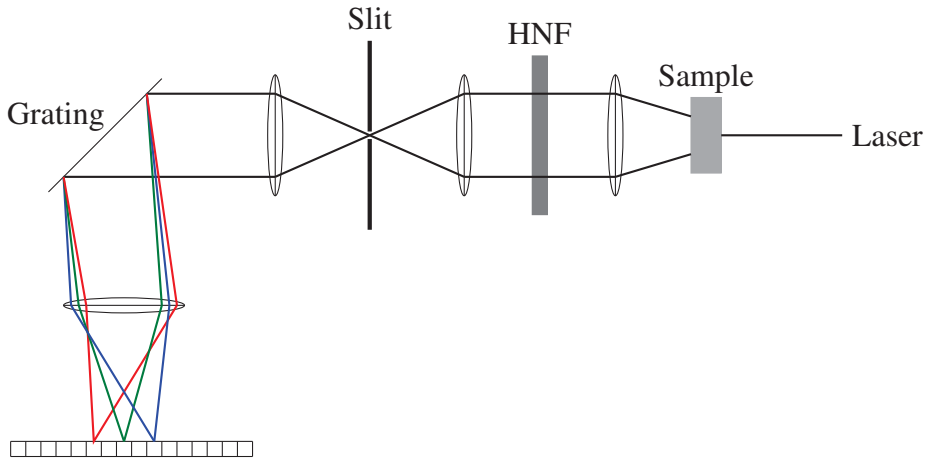

Figure 2: A simple Raman setup. HNF = holographic notch filter.

2.1.2 Holographic Bragg Filters - New Raman Notch Filter Technology

Terahertz spectroscopy can be used to probe intermolecular interactions in a crystal lattice and consequently has proved to be a useful tool for identifying and distinguishing different crystal polymorphs, which occur in many pharmaceutical products.[106] Terahertz spectroscopy typically involves measuring the interaction of a substance with THz radiation (between infrared and millimeter wavelength regions of the electromagnetic spectrum), for example by recording the THz absorption spectrum. Terahertz Raman spectroscopy, on the other hand, measures THz vibrations in an indirect manner, as neither the excitation nor scattered frequencies are in the THz region, rather it is the difference between the excitation and scattered frequencies that corresponds to the excitation of a vibration with THz frequency. To put this in perspective, a Raman band at 30 cm^{-1} corresponds to a frequency of approximately 1 THz.

Traditionally, Raman spectroscopy has been limited to the observation of signals that are quite distant from the excitation laser line (typically hundreds of wavenumbers)[107]. This is due to limitations in the ability of the filters used for Rayleigh light rejection, which becomes significantly more challenging with low-wavenumber Raman measurements[108]. These so-called notch filters are used in Raman instruments to reject the laser line (Rayleigh-scattered light), which would otherwise swamp the spectrum, before it reaches the spectrometer, while letting the faint Raman-shifted light pass through. A typ-

ical notch filter consists of layered dielectric materials, and rejection of a narrow range of wavelengths, the notch wavelength, arises from the interference of light waves reflected from layers with different refractive indices. The width of the notch is ultimately limited by the number of dielectric layers. The range accessible in the low-frequency region of a Raman instrument is limited by the bandwidth of the notch filter, which is typically hundreds of wavenumbers wide. Until quite recently, cascaded multi-stage spectrometers were required for Raman frequency measurements below 100 cm^{-1}.[108] These state-of-the-art spectrometers allow Raman shift measurements down to $\sim$5 cm^{-1} to be made, and are very flexible as they can be operated at different excitation wavelengths. However, they do not allow simultaneous measurement of both the Stokes and anti-Stokes side of a spectrum, and are complex, bulky, expensive and have low transmission and therefore poor sensitivity.[109]

Recently, however, a new type of notch filter has emerged, which can allow for ultra-low-frequency Raman measurements below 10 cm^{-1}.[110] This new approach to notch filter technology has displayed great potential for ultra-low-frequency Raman spectroscopy applications. Using this technology, ultra-low-frequency Raman measurements of sulfur (simultaneous Stokes and anti-Stokes), L-Cystine, pharmaceutical products, single-walled carbon nanotubes, silicon/silica and sapphire, all using standard single stage Raman instruments, have been reported.[107–109,111,112] This new type of notch filter offers several advantages over thin film notch filters and multi-stage spectrometers, namely significantly lower bandwidths (< 10 cm^{-1} cf. $\sim 100-200$ cm^{-1} for thin film), simultaneous measurement of both ultra-low-frequency Stokes and anti-Stokes bands, high transmission efficiency - around an order of magnitude greater than multi-stage spectrometers, high optical density (OD) and much lower cost.[107,111] This new type of notch filter is known as a volume Bragg grating (VBG) (also known as a volume holographic filter (VHG)). A VBG is a volume hologram that has been developed using holographic techniques in bulk PTR (photo-thermo-refractive) glass, such as sodium-zinc-aluminum-silicate glass.[113] This is doped with Ag, Ce, and F, which, after exposure to UV radiation and thermal development to form NaF nanoclusters, provide photo-induced refractive index modulation. This modulation is manifest in the form of parallel fringe planes in the grating material which terminate at the surface. Light passing through the grating undergoes Bragg diffraction due to the refractive index modulation, and diffraction only occurs for specific wavelengths and angles of incidence that satisfy the Bragg condition.

VBGs can be either reflective or transmitting, as shown in figure 3.[113] For a reflective VBG the notch wavelength λ_B is given by

$$\lambda_B = \lambda_0 cos(\Theta) \tag{2}$$

where λ_0 is the antiparallel diffraction wavelength and is related to the grating period Λ

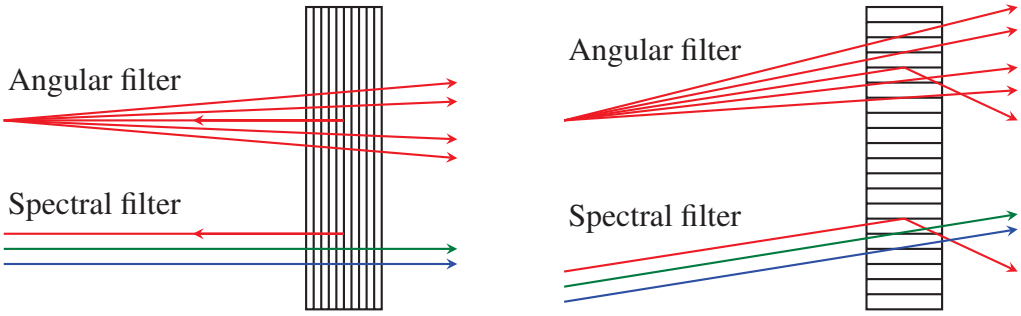

Figure 3: Reflecting (left) and transmitting (right) VBG filters.

and refractive index n by the relation $\lambda_0 = 2n\Lambda$, and Θ is the angle of incidence.[110] For each light wavelength and angle of incidence that satisfies the Bragg condition, there is actually a Bragg envelope within which light will still be diffracted efficiently. Light that does not fall within the spectral and angular bandwidths that satisfy the Bragg condition is not diffracted by the grating but passes through. The gratings can be tuned for different wavelengths or orders of diffraction by tilting with respect to the incident light beam.

VBG notch filters have bandwidths of the order of 10 cm^{-1}, enabling Raman bands with wavenumbers as low as 5 cm^{-1} to be observed.[107,108,110] In addition, they have high optical density (OD $\sim 4-5$) and high transmission (up to 95%), making them ideal for low-wavenumber Raman applications. VBGs have particularly high efficiency and transmission in the red and near-infrared. VBG notch filters designed for 785 nm laser wavelength have a bandwidth of 6 cm^{-1}, OD ~ 5, and $90-95\%$ transmission. For sufficient Rayleigh light suppression, several notch filters in series are often needed. The optical densities of a cascade of VBGs can be added if the filters are carefully aligned individually. Filters with the same angle of incidence and grating period will diffract beams that satisfy the Bragg condition for other filters if they are simply stacked together. In this case, the optical densities cannot simply be added, due to interference effects caused by double diffraction on individual VBGs. To overcome this problem, the slant angle and spacing of each grating can be varied so that the same wavelength satisfies the Bragg con-

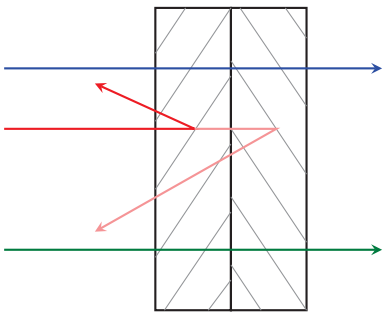

Figure 4: Diagram depicting how interference can be avoided when multiple VBG filters are used in series. The gratings are slanted at different angles so that each grating diffracts the light in a different direction.

dition for each filter, but the diffracted light from each VBG does not satisfy the Bragg condition for any other grating. This is illustrated in figure 4 for two stacked gratings. The incident beam is diffracted by each grating at such an angle that the beam diffracted by the second grating is not re-diffracted by the first.

The VBG filters incorporated into the Raman microscope were supplied by Opti-Grate Corp. Two types of filters were used, the BragGrate^{TM}notch filter (BNF) and the BragGrate^{TM}bandpass filter (BPF). These are both reflective VBGs. The BNF, which has a high optical density (OD) and narrow bandwidth (FWHM ~ 5 cm^{-1}), is used for Rayleigh line rejection. The BPF, while having lower OD, has an extremely narrow bandwidth (0.8 cm^{-1} - 8.0 cm^{-1}) and is ideal for cleaning up laser spectral noise by reflecting only the narrow laserline. Laserline cleaning is crucial to the performance of the BNFs.

2.2 Design, Fabrication and Assembly of a Raman Microscope

2.2.1 Design

Due to the close similarities between the optical configurations of Raman and fluorescence apparatus, a commercial fluorescence microscope was selected as the platform for constructing the Raman microscope. An Olympus IX70 inverted microscope was generously donated by Fonterra Corporation. This microscope has infinity optics, i.e. is designed to work with collimated light, which is an important characteristic as the VBG filters only work effectively with a well-collimated laser beam. The modification of the microscope was no simple task, as Raman microscopy is very different from normal light microscopy and requires very different optical components. While the IX70 is not built to accommodate these optics, it is, however, equipped for fluorescence microscopy, which proved to be of great benefit. A fluorescence filter cube turret can be inserted under the objective turret, which contains filters as well as a dichroic mirror that is used as a beamsplitter. Removal of the filter turret leaves a gap underneath the objective turret, as shown in figure 5, in which the microscope has been partially taken apart. Raman microscopy also requires a beamsplitter to separate the input laser and Raman-scattered beams, and in this case the plan was to use a BPF. This filter selectively reflects only the 785 nm laser line, while transmitting all other wavelengths. The only space in the microscope large enough to accommodate this optic was the gap between the objective turret and microscope base. Initially, it was thought that the BPF could be positioned underneath the objective, tilted at a 45° angle. The laser beam, which can enter through a port in the back of the microscope, would encounter the beamsplitter and be reflected up into the microscope objective. However, upon inspection of the BPF specifications it was found that Bragg diffraction will only occur at an angle of 19.8°. This requires the use of a mirror to direct the laser beam to the BPF so that the specified Bragg diffraction angle can be achieved. However, the available space for the optics is rather cramped, hence fitting both the BPF and angling mirror under the objective turret proved to be no easy task. Simple CAD drawings were made for a series of different mounts to determine which would fit in the space while still allowing fine adjustment of the mirror and BPF angles. This adjustment is crucial, due to the ultra-narrow diffraction angle window of the BPF. Suitable mounts were found (from Thorlabs Inc.), and a simple CAD diagram depicting how these mounts fit into the microscope is shown in figure 6a. A photograph of the optics and their respective mounts incorporated into the microscope is given in figure 6b.

Scattered light from the sample would be collected by the microscope objective and directed back towards the BPF, which would transmit the Raman-shifted light while rejecting most of the Rayleigh-scattered light. The scattered light then enters the main body of the microscope below the BPF. This contains three beamsplitting cubes mounted to a sliding rail, which are used to direct light through various ports in the microscope - the

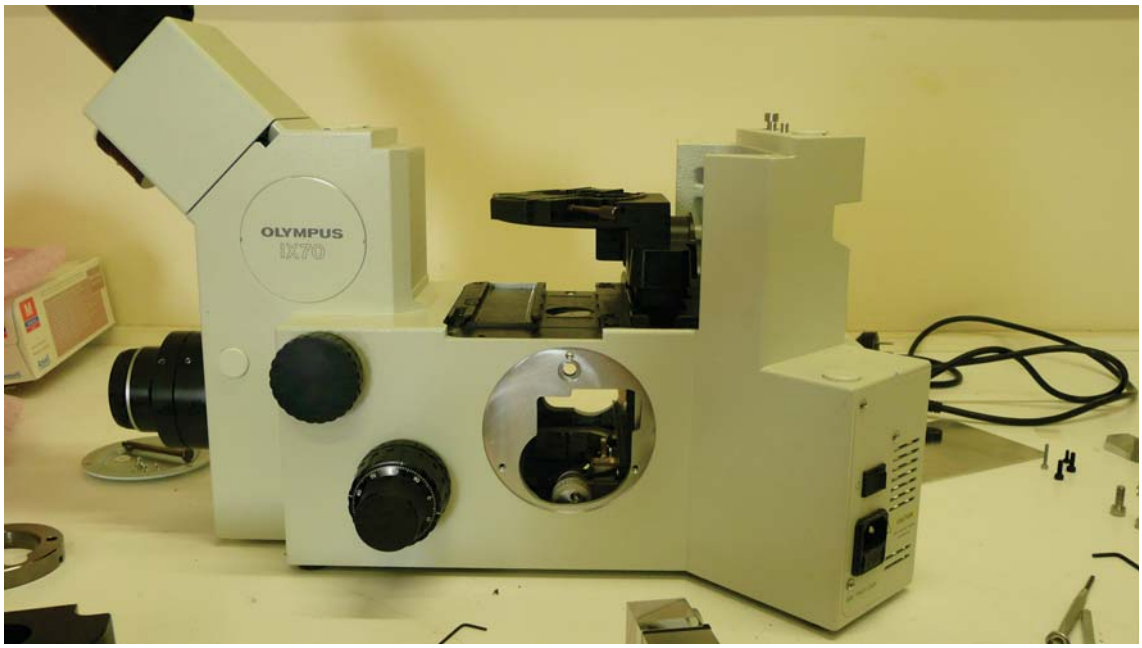

Figure 5: The IX70 microscope after removal of the lamp head, stage, objectives and beamsplitter rail.

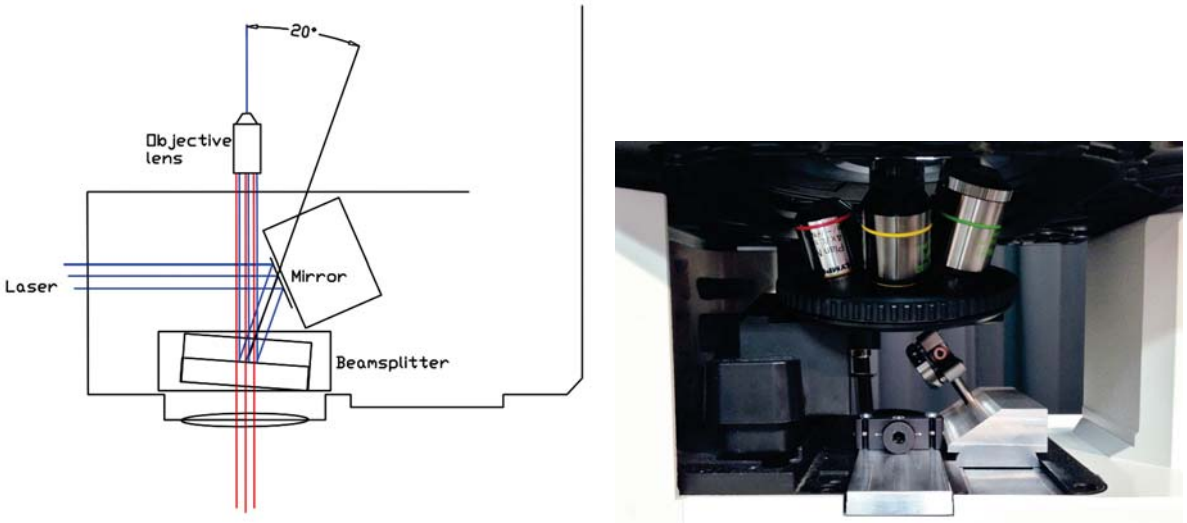

(a) **(b)**

Figure 6: (a) CAD design for 20° diffraction at the BPF and (b) photograph of actual setup.

eyepiece, camera or a port in the side of the microscope. The sideport was chosen as the best means for directing the Raman-scattered light out of the microscope. However, the corresponding beamsplitting cube is actually an 80:20 splitter, i.e. only 80% of the light is directed out the side port, while the remaining 20% is directed to the eyepiece. Thus, 20% of the signal would be lost. Raman scattering is already a very weak effect, thus it is imperative that all Raman-scattered photons be collected. The three beamsplitting cubes are all mounted to a single rail and can easily be removed. The plan was to replace the side port beamsplitter with a more suitable optic that would reflect 100% of the signal

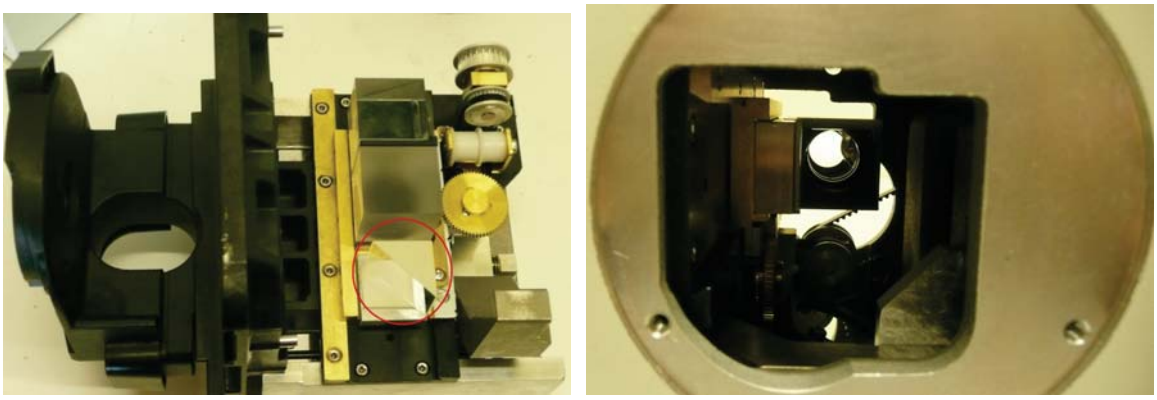

(a) **(b)**

Figure 7: (a) Prism mirror mounted to the beamsplitter rail. (b) View of the rail through a port in the side of the microscope.

out through the side port. The optic chosen for this was a right-angle prism mirror with a broad-band dielectric coating. Figure 7 shows this mirror mounted to the sliding rail, and inside the microscope as viewed through the side exit port.

2.2.2 Testing Components

The laser used in the microscope setup is a 785 nm frequency-stabilised narrow-linewidth fibre-coupled diode laser, with a maximum power output of 50 mW. Achieving good performance of the BNF filters requires that the wavelength of the excitation laser be very well matched to the filter wavelength.[107] A laser that is unstable will result in insufficient Rayleigh light suppression and the Raman signal will be overwhelmed. The beam was coupled into a single-mode fibre and then collimated using a FiberPort coupler/collimator (Thorlabs, Inc.). The lens in this optic can be aligned with five degrees of freedom, allowing excellent collimation to be achieved. A well-collimated incident laser beam is essential to obtaining the optimum optical density of a VBG, as the filter has an angular acceptance of about 5 mrad FWHM. This requires a beam divergence of less than 0.1°. A laser beam that is not properly collimated will result in part of the light not being rejected, which will effectively reduce the OD of the filter. Bragg diffraction of the collimated laser beam from a BPF filter, occurring at an angle of $\sim 20°$, is shown in figure 8a.

A Princeton Instruments PIXIS 400 camera and Acton LS 785 NIR high-throughput spectrograph were used for light collection. LightField®software was used for data acquisition, and the spectrograph was calibrated using the automated wavelength and intensity calibration package Intellical. The spectrograph has an XY fibre adapter in front of the entrance slit so that light coupled into a fibre can be delivered directly into the spectrograph. The spectrum of the 785 nm laser, delivered to the spectrograph via single-mode fibre, is given in figure 8b. The laserline has a very broad distribution, which is in direct contrast to the very narrow linewidth given in the laser specifications. Also shown is the

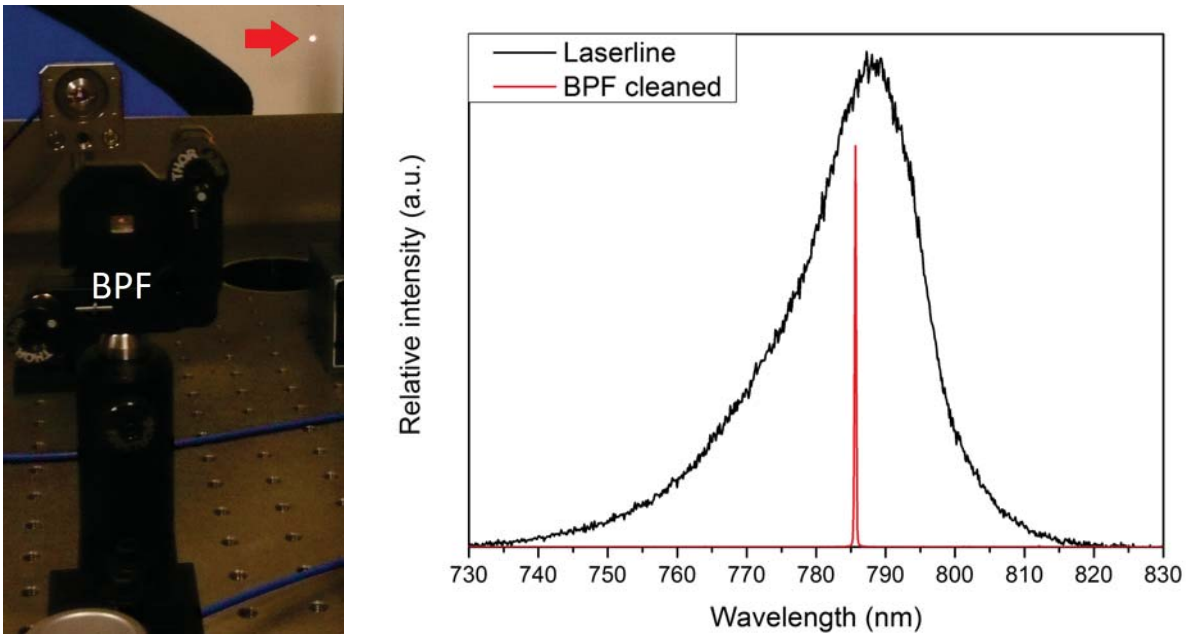

(a) **(b)**

Figure 8: (a) Image showing diffraction of the laser beam, collimated by the FiberPort, from the BPF. The diffracted beam spot is marked with a red arrow. (b) Spectrum of the laserline before and after BPF cleaning. Laser power (<0.5 mW).

spectrum of the beam after it has been cleaned with one BPF filter. In contrast, the laserline is now very narrow, with a FWHM of 0.25 nm. The spectra of the direct and cleaned laserline were both recorded at very low laser power (< 0.5 mW). When the spectrum of the laser delivered via single-mode fibre without BPF cleaning is recorded at higher laser power but shorter integration time, the linewidth becomes very narrow, as shown in figure 9a. The effect of adding one BNF filter into the path of the BPF cleaned laser beam (and angle tuned to meet the Bragg condition) is shown in figure 9b, in which great suppression of the laserline is apparent.

2.2.3 Preliminary Setups

Before setting up the full Raman microscope, a simple preliminary setup was constructed to test the suitability of the VHG filters in a Raman microscope system. In this design, a microscope objective lens was used to both focus the collimated laser beam onto a sample and collect and collimate the backscattered light. The final optimised version of this setup is illustrated in figure 10. The BPF functions as a beamsplitter, diffracting the laser and Rayleigh line while transmitting Raman-shifted photons. The objective lens was centred and aligned with the optical path using a series of mirrors and irises. The objective was held in a mount with fine x,y,z translational and rotational adjustment about two axes, which also aided in alignment. With the two irises pre-aligned in the beam path, the objective was added and alignment was monitored by adjusting the objective so that the focused

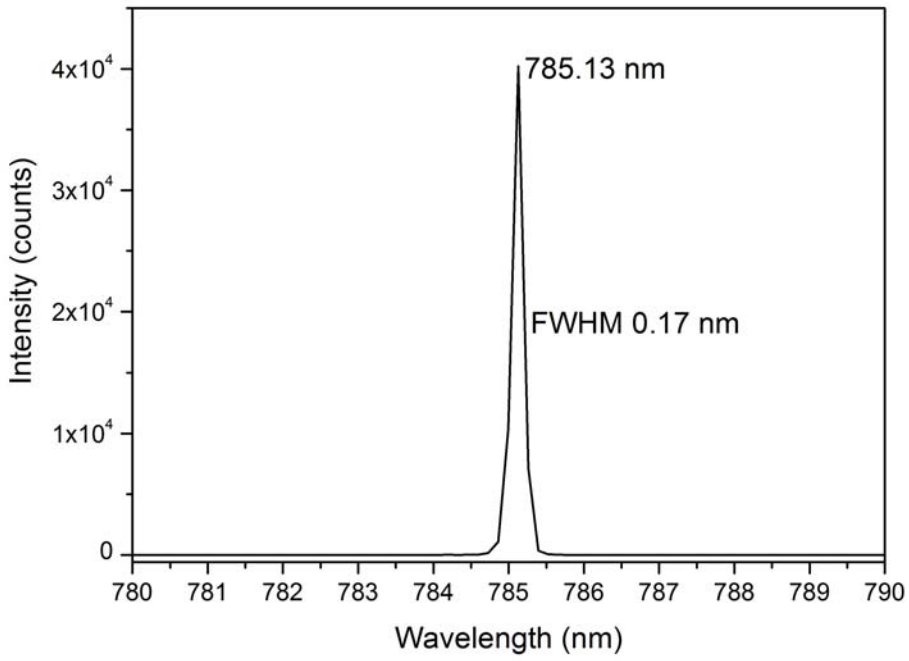

(a)

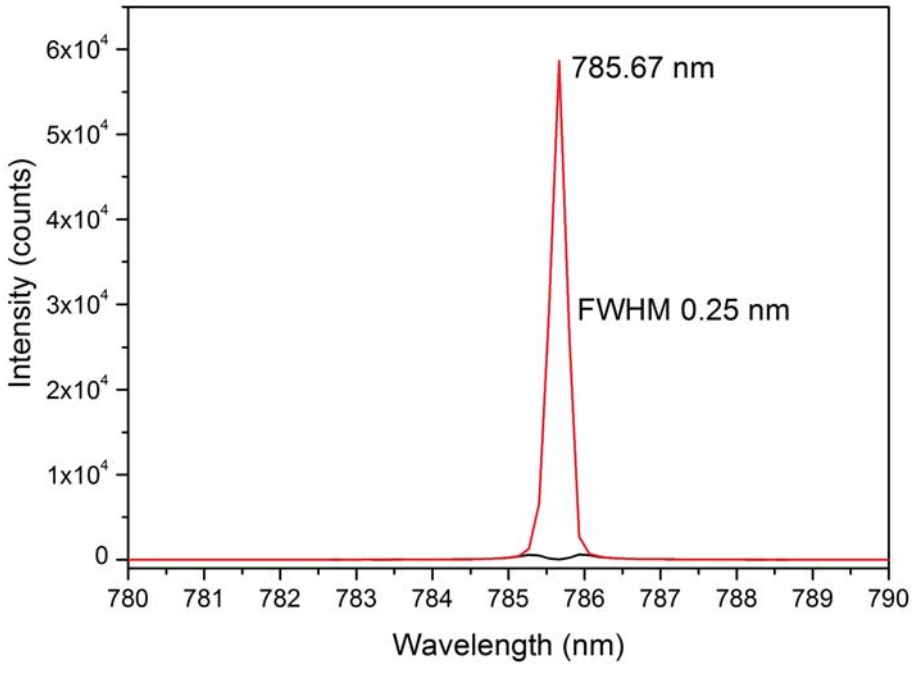

(b)

Figure 9: (a) Laser spectrum at higher power, without BPF cleaning. (b) Spectrum of BPF cleaned laserline with and without blocking BNF.

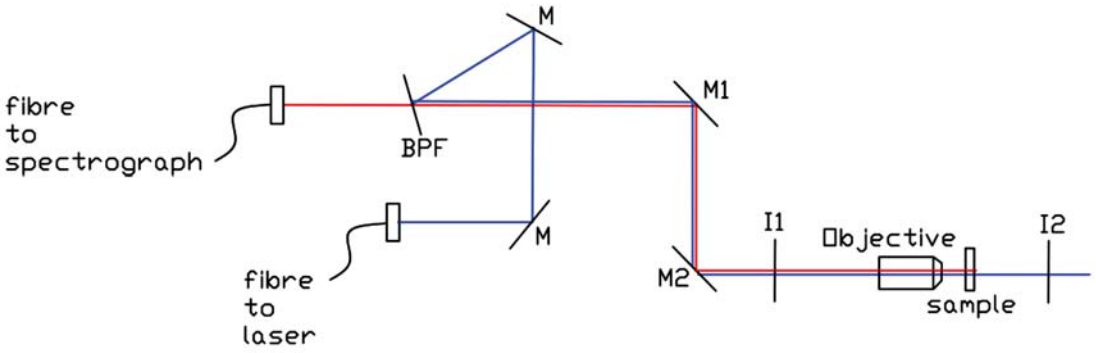

Figure 10: Diagram of the preliminary Raman setup. Optics labelled 'M' and 'I' are mirrors and irises, respectively.

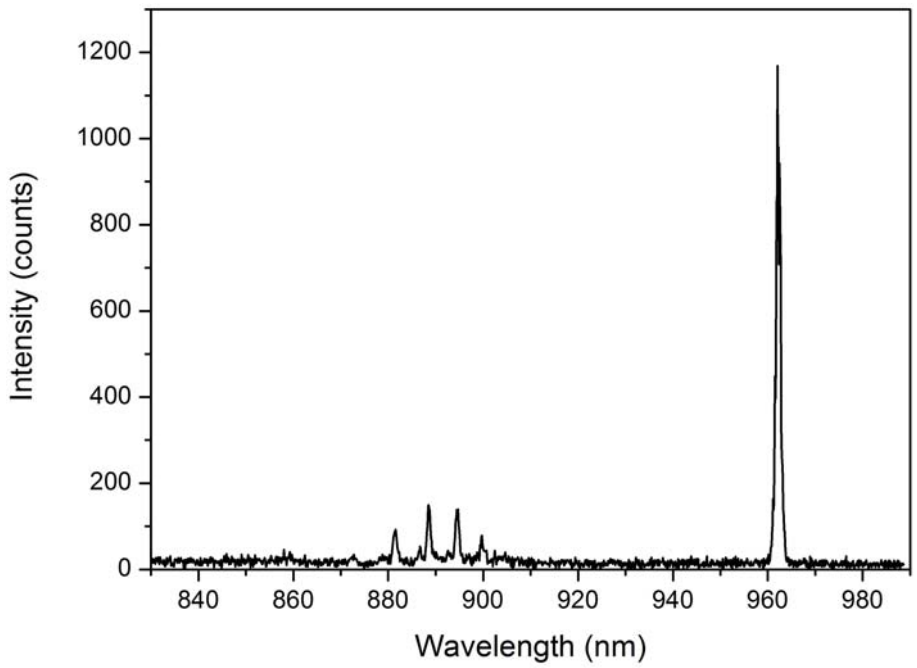

Figure 11: Spectrum of the laser background.

beam exiting the objective was centred on iris 2, while at the same time the backscattered beam reflected off a mirror placed at the objective focus was centred on iris 1. Optimum alignment is achieved when the beam remains centred on both irises as the objective is moved along the optical axis. A FiberPort was used to collect the backscattered light. This was mounted to a stage with rotational and translational adjustment, and alignment was achieved by adjusting the FiberPort and stage until optimum Rayleigh line intensity was obtained. The system was tested with cyclohexane, which is a good Raman liquid test sample. However, no cyclohexane Raman peaks could be detected in the spectrum, even after much re-alignment and painstaking iterative adjustments to all of the optical components. The spectra obtained were not flat and featureless, however. On the contrary, they were very consistent in appearance, with several rather intense peaks. These peaks could not be accounted for by anything in the sample, as they were also present with an empty glass vial, and even without any sample. A typical spectrum of these peaks is given in figure 11. To identify where the problem with this setup was and why a Raman signal could not be detected, a different arrangement was constructed, in which a second objective identical to the first was placed in a 90° configuration relative to the illuminating objective, to collect the light scattered from the sample. This is illustrated in figure 12. The three important optical components in the setup are the BPF, objective and FiberPort. With this arrangement, in which the BPF was no longer present in the path of the scattered light, clear peaks were visible in the Raman spectrum of cyclohexane. This would immediately suggest that the BPF was causing problems in the first setup. However, placing an angle-tuned BPF in the path of the scattered light did not have any significant effect on the Raman intensity, which effectively ruled out the BPF as the cause of the problem. It was found that the Raman intensity could be greatly increased by tweaking the objective lenses and FiberPort adjustments, as well as coupling of the collection fibre into the spectrograph. The optimised Raman spectrum of cyclohexane gave ~ 800 counts s^{-1} for the 801 cm^{-1} band. A typical spectrum is given in figure 13.

The two-objective setup did not identify the cause of failure with the initial single-objective setup, other than eliminating the BPF as the problem. However, since a good Raman spectrum had been obtained with this setup, it became very puzzling as to why the same could not be done using a single objective to focus and collect the light. Hence, another attempt was made with the first setup (see figure 10), which actually turned out to be successful after development of a painstaking, systematic alignment procedure. The initial spectra recorded were far from perfect and included the same background peaks that had previously been observed with this setup. However, after adding BNF filters into the scattered path to block the Rayleigh line and making adjustments to many of the optical components, the Raman peaks could be greatly optimised while diminishing the background peaks. The optimised Raman spectrum of cyclohexane is given in figure 14. While several background peaks are still present, the Raman peaks are now dominating

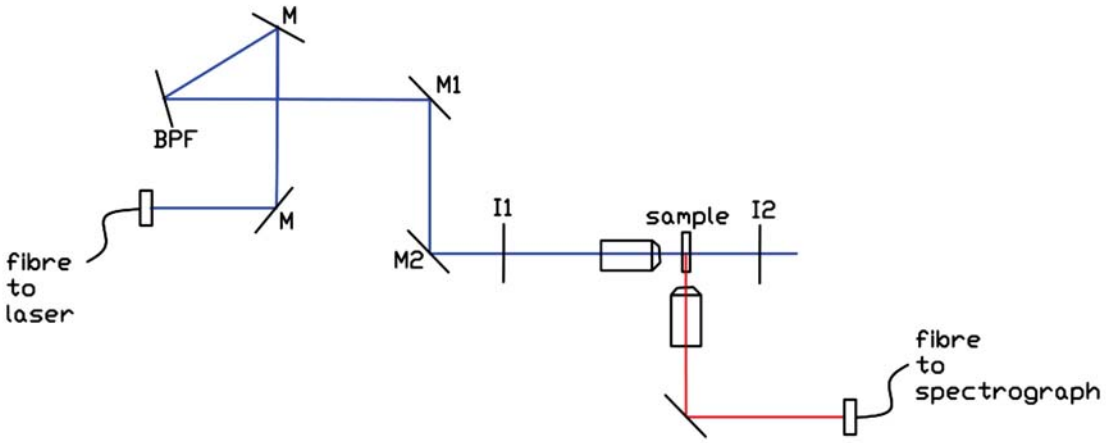

Figure 12: Raman setup with separate objectives to illuminate the sample and collect the scattered light.

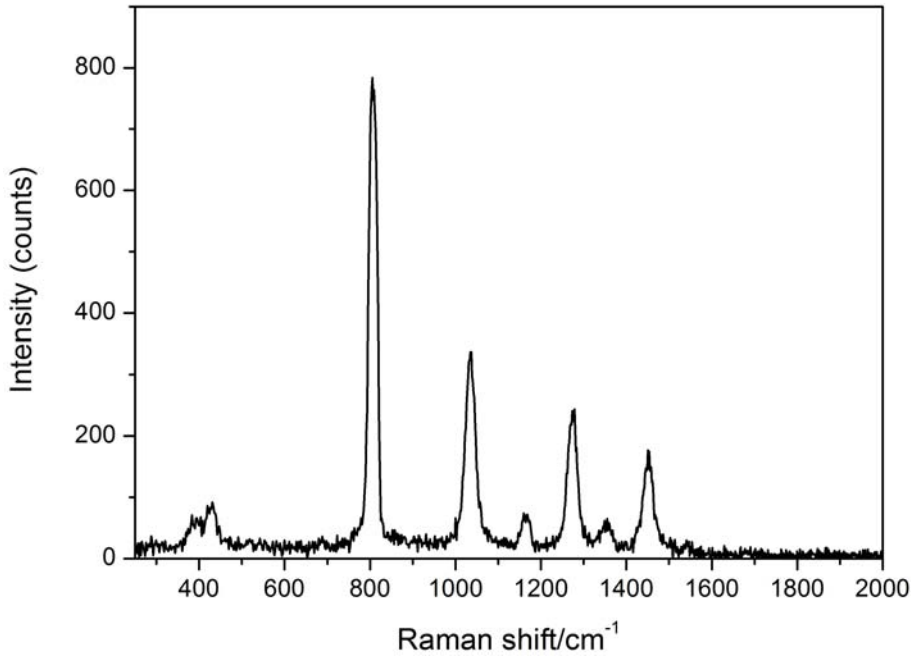

Figure 13: Raman spectrum of cyclohexane with 90° collection geometry, and Rayleigh suppression with 2 BNFs. Spectrum taken with 4x microscope objective. Integration time 1s.

the spectrum. Overall, a higher Raman intensity was obtained with the single-objective setup compared to the two-objective setup, though the background peaks were also higher. The objectives used in both setups were Olympus Plan N 4x objectives with a numerical aperture (NA) of only 0.1. NA is a dimensionless number that represents the range of angles over which an optic can accept or emit light, with a higher number corresponding to a larger range of angles. The laser beam diameter was ~ 3.5 mm, which is significantly smaller than the clear aperture of the objective lens (> 5 mm), hence the effective NA would actually be somewhat lower than that specified. All things considered, the Raman signal obtained with this setup is rather good and shows that the VBG filters should in-

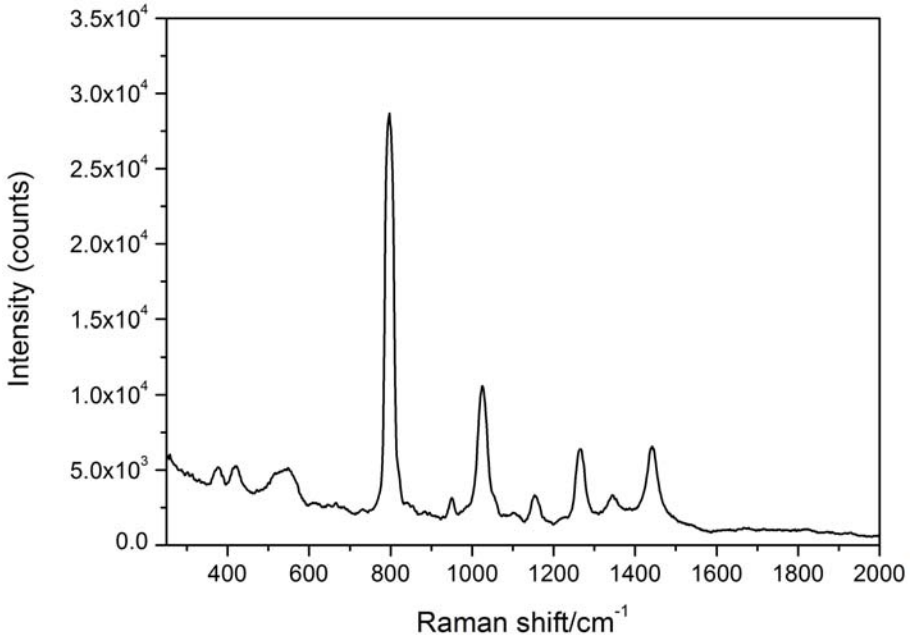

Figure 14: Raman spectrum of cyclohexane with backscattering geometry and Rayleigh suppression with 2 BNFs. Spectrum taken with 4x microscope objective. Integration time 10s, average of 10 accumulations.

deed be suitable in a Raman microscope system. Furthermore, these results look very promising when considering what kinds of Raman intensities should be attainable when objective lenses with much higher numerical apertures are used.

2.2.4 Microscope Alignment

The next step was to set up the Raman microscope. In principle, the microscope setup is very similar to the preliminary setup in figure 10, though it was anticipated that alignment would be more difficult as the objective can be moved only along the optical axis, and there are no mirrors between the BPF and objective lens, which greatly aided alignment in the preliminary setup. As mentioned earlier, the FiberPort produces a collimated beam with a diameter of ~ 3.5 mm, which is significantly smaller than the apertures of the BPF and objective lens. For optimum Raman intensity and resolution, it is important to take full advantage of the NA of the objective by uniformly illuminating the full back aperture of the objective. The largest possible beam diameter that can be produced is determined by the BPF aperture, which has dimensions 5 mm x 7 mm. One way to control and optimise the diameter of the laser beam before it enters the microscope so that the BPF is fully and uniformly illuminated is to use a beam expander. The beam expander chosen for this purpose has continuously variable beam expansion/reduction of $0.5\times$ to $2\times$ the input beam diameter. In addition, it also has beam divergence adjustment, which enables fine-tuning of the expanded beam collimation. To simplify alignment, the idea was to mount the FiberPort, beam expander and mirror for directing the expanded beam into the

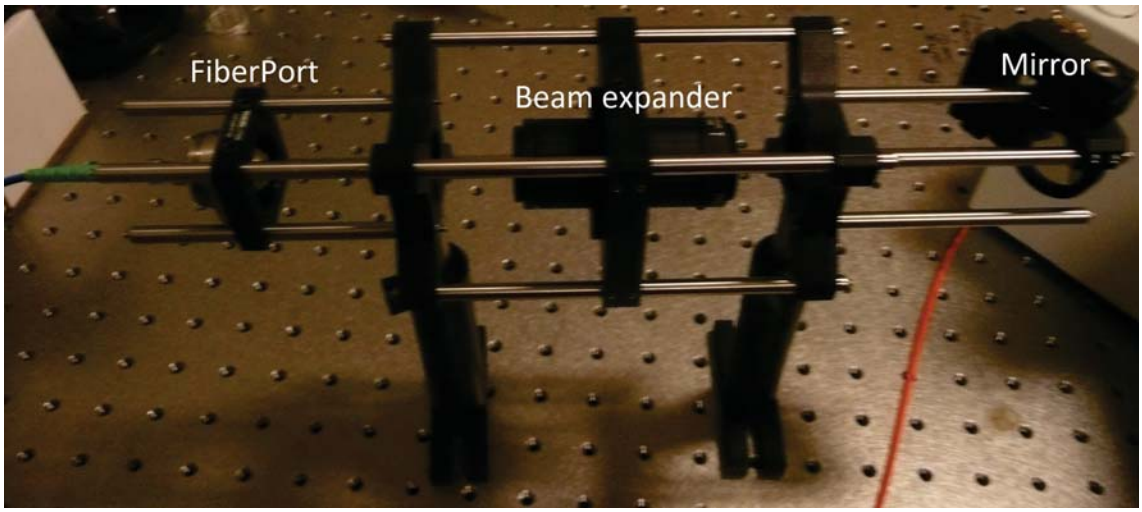

Figure 15: Beam collimating and expanding optics incorporated into a cage system.

microscope, in a cage system. This effectively aligns the components along the optical axis. The cage system setup is shown in figure 15. The expanded beam appeared to have a Gaussian-like distribution, with the intensity dropping near the edges of the beam. The beam was expanded to a diameter greater than the BPF aperture, in an attempt to cut off the lower intensity edges. The resulting beam diffracted from the BPF was rectangular in shape (corresponding to the dimensions of the optic) and appeared to have a uniform intensity distribution.

It was anticipated that alignment of the diffracted laser beam up into the microscope objective would likely be one of the main challenges in setting up the Raman microscope. Alignment of the preliminary setup showed that tiny adjustments to the alignment can severely impact the Raman signal. Hence, it was reasoned that careful pre-alignment of the optical path before attempting to collect a Raman signal would save a lot of time and frustration. One of the most important aspects to consider in aligning the microscope optics is alignment of the BPF. This must be fixed precisely below the microscope objective and be tilted at exactly the right angle so that when the Bragg condition is satisfied the beam will be diffracted up into the objective exactly along the optical axis (i.e. parallel to and centred in the objective). Once the BPF has been correctly positioned, alignment of the remaining optics should be relatively straightforward - a matter of directing the laser beam to the BPF with the mirrors so that the Bragg condition is met. The narrow angular Bragg envelope is actually advantageous for alignment in one respect, as it essentially defines the optical axis. Once the beam has been directed to the BPF at the Bragg diffraction angle it will already be aligned correctly in the objective.

To align the BPF it was necessary to first define the optical axis through the microscope objective. This was accomplished using the overhead lamp of the microscope and two irises, as illustrated in figure 16a. Without any objective lens in the turret, iris 1 was positioned underneath the lamp and roughly centred above the empty objective hole. Iris

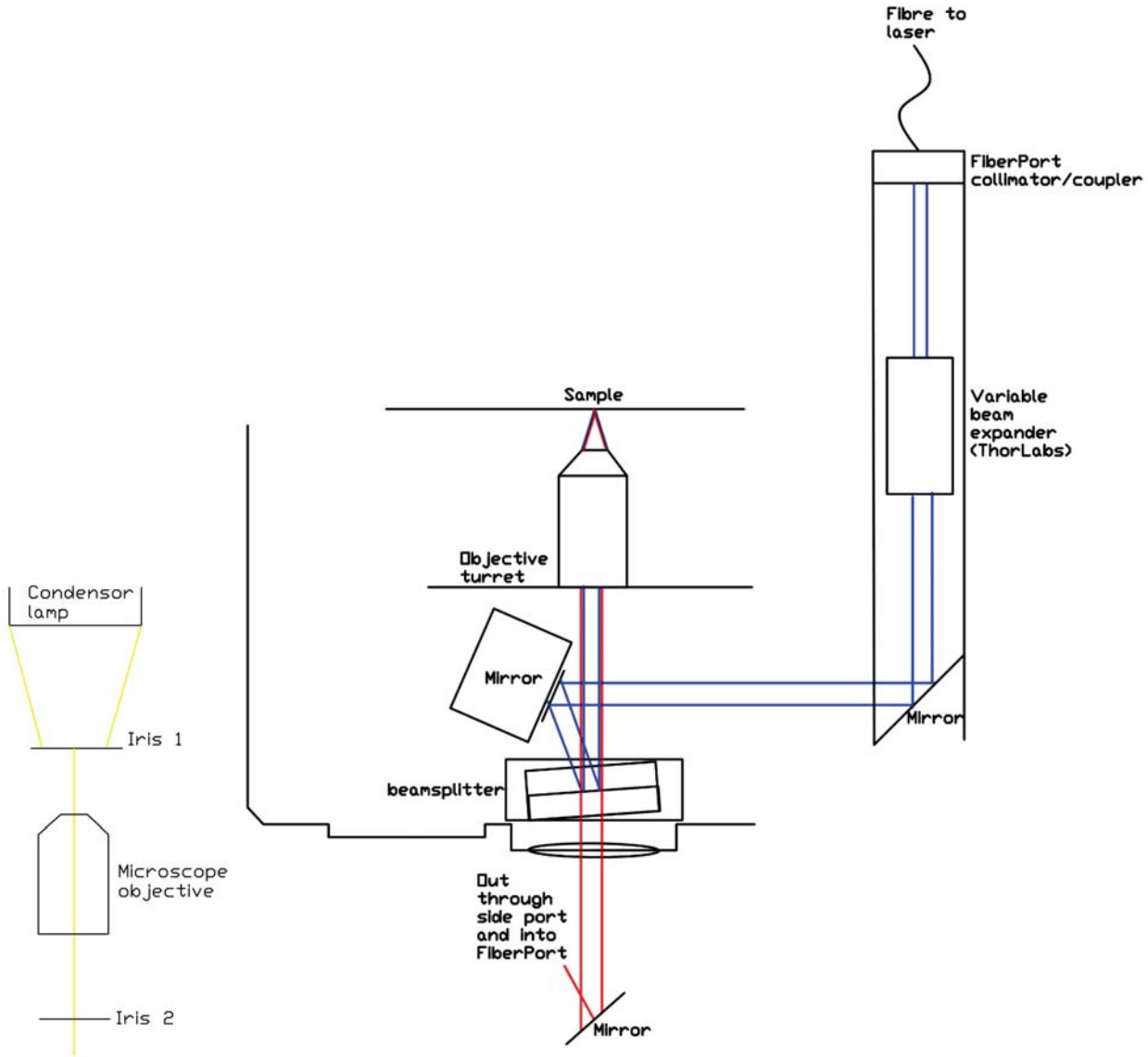

(a) **(b)**

Figure 16: (a) Drawing of the system used for initial alignment of the BPF. (b) Drawing of the first microscope setup. Note that the cage system is actually rotated 90° into the page.

2 was placed underneath the objective turret and positioned in the centre of the thin beam of light passing through iris 1. Upon rotating the turret so as to position one of the objective lenses in the beam path, the beam had drifted and was no longer centred on iris 2, indicating that the irises were not correctly aligned. The position of iris 2 was then adjusted until the beam was centred on the iris. The turret was then rotated to a different magnification objective and this time iris 1 was adjusted to achieve centering on iris 2. The turret was rotated back to the previous objective and centering achieved by adjusting iris 2. This process was repeated in an iterative procedure until the beam remained centred on both irises upon switching between the different objective lenses. The turret was then rotated through all the objective lenses as well as the empty objective slot to check that the beam remained centred for all. The two irises should now be aligned with the optical axis. The overhead lamp was then removed and the 785 nm beam emitted from the FiberPort attached to the multimode fibre was positioned above the objective turret and carefully aligned through the two irises. The laser beam should now be collinear with the optical axis. Removing iris 2, the BPF was positioned underneath the objective turret so that the laser beam was centred on the optic surface. The BPF was carefully tilted in its mount until the Bragg condition was achieved and diffraction of the beam occurred. The mirror in the Polaris mount (underneath the objective turret as shown in figure 6a) could then be positioned and centred in the path of the diffracted beam. This mirror was used to direct the beam out through the back port of the microscope, where it encountered the cage system optics. The beam was reflected off the Gimbal-mounted mirror (in the cage system) and into the beam expander aperture. The Polaris and Gimbal mirrors were adjusted until the beam passed through the centre of the telescope and was centred on the collection FiberPort at the end of the cage system. The beam should now be traveling along the reverse of the final optical path. The multimode fibre was then disconnected from the laser source, and the free end of the single mode fibre was connected to the laser. Now the beam emitted from the cage system FiberPort travels through the beam expander to the Gimbal mirror, where it is directed into the Polaris mirror inside the microscope, to the BPF, and finally, up into the microscope objective, as shown in figure 16b. Small adjustments were made to the Polaris and Gimbal mounts to optimise the intensity and distribution of the diffracted beam spot.

Following alignment of the expanded, collimated laser beam along the optical axis of the microscope, the next step was to collect a Raman spectrum of cyclohexane. The collection FiberPort was aligned in the scattered beam path exiting the microscope sideport by placing a mirror above the microscope stage and using this to reflect the beam back down the optical pathway. The small fraction of light not blocked by the BPF is directed out through the side port in the microscope and into the FiberPort, which is mounted to a movable stage with two translational and two rotational degrees of freedom, as shown in figure 17. Following this coarse alignment, the FiberPort was further aligned by mon-

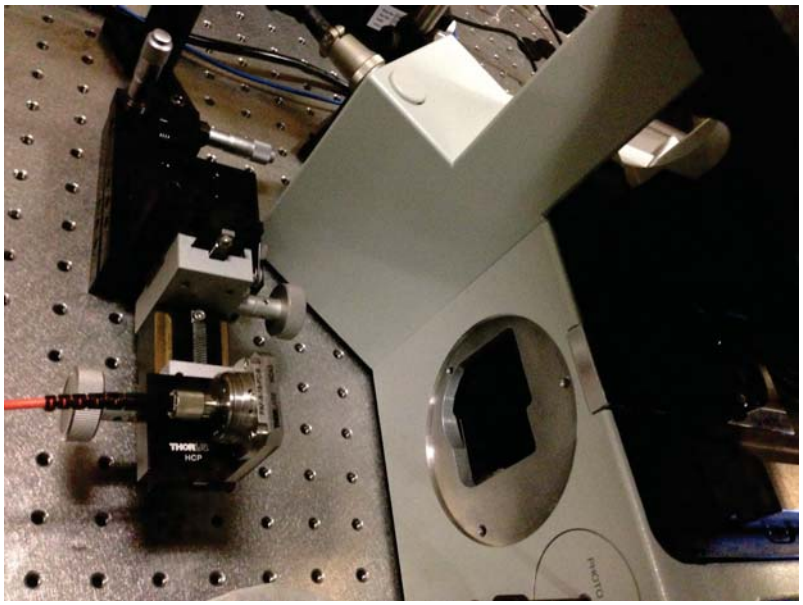

Figure 17: Photograph of the FiberPort positioned to collect the scattered light exiting the microscope side-port.

itoring the Rayleigh peak intensity (of a paper tissue sample) as adjustments were made to the FiberPort. Even after careful alignment of both the input and collection optics, no Raman peaks could be detected in the spectrum of cyclohexane. The same background peaks observed in the previous setups also dominated the spectrum. Many attempts were made to adjust the optics at various positions (microscope, collection, into spectrograph etc.) in order to detect even the tiniest Raman signal, but to no avail. It appeared that the same problems were being encountered again, even after all the careful pre-alignment. A different approach was then trialled in an attempt to align the microscope optics more accurately. This involved monitoring the alignment of the laser beam through the microscope objective using the eyepiece. The weak reflection of the laser beam at low power from a glass slide is followed through the optical train of the microscope and to the eyepiece. The beam alignment optics (mirrors and BPF beamsplitter) are adjusted until the beam appears to be centred in the objective, as observed by placing a piece of tissue paper above the objective, while at the same time the reflection from the glass slide is centred in the field of view, which is marked with a cross-hair, as observed through the eyepiece. However, even after this alignment, a Raman signal still could not be detected. Hence, microscope alignment was ruled out as being the likely cause of the problem, and the focus was turned to the collection FiberPort. Upon coupling the laser directly into the FiberPort via single mode fibre, the resulting beam did not appear to be very well collimated. After adjusting the FiberPort to properly collimate the beam and positioning in the scattered beam path, a very weak cyclohexane Raman signal was observed, though the background peaks still dominated the spectrum. After optimisation, the 801 cm^{-1} peak could be clearly distinguished, as shown in figure 18.

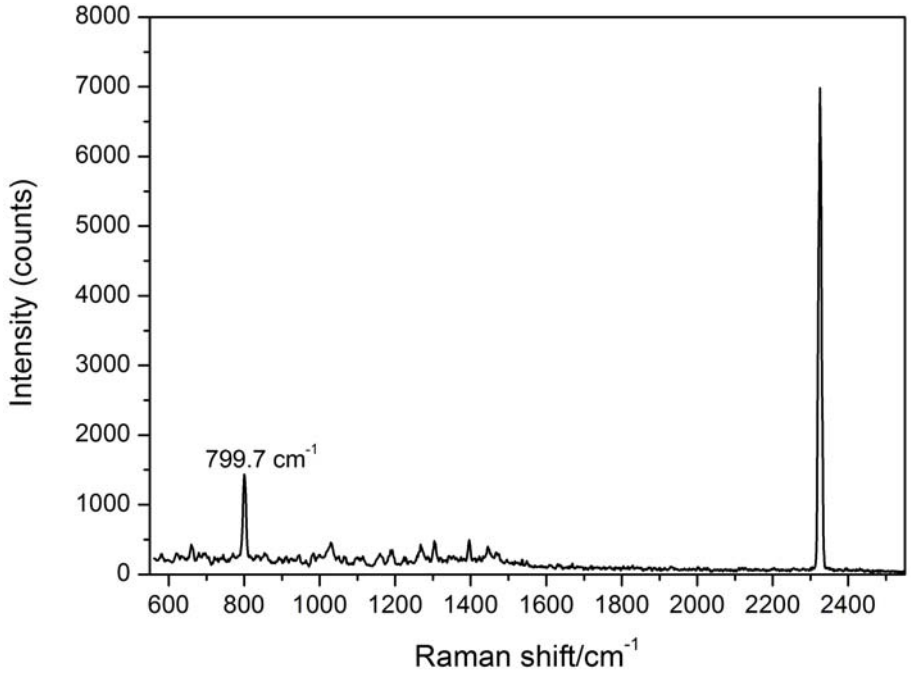

Figure 18: Initial Raman spectrum of cyclohexane, taken with a 4x microscope objective.

The next step was to investigate the cause of the background peaks that seemed to appear in all the spectra. It is possible that these peaks are laser emission lines and are being observed due to the beam not being cleaned properly. It is recommended that the laser beam be cleaned by two BPF filters, whereas in this setup only one BPF (the beamsplitter) was being used. Hence, a second BPF was incorporated into the setup to clean the beam before it enters the microscope, and the new setup is given in figure 19. Cleaning with a second BPF did not result in any reduction in intensity of the background peaks, although it did improve the baseline around the laserline. This would suggest that the BPF filters are only effective in cleaning spectral noise close to the laserline. To confirm whether the background peaks are in fact emission lines of the laser itself, spectra were recorded of the laser beam directly into the spectrograph, through a single mode fibre, reflected from a glass microscope slide and diffracted by a BPF. The same background peaks were evident in all spectra, suggesting that these are indeed laser emission background and not arising from interaction with other components in the setup. When a BNF filter was aligned in the path of the scattered beam to block the Rayleigh line, the intensity of the emission background was greatly reduced, and addition of successive BNF filters further diminished the background until the emission peaks were almost indistinguishable from the baseline. Making small adjustments to the BNF tilt angles affected the emission background intensity in the same way as they do the Rayleigh peak. Hence, it appears that these emission peaks, which are far removed from the laser line, are also being diffracted by the BNFs, and this is a rather strange result. Shown in figure 20 is the Raman spectrum of cyclohexane with the Rayleigh line being blocked by three optimally aligned BNF fil-

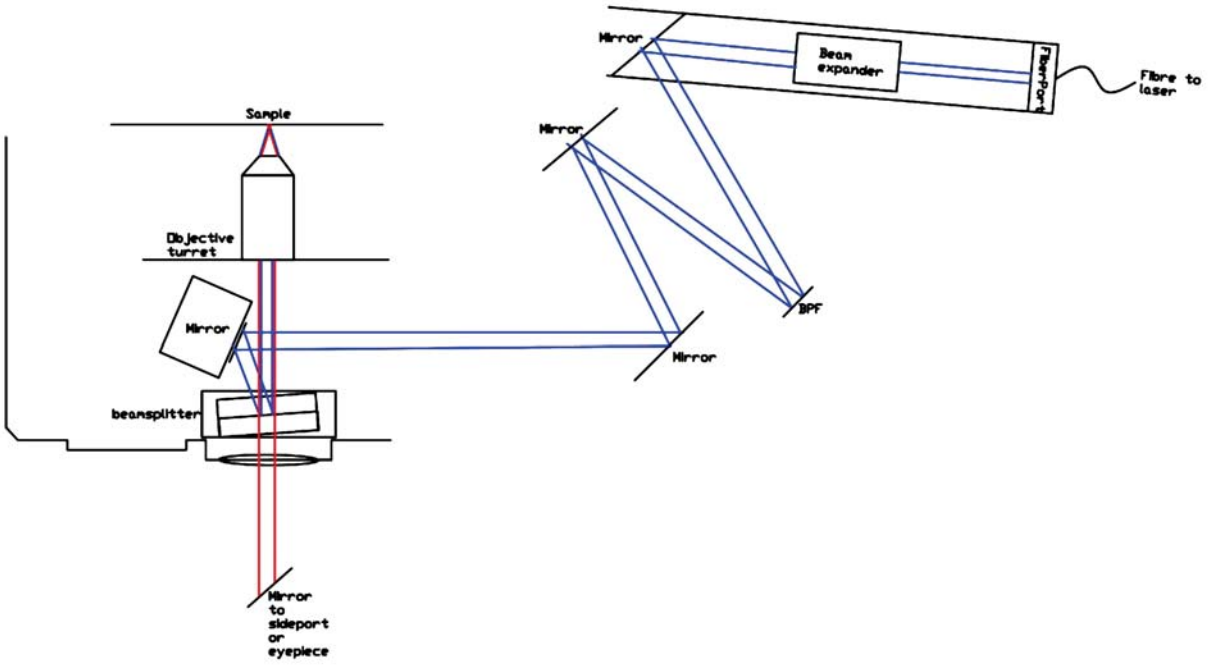

Figure 19: Drawing of the final microscope setup. Note that the input optics are actually rotated 90° into the page.

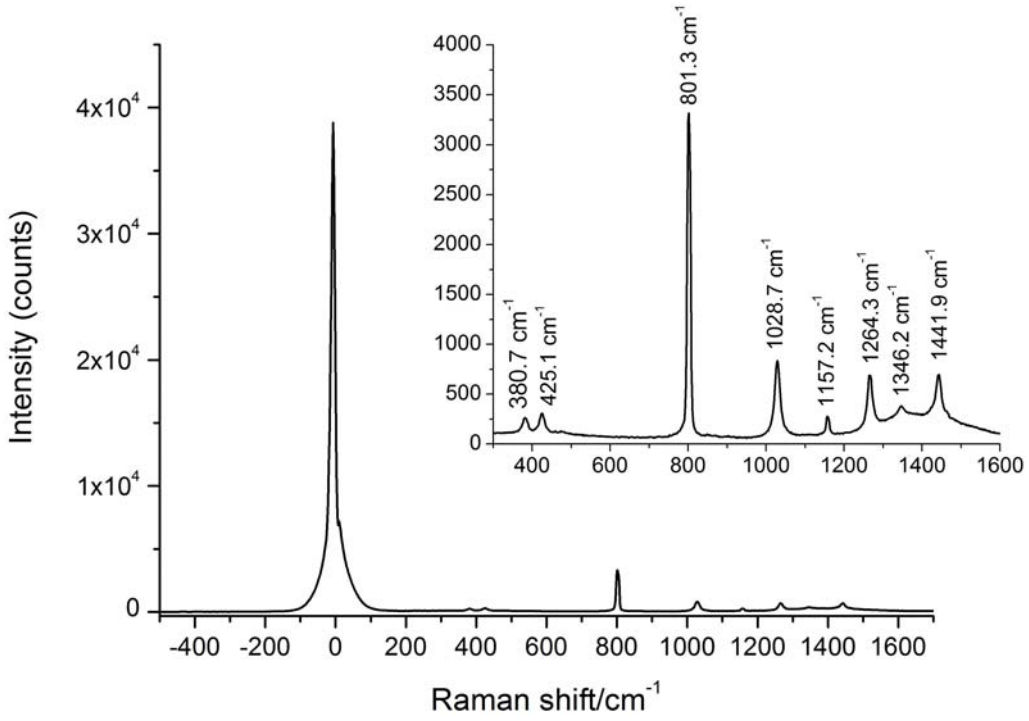

Figure 20: Raman spectrum of cyclohexane, with 3 BNFs rejecting the Rayleigh line. Taken with a 4x microscope objective. Integration time 1s, average of 10 accumulations.

ters. While the Rayleigh line still dominates the spectrum, the Raman peaks are clearly visible without the Rayleigh peak saturating the detector.

2.2.5 Optimisations and Improvements

Correspondence with Sergei Lebedkin from Karlsruhe Institute of Technology afforded very helpful insight into how the microscope setup could be improved. It was suggested that a long-focal-length achromatic lens be used to focus the scattered beam into the collection fibre, rather than the FiberPort which was currently being used for this purpose. The FiberPort is not ideal for collecting the scattered light, due to a number of reasons. It typically has poor performance in covering a broad spectral region, which may result in losses in the Raman intensity of bands far from the laser line. The FiberPort also has a rather small aperture, which could cut out some of the scattered light. Finally, it is rather difficult to precisely control the distance between the fibre and lens with the FiberPort, as three separate screws must be tightened or loosened simultaneously by precisely the same amount to control this distance while ensuring the lens also remains un-tilted. Hence, it was decided that an achromatic doublet with a 100 mm focal length would be used to collect the scattered light. Another point to consider was the choice of fibre used to collect the scattered radiation. It has been reported that using collection fibres with different core diameters give significantly different Rayleigh:Raman intensity ratios.[108] In the work described so far, a multimode fibre with a 200 μm core diameter has been used, which is significantly larger than the optimum diameter of 50 μm, which is known to give the best compromise between Rayleigh rejection and Raman intensity. A fibre with a smaller core diameter would result in better performance of the BNF filters, as a smaller focused spot size is associated with better collimation and thus higher Rayleigh rejection. Another advantage of using a smaller core collection fibre is that it will give better spatial resolution, as by default the fibre serves as the pinhole in a confocal Raman setup. Based on these considerations, a new collection fibre was chosen - a step-index multi-mode fibre with a 50 μm core diameter. This, along with the achromatic lens, was held in a cage system to aid in alignment. As shown in figure 21, the lens is mounted in a Z-axis translation mount, which allows for fine adjustment of the position of the lens along the optical axis to focus into the fibre. The fibre is held in an XY translation mount, which allows for fine adjustment of the fibre position. The entire cage system is mounted to a stage allowing translational and rotational movement in two directions, to centre the unit precisely in the scattered beam path. To align the collection optics with the optical path of the scattered beam, the 785 nm laser is first put through the collection multimode fibre, collimated by the tube lens, and directed along the reverse of the scattered optical path and into the microscope. It then travels up through the BPF and into the microscope objective. The four degrees of freedom of the cage system stage, along with the x,y fibre translations are adjusted iteratively until the beam optimally meets the Bragg condition of the BPF while remaining centred in the objective as the tube lens is moved back and forth along the optical axis.

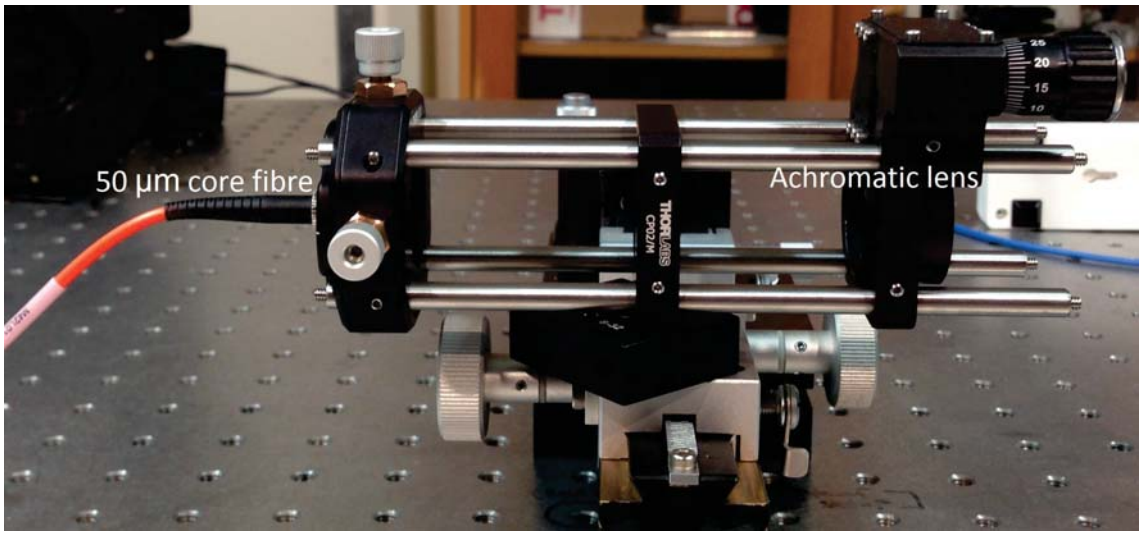

Figure 21: Photograph of the collection fibre and tube lens aligned in a cage system.

So far, only liquid samples in glass vials had been used as the Raman samples. However, these samples did not produce very good Raman spectra with higher magnification objective lenses ($>$ 4x), and this may be due to the curved surface of the glass sample vial acting as a lens. A solid sample such as a silicon wafer, which is also a strong Raman scatterer, would be a much more ideal sample to use for further optimising the microscope optics. Unlike what was observed with the cyclohexane sample, Olympus objectives of higher magnification (40x and 60x) gave a stronger Si Raman signal than the lower magnification objectives. This is due to objectives of higher magnification typically having higher numerical apertures. Polished Si wafers are a dark, shiny gray colour and are highly reflective, hence the laser beam cannot penetrate very far into the sample and effectively excites only the outermost layer of silicon. For this reason, a Si wafer is an ideal sample to use in finding the correct distance between the tube lens and collection fibre (which functions as the pinhole), as the pinhole must be positioned precisely the correct distance from the tube lens in order to collect the light scattered from the surface of sample. However, this first requires the laser to be focused (via the microscope objective) exactly at the Si surface, which is difficult to do without first having the fibre and pinhole at exactly the right distance from each other. Hence a thicker, more transparent sample would be more suitable, as the exact point of focus within the sample would no longer be critical. The sample used for this was a glass coverslip with a thickness of ~ 0.2 mm, which is much larger than the typical focused spot size of microscope objectives. While glass is not a strong Raman scatterer, glass coverslips were found to have strong fluorescent signals at 785 nm. To determine the exact position of the pinhole relative to the tube lens (achromatic lens), the initial approach was to monitor the glass fluorescence intensity as the tube lens was moved along the z-axis, where peak intensity corresponded to the correct position. The spectra of the glass coverslip and a Si wafer taken with an Olympus

60x objective after determining the correct focal distance using this method are given in figure 22. The problem with this approach, however, was that the optimum distance between the fibre and pinhole for the 40x and 60x Olympus objectives appeared to be quite different from the specified 100 mm tube lens focal length. Furthermore, Rayleigh rejection was quite poor at the optimum fluorescence or Raman intensity. A slightly different approach was tried, in which the optimal pinhole position was determined by monitoring the ratio of the fluorescence:Rayleigh peak intensities as the tube lens was moved along the z axis. This ratio should peak when the lens is at the correct distance from the pinhole (100 mm), and this is exactly what was found. However, for the 40x and 60x Olympus objectives, the fluorescence intensity at 100 mm focal distance was significantly lower than at the pinhole position that gave optimum fluorescence intensity. The difference in tube-lens-to-pinhole distance for the optimum fluorescence intensity and optimum fluorescence:Rayleigh ratio was found to be ~ 5 mm for the 40x objective and ~ 10 mm for the 60x objective. Initially, it was reasoned that this could be due to chromatic aberration occurring in the near-IR region, as most microscope objectives only have good aberration corrections in the visible wavelength region. A diagram depicting how this could occur is shown in figure 23. Chromatic aberration arises due to the wavelength-dependence of the refractive index of the lens material in the objective. The refractive index is smaller for longer wavelengths, hence Raman-shifted light collected from the objective focal point will be refracted by a smaller angle in the objective lens, and will exit the objective somewhat divergent, rather than as a collimated beam. This divergent beam will be focused by the tube lens to a point away from the focal point for a collimated beam. A problem with this explanation, however, is that different Raman or fluorescence bands at different wavenumbers did not appear to be focused differently from each other, but only from the Rayleigh line. Furthermore, the shifts in tube lens focal distance for fluorescence and Rayleigh lines appeared to be much too large to be attributed to chromatic aberration, as this would correspond to a difference of ~ 300 μm between the effective focal lengths (at the objective) for Rayleigh and fluorescent light. This is huge compared to the size of the spot focused at the sample, which is of the order of microns. If chromatic aberration was indeed the case, then for the Si wafer, effectively no Raman light should be collected when the pinhole is positioned to collect light from the 785 nm beam focal point, but this is not what was observed. The drop in intensity of the Raman bands when the tube lens focal distance was moved from that for optimum Raman intensity to that for optimum Rayleigh rejection was only about a third.

Other Olympus objectives of lower magnifications (4x - 20x) were tested to see if these would give the same puzzling behaviour observed with the 60x and 40x objectives. The results, however, were quite different. Optimum Raman intensity and Rayleigh rejection occurred simultaneously at the specified tube lens focal length, without any apparent difference in focusing of the Rayleigh and Raman-shifted light. This behaviour was also

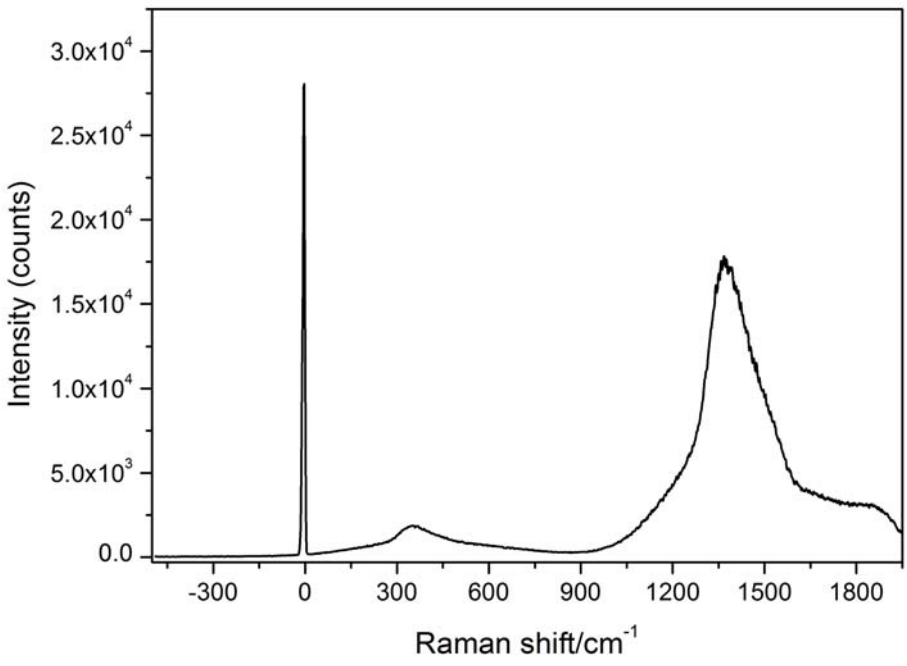

(a)

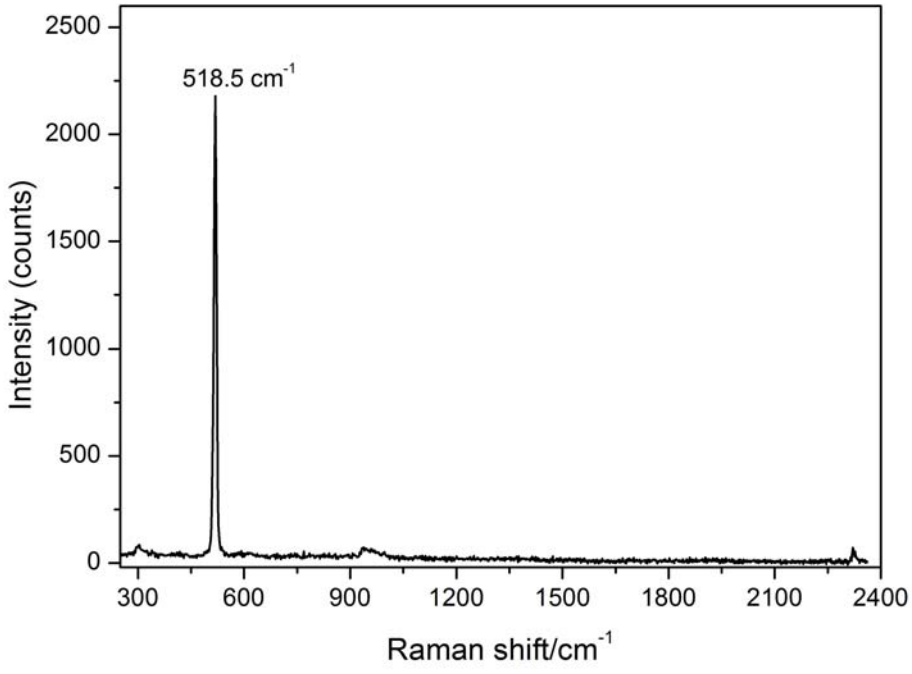

(b)

Figure 22: Spectra of (a) fluorescent glass coverslip and (b) Si wafer, taken with a 60x Olympus objective. Integration time 10s.

observed with a set of non-branded simple achromat 10x, 20x and 40x objectives. Furthermore, these objectives gave significantly higher Raman light collection than the Olympus objectives - around an order of magnitude. These objectives are of a much simpler design than the Olympus objectives, having only a few lens elements, which would give them higher transmission in the near-IR. This could in part explain the superior perfomance of

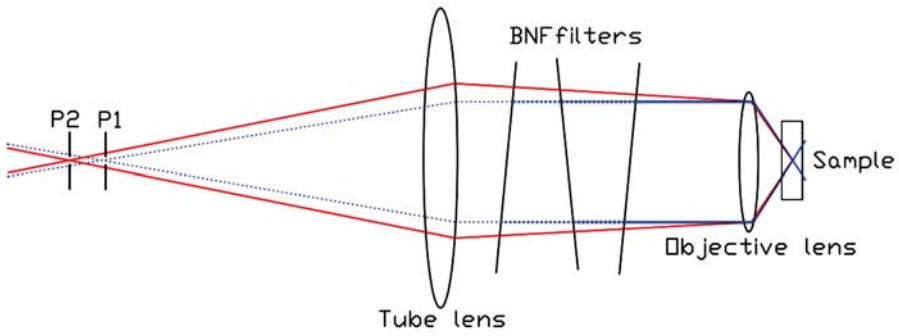

Figure 23: Diagram depicting how chromatic aberration occurring in the microscope objective lens can lead to different effective focal lengths of the tube lens for Rayleigh (blue) and Raman-shifted (red) light. P1 and P2 are the pinhole positions at which optimum Rayleigh rejection and Raman intensity occur, respectively. Drawing not to scale.

these objectives. A Raman spectrum of Si wafer taken with the 40x achromat objective is given in figure 24a. A number of Nikon and Olympus 100x oil immersion objectives were also trialled, and the Si wafer Raman spectrum using one of these is given in figure 24b. These objectives were all of a quite simple design and had similar performances. The 100x objectives gave excellent Rayleigh rejection, though the Rayleigh line is significantly broadened at the base. This behaviour has not been observed in non-oil (dry) objectives and can be attributed to the immersion oil, which is in direct contact with the sample.

Figure 24 suggests that objectives with higher numerical apertures have better performance in terms of both Raman signal intensity and Rayleigh rejection. In optical microscopy, the relationship between image brightness, NA and objective magnification for epi-illumination (analogous to back-scattering geometry in Raman spectroscopy) is given by the following relationship:

$$F \approx 10^4 \times NA^4/M^2 \tag{3}$$

where F is the light-gathering power of the objective, NA is the numerical aperture and M is the objective magnification. In principle, this can also be applied to a Raman microscope. For a given objective lens, the Raman intensity I can be approximated as:

$$I \propto NA^4/M^2 \tag{4}$$

To test whether this relationship does indeed hold for the Raman microscope, the Si wafer Raman spectrum was recorded with identical experimental parameters (laser power, integration time) with all the microscope objectives that have been tested so far. Figure 25 gives a comparison of the spectra recorded with the series of achromat objectives.

Plotting the intensity of the ~ 520 cm^{-1} peak as a function of the objective NA effectively demonstrates the performance of each objective, as shown in figure 26a for the

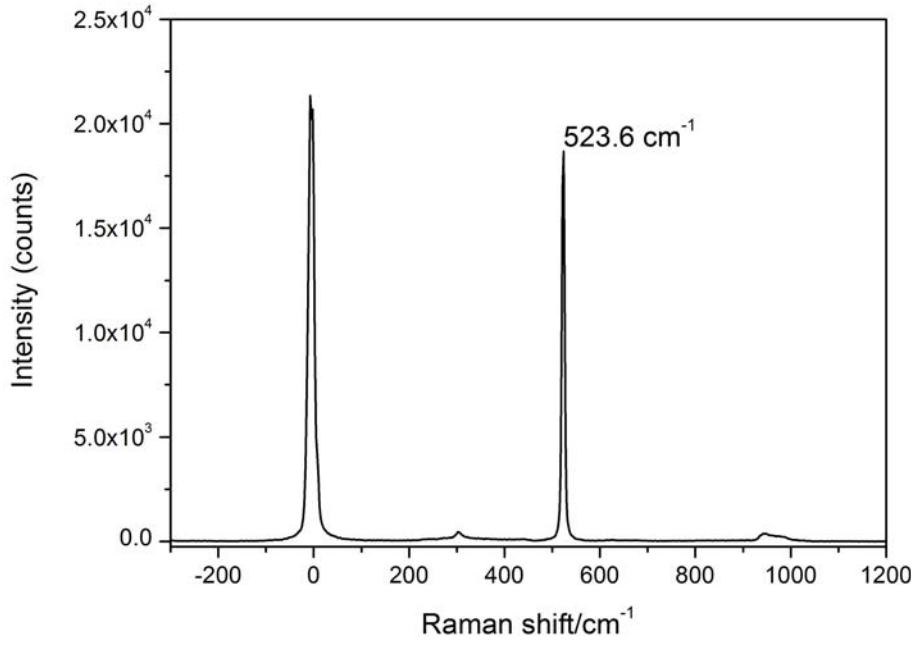

(a)

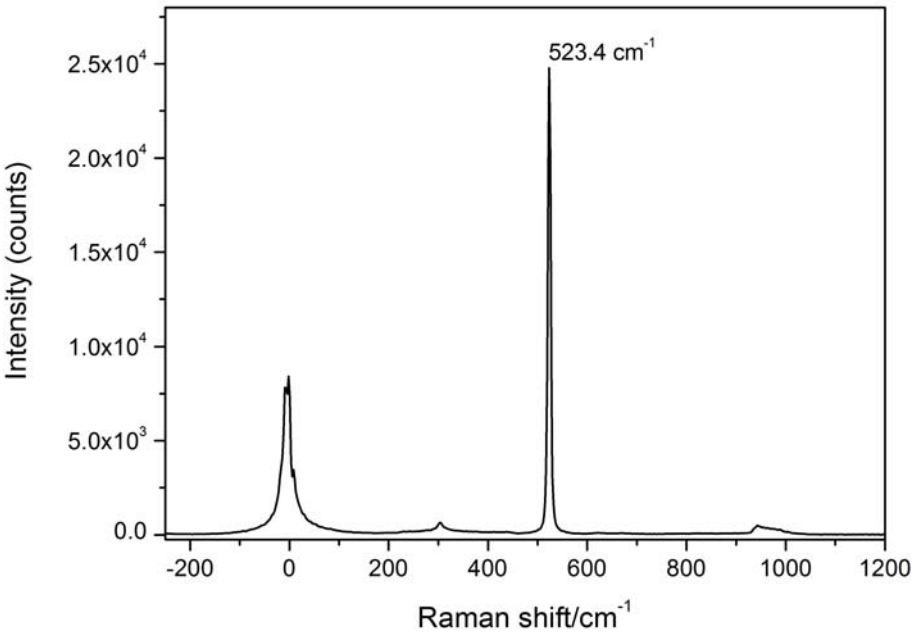

(b)

Figure 24: Raman spectra of Si wafer, taken with 40x (a) and 100x oil (b) objectives. Integration time 1s

Olympus 4x, achromat 10x, 20x and 40x, and 100x oil objectives. Included for comparison are the intensities calculated using the approximation in equation 4. A scaling factor was included in these calculations. The experimental data shows good agreement with the calculated behaviour, except for the point corresponding to the 40x objective, which gives exceptionally high Raman collection. A similar plot was made for the Olympus microscope objectives, and this is shown in figure 26b, with the data from 26a included for comparison. It is apparent that the performance of the Olympus objectives are very

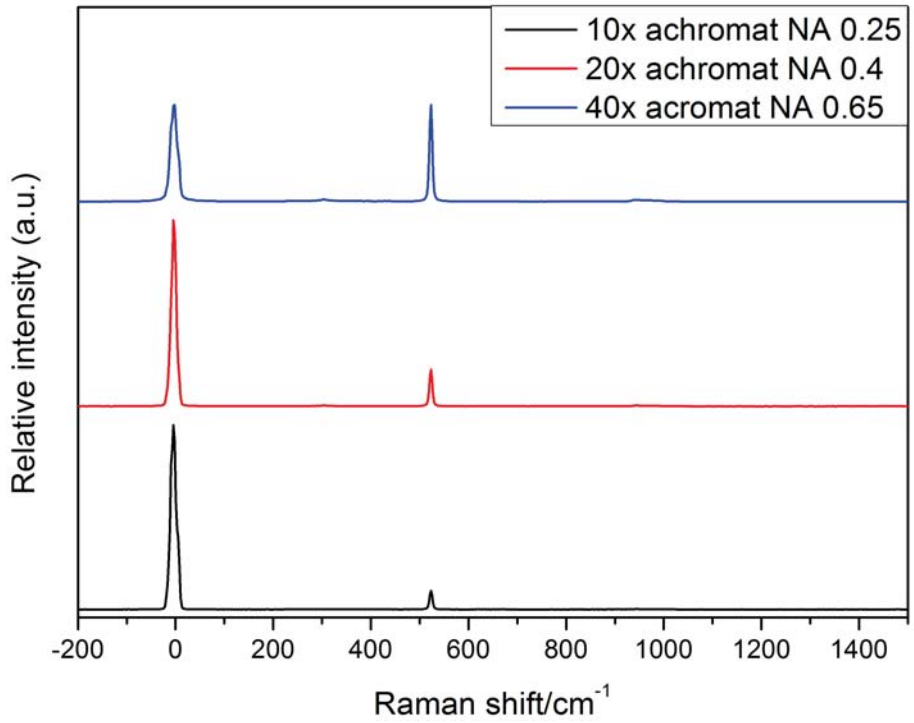

Figure 25: Raman spectra of Si wafer, taken with a series of achromat objectives. Integration time 1s, average of 10 accumulations.

poor compared to the first set. Higher NA also results in better Rayleigh rejection, and this effect is clearly seen by plotting the Raman:Rayleigh intensity ratio as a function of the NA, as shown in figure 26c. Higher NA is associated with a smaller focused spot size, which results in better light collimation, and in turn better Rayleigh rejection by the BNF filters.

The numerical aperture is also an important factor in determining the spatial resolution of the Raman microscope. Ultimately, the resolution is diffraction limited to about half the laser wavelength. For a 785 nm laser, this corresponds to a resolution of 392.5 nm. The focused spot diameter of a laser beam is given by the equation

$$d = \frac{1.22\lambda}{N.A.} \tag{5}$$

where λ is the laser wavelength and N.A. is the numerical aperture. The spatial resolution corresponds to half the focused beam diameter. For a 785 nm beam in an objective with NA 0.65 (as for the 40x achromat objective), the beam diameter is 1473 nm, and the spatial resolution 737 nm. By increasing the NA to 1.22, the focused beam diameter drops to 785 nm - the diffraction limit. Hence, further increasing the objective NA above 1.22 will not improve the spatial resolution.

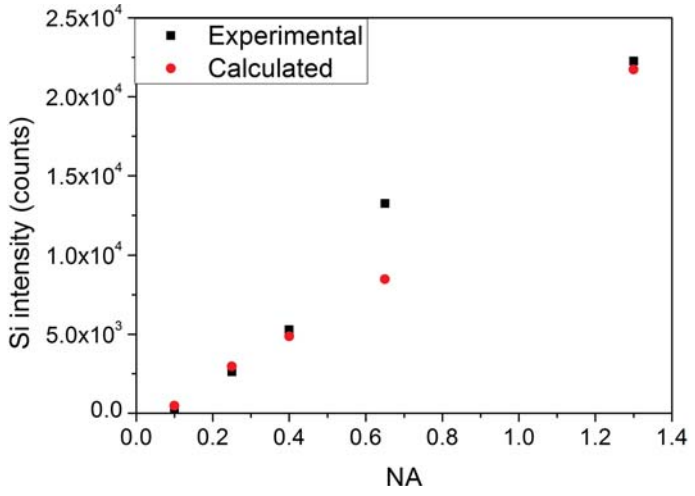

(a)

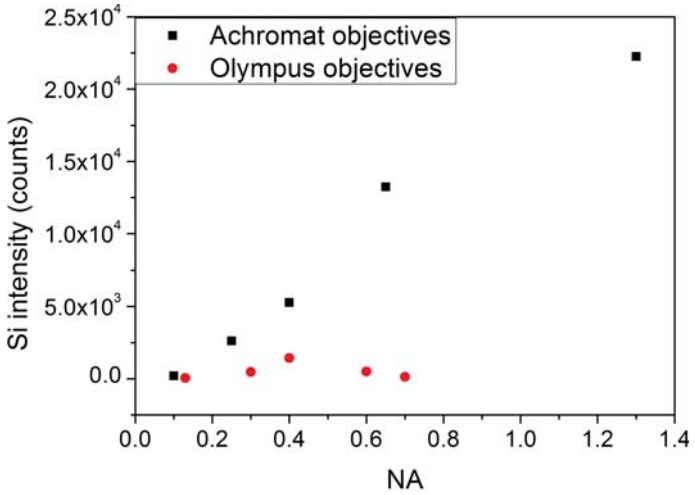

(b)

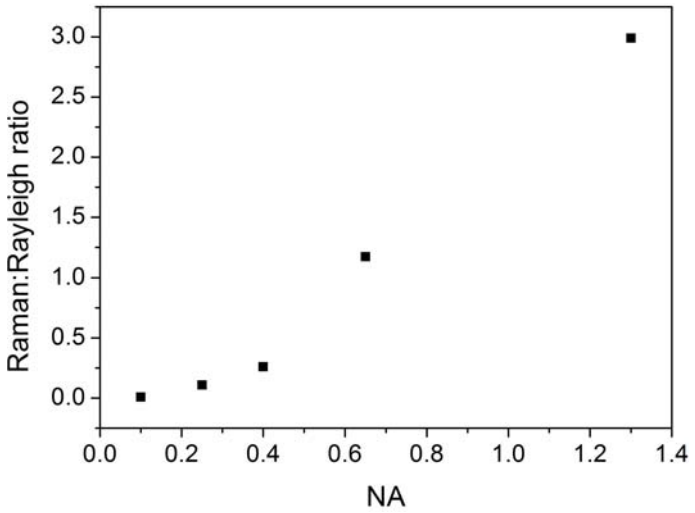

(c)

Figure 26: Plots of Si intensity vs NA (a) and (b) and Raman:Rayleigh ratio vs NA (c) for different microscope objectives.

2.2.6 Benchmarking Microscope Performance

The full microscope setup equipped for 785 nm excitation is shown in figure 27. Several different samples were tried with this instrument to test its low-wavenumber capability. These included HOPG, L-cystine and Sulfur, which all have known frequency bands in the THz region. The spectra are given in figure 28. The low-frequency mode around 40 cm^{-1} for HOPG is consistent with the "shear mode" given in the literature[104]. The Stokes/anti-Stokes Raman spectra of sulfur and L-cystine also have low-frequency bands that are in good agreement with the literature.[108] Even the band at 14 cm^{-1} for L-cystine is clearly resolved from the Rayleigh line. These spectra demonstrate that the low-frequency capabilities that the microscope was specifically designed for have been successfully implemented.

Figure 29 compares the spectra of L-cystine obtained using multimode collection fibres with different core diameters. The 50 μm core fibre gives much better spectral resolution than the 200 μm core fibre, with a comparatively small loss in intensity. Many bands, including the low-frequency bands at 14 and 30 cm^{-1}, are not resolved with the 200 μm fibre.

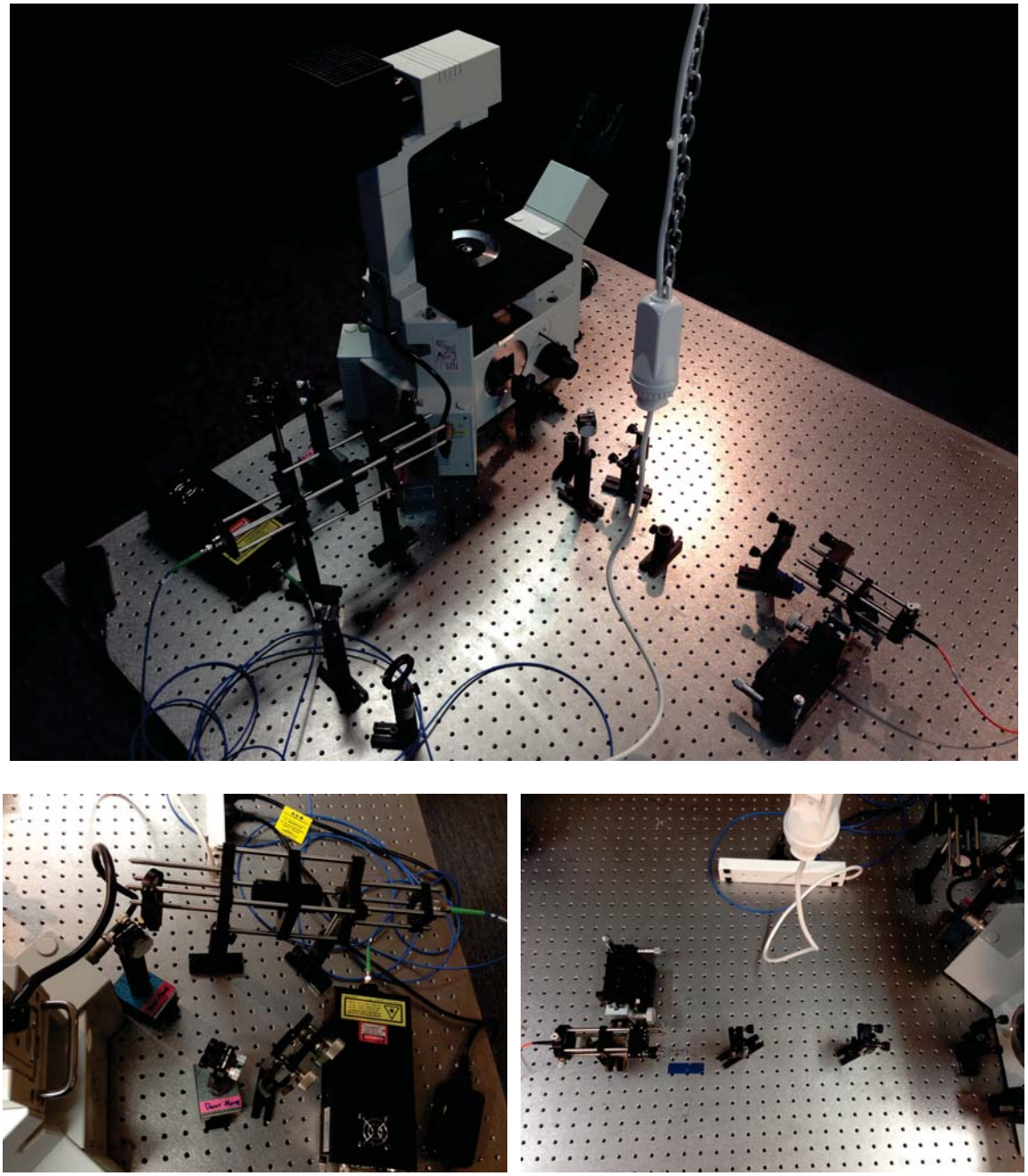

Figure 27: Full microscope setup.

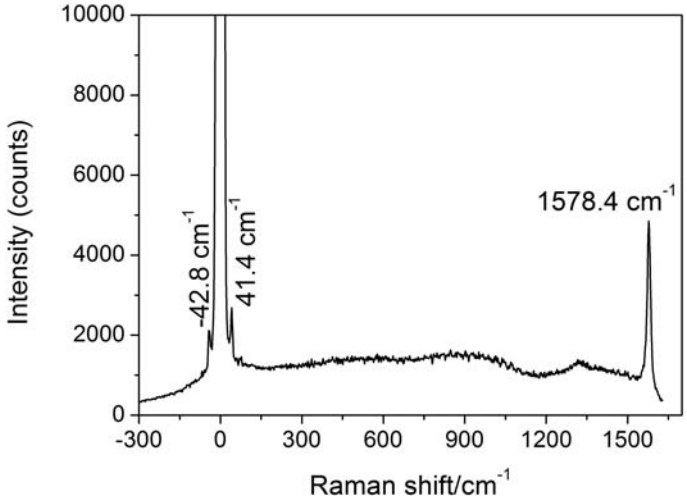

(a)

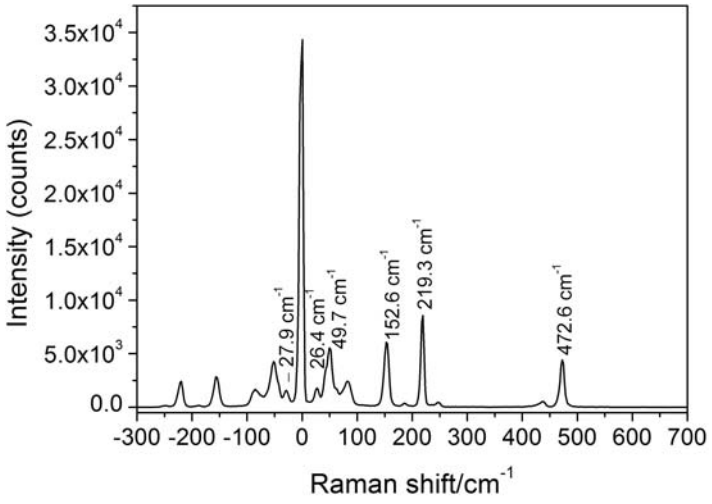

(b)

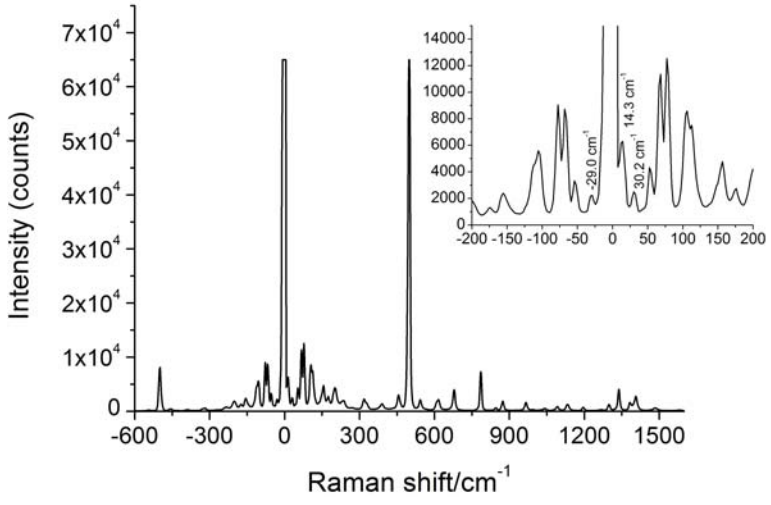

(c)

Figure 28: (a) Raman spectrum of HOPG, laser power 5 mW, integration time 60s. (b) Raman spectrum of Sulfur, integration time 1s. (c) Raman spectrum of L-cystine, laser power 5 mW, integration time 30s. All spectra were taken with a 40x achromat objective.

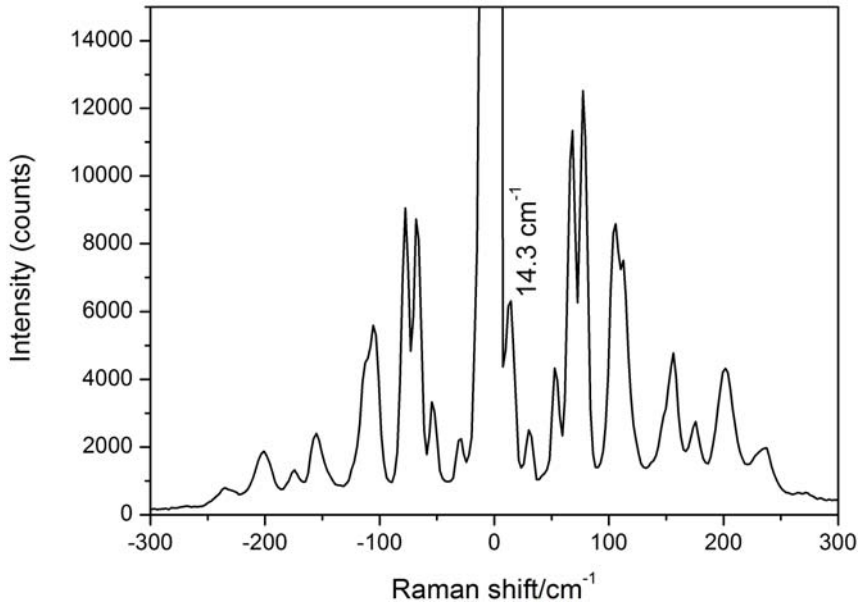

(a)

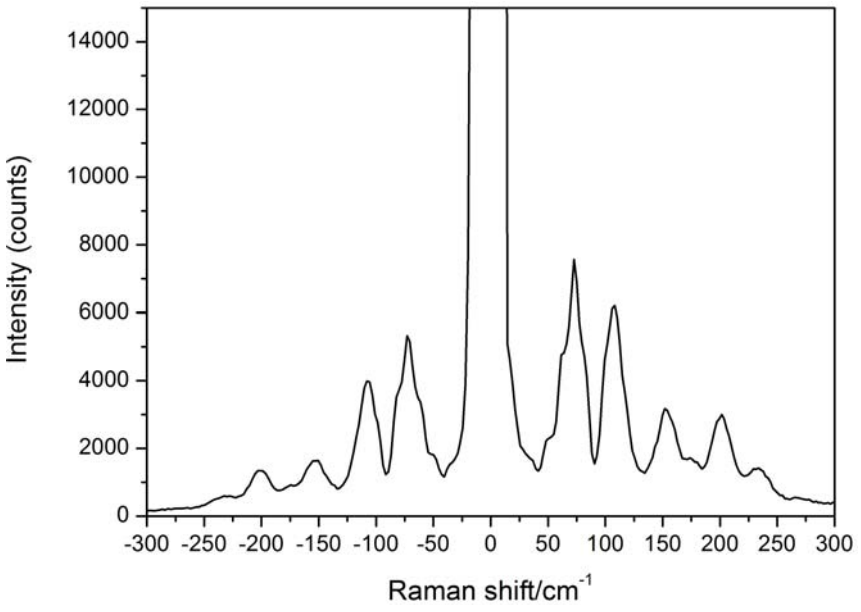

(b)

Figure 29: Raman spectra of L-cystine with multi-mode collection fibres with different core diameters. Spectra were acquired with a 40x achromat objective and laser power of 5 mW. (a) 50 μm core fibre diameter, integration time 30 s. (b) 200 μm core fibre diameter, integration time 10 s.

2.2.7 Incorporating Additional Excitation Wavelengths

The next step was to set the microscope up for 532 and 488 nm excitation wavelengths. This required the incorporation of additional VBG filters into the optical path, as each filter is specific for only one operational wavelength. The 532 nm laser used was a Cobolt Samba single-mode diode laser with an extremely narrow linewidth (<1 MHz) and maximum power output of 300 mW. The 488 nm laser used was a Sapphire SF 488 laser from Coherent Scientific. This is an OPSL (Optically Pumped Semiconductor Laser) with a linewidth <1.5 MHz and maximum power output of 100 mW. Sets of VBG filters for both excitation frequencies were incorporated into the microscope setup in the same way as the filters for 785 nm excitation were. The design of the microscope allowed the BPF beamsplitters to be slid into the slot underneath the microscope objective turret, replacing the 785 nm BPF. The Bragg diffraction angles were designed to be $\sim 20^{\circ}$, very close to that of the 785 nm BPF. This is important, as the BPF and Polaris mirror arrangement only works within a narrow window around the 19.8° diffraction angle of the 785 nm BPF. The 532 and 488 nm lasers are free-space and produce collimated beams with diameters of $\sim 700\ \mu$m. Both lasers have very low beam divergence; < 1.2 mrad (532 nm) and < 1.3 mrad (488 nm). For the 488 nm laser, the free-space beam was directed into the microscope using the mirrors already set up for the 785 nm laser to steer the beam. For the 532 nm laser, which was not kept on the same optical table as the microscope, the beam was first coupled into a single-mode polarisation-maintaining (PM) fibre using a FiberPort (both from Thorlabs Inc). The MFD (mode field diameter) of this fibre is only $\sim 3.4 \pm 0.5\mu$m, thus coupling of the beam into the fibre was a tedious and time-consuming process. Two mirrors were used to steer and align the beam into the fibre. The beam was first coupled into 200 μm and 50 μm core fibres to pre-align the beam in order to ease precise alignment into the PM fibre. The maximum coupling efficiency that could be achieved using this process was $\sim 45\%$. Once coupling had been achieved, the beam exiting the other end of the fibre at the microscope was then collimated with another FiberPort and steered into the microscope using the available mirrors. For both 488 and 532 nm excitation, an Acton SpectraPro 2500i 0.500 m focal length triple grating imaging monochromator/spectrograph with a liquid nitrogen-cooled Roper Scientific Spec-10 CCD detector operated at -110° C was used, and controlled using WinSpec 32 software. The Raman-scattered beam was directed into an achromatic lens and focused into a multimode 50 μm core diameter fibre, which was coupled into the spectrograph. Alignment of the microscope and collection optics was performed in a similar procedure to that for the 785 nm setup. However, as the glass coverslips did not fluoresce with 532 or 488 nm excitation, a Si wafer was used instead during alignment of the collection optics. The Raman shift axis was calibrated in WinSpec using the known Raman frequencies of cyclohexane or PMMA (poly(methyl methacrylate)). Spectrometer diffraction gratings with

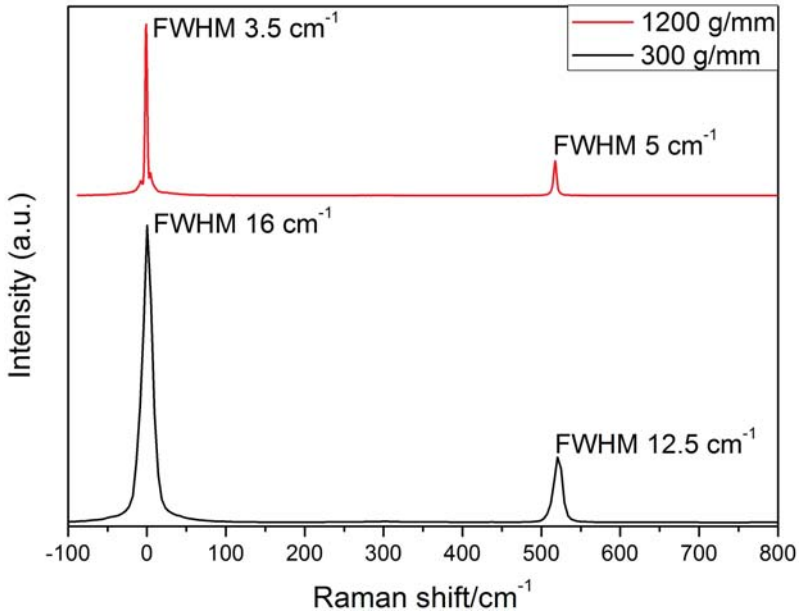

Figure 30: Raman spectra of Si wafer acquired with two different spectrograph gratings using 532 nm excitation.

300 g/mm or 1200 g/mm were typically used during sample collection. Figure 30 shows Raman spectra of a Si wafer taken with different gratings. Significant linewidth broadening is apparent for the 300 g/mm grating when compared to the 1200 g/mm grating. Shown in figure 31 are the Raman spectra of sulfur and L-cystine. The low-frequency bands are clearly visible.

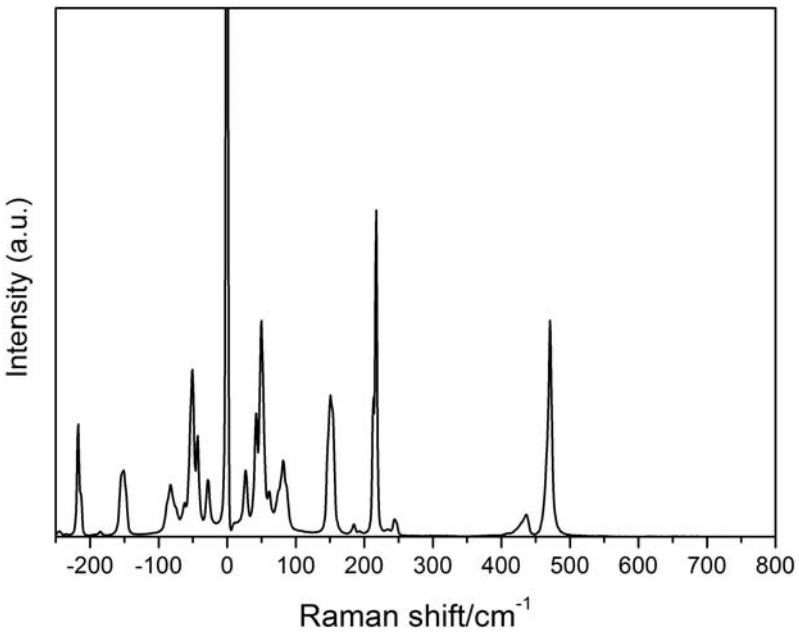

(a)

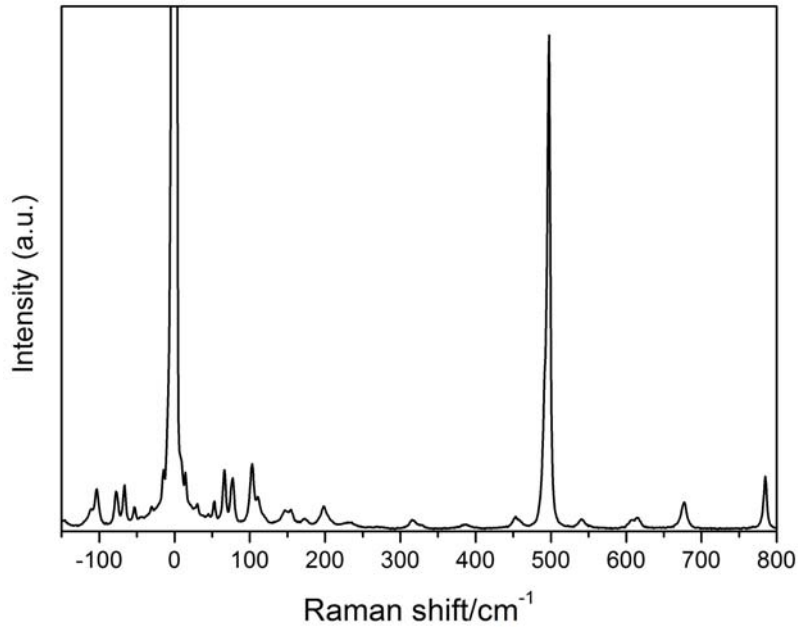

(b)

Figure 31: Raman spectra of (a) sulfur and (b) L-cystine, taken with 532 nm excitation.

2.2.8 Polarised Raman

The microscope was also equipped for polarised Raman experiments, for the characterisation and identification of graphene nanoribbon edges. The polarised Raman capability of the setup was first tested on liquid samples, using the 785 nm laser. This laser is linearly polarised, so all that is required for the polarisation setup is to insert an analyser in the path of the scattered beam. There is no need to control the direction of incident polarisation for liquid samples as the orientations of the molecules in solution are averaged by random rotations. With the polarisation analyser set parallel and then perpendicular to the incident linear polarisation, the depolarisation ratios of bands in the Raman spectra can be calculated. The analyser chosen for this purpose was a high-quality nanoparticle linear film polariser with a very high extinction ratio (>10,000:1) and excellent transmission in the near-IR. The polarised Raman spectra of cyclohexane is given in figure 32. This gave a depolarisation ratio of ~ 0.04 for the 801 cm^{-1} band.

For solid samples such as graphene, polarised Raman spectra cannot simply be obtained by analysing the polarisation of the scattered beam. The direction of the incident polarisation must also be controlled. This is because a graphene sheet has a defined orientation that is not averaged by random rotations, hence will also have a fixed and defined orientation relative to the direction of linear polarisation of the exciting radiation. The incident plane of polarisation can be controlled with a waveplate. This was first tested with the 532 nm diode laser, using a linear polariser as the sample. The 532 nm laser has a polarisation ratio $> 100:1$, as does the 488 nm laser, however this ratio is degraded via the various optical components it encounters along the way from the pre-fibre-coupled free-

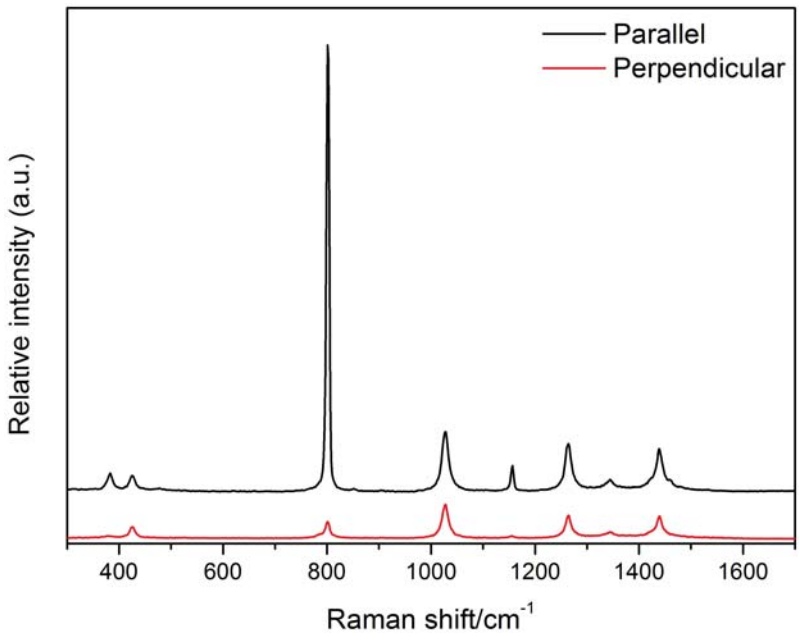

Figure 32: Polarised Raman spectra of cyclohexane, taken with a 4x objective. Integration time 30s.

space beam emitted by the laser to the final beam entering the microscope. In addition, the polarisation of the beam after being coupled into the PM fibre was found to be somewhat elliptical rather than linear. For these reasons, a linear polariser was placed in the path of the beam entering the microscope, prior to it encountering the λ/2 waveplate, to effectively clean up the polarisation. These efforts afforded Raman spectra that displayed excellent polarisation-dependent behaviour, as shown in the results of the polarised Raman experiments on the linear polariser sample given in figures 33 and 34. Rotating the sample orientation relative to the input laser polarisation (figure 33a and 33b) was found to have the same effect as rotating the polarisation of the input beam (figure 34). The polarisation-dependent behaviour was found to be very consistent at different positions on the sample and at different rotations. These results demonstrate the excellent polarisation capabilities of the Raman microscope. The 488 nm laser gave very similar polarisation perfomance and was predominantly used in the polarised Raman experiments of GNRs, as this affords the smallest possible spatial resolution of all three available laser wavelengths when used with a 100X microscope objective. At 488 nm, diffraction-limited resolution (λ/2) is 244 nm, which is comparable to the widths of the GNRs used in the experiments.

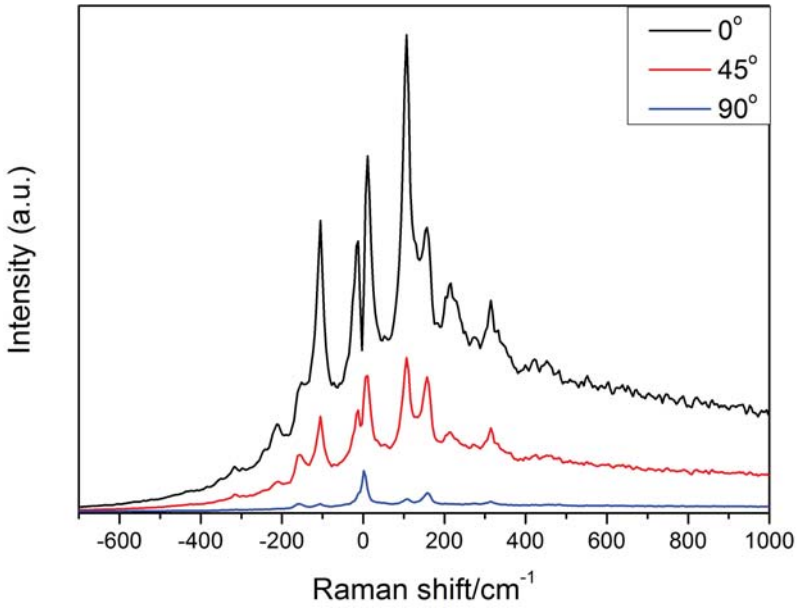

(a)

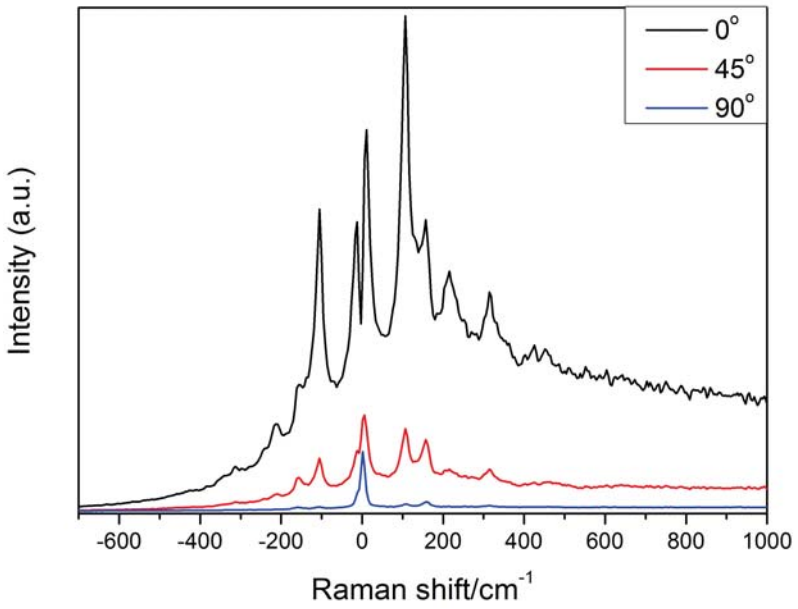

(b)

Figure 33: Polarised Raman spectra of a linear polariser acquired with 532 nm excitation. (a) Sample rotated 0 through 90°, without an analyser in the scattered beam path. (b) Sample rotated 0 through 90°, with an analyser in the scattered beam path set parallel to the input laser polarisation.

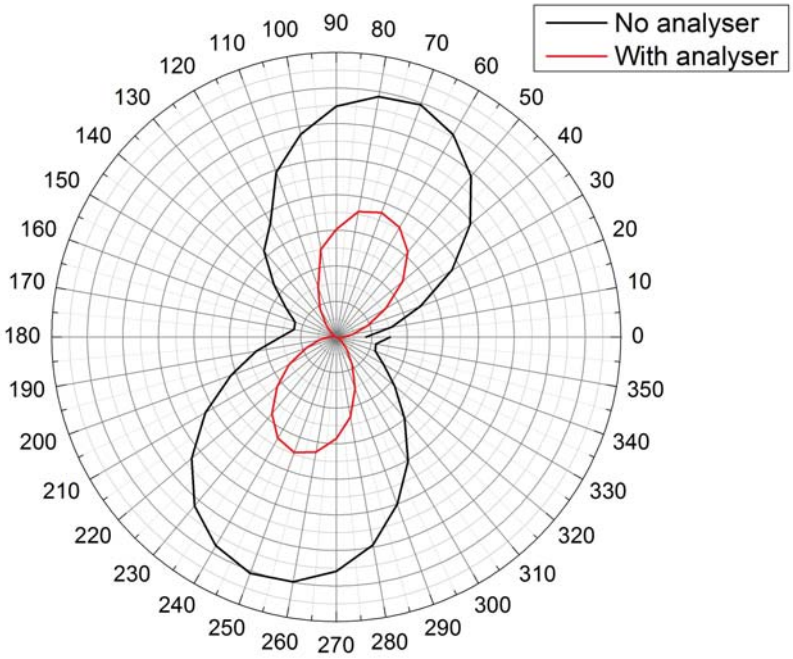

Figure 34: Polar plot of the Raman intensity of the linear polariser sample as a function of degree of rotation of the laser polarisation by a $\lambda/2$ waveplate. Plots are shown with spectra acquired with and without an analyser in the scattered beam path set parallel to the input laser polarisation. Raman intensities at each angle were calculated using the integrated intensity of the band at ~ 105 cm^{-1}.

2.3 Conclusion

This chapter detailed the development of the Raman microscope, beginning with the assembly of the optical components required to build a simple setup, through to the extension of this basic setup to a microscope platform with multi-Raman functionalities. The resulting Raman microscope is a flexible and highly versatile instrument equipped with three laser excitation wavelengths and capable of producing high-quality THz Raman spectra and polarised Raman measurements. This work proved to be the foundation for much of the success achieved in the following endeavours in this project, as the microscope was found to be invaluable for the edge characterisation of GNRs, as well as helpful for the characterisation of edge-functionalised GNRs. Although the THz Raman feature was not fully utilised in characterising the shear mode of GNRs in this project, due to problems with sample preparation and frequency dependence (as will be discussed in the following chapters), this capability is highly advantageous for the characterisation of many other types of samples, for which it is currently being used and will continue to be used by others in the future. As an example of this, the microscope is currently being used in other work to study the behaviour of low-frequency Raman bands and polarisation-dependent behaviour of MoS_2 nanoribbons.

3 Experimental methods

3.1 Production of GNRs

3.1.1 Nanotomy-Based Mechanical Cleavage of HOPG

The procedure for the production of GNBs (graphite nanoblocks) was based on the method developed by Mohanty et al.[83] In this technique, an HOPG block (purchased from NT-MDT) was cleaved by a diamond knife mounted in a microtome at controlled thickness to produce GNBs of corresponding thickness. A Leica Ultracut R microtome was used with a 4 mm DiATOME Ultra 45° diamond knife. The graphene planes of the HOPG were held perpendicular to the diamond knife edge, with the edge of the knife carefully aligned to the HOPG cutting face. I.e. the knife cuts against the grain of the HOPG. Figures 35a and 35b show the sample setup in the microtome. In brief, the microtome alignment procedure was as follows: first, the diamond knife was moved forward on the stage to approach the edge of the HOPG block until it was within a few hundred microns of the block. The top and bottom edges of the block were then aligned parallel to the knife edge, and the entire cutting face length also aligned with the knife edge. Detailed descriptions of this procedure can be found in reference[83]. The GNBs were cut into a water-filled boat, where they collected at the edge of the knife and were eventually pushed out onto the surface of the water, as shown in figure 35c. The water contained a small amount of surfactant to aid in wetting of the diamond knife. Initially, a cutting speed of 0.8 mms^{-1} was used, corresponding to the production of $\sim 1.7 \times 10^9$ GNRs (graphene nanoribbons) per cut for an HOPG block of ZYA grade with a thickness of ~ 0.5 mm and arbitrary ribbon length of 5 μm. This corresponds to $\sim 8 \times 10^{11}$ GNRs produced per hour. For GNRs with a shorter length of 1 μm, the number produced per hour would be $\sim 4 \times 10^{12}$. For some samples, GNBs were also cut dry into air with the knife boat empty. During the cutting process, many GNRs were produced per full HOPG length, due to the mosaic nature of the HOPG. AFM (atomic force microscopy) images of GNRs from ZYA grade HOPG showed ribbons with lengths up to 10 μm. TEM (transmission electron microscopy) images of GNRs cut from a lower grade ZYB HOPG block showed ribbons that appeared to be somewhat shorter on average, though this was difficult to gauge accurately due to the problem of aggregation. Increasing the cutting speed to 7.5 mm s^{-1} allowed for the faster production of GNRs, and did not appear to have any significant effect on the ribbon quality. Typically, GNB sample weights of a few hundred micrograms were produced in ~ 2 hours.

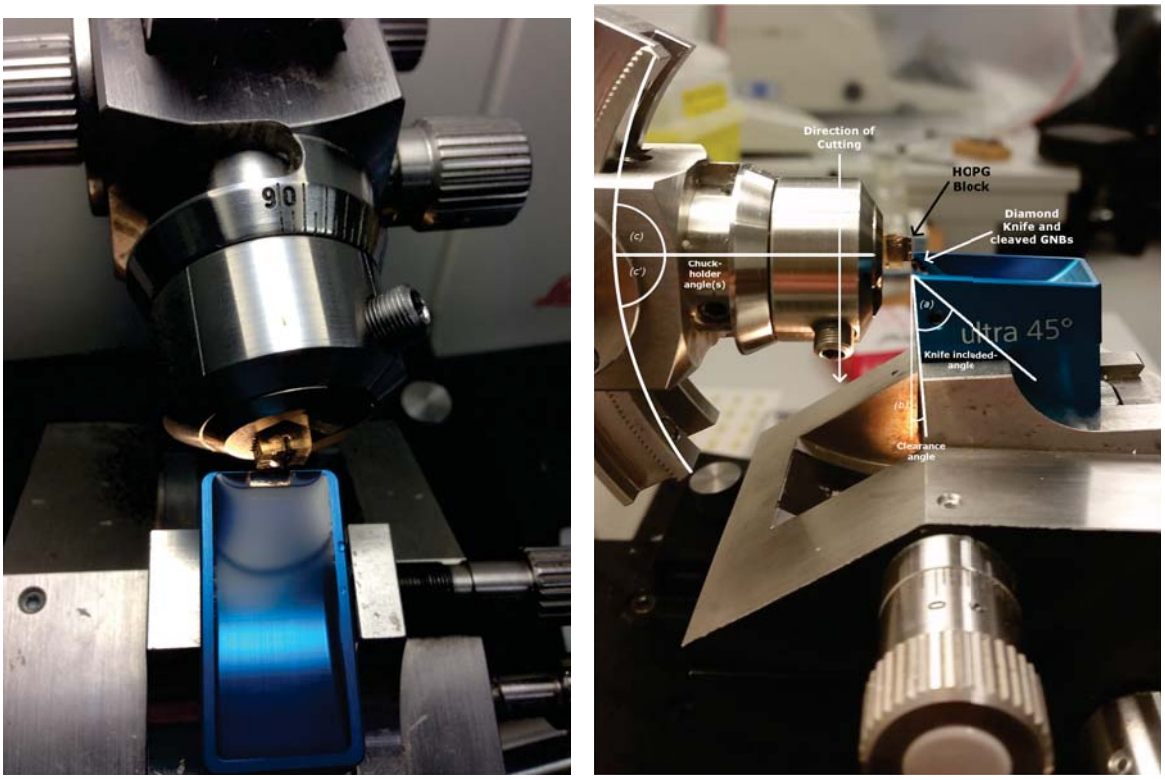

(a) **(b)**

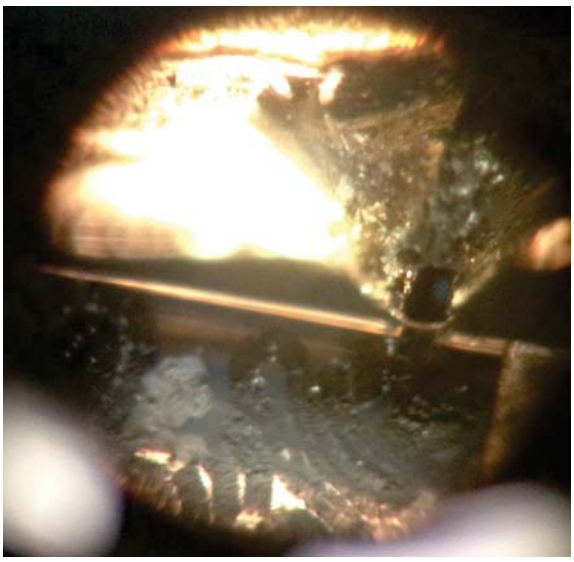

(c)

Figure 35: (a) View from the top showing the water-filled knife boat and HOPG sample mounted in araldite resin held in the microtome sample holder chuck. The sample is aligned and ready for commencement of cutting. (b) View from the side. Figure reproduced with permission from Samuel Brooke. (c) View through the eye-piece of GNBs being sliced from the HOPG block at the knife edge. The blocks connect to form a ”snake” that floats on the water.

3.1.2 Exfolation of GNBs

Exfoliation of GNBs to produce GNRs.

Wet-cut GNBs, collected in small glass vials, were rinsed with MilliQ water to remove any residual surfactant from the microtomy process and dried to give a black powder. The procedure[83] given for the exfoliation of the GNBs involves the use of chlorosulfonic acid, which reacts violently with water and is thus difficult to work with. For this reason, a different method was used for exfoliation, namely ultrasonication. The dried wet- or dry-cut GNBs were sonicated in isopropanol (IPA), a solvent which has previously been reported[114] to stabilise graphene flakes in solution to a reasonable concentration of 3.3 mg/mL, at low power (effective power output range $\sim 15-50$ W) for $24-48$ hours in a Bandelin SONOREX^{TM} Digital 10P ultrasonic bath with a capacity of 5.5 L. The ultrasonic bath is cooled by circulating water. The resulting dispersions had a concentration of ~ 0.5 mg/mL. After sonication, the black GNB particles were no longer visible and the solution had turned a dark grey colour, indicating successful exfoliation and stabilisation. A variation on this method involved using a surfactant solution of SDS (sodium dodecyl sulfate) in MilliQ water instead of IPA. For the surfactant-based exfoliation, 0.5 mL of a 1.1 mM (below the CMC (critical micelle concentration)) solution of SDS in MilliQ water was added to GNBs and sonicated for 24 h at low power. The ratio of surfactant to graphene corresponded approximately to monolayer coverage of the surfactant on the graphene surface. Details of this calculation are given in Appendix A. Following exfoliation in IPA or SDS solution, the sample was centrifuged in a Sigma 1-14 microcentrifuge at 2000 rpm for 10 min to settle any aggregates. The top layer was removed and used for AFM and Raman analysis. The dispersions of GNRs in SDS solution were found to be much more stable than those in IPA, with the former remaining dispersed after several weeks while the latter completely settled out after just a few days.

3.2 Characterisation of GNRs

3.2.1 AFM

A Nanosurf easyScan 2 AFM was used in tapping mode with Tap190DLC silicon cantilevers from BudgetSensors. Gwyddion software was used for measuring height profiles and correcting artefacts in AFM images. Samples for AFM were prepared by dispersing $2-5$ μL of dilute sample solution onto freshly-cleaved mica substrates. The high hydrophobicity of the ribbons and their tendency to aggregate made AFM characterisation of single ribbons difficult, and the majority of the time only aggregates were seen in the AFM scans. In an attempt to improve surface coverage and give a more even coating of ribbons, an airbrush was used to spray a fine mist of the sample solution onto the mica surface. This allowed for more rapid drying and appeared to work reasonably well for surfactant-dispersed samples, which have a higher surface tension and thus dry much more slowly, whereas the drop-drying method still worked better for IPA-dispersed samples. Aggregates were still seen in the majority of scans, with individual ribbons appearing only occasionally.

3.2.2 TEM

The TEM used was a Tecnai^{TM} G^2 Spirit BioTWIN from FEI. GNR samples for TEM were prepared on formvar-coated copper grids. Ethanol was found to be the best solvent for TEM as it left behind minimal residue on the grid upon drying. Dilute solutions of ribbons were dropped onto the grids, left for 3 mins, then drawn off to leave a thin film of GNRs on the formvar.

3.2.3 Raman Microscopy

The home-built Raman microscope described in the previous chapter was used for all Raman characterisation of GNR samples, using excitation laser wavelengths of 488, 532 and 785 nm. The 40X achromat objective with NA 0.65 was used for Raman analysis of bulk GNR samples. For these samples, a $\lambda/4$ waveplate was sometimes placed in the path of the excitation laser beam to convert the polarisation from linear to circular, in order to produce more averaged and consistent D and G band intensities.

Substrate preparation

For Raman analysis of bulk (densely aggregated) GNR samples, the samples were deposited onto a mica or quartz substrate by the drop-drying method. For polarised Raman measurements of few-layer ribbons, mica was no longer a suitable substrate due to its Raman background. For this reason, quartz, which has an almost flat background in the regions of the D, G and 2D bands, was used as a substrate for thin-layer GNR sam-

ples. To prevent aggregation, the quartz substrates were silanised to make them more hydrophobic. The procedure for this was as follows: quartz coverslips were pre-cleaned with methanolic HCl and fuming sulfuric acid, followed by treatment with the chlorinated organopolysiloxane reagent Sigmacote®. This involved covering the coverslips with a layer of the Sigmacote® solution, with the silanisation reaction occuring almost instantaneously. After removal of the solution layer, the coverslips were air dried and rinsed with MilliQ water to remove the HCl by-products. Dilute solutions of GNRs in IPA and SDS solution were deposited by pipetting small volumes ($1-20\mu$L) directly onto the silanised quartz. For solutions in IPA, the droplet was allowed to dry completely, which occurred rapidly. For the surfactant-dispersed samples, the droplet was left on the surface of the hydrophobic substrate for ~ 30 mins, then removed from the substrate by tilting until it slid off, leaving behind a thin layer of partially-aggregated GNRs. Quartz substrates could be re-used after removing the GNRs from the surface by sonication in SDS solution and removing the organosilane layer by soaking in a 15% NaOH solution overnight.

Polarised Raman microscopy

Polarised Raman microscopy was conducted on GNRs dispersed on silanised quartz substrates. Using a 100X magnification oil immersion objective with NA 1.25 to give the highest possible resolution, small aggregates of presumably a few ribbons were visible amongst larger aggregates. These were centred in the eyepiece cross-hairs to bring them into the focus of the laser beam. A $\lambda/2$ waveplate was used to rotate the plane of polarisation of the laser beam exciting the sample. A laser power of $\sim 1-2$ mW was typically used. A Physik Instrument (PI) E710.3CD piezo stage with minimum step size <10 nm was used to move the sample precisely in the focus of the laser beam. The small step size of the stage also allowed the sample to be scanned across the laser focus while monitoring the Raman spectrum. In this way, the piezo stage could be used to locate a region of interest, which could then be probed for I_D/I_G intensity changes by capturing the Raman spectra at incremental rotations of the laser polarisation (generally in the range $0-180^\circ$).

Analysis of Raman spectra

Raman spectra were analysed, manipulated and plotted using Bruker OPUS 7.2 spectroscopy software and OriginLab® OriginPro 8.5 graphing software. Spectra were first baseline-corrected in OPUS using a "rubberband" baseline correction method. In this method, a curve is stretched between the two endpoints of the spectrum, following the minima as it is pressed onto the spectrum. This rubberband baseline is then subtracted from the spectrum. Curve-fitting was then performed on the baseline-corrected spectra to determine peak positions, widths and intensities. Mixed Lorentzian and Gaussian functions were fit to the peaks and optimised in a local least squares and/or Levenberg-Marquardt algorithm, for example as shown in figure 36. Peak ratios (e.g. I_D/I_G) were

calculated from the integrated intensities.

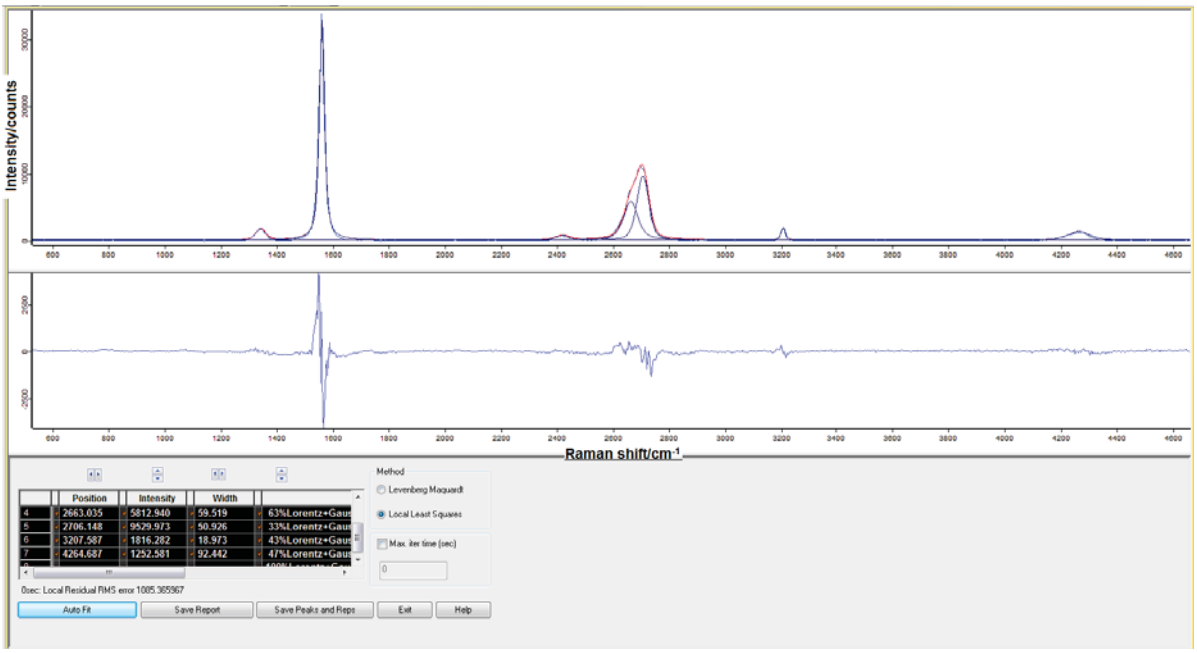

(a)

Position	Intensity	Width	Integral	Shape
1341.173337	1647.177368	43.497386	76266.844768	0%Lorentz+Gauss
1560.408295	32801.171875	22.541417	1085145.425568	80%Lorentz+Gauss
2419.097746	692.167969	56.328312	41502.134193	0%Lorentz+Gauss
2663.151436	5842.868687	59.494346	480368.304550	63%Lorentz+Gauss
2706.197108	9517.694821	50.777888	594928.822687	33%Lorentz+Gauss
3207.535000	1799.103271	19.243314	42125.803262	30%Lorentz+Gauss
4262.055809	1244.706299	92.780707	147348.420389	42%Lorentz+Gauss

(b)

Figure 36: Curve-fitting procedure in OPUS for a typical Raman spectrum of GNRs. (a) Model setup window and (b) generated output.

3.3 Functionalisation of GNRs

3.3.1 Chemical Methods

Ester coupling

Prior to functionalisation, GNRs were first reduced with $NaBH_4$ to convert carbonyl groups to hydroxyls. In this method, an excess of $NaBH_4$ (~ 0.01 M concetration) dissolved in methanol or water was added to a solution of GNRs sonicated in IPA, THF (tetrahydrofuran) or SDS-in-water and sonicated for $1-2$ hours. The pH of a 0.01 M solution of $NaBH_4$ in water was measured to be ~ 9.4, thus it will only decompose $\sim 15\%$ in one hour. The reduced GNR solution was then spun down in the centrifuge for $1-2$ mins at $10,000-12,000$ rpm. The supernatant was removed by Pasteur pipette, leaving a black pellet of reduced GNRs (r-GNR) at the bottom of the vial. This was then re-suspended in water for purification, re-sonicated and re-spun. The supernatant was once again removed and the successive rinses, sonications and spins repeated up to ten times for purification. This purification procedure will hence be referred to as the "rinse-and-spin" technique.

Purified r-GNRs were edge-functionalised with small carboxyl-containing compounds such as 4-aminobenzoic acid (4-ABA) via ester bond formation. In this procedure, EDC (1-Ethyl-3-(3-dimethylaminopropyl) carbodiimide), DMAP (4-Dimethylaminopyridine) and the carboxylated precursor were dissolved DMSO (dimethyl sulfoxide) by stirring for 30 mins. All reagants were used in mg amounts - in large excess to the GNRs. EDC and DMAP were used in a 1:1 molar ratio. The mixture was then added to a solution of r-GNRs in DMSO and left to react overnight in the sonicator. The resulting f-GNR solution was then purified in DMSO via the rinse-and-spin technique. Controls to test for the non-covalent binding of the carboxylated molecule to the GNRs were prepared and purified similarly except that the EDC and DMAP for carboxyl activation were omitted. The same EDC/DMAP ester coupling method was also used for the functionalisation of graphene oxide (GO).

Amide coupling

As-cut GNRs were edge-functionalised with small amine-containing compounds such as sulfanilic acid (SA) via amide bond formation. In this procedure, EDC and NHS (N-hydroxysuccinimide) was added to a solution of GNRs in DMF (dimethylformamide) and sonicated for ~ 2 hr. A solution of the amine precursor dissolved in DMF was then added to the activated GNR solution and the mixture left to react overnight in the sonicator. All reagants were used in mg amounts - in large excess to the GNRs. EDC and NHS were used in a 1:1 molar ratio. The resulting f-GNR solution was then purified in DMF via the rinse-and-spin technique. Controls to test for the non-covalent binding of the amine-containing molecule to the GNRs were prepared and purified similarly except that the EDC and NHS for carboxyl activation were omitted. The same EDC/NHS amide coupling method was

also used for the functionalisation of graphene oxide (GO).

Aryldiazonium grafting

Diazonium reactions were performed on exfoliated GNRs and GNB stacks. For GNRs, the reactions were performed under sonication, while for GNBs they were performed with gentle stirring. Both types of reactions were run in an ice bath for ~ 4 hours. Three different solvents/mixtures were used: DMF/DMSO, DMF and SDS in MilliQ water. Controls were prepared by substituting the diazonium salt for the amine-containing molecule. All samples were purified via the rinse-and-spin procedure. Two different methods were used for the formation of the aryldiazonium salts, and these are described in the following paragraphs.

In the first method, the diazonium salts were prepared with HCl. The procedure is as follows: 0.55 mmol of the amine precursor (sulfanilic acid or 4-nitroaniline) was dissolved in 1 mL of 2% NaOH in a warm water bath. After cooling to room temperature, 0.04 g $NaNO_2$ was added, and the mixture was added to 2 mL of ice MilliQ water and 0.2 mL of conc HCl under stirring in an ice bath, with the reaction vessel wrapped in Al foil. The temperature was kept at 0° and stirred for 15 min. 0.3 mL of this diazonium salt solution was then added dropwise into a 1 mL solution of GNBs or GNRs in water, and either stirred or sonicated in an ice bath for 4 hr, with the bath wrapped in aluminum foil.

In the second method, the diazonium salts were prepared with HBF_4. The procedure is as follows: 5 mmol of the amine precursor was dissolved in 1 mL MilliQ water and 1 mL HBF_4. 5 mmol of $NaNO_2$, dissolved in a minimum amount of cold MilliQ water, was added dropwise to the solution with stirring. The resulting solid was filtered and rinsed with ice-cold methanol and diethyl ether. For re-crystallisation, the solid was dissolved in a minimum amount of ice-cold acetonitrile and 200 mL ice-cold diethyl ether was slowly poured down the side of the beaker to precipitate the aryldiazonium salt. The solid was then filtered and rinsed three times with ice-cold diethyl either. For the functionalisation reaction with GNRs, a few mg of the aryldiazonium salt was dissolved in 1 mL ice-cold DMF (or other appropriate solvent). This was added to a solution of GNRs or GNBs in DMF (or other solvent) in an ice-filled sonic bath (or in an ice bath on a stir plate). The bath was covered with aluminum foil and the reaction was performed under sonication (or stirring) for 4 hr.

3.3.2 FTIR Spectroscopy

A Thermo Nicolet ATR-FTIR (attenuated total reflection Fourier transform infrared) instrument was initially used for characterisation of GNR samples. OMNIC^{TM} software was used to operate the FTIR instrument. Samples dispersed in IPA were dropped onto the Ge ATR crystal and left to air dry. Repeated drops were required to get a decent sample thickness.

FTIR microscopy was found to give higher quality spectra with higher S:N (signal-to-noise) ratios than ATR-FTIR as it allowed for sampling of much smaller, concentrated amounts of sample (sample area $\sim$ 20 x 20 μm). The microscope used was a Thermo Nicolet 6700 FT-IR spectrometer with a microscope attachment. The microscope was operated with OMNIC^{TM} spectroscopy software, and 512 or 1024 scans were typically sufficient to give quality spectra. A high level of water vapour background was generally seen in the FTIR spectra, even after extended purging of the sample chamber with nitrogen gas. Samples were prepared on gold-coated glass coverslips for reflectance mode. To increase the hydrophobicity of the Au, SAM formation with 1-dodecanethiol and the perfluorinated analogue HDFT (heptadecafluoro-1-decanethiol) was performed. In this procedure, the gold-coated substrate was immersed in a 1 mM solution of the alkanethiol in ethanol for 24 hr, followed by rinsing with ethanol and drying. 1 μL droplets of ribbons dispersed in MilliQ water were dried down into small concentrated spots after pipetting onto the SAM-Au substrates. Placing the substrates on a hotplate with low heating facilitated drying. The gold-coated substrates could be re-used after removing the ribbon spots and SAM monolayer by immersing in 0.5 M $NaBH_4$ in 1:1 H_2O/ethanol for 10 mins, followed by rinsing with ethanol and MilliQ water. For transmission mode, samples were prepared on CaF_2 by the drop-drying method.

FTIR spectra were analysed, manipulated and plotted using Bruker OPUS 7.2 spectroscopy software and OriginLab® OriginPro 8.5 graphing software. Kramers-Kronig (KK) transformations were typically performed on data acquired in reflectance mode to improve the spectrum appearance, for example as shown in figure 37a. Baseline correction of the KK-transformed spectrum using the rubberband correction method described in section 3.2.3 afforded the spectrum shown in figure 37b, in which the peaks are clearly visible.

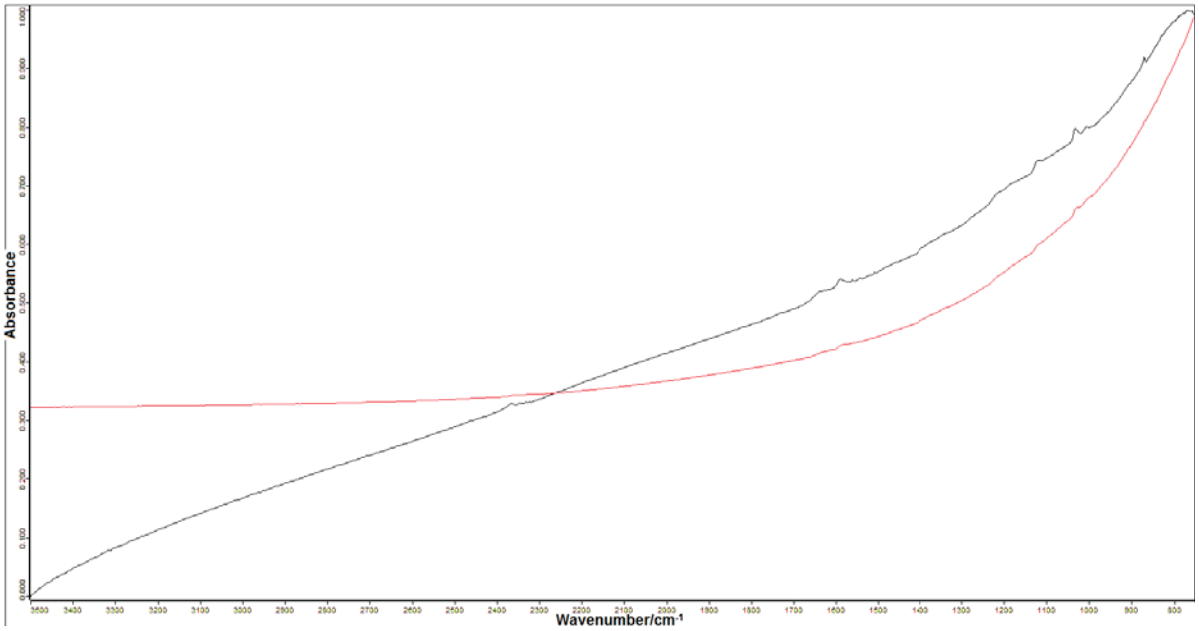

(a)

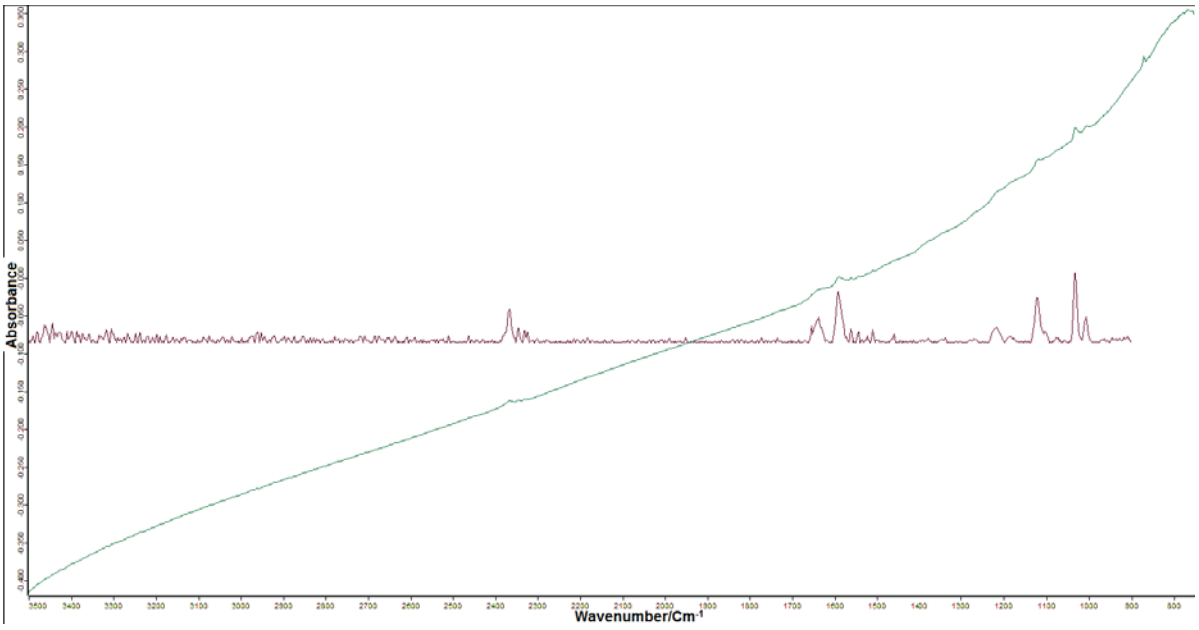

(b)

Figure 37: FTIR spectra of GNR edge-functionalised with sulfanilic acid. (a) Red spectrum: Reflectance IR spectrum. Black spectrum: after Kramers-Kronig transformation. (b) Green spectrum: after Kramers-Kronig transformation. Purple spectrum: after baseline correction. The purple spectrum has been enlarged.

3.3.3 Raman Microscopy

Raman microscopy experiments of modified GNR samples were conducted similarly as described for unmodified samples in section 3.2.3.

3.3.4 SERS

Two different methods were used for the preparation of GNR samples for SERS (surface-enhanced Raman spectroscopy). The first of these involved the production of superhydrophobic substrates by the deposition of a rough metal coating of Ag or Au onto a polished Cu-coated Si wafer followed by immersion of the metal into a 0.01 M solution of $AgNO_3$ or $HAuCl_4$, followed by SAM formation by immersion in a 1 mM solution of dodecanethiol. To prepare a film of GNRs on the superhydrophobic substrates, the substrates were dipped in solutions of the ribbons.

In the second method, Ag nanoparticles were prepared via the Kitaev[115] method. The procedure was as follows: 4.0 mL of 1.25×10^{-2} M trisodium citrate, 1.0 mL of 3.75×10^{-3} M silver nitrate, 9.0 mL MilliQ water, and 10.0 mL of 5.0×10^{-2} M hydrogen peroxide were added to 50 mL glass or plastic tubes, followed by the addition of 0.8 mL of 1.0×10^{-2} M potassium bromide and 5.0 mL of 5.0×10^{-2} M sodium borohydride. Upon addition of $NaBH_4$, nucleation of the Ag nanoparticles was initiated, followed by further growth until a stable yellow colour was reached after a few minutes. This relatively simple procedure enables the size, and hence plasmon frequency, of the nanoparticles to be tailored simply by the amount of KBr added to the reaction. KBr acts to modify the shape and size of the nanoparticles by reacting with Ag^+ on the surface of the growing nanoparticles, forming AgBr and arresting further growth. KBr reacts more with certain crystal faces, tending to stabilise (100) faces, so growth on these faces is inhibited, resulting in alteration of the size and shape of the nanoparticles.[116] The addition of 0.8 mL of KBr resulted in yellow nanoparticles with an absorbance maximum of approximately 410 nm. GNR samples were sonicated in 0.01 M CTAB (cetyltrimethylammonium bromide) solution in MilliQ water to provide a negative charge. These were then mixed with the citrate-capped Agnps (Ag nanoparticles) and deposited onto a quartz substrate by the drop-drying method. SERS control samples were prepared by mixing a solution of CTAB with a solution of Agnps, and drop-dried onto a quartz substrate.

3.3.5 THz Spectroscopy

For the Far-IR measurements at the Australian Synchrotron, GNRs and GO were functionalised with a variety of small molecules via the ester and amide coupling routes. Samples were prepared in either dry IPA or THF (solvents dried with molecular sieves). Triethylamine and trifluoroacetic acid were added to some samples to convert carboxyl and amine groups to their salts, respectively. Small molecules such as urea were added to others as

hydrogen bond donors/acceptors. These additional modifiers were added in approximate 10X excess to the expected number of edge functional groups, which for a typical sample was calculated to be $\sim 10^{-7}$ mol. The full list of samples prepared is given in table 1. Due to time constraints at the Synchrotron, spectra were obtained for only a fraction of these samples. Samples were re-sonicated at the Synchrotron itself to re-disperse the ribbons. This proved to be somewhat problematic, as the bath sonicator available for use was not that effective and the ultrasound was found to be highly unevenly distributed throughout the bath. This led to some delays in sample preparation. Samples were initially prepared for ATR-FTIR mode by pipetting drops onto the diamond ATR crystal. However, the samples did not spread at all evenly over the crystal, as required for obtaining quality spectra, and this problem was exacerbated by the tiny quantities of sample available. Preparing samples on polyethylene (PE) wedges for transmission mode was found to be much more effective, as the hydrophobic surface of the PE was found to facilitate the even deposition of concentrated spots of sample. The wedges were polished to give a smooth surface prior to sample deposition. The samples were deposited by drying successive 5 μL aliquots of sample solution onto the PE substrate. Some samples were also run in a Janis cryostat chamber cooled with liquid nitrogen.

3.3.6 XPS

GNR samples were prepared to send away for XPS (X-ray photoelectron spectroscopy). These included wet- and dry-cut GNRs and GNRs edge-functionalised with a range of small molecules. These were prepared in dry THF and deposited onto piranha-cleaned Si wafer via the drop-drying method. The samples did not spread well over the highly hydrophilic SiO_2 surface and dried very unevenly. Some preliminary data was recorded, which showed promising N and S signals for GNRs edge-functionalised with sulfanilic acid. However, due to an unfortunate shutdown of the XPS instrument shortly after collection of this preliminary data, this data was lost and no further data could be recorded from the samples.

Table 1: Samples prepared for the Far-IR beamline at the Australian Synchrotron. Only the samples highlighted in red were actually run.

Sample	Added molecules	Solvent		Key	
As-cut GNR		IPA		Et_3N	triethylamine
As-cut GNR	Et_3N	THF		TA	terephthalic acid
r-GNR		IPA		TMA	trimesic acid
r-GNR	Et_3N	THF		BTB	benzene 1,3,5-tribenzoic acid
r-GNR-TA				EDA	ethylenediamine
r-GNR-TA	Et_3N			TFA	trifluoroacetic acid
r-GNR-TA	CH_3COOH	IPA		SA	sulfanilic acid
r-GNR-TMA		IPA		4-NA	4-nitroaniline
r-GNR-TMA	Et_3N	THF		IPA	isopropanol
r-GNR-TMA	CH_3COOH	IPA		THF	tetrahydrofuran
r-GNR-BTB	TFA	IPA			
r-GNR-BTB	Et_3N	THF			
r-GNR-BTB	CH_3COOH	IPA			
r-GNR-TA-EDA		THF			
r-GNR-TA-EDA	Et_3N	THF			
r-GNR-TMA-EDA		THF			
r-GNR-BTB-EDA	Et_3N	THF			
r-GNR-TA-EDA	TFA	IPA			
r-GNR-TMA-EDA	TFA	IPA			
r-GNR-BTB-EDA	TFA	IPA			
r-GNR-TA-EDA	EtOH	IPA			
r-GNR-BTB-EDA	EtOH	IPA			
r-GNR-TA-SA	TFA	IPA			
r-GNR-BTB-SA	TFA	IPA			
r-GNR-TA-SA	Et_3N	THF			
r-GNR-BTB-SA	Et_3N	THF			
r-GNR-TA-4-NA		THF			
r-GNR-TMA-4-NA		THF			
r-GNR-TA-4-NA	Et_3N, urea	IPA			
r-GNR-TMA-4-NA	Et_3N, urea	IPA			
GO		IPA			
GO	Et_3N	THF			
r-GO		IPA			
r-GO	Et_3N	THF			
r-GO-TA	TFA	IPA			
r-GO-TA	Et_3N	THF			
r-GO-TA-EDA		THF			
r-GO-TA-EDA	Et_3N	THF			
r-GO-TA-EDA	TFA	IPA			
r-GO-TA-4-NA		THF			
r-GO-TA-4-NA	Et_3N, urea	IPA			

4 Structure of Graphene Nanoribbons

4.1 Introduction

This chapter explores the production and characterisation of GNRs (graphene nanoribbons) prior to edge modification. GNRs have been produced by a variety of different techniques, including lithography, chemical vapour deposition, chemical and sono-chemical methods and unzipping of carbon nanotubes.[2,117] However, very few of these techniques can produce high-quality graphene nanoribbons at high through-put and purity, and with uniform and controllable widths - factors which are all highly desirable. Recently, a novel method for GNR production has emerged, which combines all the desirable factors in a simple, fast and scalable "nanotomy"-based method.[83] The key technique that distinguishes this method from numerous others is the use of mechanical force to effectively cleave graphene sheets. This involves cutting highly-oriented pyrolytic graphite (HOPG) with a diamond knife at controlled thickness to produce GNRs with corresponding widths. Thus, this unique and effective method was utilised for the production of GNRs in this project.

Knowledge of the physical and chemical structure of the GNR edges is important for developing effective strategies for edge modification, as the purity, level of defects and edge smoothness/geometry will all have significant effects on the reactivity of the carbon atoms making up the graphene lattice. Armchair and zigzag edges are known to exhibit different chemical reactivities, and in zigzag GNRs, unpaired π electrons are distributed on the edge carbon atoms, giving them partial radical character.[118] These localised states are not present in armchair edges, giving zigzag edge carbon atoms unique chemical reactivity. Thus, the ability to determine the average edge smoothness and geometry is an important factor for edge functionalisation. This can be useful in determining whether functionalisation strategies targeting specific armchair/zigzag geometry (e.g. Diels-Alder, radical chemistry) should be used, as opposed to strategies targeting functional groups expected to be already present at the edges of the as-cut ribbons (e.g. COOH, OH), regardless of edge smoothness and geometry.

Raman spectroscopy is an ideal tool for the characterisation of graphite and graphene materials, as the absence of a band-gap allows for both the physical and electronic structure to be probed, due to resonance with all incidence wavelengths.[102] The simplicity of the appearance of the Raman spectrum of graphene and graphite can be misleading, as a wealth of useful information may be garnered by careful and detailed analysis of the peaks. As will be described in the following section, the D, G, C (shear mode) and 2D peaks of graphene and graphite can provide important information on the level of defects, proportion of edges, edge structure (including smoothness and geometry) and graphene interlayer interactions, to name a few. In the context of this study exploring the edge structure of GNRs, the D band is of particular importance, as it can be used to

directly distinguish armchair from zigzag from disordered edges, via polarised Raman microscopy. Thus, Raman spectroscopy is a powerful and effective tool for the characterisation of GNRs and is especially useful in probing the graphene edge structure. For this reason, it was heavily utilised in this chapter, and was the primary technique used for the characterisation of GNRs. AFM and TEM were complementary techniques used to provide images of the GNRs in order to evaluate the quality of the ribbons produced via the nanotomy method. Since the D band can give an idea of the relative amount of disorder in graphene nanoribbons, in addition to its usefulness in determining edge structure, Raman spectroscopy can also be used to probe other aspects of the structure of GNRs, such as their width and layer number, as well as the effect of cutting and exfoliation parameters, by looking for changes in the D band intensity (via the D:G ratio).

4.1.1 Overview of the History and Development of the Understanding of Raman Processes in Graphene and Graphite

As Raman spectroscopy is the main technique used to characterise GNRs in this study, a detailed description of the Raman processes in graphene is given in the following section, beginning here with a brief history of Raman scattering in graphene and graphite. The first Raman spectrum of graphite was reported by Tuinstra and Koening in 1970.[102,119] In this study, a single peak at 1575 cm^{-1} was reported for single-crystal graphite, with an additional band at 1355 cm^{-1} for other more disordered forms of graphite (e.g. commercial graphite). The intensity of this band was found to be inversely proportional to the size of the crystallite. This was the first observation of the so-called D and G bands (though these names were not assigned until 1977 by Vidano and Fishbach[120]). The G band was assigned to an E_{2g} Raman-active phonon mode, and the 1355 cm^{-1} band to an A_{1g} breathing mode that becomes Raman active in a finite lattice. Additional peaks in the Raman spectrum of graphite were later discovered; the $\sim$ 1620 cm^{-1} (D') and $\sim$ 2700 cm^{-1} (2D) bands by Vidano and Fishbach[120] and the overtone bands at $\sim$ 2450 cm^{-1}, $\sim$ 2950 cm^{-1} (D + D") and $\sim$ 3250 cm^{-1} (2D') by Nemanich & Solin[121,122] and Vidano[123]. The defect-related bands, including their overtones and combination modes, were found to exhibit shifts in wavenumber with excitation energy, while the G band, the only first-order mode in graphite, did not show such shifts. Thus, it was reasoned that the disorder-related bands could not be assigned to maxima in the phonon density of states (PDOS), as these maxima are an intrinsic property of the material and cannot change with excitation energy. On the basis of these studies showing dispersion for defect-related bands, it was proposed by Pocsik et al.[124] that a resonant process involving strong Raman enhancements occured whenever the phonon wave vector was equal to the wave vector of the excited electron transition, i.e. the k=q quasi-selection rule. However, this rule did not have any physical basis and could not adequately account for the experimental observations associated with the D peak Raman spectrum. In 2000, the double resonance model for D band activation

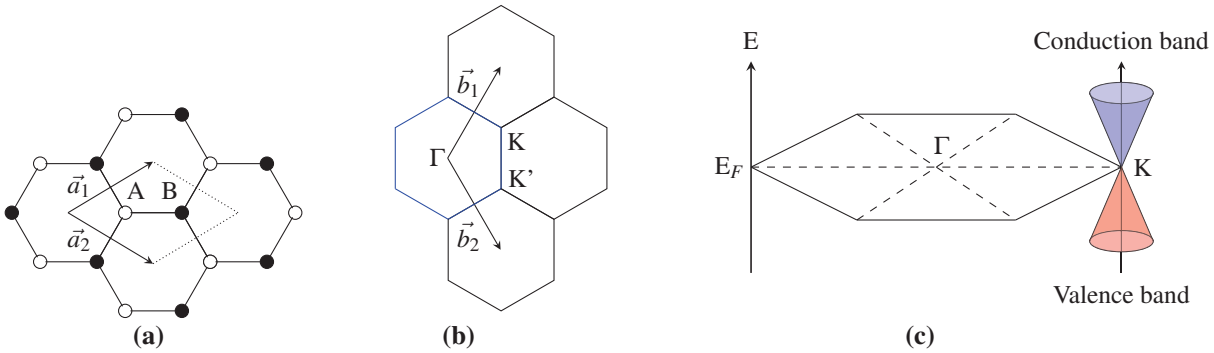

Figure 38: (a) The unit cell of monolayer graphene, spanned by the vectors $\vec{a}_1$ and $\vec{a}_2$. (b) The reciprocal lattice with the first Brilluoin zone highlighted in blue. The points Γ, K and K' mark the zone centre and inequivalent corners, respectively. The unit cell is spanned by the vectors $\vec{b}_1$ and $\vec{b}_2$. (c) Electronic band structure at the Dirac (K) point. E_F is the Fermi energy.

was first introduced by Thomsen and Reich.[125] This became what is now the currently accepted model for D band activation, and is described in detail in the following section.

4.1.2 Theory of Raman Scattering Processes in Graphite and Graphene

There are two carbon atoms in the unit cell of monolayer graphene, which make up two different sublattices, A and B, as shown in figure 38a.[98] The first Brillouin zone (BZ) of two-dimensional graphene has a hexagonal structure, as illustrated in figure 38b. Figure 38c shows the electronic dispersion in graphene, with the valence and conduction bands touching at the inequivalent corners of the BZ (K and K'). Around the point of intersection (the Dirac point) the dispersion is linear, with the density of states converging to zero, leading to the massless-like behaviour of electrons in graphene. Graphene has six normal phonon modes at the BZ centre, two of which are doubly degenerate.[102] These modes are A_{2u} + B_{2g} + E_{1u} + E_{2g}. The two degenerate modes are the in-plane optical E_{2g} mode, which is Raman active, and the out-of-plane optical B_{2g} mode, which is not Raman active. The E_{2g} mode corresponds to iTO and iLO in-plane phonon modes, which correspond to vibrations of sublattices A and B against each other.[98] These are responsible for the G band, the only normal first-order Raman process in graphene. In graphite, the number of carbon atoms in the until cell is doubled, thus the number of optical modes is also doubled, and infrared-active modes are generated.[102] One of these modes is a new doubly-degenerate Raman-active E_{2g} mode, which is responsible for activation of a low-frequency band, which will be discussed later. The D and 2D bands arise from iTO phonon modes near the K point.[98] Unlike the G band, the D and 2D bands exhibit strong dispersion, with their frequencies shifting with the laser excitation energy. For the D band, the frequency increases linearly with increasing laser energy, with a slope of ~ 50 cm^{-1}, and for the 2D band, a slope of ~ 100 cm^{-1}. This dispersion can be accounted for in the double resonance (DR) model of Raman scattering in graphene.

The linear gapless electronic dispersion of graphene has important consequences for its Raman processes, as it enables resonance to occur for any laser frequency in the IR − UV range.[102] The lattice constant, a, for graphene is ~ 1.42 Å. For Raman excitation energy in the range $1.2 - 5.4$ eV, the wave vectors of the incident and scattered photons are much smaller than π/a, which is the magnitude of a phonon at the BZ boundary. For an excitation wavelength of 532 nm, the magnitude of the photon wavevector is 1.18×10^5 cm^{-1}. In comparison, the value of π/a is 2.21×10^8 cm^{-1}. By momentum conservation, the wave vector of the phonon involved in the Raman scattering event must then also be much smaller than π/a. Thus, as a consequence of the fundamental Raman selection rule, only phonons near the BZ centre can participate in first-order Raman scattering. For Raman processes involving two phonons, the fundamental selection rule can be satisfied by q + (-q) = 0, where q is the phonon wave vector. The only single-phonon modes that satisfy the fundamental Raman selection rule are those that generate the G and low-frequency C bands.

The D band of graphene appears at ~ 1350 cm^{-1}, and arises from a second-order double resonance (DR) scattering process.[98] This is an A_{1g} breathing mode of the hexagonal rings, as shown in figure 39a. The well-known DR process has been used extensively in the literature to describe the mode of D band activation. This process initiates with excitation of an electron-hole pair from the valence to the conduction band upon absorption of a photon, as shown in figure 39b.[98] This is followed by inelastic scattering of the electron or hole by a phonon and elastic scattering by a defect. The final step involves recombination of the excited electron and phonon, along with emission of a photon. The 2D band also arises via DR, and in this case, both processes are inelastic scattering processes involving two phonons. This is the second order of the D band and does not require a defect for activation, as momentum conservation is instead satisfied by two phonons having opposite wavevectors. Thus, the 2D band is always present in the spectrum. The D and 2D modes are known as intervalley scattering processes, as the DR process connects

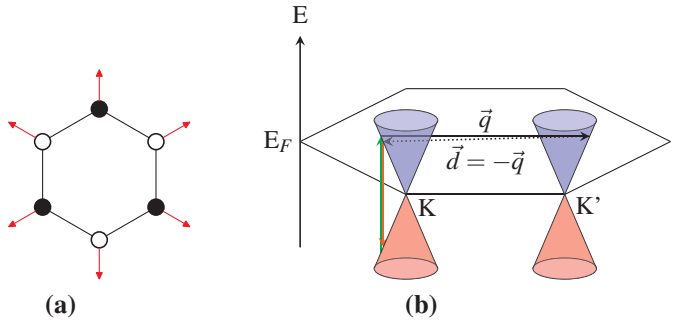

Figure 39: (a) Breathing mode for the D band of graphene. (b) Double resonance model for activation of the D band in graphene. The green and orange arrows represent photon absorption and emission, respectively. $\vec{q}$ and $\vec{d}$ are the wave vectors of the phonon and defect, respectively. Figures adapted from Ferrari et al.[102] and Krauss et al.[126]

two points within different cones around K and K'. Intravalley scattering can also occur, which connects two points within the same cone (around K or K').[102] The so-called D' band is due to intravalley DR, and occurs at $\sim$ 1620 cm^{-1} in the spectrum of defected graphene.

The Raman scattering processes in graphene can also be described in the real-space picture (see figure 40a), in which a quasi-classical treatment of the electron and hole motion is used.[102] For the electron and hole to meet at the same point, and thus recombine with emission of a photon, the phonon involved must scatter the e and h backwards, and this is known as the backscattering condition. The e-h pair generated during D band activation can be regarded as wave packets of approximate size $\hbar v_F/\varepsilon \sim 0.6$ nm (for 514 nm excitation), where v_F is the Fermi velocity and ε is the electron energy.[99] Momentum conservation dictates that for radiative recombination of the e-h pair to occur, leading to emission of a photon, the electron and hole must meet with nearly opposite momenta and in the same region of space. The process is achieved by defect activation involving inelastic scattering of the electron or hole by a phonon and elastic scattering by a defect. Both the phonon and defect scattering events must be backscattering to satisfy the requirement that the electron and hole recombine with opposite momenta. Figure 40b nicely illustrates the constraints that the phonon scattering process must satisfy for D band activation to occur; (1) one end of the phonon wave vector, q, must be on the Dirac cone surrounding K, and the other must be on the cone surrounding K', and (2) backscattering can only occur if q' = -2k', given that q = K + q'. The momentum conservation and backscattering con-

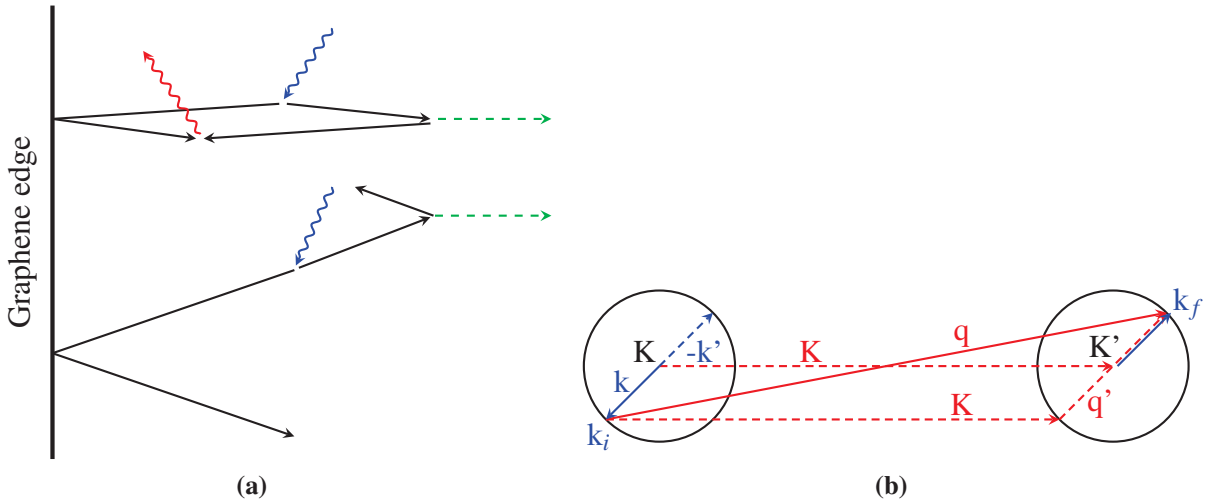

Figure 40: (a) Representation in real space of D peak Raman scattering at an ordered edge. In this diagram, the incident and scattered photons are denoted by the blue and red wavy arrows, respectively, the trajectories of the electron and hole by the black arrows and the emitted phonon by the green dashed arrows. At normal incidence, backscattering is possible, whereas at oblique incendence specular reflection occurs, thus radiative recombination of the electron and hole is not possible. (b) Reciprocal space representation of the backscattering constraint in DR Raman scattering. An electron (k) is backscattered by a phonon (q) from k_i = K + k to k_f = K' -k'. As q = K + q', backscattering can only occur if q' = -2k'. Figures adapted from Ferrari et al.[99]

straints also apply to defect scattering. Thus, momentum conservation dictates that d = -q, where d is the defect wave vector. Hence, the condition d = K' + 2k' for backscattering is also satisfied.

From figure 40a, it is clear that there are geometric considerations for electron backscattering from phonons and edges.[99] From the real space consideration of D band activation at an ordered edge, the electron and hole must meet and radiatively recombine, which requires that the electron momentum be perpendicular to the edge, i.e. backscattering is only possible at normal incidence.[102] An oblique incidence will give specular reflection and the electron and hole cannot meet at the same point to recombine radiatively. Figure 41a shows the change in momentum of an electron backscattered from armchair (d_A) and zigzag (d_Z) edges. The DR process requires that the wave vector of the defect involved in the elastic scattering process connect points on the circles surrounding the inequivalent points K and K'. These circles represent the set of electron wave vectors with radius $\vec{k}$ that can be excited by a laser photon and therefore participate in the DR process. From figure 41b, it can be seen that only d_A is directed along K − K' (i.e. intervalley), while d_Z is not. Thus, only the armchair edge can satisfy the requirements for D band activation. In contrast, the D' peak, which involves an intravalley scattering process, can be activated by both armchair and zigzag edges, as both d_A and d_Z can connect points on the same circle surrounding K or K'. As a result of the backscattering condition, the D band intensity exhibits a strong polarisation dependence with linearly polarised light, with the D band intensity $I(D) \propto cos^2\theta$, when all polarisations of the scattered light are detected.[99,102] With an analyser in the scattered path, set parallel to the input polarisation, the dependence becomes $I(D) \propto cos^4\theta$. The D' peak shows a similar behaviour to the D peak. If the edge has some degree of disorder, i.e. is not a perfect armchair edge, I(D) does not go to zero for polarisation perpendicular to the edge direction, rather the contributions from

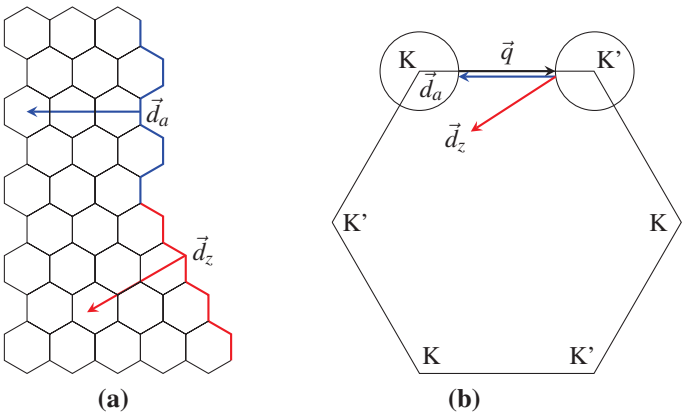

Figure 41: (a) Wavevectors of defects for armchair ($\vec{d}_a$) and zigzag ($\vec{d}_z$) edges in graphene. (b) Mechanism of DR process for armchair and zigzag edges in the first BZ. The circles surrounding the K and K' points represent the set of electron wave vectors that can be excited by a laser photon and participate in the DR process. Figures adapted from Krauss et al.[126]

both armchair and zigzag segments will alter the polarisation dependence, and the ratio $I(D)_{min}/I(D)_{max}$ can be used to measure the degree of disorder at the edge.

The G band originates from the degenerate LO and TO phonon modes (see figure 42) at the BZ centre (i.e. Γ point). These two modes contribute equally to the G band in the graphene basal plane, without any polarisation dependence.[103] At the graphene edge, however, the two degenerate phonons do not participate equally in the scattering process, and a polarisation dependence emerges. This polarisation dependence is due to effects of the modification of the frequency and lifetime of a phonon mode by the electron-phonon coupling (EPC), known as the Kohn anomaly.[127] This Kohn anomaly effect is only present for the LO modes and not the TO modes. As a result, the LO modes become inactive near a zigzag edge, while the TO modes are not active near an armchair edge. Hence, the G band is activated only at parallel incident polarisation for the armchair edge, and only at perpendicular polarisation for the zigzag edge, giving $I(G) \propto cos^2\theta$ at an armchair edge and $I(G) \propto sin^2\theta$ at a zigzag edge.

Graphite and multilayer graphene have an additional Raman-active mode arising from the low-frequency doubly-degenerate E_{2g} mode.[102] In graphite, this appears at ~ 42 cm^{-1}. This mode is known as the low-frequency "shear" mode, or C peak, due to its sensitivity to the interlayer coupling of graphene planes.[104] This doubly-degenerate mode involving atoms in graphene layers collectively vibrating relative to neighbouring layers shows a shift to lower frequency with increasing number of graphene layers, reaching ~ 31 cm^{-1} for bilayer graphene, and is absent altogether for single-layer graphene. The C peak is an out-of-plane mode, thus can be used as a direct probe of the graphene layer number.[102] For graphene with N layers, there are actually $N-1$ shear modes, with the highest frequency Raman-active mode corresponding to the C peak.[104] The other modes are expected to have significantly weaker intensity, based on DFT calculations. The frequency of the C peak in cm^{-1} for N-layer graphene is given by the following equation[102]:

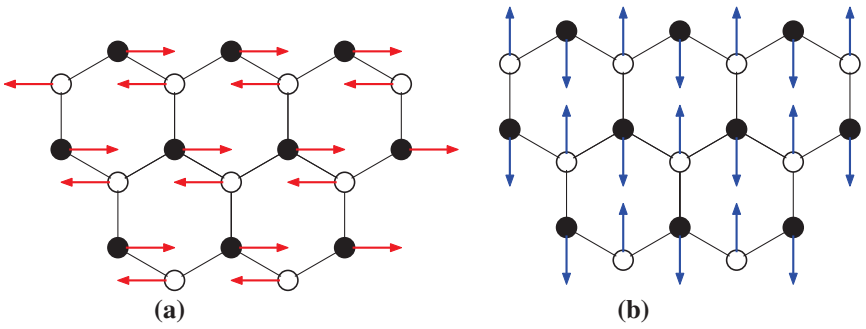

Figure 42: The doubly degenerate E_{2g} LO (a) and TO (b) phonon modes of the G band in graphene. Figure adapted from Sasaki et al.[127]

$$Pos(C)_N = \sqrt{\frac{2\alpha}{\mu}}\sqrt{1+cos\left(\frac{\pi}{N}\right)} \times \frac{1}{2\pi c} \tag{6}$$

where α is the interlayer coupling, with a value 12.8×10^{18} N m^{-3}, and μ is the graphene mass per unit area, with a value 7.6×10^{-27} kg Å^{-2}.

The shift in frequency of the C peak in going from bulk graphite to bilayer graphene is shown in figure 43. This diagram shows the calculated symmetries and frequencies of the N$-$1 low-frequency modes of graphene with $2-5$ layers. Only the highest frequency C mode for bulk graphite is given. The shift to higher frequency of the C peak with increasing number of graphene layers is attributed to interference from neighbouring layers resulting in suppression of the interlayer vibration.[129]

The 2D band is also sensitive to the number of graphene layers, even though it is an in-plane mode.[102] This is due to effects of the electronic band structure, which changes with the number and relative orientation of the graphene layers, on the resonant Raman process giving rise to the 2D band. The shape and relative intensity of the 2D band

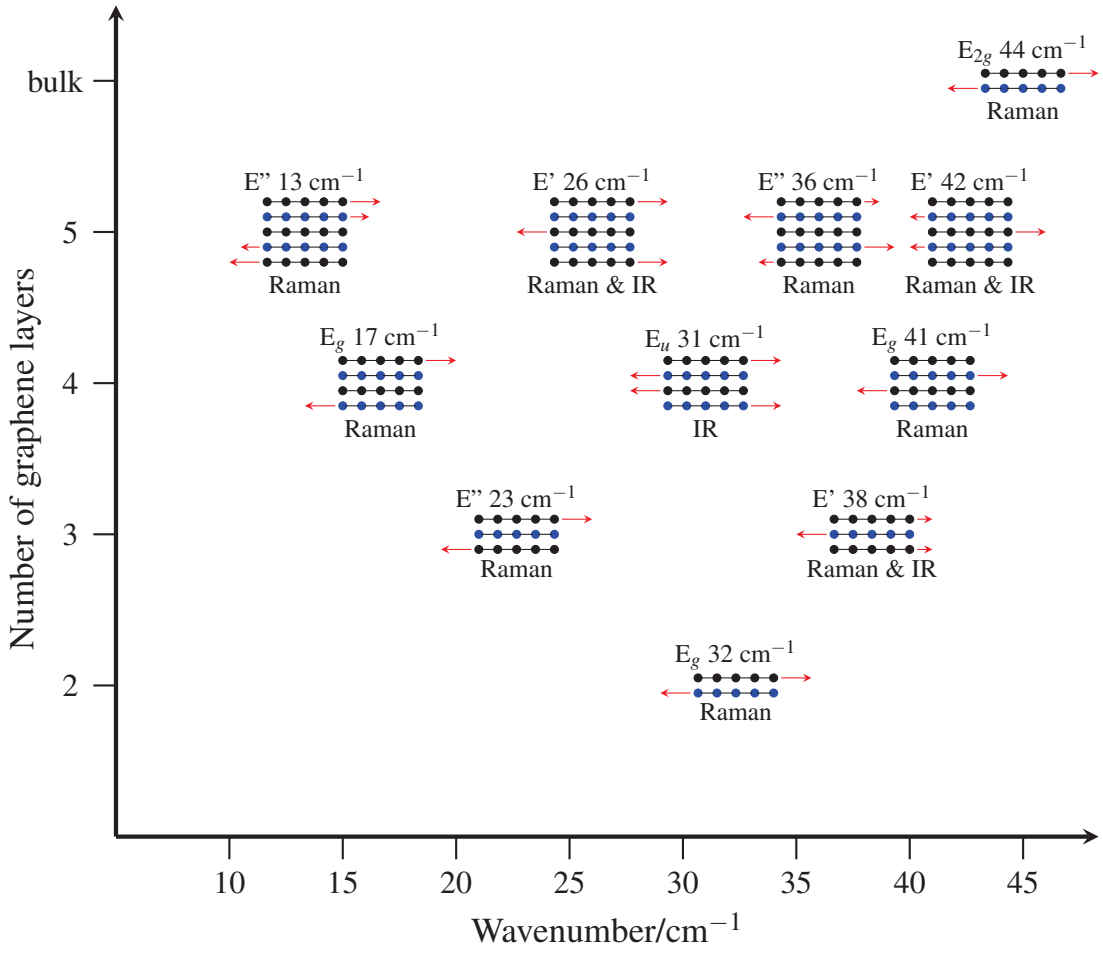

Figure 43: Calculated symmetries and frequencies for the shear modes of graphene with differing layer numbers. Figure adapted from Tan et al.[104]

undergoes substantial changes going from monolayer graphene to HOPG. For single-layer graphene, the 2D band consists of a single Lorentzian peak with a FWHM of ~ 24 cm^{-1}.[98] Additionally, the 2D band intensity is large relative to that of the G band. For bilayer graphene, the electronic and phonon bands both split into two, due to in-phase and out-of-phase components for motions of the two layers relative to each other. As a result, there are four different scattering processes, which give rise to four Lorentzians making up the 2D band for bilayer graphene. For trilayer graphene, there are fifteen possible Raman peaks in the 2D band. Since the energy separations for some of the Raman processes are very small, the 2D band can be approximated with a fit of six Lorentzians. As the number of graphene layers increases, the complexity of the 2D band also increases. For HOPG, the 2D band consists of numerous peaks that merge to form two main groups of peaks that can be fit with just two Lorentzians.

The DR model of Raman scattering in graphene is the most widely known and used. However, there are certain effects not fully covered in the DR approach, such as the effects of π electron confinement in edges or defects on the Raman scattering. A new approach was developed by Tommasini et al. to explain these effects, and this approach is based on molecular models of graphite, thus named a "molecular" approach.[130] The models used in this study were PAHs (polycyclic aromatic hydrocarbons), as they exhibit G and D bands in their Raman spectra. Adjusting the size and shape of the PAH system allowed for the degree of π electron confinement to be tuned. The model is based on the Peticolas et al.[131] expression for the Raman scattering cross section, simplified for PAHs and evaluated using a Huckel approach. This gives rise to a so-called Raman bond scattering parameter, which represents the change in bond order upon excitation, and was used to determine bond contributions to Raman scattering. Thus, the contributions of each bond to a given Raman-active vibration, such as the D and G modes, were able to be mapped in real space. The simplicity of this approach allowed it to be applied to larger graphitic systems such as graphene flakes. Analysis of armchair and zigzag graphene flakes revealed a difference in the pattern of Raman bond parameters, which was used to explain the well-known differences in Raman scattering from armchair and zigzag edges.

4.2 Results and Discussion

4.2.1 Raman Spectroscopy of HOPG and Graphene Samples

As the GNRs produced via the nanotomy[83] method are cut directly from a block of HOPG, it is useful to first study the Raman spectra of HOPG for comparison with the spectra of the GNRs. The freshly-cleaved surface of an HOPG block will also contain edges, thus it can make a useful template and test of the polarised Raman behaviour of the D band arising from the edge. Figure 44a shows the first Raman spectrum of HOPG acquired with the Raman microscope set up with a 785 nm laser. Spectra are shown taken at two different positions on the HOPG block, with the absence of a D band in the red

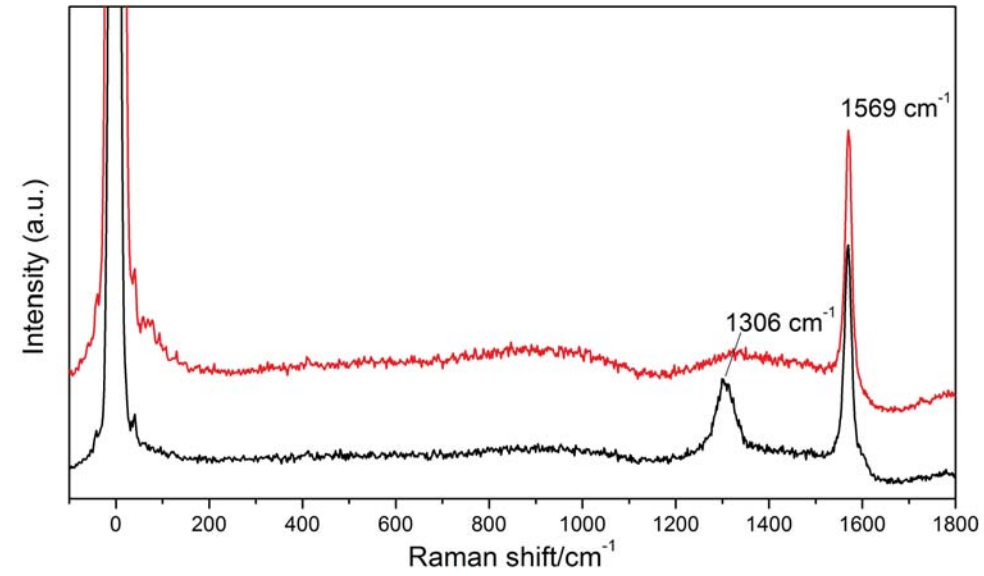

(a)

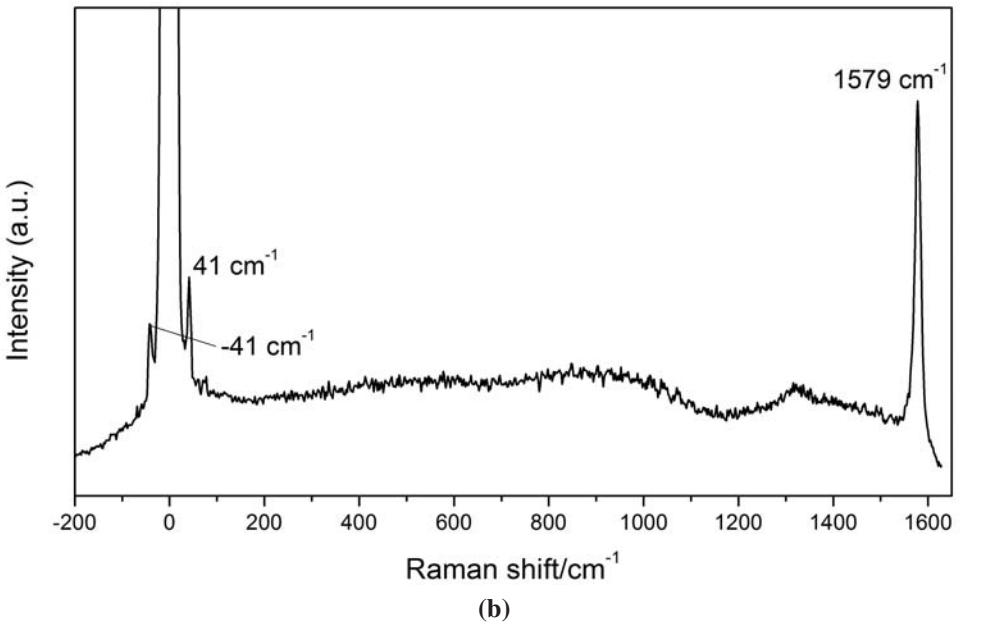

(b)

Figure 44: Raman spectra of HOPG acquired with 785 nm excitation.

spectrum indicating a pristine, defect-free graphene sheet. Thus, this should represent a typical Raman spectrum of a continuous graphite sheet without edges or defects. This is indeed the predominant appearance of the spectrum as the laser beam is scanned across the sample, indicating a high quality HOPG with large grain size. Occasionally, a D band appears, as seen in the black spectrum, indicating that one or more HOPG edges have come into focus. Also apparent in both spectra are the C peaks[104] near ± 40 cm^{-1}. The

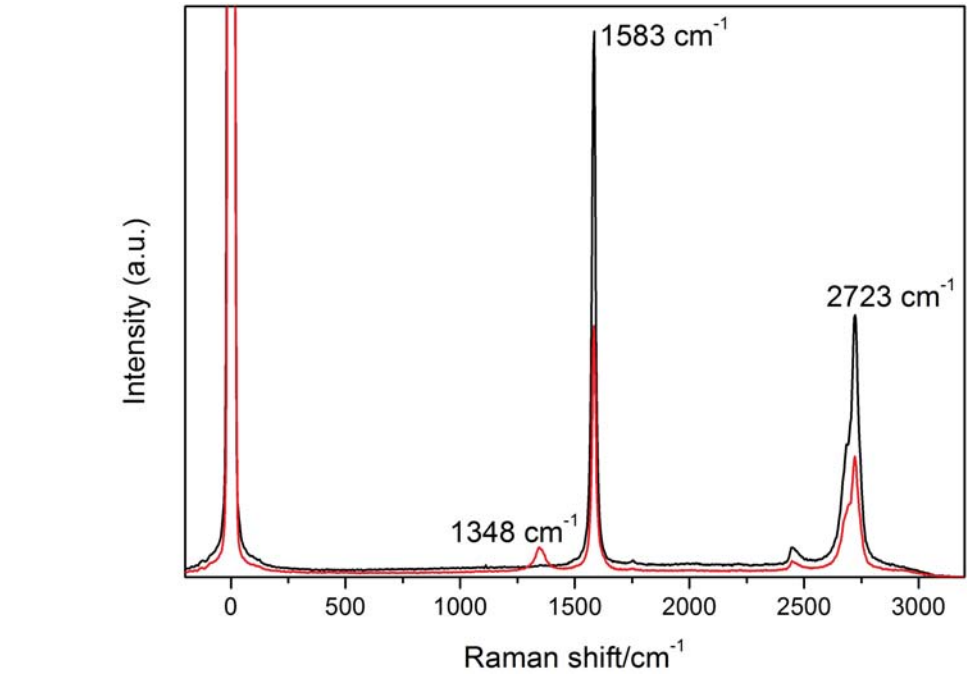

(a)

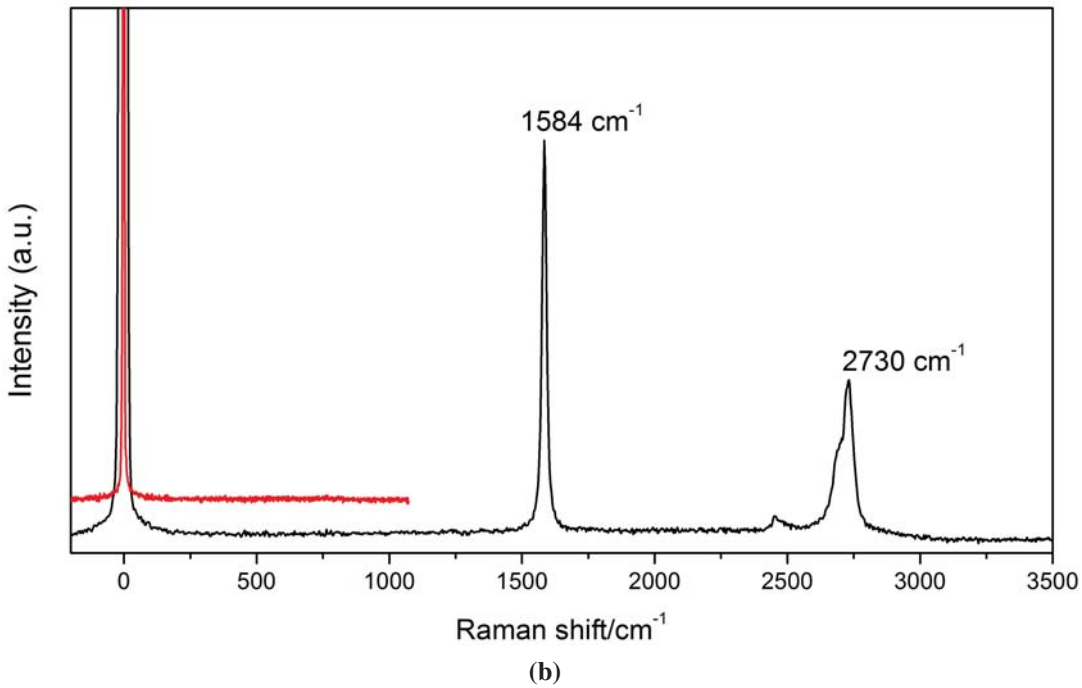

(b)

Figure 45: Raman spectra of HOPG acquired with 532 nm excitation.

C peaks are seen more clearly in the spectrum shown in figure 44b. These spectra were taken with a 40X objective with NA 0.65, and with 785 nm excitation this gives an estimated laser beam diameter of $\sim$1.5 μm at focus. The Raman spectra of the same HOPG sample taken with 532 nm excitation is given in figure 45a. Again, spectra were taken both in a pristine area of the basal plane, and in an area containing edge(s), as evidenced by the absence and presence of a D band. These spectra were acquired at low resolution (300 g/mm grating) so that the range would be sufficiently large enough to include the 2D band. This results in broadening around the Rayleigh line, which extends quite far into the low-frequency region. Shown in figure 45b is the same spectrum taken with higher resolution (1200 g/mm grating), and the Rayleigh line is now much sharper, with the baseline much more flat in the low-frequency region. However, there is no C peak in any of the spectra acquired at 532 nm. According to Tan et al.[104], the ratio of integrated C and G peak areas changes with excitation energy, with I(C)/I(G) $\sim$ 0.007 for graphite at 633 nm, and $\sim$ 0.0014 at 532 nm. These ratios are dependent on the EPC (Electron Phonon Coupling), which is much smaller for the C peak than for the G peak. The spectrum acquired at 785 nm in figure 44b gives an I(C)/I(G) ratio of 0.22. Thus the C peak intensity at 532 nm would only be a fraction of that at 785 nm, which would explain why it is not visible in the spectrum given in figure 45b.

A Raman study of different types of graphene samples was conducted, to investigate any differences in the appearance of the graphene Raman bands. These included HOPG, as well as a range of single-layer, bi-layer and multi-layer CVD graphene test samples on glass, Ni and SiO_2/Si substrates. Given in figure 46 are the Raman spectra of these

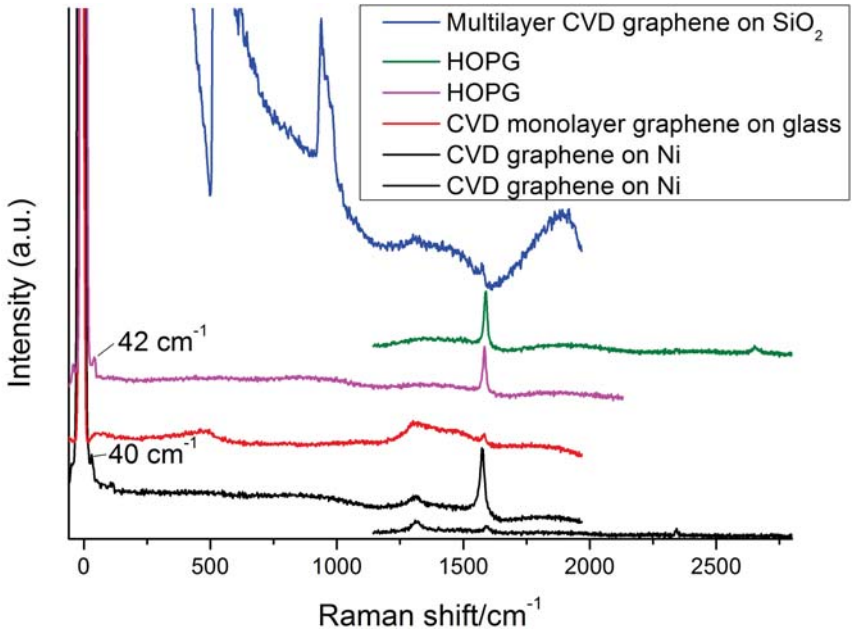

Figure 46: Raman spectra of HOPG and various graphene samples acquired with 785 nm excitation. The intense band in the blue spectrum is due to the SiO_2 substrate.

samples taken with 785 nm excitation. The C peak is seen in the spectrum of CVD graphene on a Ni substrate, and the fact that it is very close in wavenumber to the C peak of HOPG suggests that this is many-layer graphene. The C peak is absent in the spectrum of CVD monolayer graphene on a glass substrate, indicating single-layer graphene. The high level of background from the SiO_2 substrate precludes the observation of the C peak in multilayer CVD graphene. The 2D band is weakly visible for HOPG, but interestingly is absent for CVD graphene on Ni, as seen in the lower spectrum. The D:G ratio appears to vary quite considerably at different regions on this sample, as illustrated by the two different scans. Overall, the graphene test samples show relatively low D band intensities, particularly in comparison to GNRs (as will be shown in a later section), suggesting a low proportion of edges and defects.

Figures 47 through 49 show Raman spectra of the same samples as in the previous figure, but taken with 532 nm excitation. Like HOPG, the C peak is also absent for all the graphene samples with 532 nm excitation. However, in these spectra, the 2D band can be used to infer the number of graphene layers in the sample via curve-fitting of the band with Lorentzians, as described by Dresselhaus et al.[98] As the spectra were acquired at low resolution (300 g/mm grating) so that the full spectral range of interest could be covered in a single spectrum, only a maximum of two bands could be reliably fit to the data for each spectrum. For HOPG, the shape of the two Lorentzians fit to the 2D band is in good agreement with the literature for bulk graphite.[98] The monolayer graphene samples all show a sharp 2D band that is higher in intensity than the G band and can be fitted with a single Lorentzian. Some of the multilayer CVD graphene samples have a 2D band that can be fitted with two Lorentzians, though with a different shape than HOPG. The positions and intensities of these Lorentzians relative to the G band would suggest bilayer graphene for the multilayer CVD graphene on SiO_2, and trilayer graphene for the CVD graphene on Ni. However, these assignments are only tentative, as the low resolution prevents fitting of the other Lorentzians for bilayer and trilayer graphene, which is needed to provide a more definitive assignment.

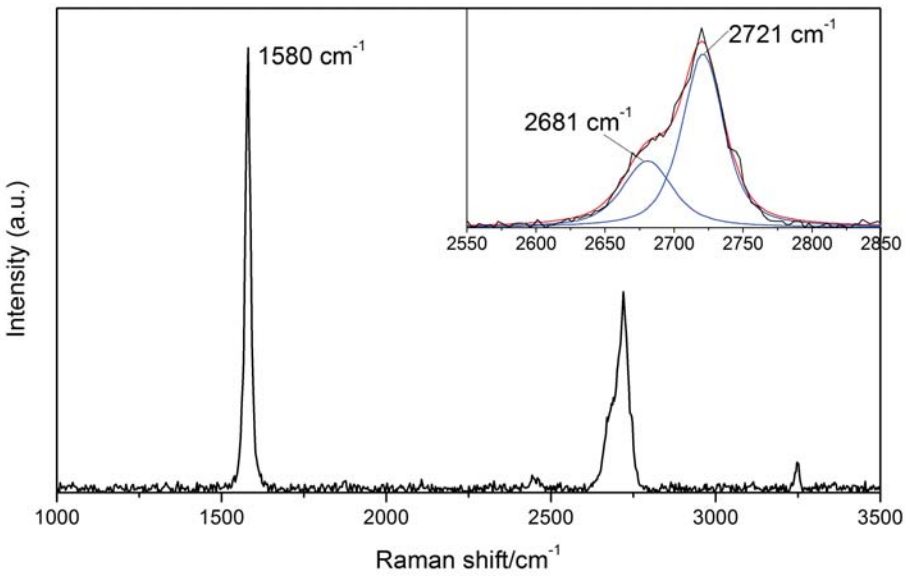

(a)

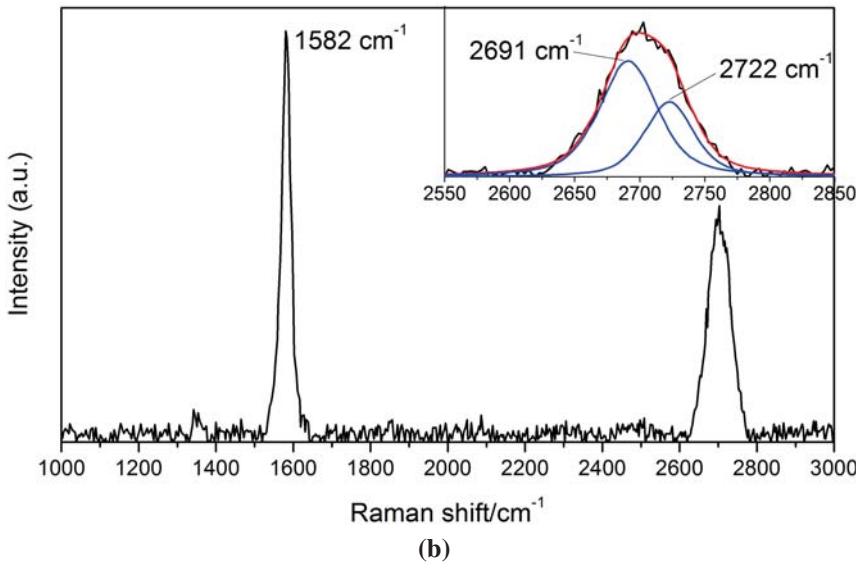

(b)

Figure 47: Raman spectra of (a) HOPG and (b) CVD graphene on a Ni substrate. Spectra were acquired with 532 nm excitation.

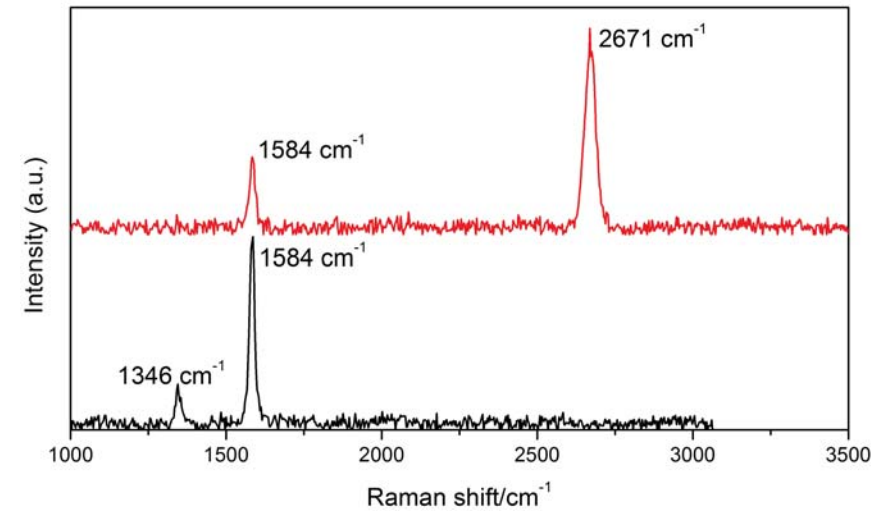

(a)

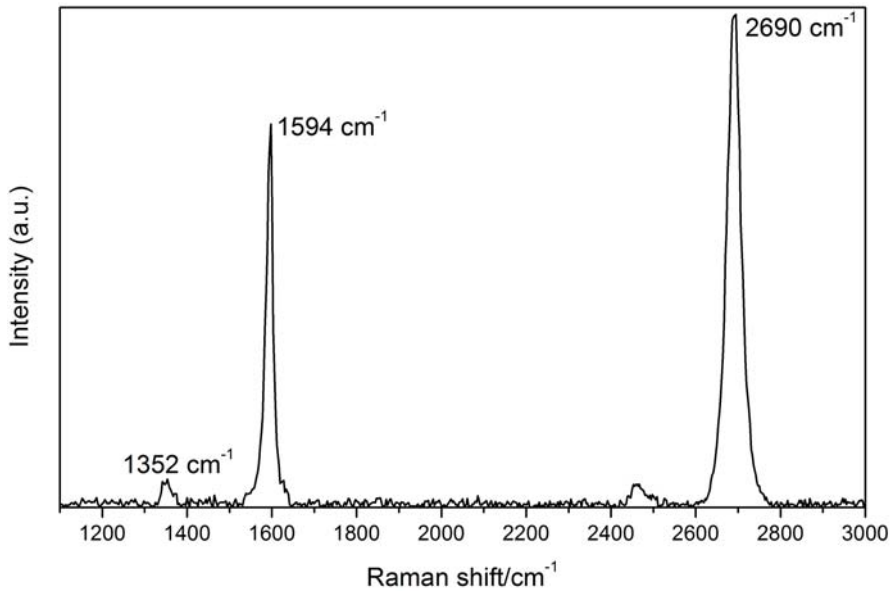

(b)

Figure 48: Raman spectra of monolayer CVD graphene on (a) a glass substrate and (b) an SiO_2 substrate. Spectra were acquired with 532 nm excitation.

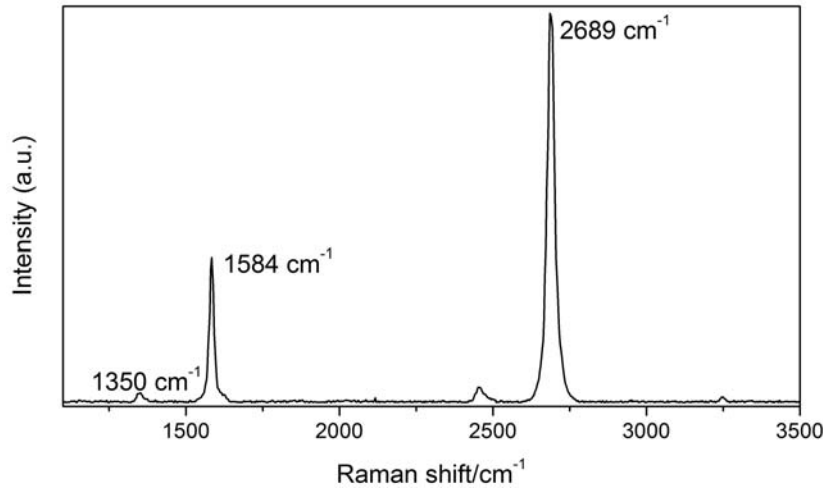

(a)

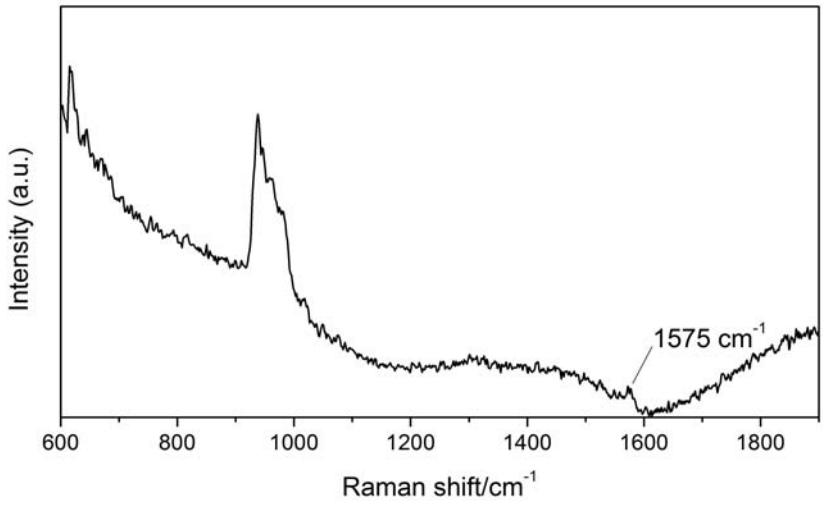

(b)

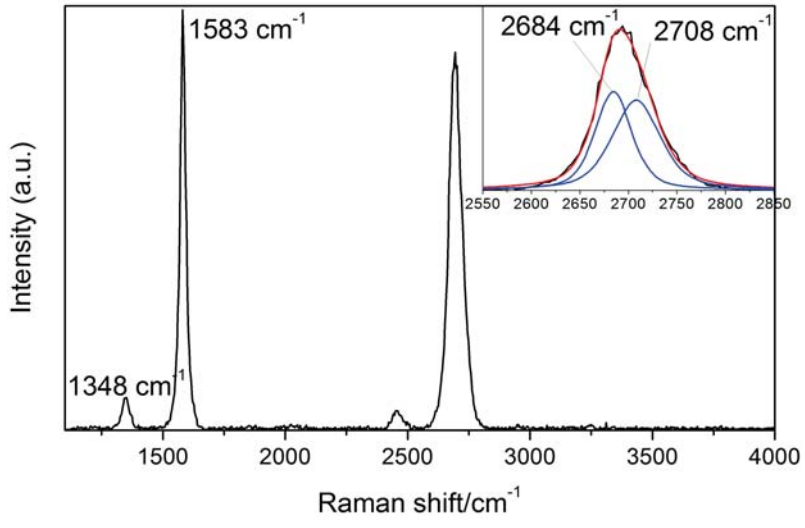

(c)

Figure 49: Raman spectra of (a) single/double CVD graphene (b) and (c) multilayer CVD graphene, all on an SiO_2 substrate. Spectra were acquired with 532 nm excitation.

4.2.2 Fabrication of Graphene Nanoribbons

The ability to produce high-quality graphene nanoribbons with uniform and controllable size is a key element to the success of this project. The recent method developed by Mohanty et al. combines all of these qualities in a simple nanotomy-based procedure.[83] The key technique that distinguishes this method from numerous other procedures in the literature is the use of mechanical force to effectively cut graphene sheets, rather than chemical methods which often result in heavily oxidised graphenes. The method involves the repeated cutting of an HOPG block by a diamond knife using a microtome - a machine which is primarily used for sectioning biological samples. The width of the GNRs produced is controlled by the step size of the knife. Mohanty et al.[83] produced ribbons with widths ranging from ~ 5 nm $-$ 600 nm. The method is outlined in figure 50. Following cleavage by the diamond knife, the graphite "nanoblocks" (GNBs) are collected in a water bath, and then exfoliated to produce nanoribbons. The method for exfoliation used in this procedure involves chlorosulfonic acid, which reacts violently with water and hence is difficult to work with. There are however, numerous other methods in the literature for graphene exfoliation, most of which involve sonication at low power in a solvent or aqueous surfactant solution.[17,132,133] These methods generally require chemicals that are much safer and easier to work with than chlorosulfonic acid.

The sonication-based methods can be divided into two general groups: solvent-based and surfactant-based. The organic solvent N-methyl-pyrrolidone (NMP) is known to effectively exfoliate graphene, and has been found to give graphene concentrations up to 1.2 mg mL^{-1}.[17] Exfoliation of graphite requires the strong graphene interlayer interactions to be overcome, and this can only occur if the energetic penalty for the separation of graphene layers and their subsequent solvation is very small.[16] This requires that the graphene-solvent interactions be comparable to the graphene-graphene interactions, and the energetic cost can be expressed as the enthalpy of mixing per unit volume, given by

$$\frac{\Delta H_{mix}}{V_{mix}} \approx \frac{2}{T_{flake}}(\delta_G - \delta_{sol})^2\phi \tag{7}$$

where T_{flake} is the graphene flake thickness, δ_G and δ_{sol} are the graphene and solvent surface energies, respectively, and ϕ is graphene volume fraction. The presence of ϕ/T_{flake} in the equation indicates that the graphene surface area is an important determinant of the ease of exfoliation, with a smaller graphene area corresponding to better exfoliation. This can be simply rationalised by considering the interactions holding graphene sheets together, which all need to be broken for exfoliation to occur. Smaller graphenes will have a smaller number of interlayer interactions, hence the energetic cost of exfoliation will be lower than for larger graphene flakes. This is advantageous in working with nanoribbons. The equation shows that solvents with very similar surface energies to that of graphene

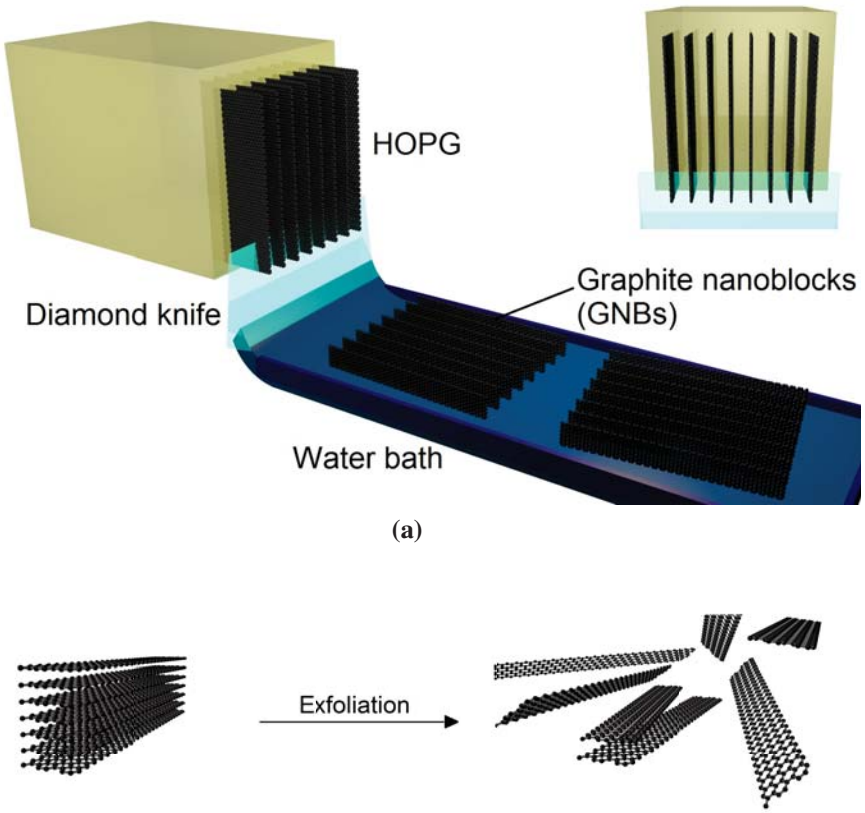

Figure 50: Nanotomy method for the production of GNRs. (a) An HOPG block is cleaved by a diamond knife into GNBs. (b) The GNBs are then exfoliated into GNRs. Figure reproduced with permission from Samuel Brooke.

will have an enthalpy of mixing close to zero, resulting in good exfoliation. The best solvents, however, generally have high boiling points ($\sim 200^{\circ}$C for NMP), which present problems when the solvent needs to be removed, for example in depositing graphene flakes onto substrates for AFM or TEM. Hence, the best choice of solvent will be a compromise between graphene yield and desirable solvent properties, e.g. low boiling point. The solvents acetone, chloroform and isopropanol, which have much lower boiling points, have been found to exfoliate graphene to reasonable concentrations - up to 0.5 mg mL^{-1}.[114] Due to GNRs being significantly easier to exfoliate than large graphene flakes, this should allow for the use of less "ideal" solvents with more desirable properties, as well as more gentle exfoliation conditions, e.g. lower power and shorter time.

Graphene is also known to be exfoliated effectively in aqueous surfactant solutions, which require only very low surfactant concentrations (below the critical micelle concentration (CMC) of most surfactants) to achieve good exfoliation.[133] Common surfactants such as SDS, SDBS and CTAB have been found to give good graphite exfoliation.[134,135] Surfactant molecules stabilise the exfoliated graphenes by interaction of the hydrophobic tail with the graphene plane, leaving the polar head group free to interact with the sur-

rounding water, thus effectively solubilising the graphene. Re-aggregation is prevented by the repulsive interactions between the polar head groups of nearby surfactant-coated graphenes.[135]

4.2.3 Characterisation of GNRs by Raman Spectroscopy, AFM and TEM

An AFM image of GNBs cut at 100 nm width via the nanotomy method described in the previous section is given in figure 51a. The GNBs were transferred directly to the AFM substrate without sonication, though they do appear to be at least partially exfoliated, as numerous GNRs are visible in the AFM scan. These were measured to be approximately 100 nm in width, which is consistent with the width at which they were cut, and with lengths of several microns. The Raman spectrum of this sample is given in figure 51b. The D band is much more prominent in this spectrum compared to the HOPG and graphene test samples shown earlier, indicating a significantly higher proportion of edges. The D' band around 1610 cm^{-1} is also now present. A faint C peak is visible at ~ 37 cm^{-1}, which is somewhat lower in frequency than the C peak for HOPG.

Following exfoliation of the GNBs in surfactant solution (SDS) via ultrasonication for 24 hours, the GNRs were dispersed onto a mica substrate, and AFM images of these are given in figure 52. Numerous GNRs are visible, and these appear to be at least several microns in length. These are similar in appearance to AFM images of GNRs reported in the literature.[75,83,117,136] Figures 52c and 52d show the topography profiles of the ribbons marked in figure 52b. Both ribbons appear to have a width of approximately 100 nm. Ribbon 1 has a height of ~ 2 nm, suggesting that this is a multi-layered ribbon, whereas ribbon 2 has a height of only ~ 0.5 nm, which probably corresponds to a single-layer GNR. Most of the GNRs shown in figure 52a have similar heights to ribbon 2. An AFM image of a similar sample, along with its profile, is given in figure 53. The AFM images demonstrate the successful exfoliation of GNBs into single- and few-layer GNRs that appear to be of high quality.

Though the AFM images in the previous figure show well-separated, single-layer ribbons, these do not at all represent the "typical" AFM image of the GNR sample, as most scans showed only aggregates. An example of the types of aggregates typically observed is given in figure 54. More AFM scans of GNRs can be found in Appendix B. Measures were taken to improve the dispersion of ribbons on the mica substrate, including the use of an airbrush to spray a fine mist of ribbon solution onto the surface. These did not produce any significant improvement in the quality of ribbon coverage, and ribbon aggregation remained a problem throughout all the experimental work.

TEM images of GNRs dispersed on formvar-coated TEM grids are shown in figures 55 and 56. More images can be found in Appendix B. These images show ribbons predominantly folded/rolled-up or aggregated, similar to those observed with AFM. The study by Mohanty et al.[83] showed TEM images of single-layer GNRs lying flat on the substrate

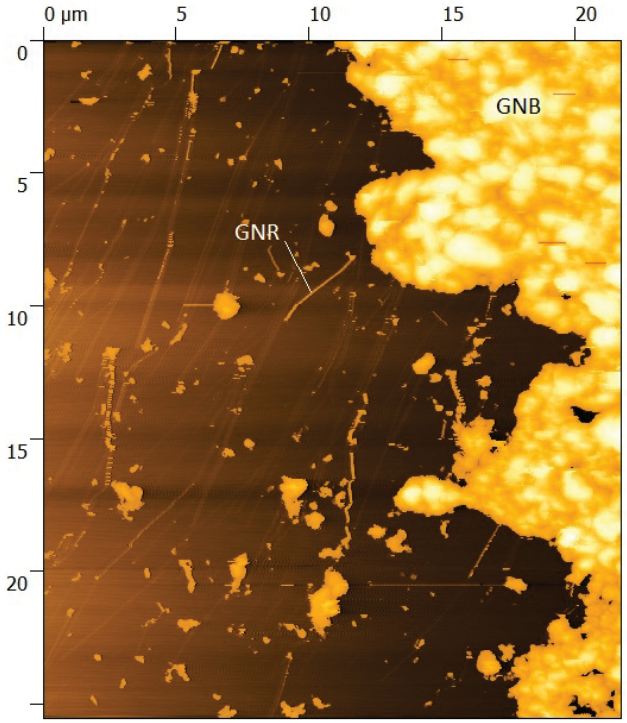

(a)

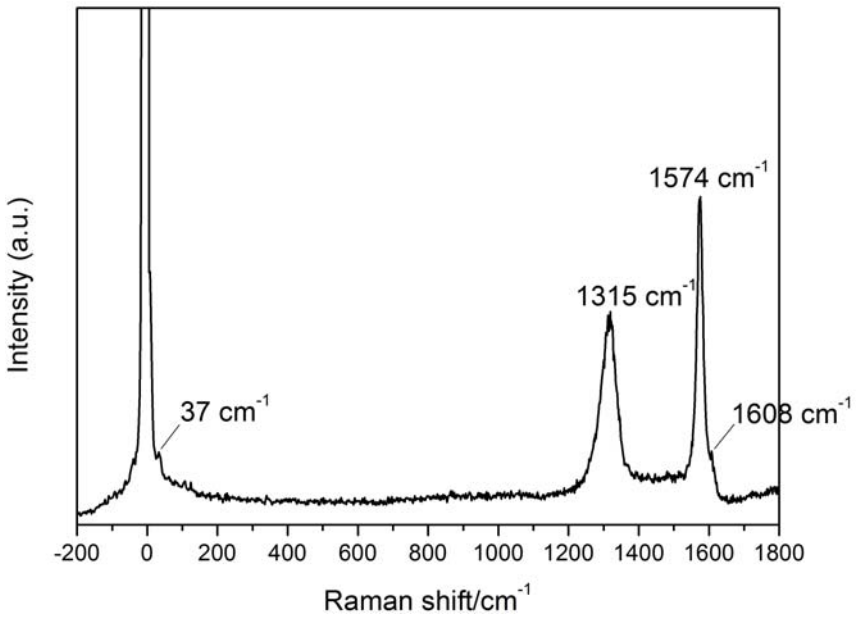

(b)

Figure 51: (a) AFM image of 100 nm wide GNBs on a mica substrate, acquired in tapping mode. (b) Raman spectrum of GNBs on mica acquired with 785 nm excitation.

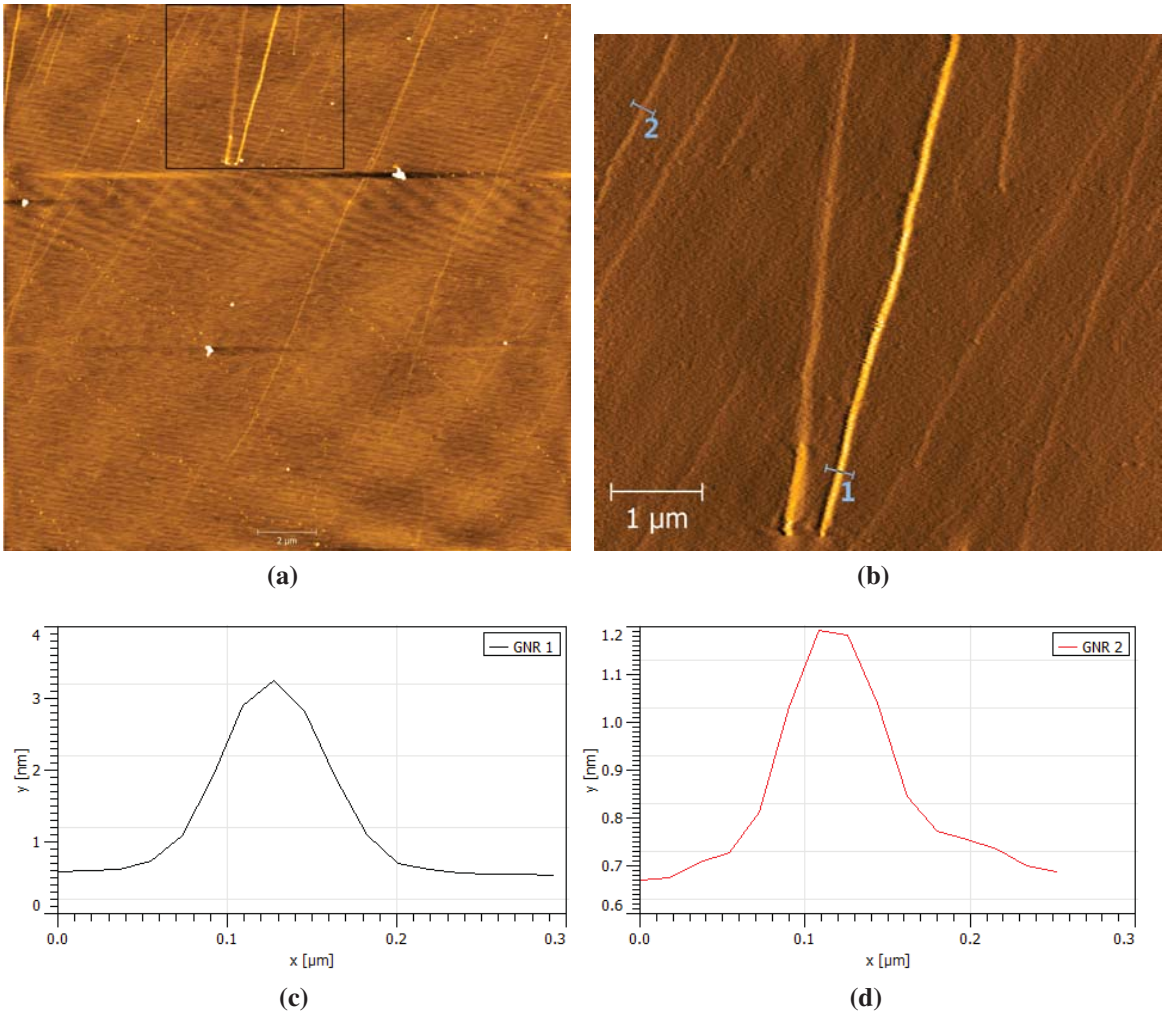

(a) (b)

(c) (d)

Figure 52: (a) AFM image of exfoliated GNRs. (b) Zoomed-in portion of the region marked by the black rectangle in (a). (b) and (c) Topography profiles showing heights and widths of the nanoribbons marked in (b).

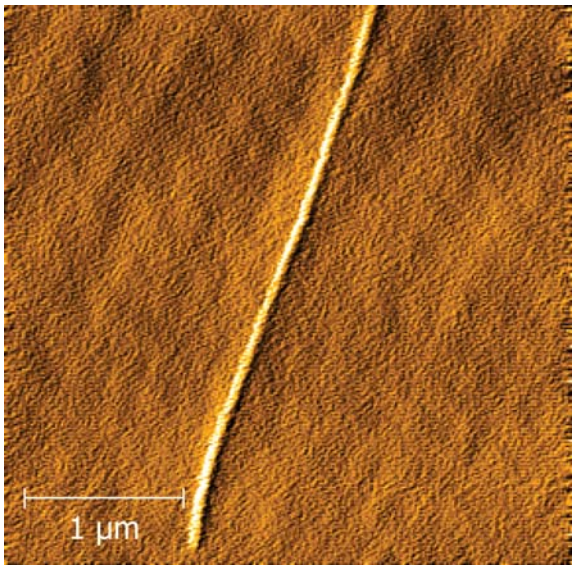

(a)

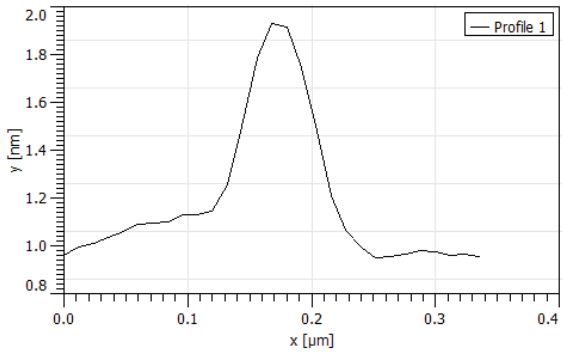

(b)

Figure 53: AFM in tapping mode of 100 nm GNR on a mica substrate.

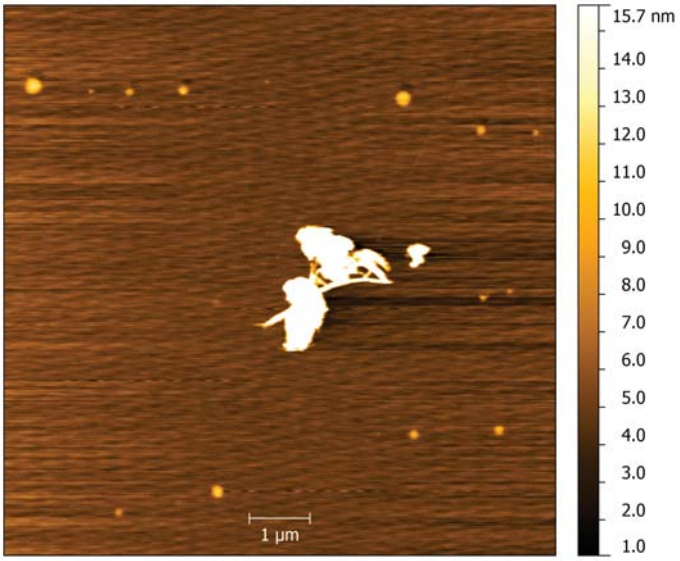

(a)

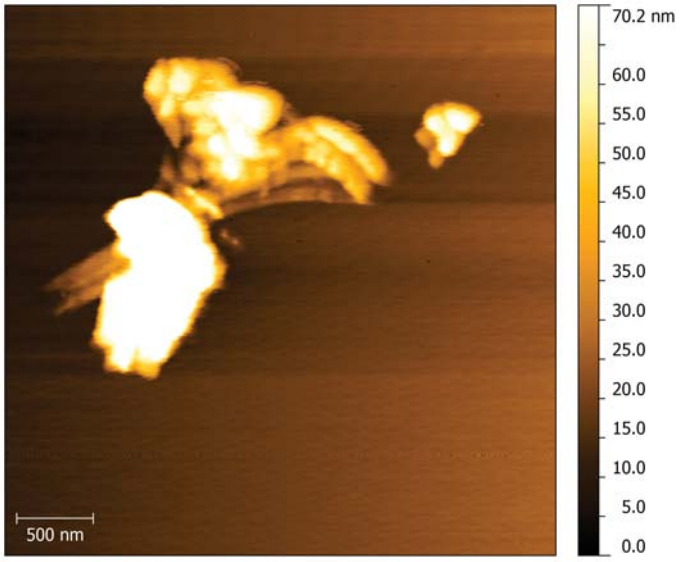

(b)

Figure 54: AFM in tapping mode of a GNR aggregate on mica.

without aggregation, folding or rolling up. However, the GNRs shown like this are small in width (up to 60 nm). For their ribbons with larger widths (>100 nm), some folding of the ribbons was apparent. In addition, a different procedure for ribbon exfoliation was described in their work. Unlike the gentle sonication-based exfoliation used here, a more harsh method involving chlorosulfonic acid was used, which was shown to give significant sulfonation at the GNR edges. This could lead to an increase in the ribbon rigidity by providing charged groups at the edge to provide electrostatic repulsion and thus prevent significant aggregation and rolling/folding.

Though it is difficult to get an idea of average ribbon width at each cutting width in the range $20 - 500$ nm, where partial individual ribbon segments are visible there does appear to be significant variation in actual width within each sample. This is due to the rather low cutting width reproducibility of the microtome used. In contrast, the AFM images obtained from the much smaller HOPG block used in the earlier work do seem to show much more consistent widths. This would suggest that cutting from a smaller block at lower speed gives more consistent ribbon width.

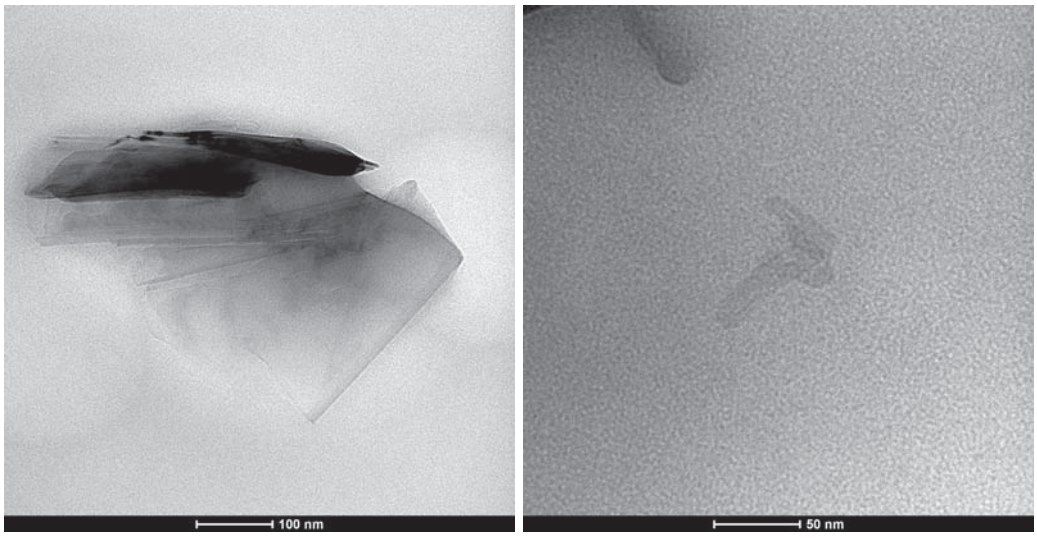

(a) **(b)**

Figure 55: TEM images of GNRs cut at (a) 300 nm and (b) 20 nm.

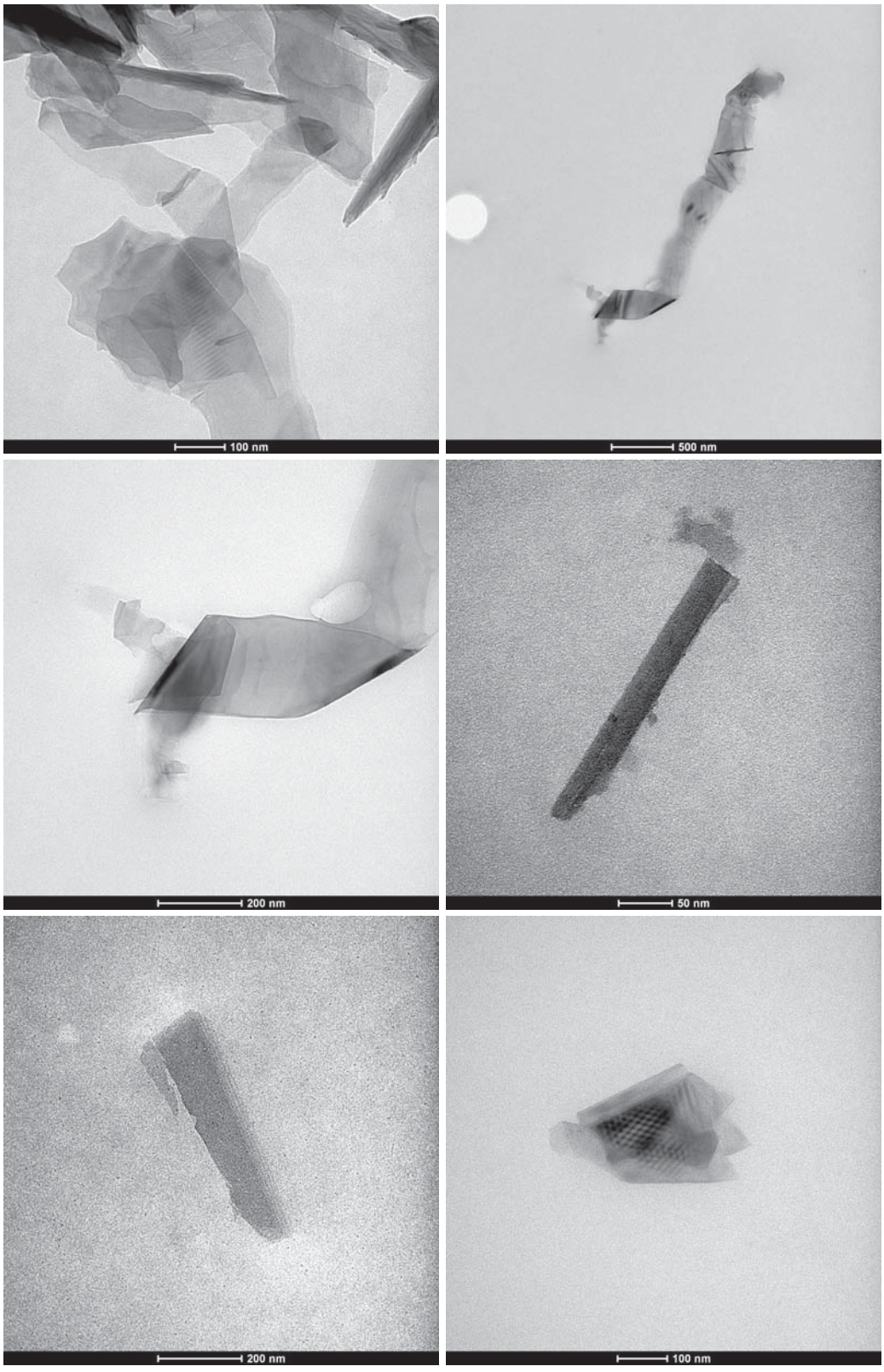

Figure 56: TEM images of GNRs cut at 100 nm.

4.2.4 Raman Spectroscopy for the Determination of Layer Number in GNRs

The shear mode of graphene

The low-frequency C peak observed in multilayer graphene can be used to directly determine the number of layers in a graphene sample, due to its sensitivity to the interlayer coupling of graphene planes.[104] This peak has been observed in HOPG and some of the graphene test samples shown in section 4.2.1, thus the next step was to investigate the behaviour of this peak in GNRs. This peak has only been observed with 785 nm excitation, and as shown previously, does not appear in the Raman spectrum with 532 nm excitation. This presents somewhat of a problem, as the minimum diffraction-limited laser focus spot size with 785 nm is significantly larger than the GNR width, thus the Raman intensity for a single or multi-layer ribbon would be quite small. In addition, as will be discussed in a later section, depositing GNRs on Raman substrates to give single ribbons was found to be very difficult, with only visible aggregates observed under the optical microscope giving a Raman signal, even with 488 nm excitation. Thus, only aggregates of GNRs showed Raman peaks in their spectra with 785 nm excitation. Figure 57 shows the low-frequency region of the Raman spectra of HOPG, GNBs and GNRs on a mica substrate. C peaks are visible in each spectrum, with those of the GNB and GNR samples significantly weaker than those of HOPG. Spectra from several areas of the GNR sample were recorded, with the C peak appearing between $30 - 35$ cm^{-1}. The C peak shows a shift to lower frequency from HOPG $>$ GNB $>$ GNR, with the largest shift of 4 cm^{-1} occurring between HOPG and the GNB sample. Interestingly, the C peak of the GNB sample is lower in frequency

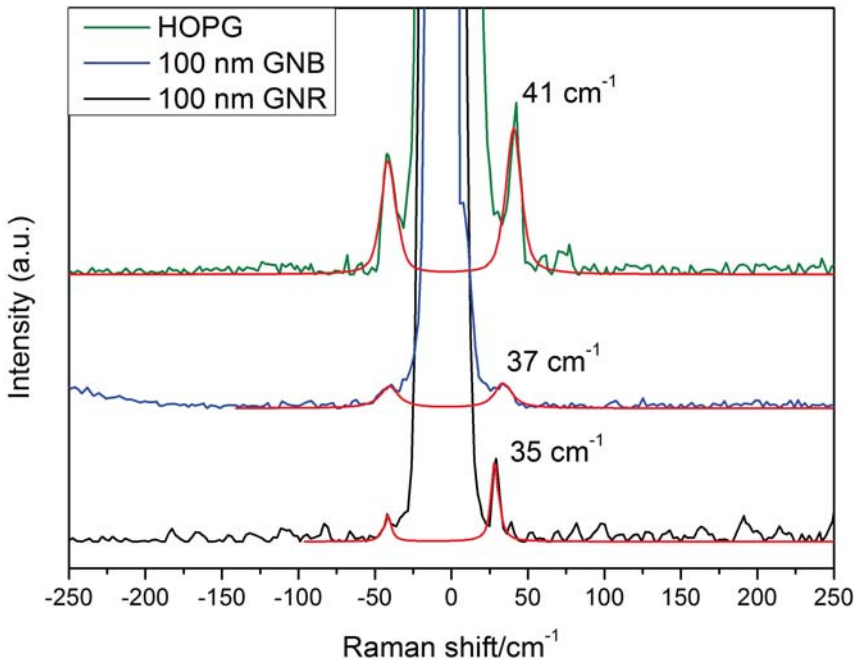

Figure 57: Raman spectra acquired with 785 nm excitation of the low-frequency region of HOPG, 100 nm GNB and 100 nm GNR. The C peaks are fit with Lorentzians.

than that of HOPG, though this sample is unexfoliated and still contains many layers of ribbons. Thus, it would appear that the interlayer interactions in GNBs are modified from that of the bulk HOPG, possibly due to modification of the relative layer orientation and spacing induced during the cutting process. The difference in C peak frequency between GNBs and GNRs is only of the order of a few cm^{-1}, which confirms that these are ribbons with at least several layers.

The 2D band

The 2D band is also sensitive to the number of graphene layers, and as was shown in section 4.2.1, the shape and intensity of the 2D band changes going from HOPG to multilayer to monolayer graphene. Shown in figure 58 are the 2D Raman spectra of GNRs with widths 100 nm and 300 nm. The shape of the 2D band for both samples is different from that for HOPG, which shows a main peak at ~ 2720 cm^{-1} with a lower-intensity shoulder at ~ 2680 cm^{-1}. The 2D bands of the GNR samples can be fitted with two Lorentzians, and these are more equal in intensity and closer in frequency than in HOPG. Thus, it would appear that the 2D band for GNRs is also modified from that of the bulk, likely due to modification of the interlayer interactions in aggregated ribbons, in which the relative orientations of the different graphene planes would be more disordered compared to HOPG.

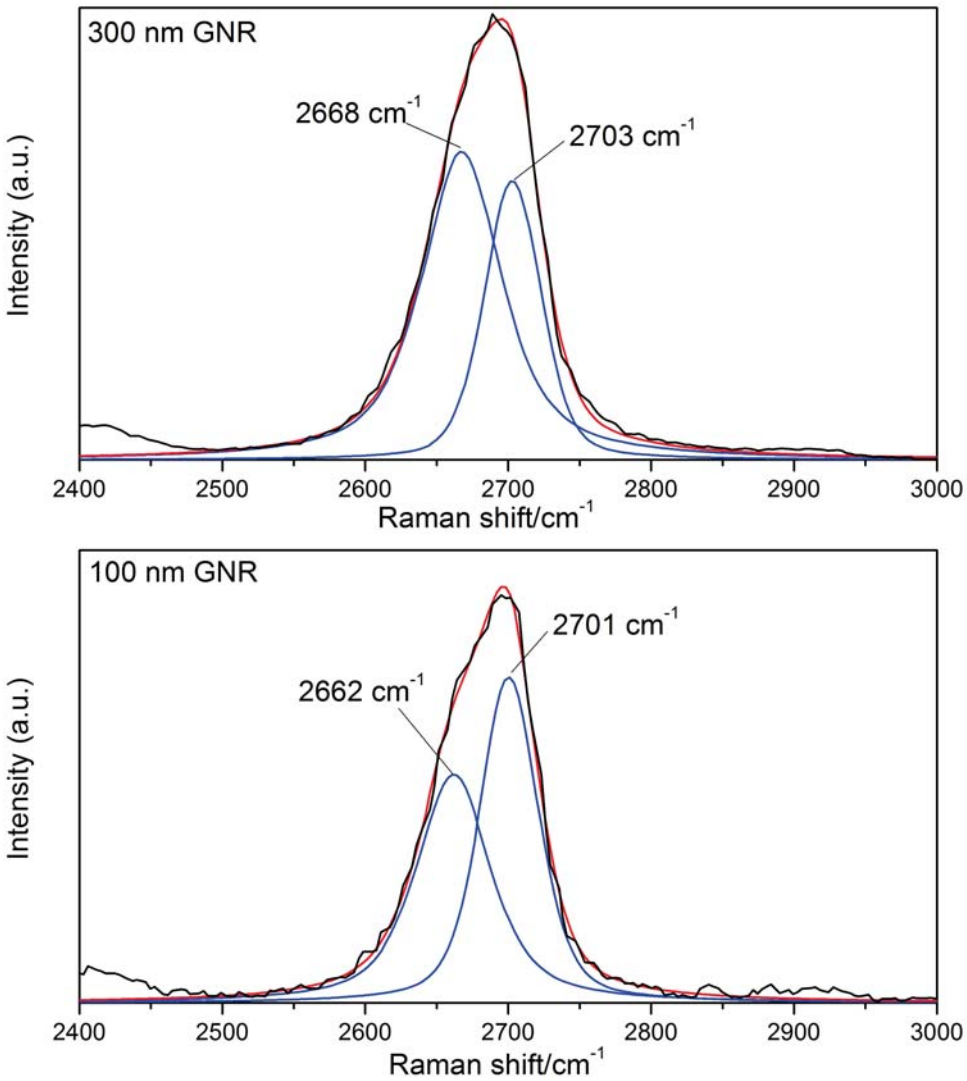

Figure 58: 2D bands of Raman spectra of 100 nm and 300 nm wide GNRs fit with Lorentzians.

4.2.5 D:G Ratios of GNRs

The dependence of the D band in graphene and graphite materials on the presence of defects or edges makes its intensity a good measure of the amount of disorder in a sample. For GNRs with minimal to no defects in the basal plane, the D band becomes even more useful, as its Raman intensity is directly related to the ribbon width and edge geometry (i.e. armchair vs zigzag), as well as the overall smoothness of the edges. This section explores the relationships between D band intensity and ribbon width, as well as the effects of cutting parameters, in particular wet- vs dry-cutting. The effects of edge geometry and roughness/disorder is covered in the next section via the use of polarised Raman microscopy.

The work by Mohanty et al. on the development of the nanotomy method for the production of GNRs included some Raman analysis.[83] GNR edge quality was measured using D:G ratios calculated from Raman spectra that were the average of several GNRs. Narrower ribbons were reported to give relatively higher D:G ratios. However, the range in widths of ribbons used in determining the D:G values was quite small ($15 - 50$ nm), and the difference in D:G ratios was not that large (only $\sim 20\%$ variation between 15 nm and 50 nm widths). Additionally, the variation in D:G ratios reported within the same sample ($0.25 - 0.4$ for 15 nm GNR) was even larger, even though TEM images showed a very small standard deviation in ribbon width variation ($\sim 1 - 5$ nm). No reports of using polarised Raman microscopy for determining edge type and quality were given. Thus, it would appear that a more thorough Raman analysis would be useful to properly investigate the relationships between the D band intensity and the structure of the edge.

The first set of experiments in this study looked at the relationship between D:G ratios and the width at which the ribbons were cut, as well as any effects of sonication power during exfoliation and differences between cutting the ribbons dry or into a water bath. Figures 59 and 60 show the results of this study. To ensure that the D:G ratios represented the average of a typical ribbon, the averages of multiple Raman spectra were used for the D:G calculations for each sample. In addition, densely aggregated samples were used for each scan, thus each Raman spectrum acquired also represents the average contributions of numerous randomly-oriented GNRs. Both wet- and dry-cut GNRs show a shift to lower D:G ratio as the ribbon width increases. For wet-cut ribbons, sonication had negligible effect on the D:G ratios, whereas for dry-cut GNRs, the D:G ratios appeared to decrease somewhat with increasing sonication power, which is a rather interesting result. These results would suggest that sonication does not result in ribbon breakage, which would be expected to be associated with an increase in the D:G ratio. Figure 60a shows D:G ratios for wet- and dry-cut GNRs averaged over all sonication powers, and figure 60b shows averaged D:G ratios plotted as a percentage of the ratio for 20 nm-wide GNRs compared with that calculated based on edge:basal carbon ratios. For comparison, averaged D:G

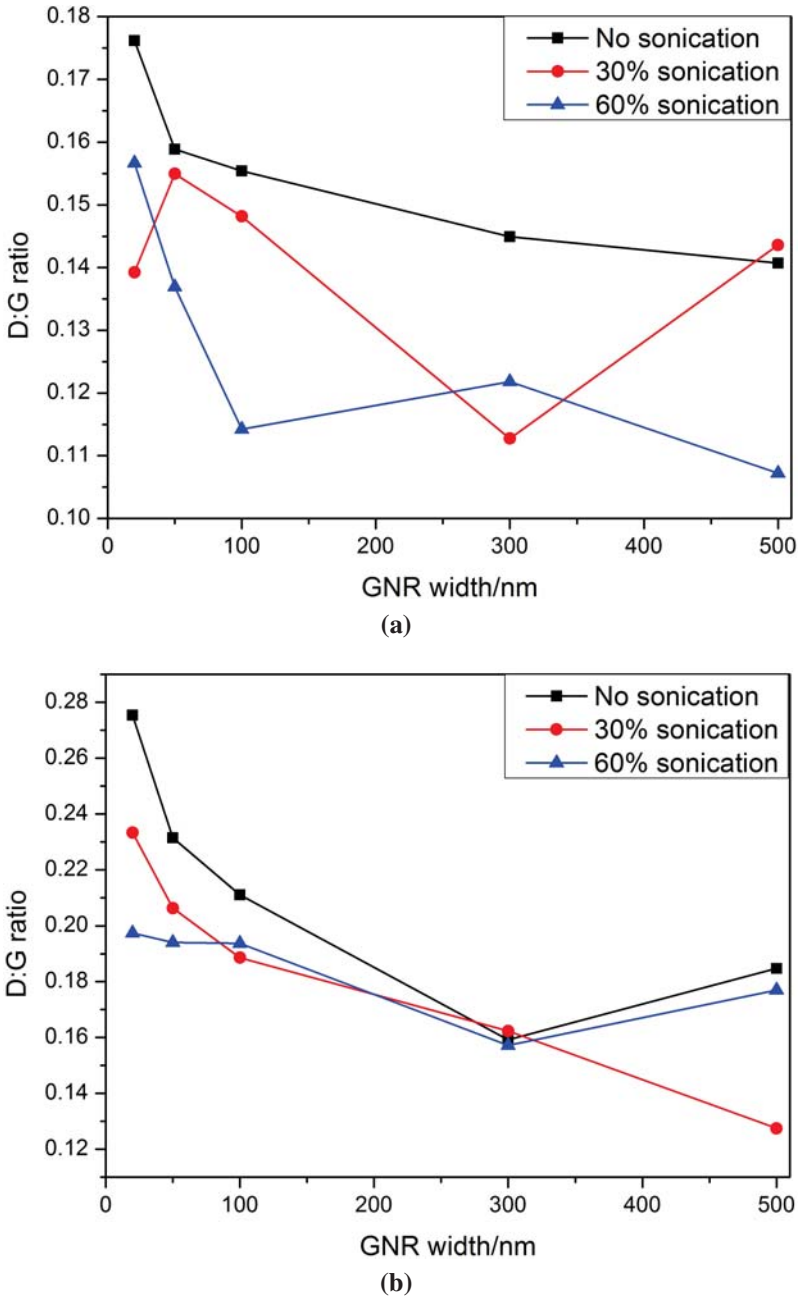

Figure 59: D:G ratios for (a) dry- and (b) wet-cut GNRs plotted as a function of ribbon width. All Raman spectra were acquired with 488 nm excitation.

ratios are also plotted with averaged 2D:G ratios as a percentage of the respective ratio for 20 nm width (figure 60c). There is a significant difference in D:G ratios for wet- vs dry-cut ribbons over all widths. The changes in 2D:G ratios are much smaller than the D:G changes, with 2D:G ratios showing a small overall increase with increasing ribbon width, which is opposite in direction to the D:G changes. Wet-cut ribbons show a greater overall change in D:G ratio than dry-cut ribbons - a reduction of 33.7% vs 19.6%. These results show good agreement with Mohanty et al.[83], who report a D:G decrease of 21.4% going from GNRs with width 15 nm to 50 nm.

Shown in figures 61 and 62 are similar plots to those in figures 59 and 60, except

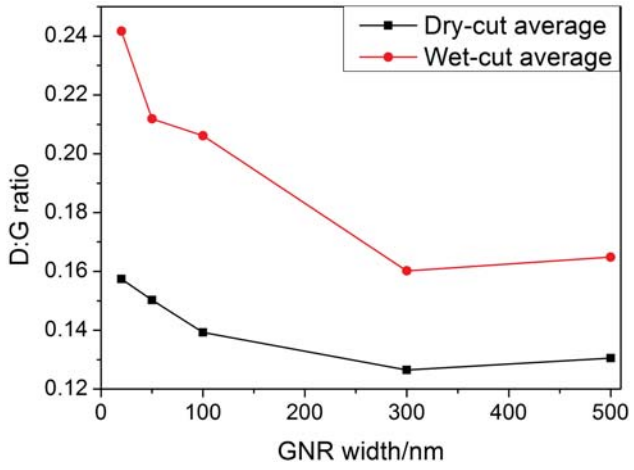

(a)

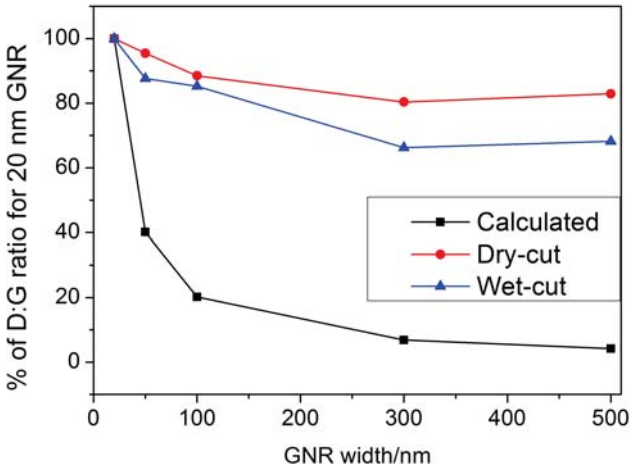

(b)

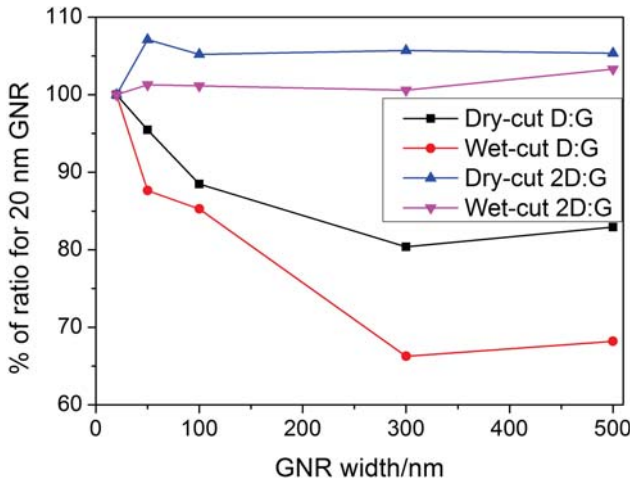

(c)

Figure 60: (a) Averaged D:G ratios over all sonication powers plotted as a function of ribbon width. (b) Averaged D:G ratios plotted as a % of the ratio for 20 nm GNR. Included for comparison are the expected ratios based on calculated edge:basal ratios. (c) D:G and 2D:G ratios plotted as a % of the respective ratio for 20 nm GNR. All Raman spectra were acquired with 488 nm excitation.

the D:2D ratio is used instead of D:G. The D:2D plots are very similar to the D:G plots, suggesting that the D:G changes are in fact due to changes in the D band alone and not the G band. This is also shown in the 2D:G plots in figure 60c, which show only small changes with ribbon width compared to the D:G. These results suggest that the D band intensity changes are directly linked to the change in the proportion of edge carbon atoms with ribbon width. Comparing change as a percentage of D:G or D:2D of 20 nm GNR, this change follows a decrease for 50 and 100 nm GNR and is similar for both wet- and dry-cut GNRs. Above 100 nm, however, this trend breaks down somewhat. This suggests that beyond 100 nm width, there is a breakdown in the reliability of the cutting process.

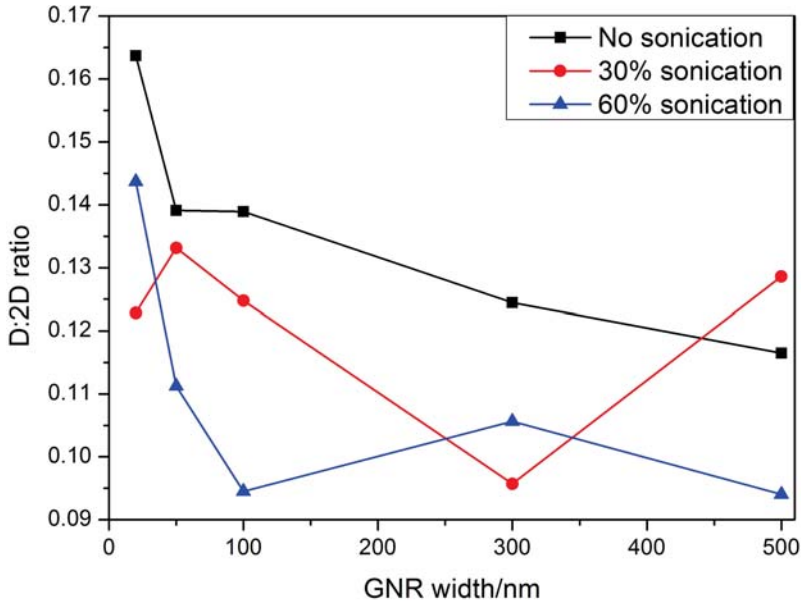

(a)

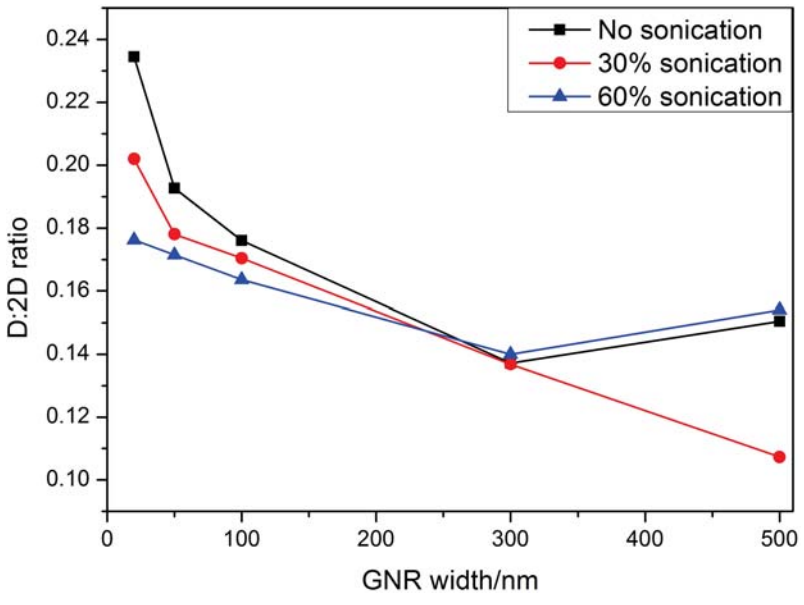

(b)

Figure 61: D:2D ratios for (a) dry- and (b) wet-cut GNRs plotted as a function of ribbon width. All Raman spectra were acquired with 488 nm excitation.

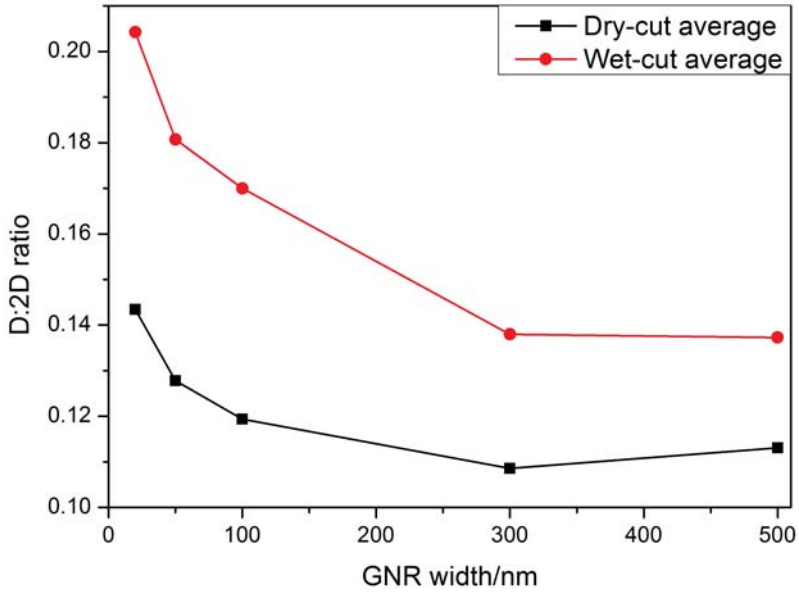

(a)

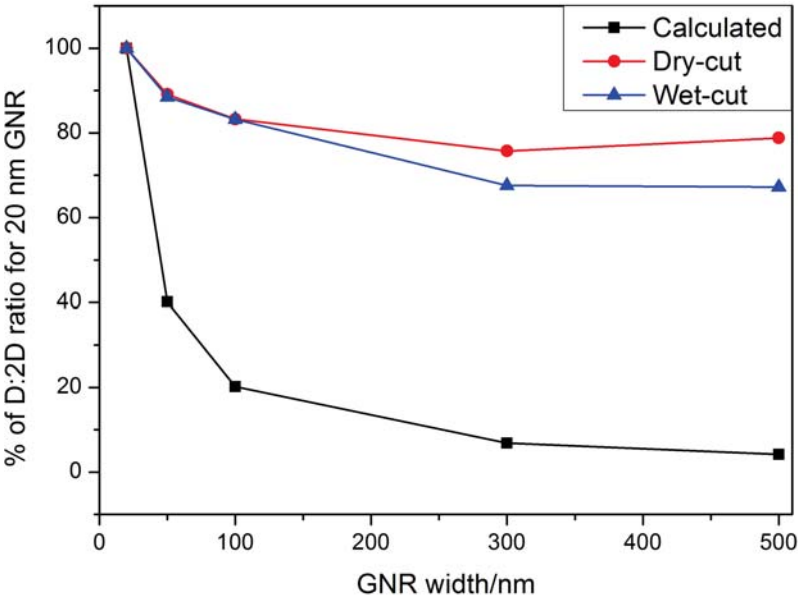

(b)

Figure 62: (a) Averaged D:2D ratios over all sonication powers plotted as a function of ribbon width. (b) Averaged D:2D ratios plotted as a % of the ratio for 20 nm GNR. Included for comparison are the expected ratios based on calculated edge:basal ratios. All Raman spectra were acquired with 488 nm excitation.

The second set of experiments aimed to investigate any effect of microtome cutting speed on the average D:G ratios for both wet-and dry-cut 100 nm GNRs. The GNRs in the first set were cut at a speed of 7.5 mm/s. For the second set, this speed was reduced to 0.8 mm/s. According to Mohanty et al., faster cutting speeds give rise to increased edge roughness, which manifests as an increase in the D:G ratio.[83] They found that mapping the average D:G ratio with cutting speed shows a large variation, with D:G ~ 0.83 at 1 mm/s compared with ~ 0.22 at 0.4 mm/s, for ribbons with a width of 15 nm. Interestingly,

the D:G and D:2D ratios shown in figures 59 - 62 are all $<<$ 0.8 even though the GNRs were cut at a speed much higher than that reported by Mohanty et al. Figures 63 and 64 show the averaged Raman spectra of 100 nm-wide GNRs chopped at 0.8 mm/s, taken with 532 nm and 488 nm excitation. Table 2 displays the average D:G and D:2D ratios for wet- and dry-cut GNRs at each excitation wavelength. Both the D:G and D:2D ratios are substantially higher for wet-cut GNRs, which is consistent with figures 59 and 61. The D:G and D:2D ratios do not show any apparent decrease with the lower cutting speed, which suggests that, in these sets of experiments, the cutting speed did not have any significant effect on the average edge roughness.

Figure 65 and tables $3 - 5$ show the variation in D:G ratios between different scans for the GNR samples shown in figures $59 - 64$. There appears to be significant variation in D:G ratios between Raman spectra acquired from different regions within the same

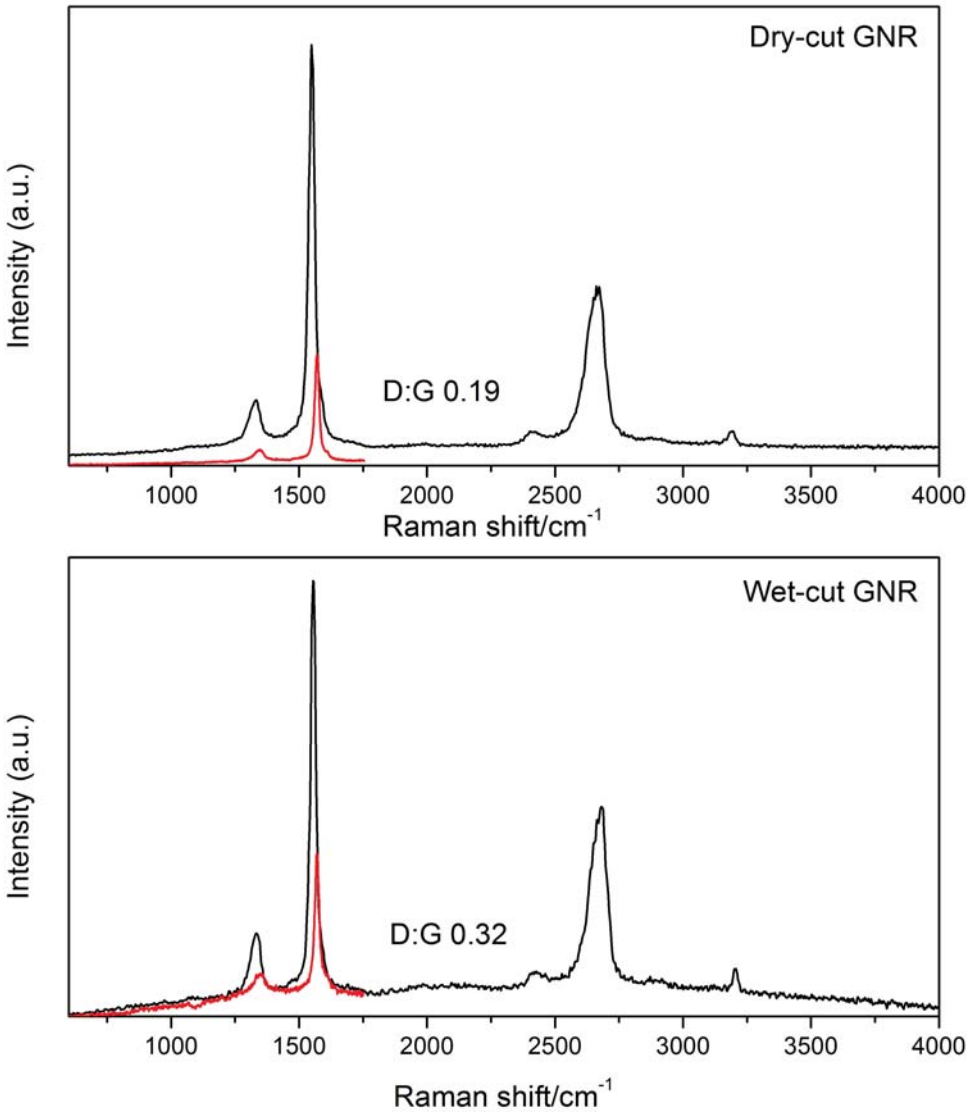

Figure 63: Averaged Raman spectra of wet- and dry-cut 100 nm GNRs acquired with 532 nm excitation.

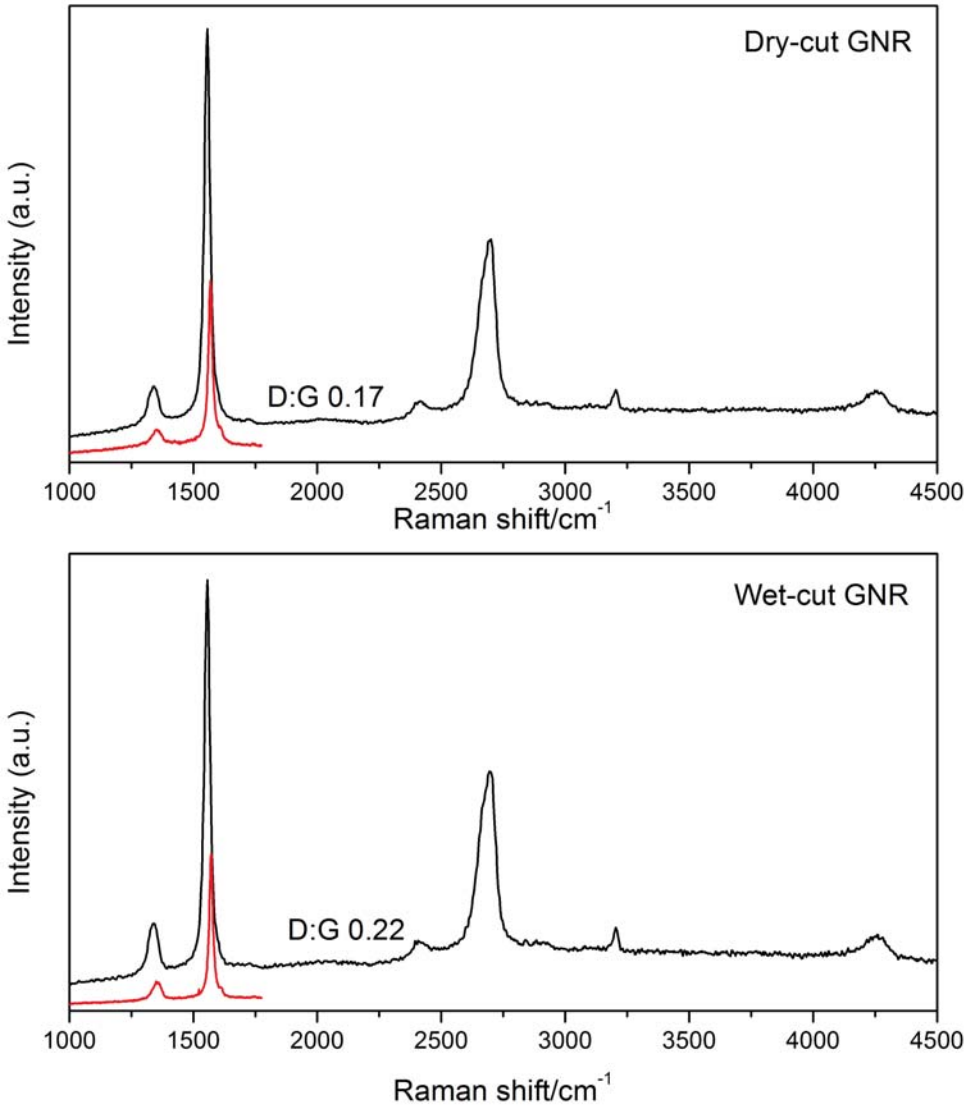

Figure 64: Averaged Raman spectra of wet- and dry-cut 100 nm GNRs acquired with 488 nm excitation.

Table 2: Comparison of average D:G and D:2D ratios for 100 nm wet- and dry-cut GNRs with 532 nm and 488 nm excitation. The averaged Raman spectra used to calculate these ratios are shown in figures 63 and 64.

Excitation wavelength	Dry-cut		Wet-cut	
	D:G	D:2D	D:G	D:2D
532 nm	0.19	0.19	0.27	0.23
488 nm	0.17	0.16	0.22	0.17

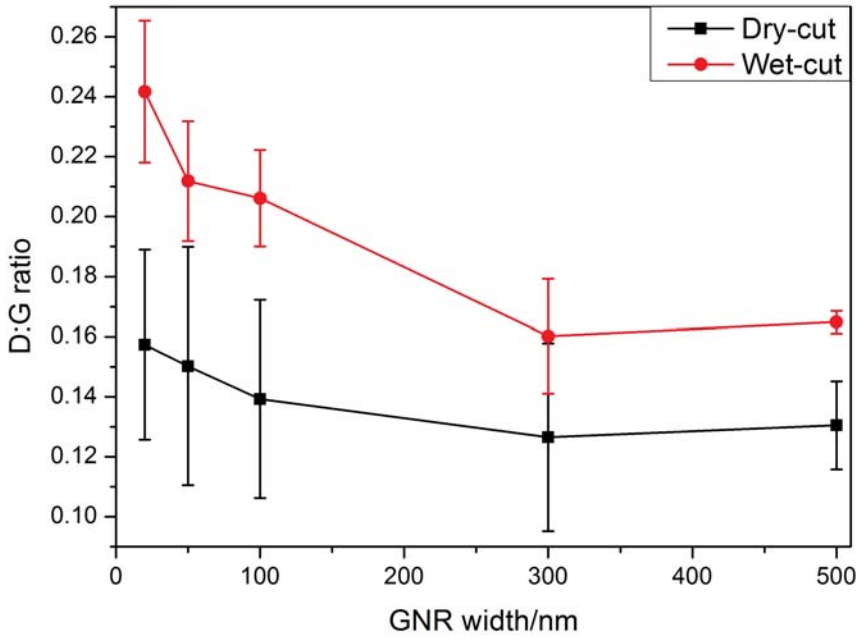

Figure 65: Averaged D:G ratios plotted as a function of ribbon width (see figure 60a) with error bars.

sample, and this holds for all GNR samples. This is similar to the findings by Mohanty et al.[83] Interestingly, though, the wet-cut samples show consistently lower variation in D:G ratio over all sizes. Reducing the cutting speed for 100 nm GNRs did not result in a decrease in D:G variation (see table 5). The cause of the large variation in D:G ratios between replicate measurements is unlikely to be due to insufficient signal:noise ratios, as the samples were densely aggregated and gave strong Raman signals, particularly with the integration times set at at least a minute. Rather, the variation is most likely due to inhomogeneity in the sample itself, as the mechanical fracturing process produces some powdering at the edges of the HOPG block, as can be seen in some of the TEM images given in Appendix B.

Table 3: Variation in D:G ratios for the dry-cut GNRs in figure 65.

	20 nm	50 nm	100 nm	300 nm	500 nm
SD	0.032	0.040	0.033	0.031	0.015
RSD (%)	19.3	28.2	23.2	20.8	10.3

Table 4: Variation in D:G ratios for the wet-cut GNRs in figure 65.

	20 nm	50 nm	100 nm	300 nm	500 nm
SD	0.024	0.020	0.016	0.019	0.004
RSD (%)	8.6	8.6	7.6	12.0	2.0

Table 5: Variation in D:G ratios for the 100 nm GNRs in figures 63 and 64.

		Dry-cut	Wet-cut
488 nm	SD	0.057	0.045
	RSD (%)	33.1	20.9
532 nm	SD	0.077	0.093
	RSD (%)	39.7	29.0

4.2.6 Polarised Raman Microscopy of GNRs

As described in section 4.1.2, polarised Raman microscopy is a very useful technique for probing the edge structure of graphene, due to the unique polarisation dependences of the D and G bands. Since GNRs contain a high proportion of edges, characterising the edge structure is of particular importance as the edges can greatly affect the nature and properties of the ribbons. The use of polarised Raman for the determination of edge type is frequently encountered in the literature, and the polarisation behaviour of the D band is most often explained using the popular "double resonance" model. However, most studies treat the edges as perfect armchair or zigzag edges. In more realistic applications, the graphene edges studied will likely not be perfectly smooth, but will be more disordered, consisting of a mix of shorter armchair and zigzag segments. A study by Ferrari et al.[99] considers the case of Raman scattering from generally disordered edges, and this interpretation was found to be very useful in the analysis of polarised Raman microscopy of GNRs in this project. A discussion of the theory of polarised Raman spectroscopy applied to disordered edges is given in the following paragraphs. This treatment is later used in the analysis and interpretation of polarised Raman of GNRs produced via the nanotomy method.

Under the DR Raman model for activation of the D band of graphene, for which a detailed description was given in section 4.1.2, an incident photon generates an electron-hole pair.[102] This e-h pair can be regarded, using a quasiclassical picture, as wave packets of approximate size $\hbar v_F/\varepsilon \sim 0.6$ nm (for 514 nm excitation), where v_F is the Fermi velocity and ε is the electron energy.[99] Momentum conservation dictates that for radiative recombination of the e-h pair to occur, leading to emission of a photon, the electron and hole must meet with nearly opposite momenta and in the same region of space. The process is achieved by defect activation involving inelastic scattering of the electron or hole by a phonon and elastic scattering by a defect. Both the phonon and defect scattering events must be backscattering to satisfy the requirement that the electron and hole recombine with opposite momenta. Due to geometric constraints imposed by the momentum conservation and backscattering conditions, the D band cannot be activated by a perfect zigzag edge, but only by an armchair edge. The backscattering condition also leads to a polarisation dependence of the Raman intensity, with the intensity of the D band $\propto cos^2(\theta_{in})$, where θ_{in} is the angle between the incident polarisation and the edge direction.

In terms of their polarisation dependence, disordered edges can be regarded as a series of short, separate segments with perfect armchair/zigzag geometry, with D band contributions coming from only the armchair segments.[99] This leads to the following D band polarisation dependence for a general, disordered edge:

$$I(D)(\theta_{in}) = I(D)_{min} + [I(D)_{max} - I(D)_{min}]cos^2(\theta_{in} - \theta_{max}) \quad (8)$$

where $I(D)_{min}$ and $I(D)_{max}$ are the max and min D band intensities and θ_{max} is the angle of max intensity. For a long armchair segment, θ_{max} is expected to be along the armchair direction, with a small $I(D)_{min}/I(D)_{max}$ ratio. With decreasing length of the armchair segment, this ratio increases (with a maximum value of 1 indicating no polarisation dependence). The armchair segments in a disordered edge that is not perfectly smooth may not necessarily be oriented all in the same direction, but can be any of up to three orientations, that is, along the average edge direction or at an angle $\pm 60^\circ$. Hence, for a disordered edge the D band intensity contributions from all of the armchair segments can be added as in the following expression:

$$\begin{aligned} &(1-f)[\rho_{A_0}+(1-\rho_{A_0})cos^2\theta_{in}] \\ &+(f/2)[\rho_{A_0}+(1-\rho_{A_0})cos^2(\theta_{in}-60^\circ)] \\ &+(f/2)[\rho_{A_0}+(1-\rho_{A_0})cos^2(\theta_{in}+60^\circ)] \end{aligned} \tag{9}$$

where f is the fraction of segments oriented at $\pm 60^\circ$ and ρ_{A_0} is the $I(D)_{min}/I(D)_{max}$ ratio for a long armchair segment. Thus, the overall $I(D)_{min}/I(D)_{max}$ ratio for a disordered armchair edge is:

$$\rho_A = \frac{\rho_{A_0}+3f/(4-3f)}{1+3f\rho_{A_0}/(4-3f)} \geq \rho_{A_0} \tag{10}$$

A disordered edge with an average zigzag geometry will still have armchair segments, and these will now be oriented at $\pm 30^\circ$ relative to the average zigzag edge direction. The contribution from these two possible orientations of armchair segments can be equal or otherwise favouring one or another of the two directions. Hence, for a zigzag disordered edge, the intensity contributions are added as follows:

$$f_1[\rho_{A_0}+(1-\rho_{A_0})cos^2(\theta_{in}-30^\circ)]+f_2[\rho_{A_0}+(1-\rho_{A_0})cos^2(\theta_{in}+30^\circ)] \tag{11}$$

where f_1 and f_2 denote the fraction of armchair segments oriented at -30° and $+30^\circ$, respectively. The overall $I(D)_{min}/I(D)_{max}$ ratio for a disordered zigzag edge is then:

$$\rho_Z = \frac{\rho_{A_0}+(2-k)/(2+k)}{1+\rho_{A_0}(2-k)/(2+k)} \tag{12}$$

where $k=\sqrt{1+3\frac{(f_1-f_2)^2}{(f_1+f_2)^2}}$. For an edge with $f_1=f_2$, θ_{max} will be 0 and ρ_Z will be between 1/3 and 1, depending on the length of the armchair segments.

The G band is also polarisation-dependent at the graphene edge, with $I(G) \propto cos^2\theta$ at a perfect armchair edge and $I(G) \propto sin^2\theta$ at a perfect zigzag edge.[103] For a disordered

edge, both armchair and zigzag segments will contribute to the G band Raman intensity with opposite polarisation dependences, thus the $I(G)_{min}/I(G)_{max}$ ratio for a disordered edge is expected to deviate quite significantly from zero. If the relative proportions of armchair and zigzag segments are quite close, the G band will likely show only a weak $cos^2\theta$ or $sin^2\theta$ dependence, whereas if one geometry is strongly favoured over the other, the G band polarisation dependence will be stronger.

Prior to polarised Raman analysis of GNRs, the first step was to test the polarisation behaviour of HOPG. HOPG should have few defects in the basal plane, and indeed this would appear to be the case, due to absence of a D band in most regions of the HOPG sample. Thus, any D band intensity should indicate the presence of (an) edge(s). Figures 66 and 67 show the results of the polarised Raman analysis of HOPG in a region where the presence of the D band indicated that one or more edges were in the laser focus. In this experiment, a $\lambda/2$ waveplate was used to rotate the plane of polarisation of the linearly polarised laser used to excite the sample, and the scattered light was collected at all polarisations (i.e. without an analyser). Figure 66a plots the intensities of the D and G bands as a function of the degree of rotation of the initial polarisation of the laser. The initial polarisation is arbitrarily set to 0°. Also shown are the Raman spectra of HOPG at the polarisation angles giving max and min D band intensity (see figure 66b). Both the D and G bands show intensity changes as the input polarisation is rotated. The D band (more specifically, the D:G ratio) shows a loose $\cos^2\theta$ dependence, as shown in figure 67a. The G band shows a somewhat similar, though much weaker pattern as the D band and D:G ratio. This would suggest that the edge contribution to the G band can be distinguished from the G band arising from the basal plane, which is not expected to show any polarisation dependence. In figures 67a and 67b, the x-axis has been normalised so that max D:G ratio occurs at 0°. Thus, according to Ferrari et al.[99], the polarisation dependence of the D:G ratio can be expressed as $I(D:G)\theta_{in} = 0.17 + (0.4 - 0.17)\cos^2(\theta_{in})$, which gives $I(D:G)_{min}/I(D:G)_{max} = 0.43$. This ratio is relatively high, and the $\cos^2\theta$ dependence a rather poor fit, thus would suggest disordered edges and/or multiple misoriented edges in the beam focus. The G band also shows an approximate, though very poor, $\cos^2\theta$ dependence, which would suggest a predominance of armchair segments.

Polarised Raman analysis of single-ribbon GNRs requires that the ribbons be suitably deposited onto a substrate. The AFM and TEM images discussed previously have shown that a persisting problem in characterising single GNRs is the difficulty in achieving uniform deposition of ribbons onto a substrate. Significant effort has been put into attempting to solve this problem, and this has shown that achieving well-separated ribbons is very difficult and that it is realistic to expect, at best, partial aggregation on a substrate, with the observation of well-separated single/few-layer ribbons being the exception rather than the norm. An ideal substrate, e.g. with a hydrophobic surface, should promote even adhesion of the GNRs to the surface with minimal aggregation. In addition, for Raman consid-

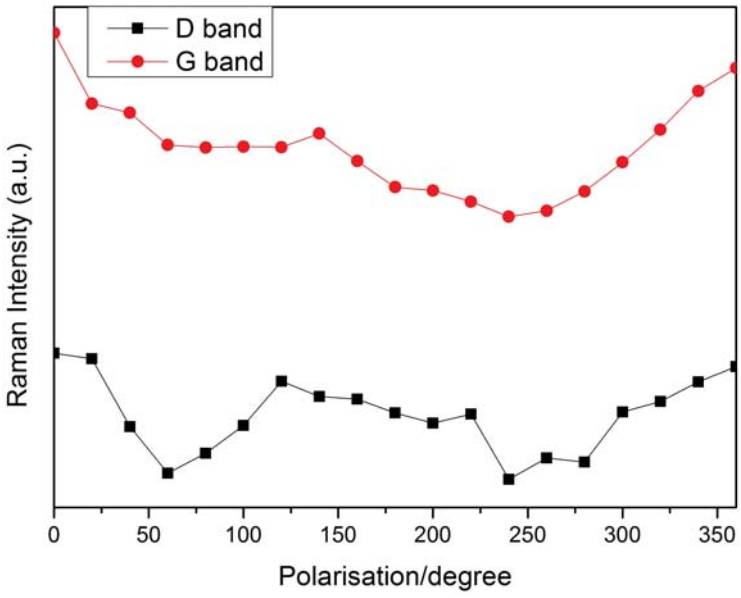

(a)

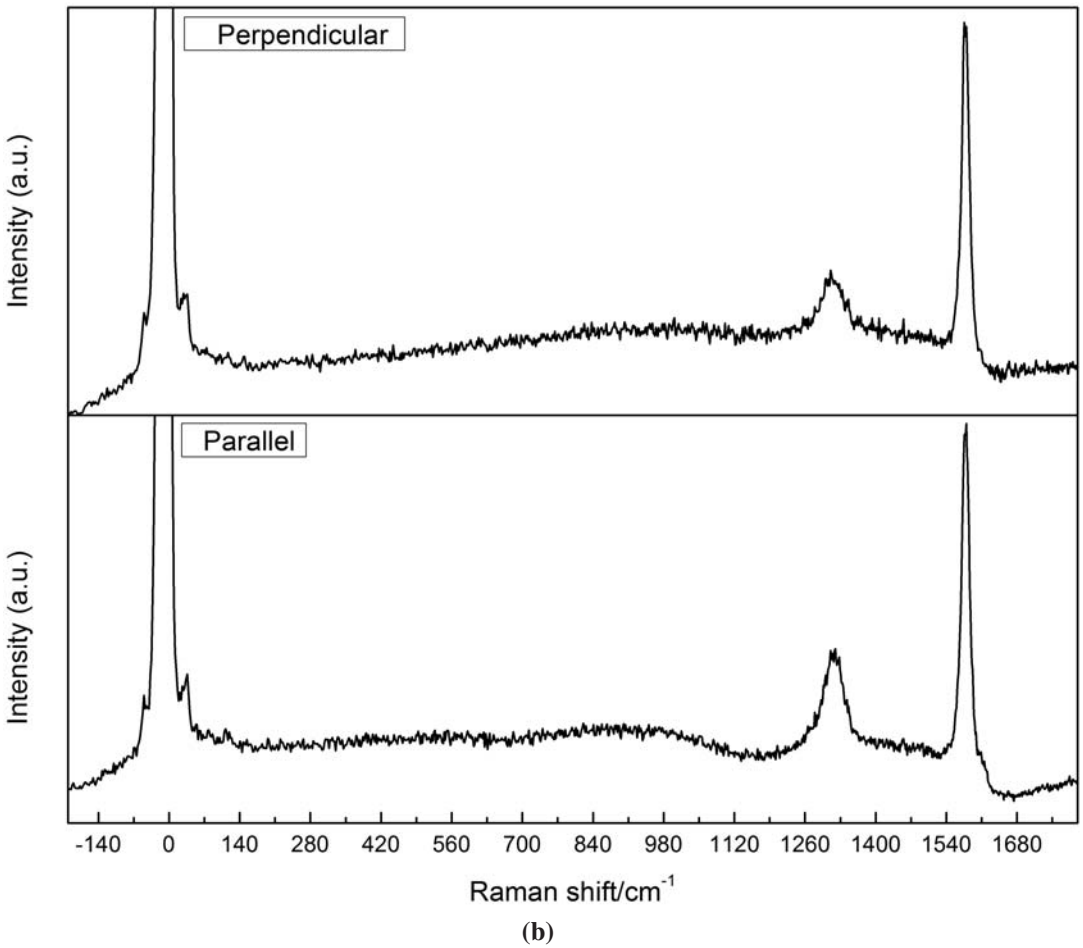

(b)

Figure 66: (a) Intensities of the D and G bands of HOPG plotted as a function of the degree of rotation of the plane of polarisation of the input laser beam. (b) Raman spectra of HOPG at parallel (perpendicular) polarisation giving max (min) D band intensity. Raman spectra were acquired with 785 nm excitation.

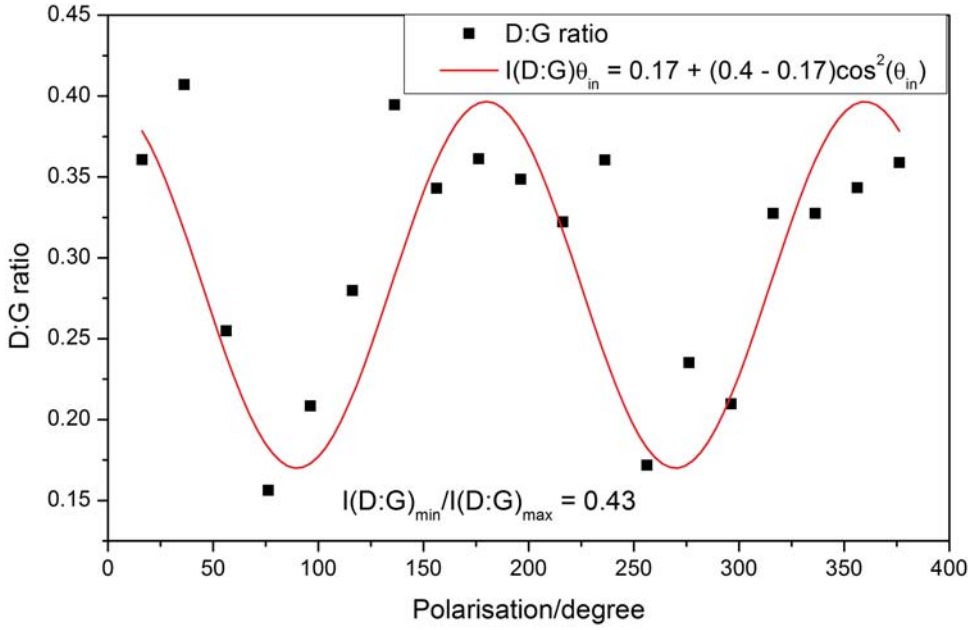

(a)

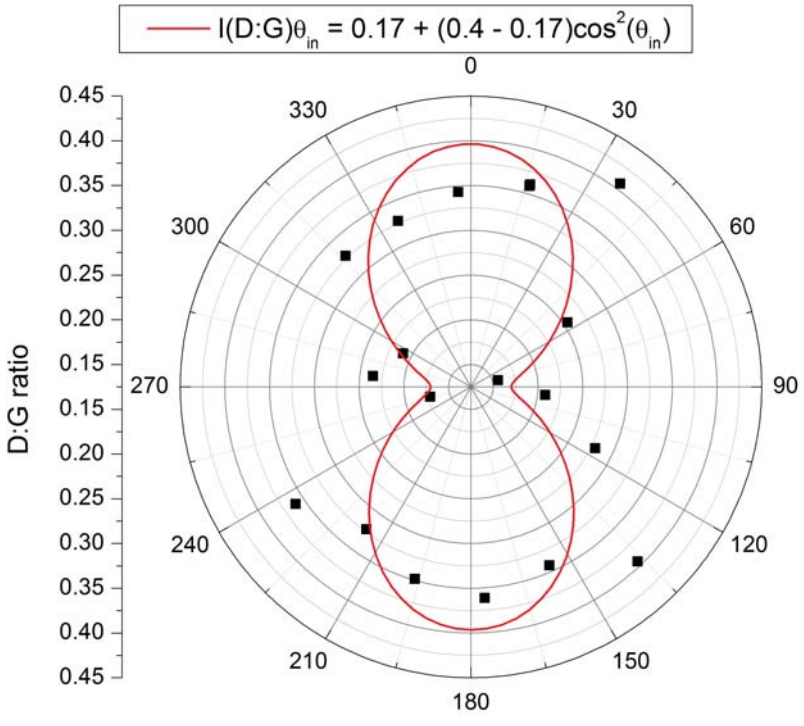

(b)

Figure 67: D:G ratio of HOPG Raman spectra plotted as a function of polarisation, with a $\cos^2\theta$ fit.

erations, the substrate must be transparent to the excitation wavelength and contribute minimal Raman signal to prevent obscuring the graphene Raman peaks. Thin glass coverslips were initially used as the Raman substrates, however these are quite hydrophilic and were found to promote rapid aggregation of the ribbons. In addition, the glass exhibited fluorescence, which though quite weak, was enough to partially obscure the D and G graphene Raman bands. Quartz, on the other hand, was found to be an ideal substrate for polarised Raman analysis of single ribbons, as it has very low Raman background and is available as thin (down to 100 μm) coverslips, allowing the use of 100X oil objectives to give diffraction-limited resolution. With a laser wavelength of 488 nm, a focused spot size close to this can be achieved using a high NA objective (e.g. 100X objective with NA 1.3), giving diffraction-limited resolution of half the laser wavelength. This resolution is comparable to GNRs with widths a few hundred nm, thus observation of single ribbons should be achievable. However, quartz is not an ideal substrate for achieving uniform ribbon deposition as it is highly hydrophilic, and ribbons are observed to aggregate very rapidly on hydrophilic substrates. A solution to this was to silanise the quartz surface with an organosilane to make it more hydrophobic and thus amenable to uniform ribbon deposition. This approach was taken and found to be relatively successful, as ribbons did appear to disperse much more evenly and formed fewer and smaller aggregates compared to untreated quartz. Aggregation was still a problem to some extent though, and it was difficult to determine if there were single/few-layer ribbons present as these are too small to detect with optical microscopy. By scanning the laser beam across the sample in small steps using a piezo stage, one would expect to encounter single or few-layer ribbons. However, this was a time-consuming process, especially considering that single ribbons would require longer integration times to detect. Indeed, graphene peaks were only observed in the Raman spectrum when focused on visible aggregates, and regions in which there were no visible aggregates did not yield graphene bands that would indicate the presence of single/few-layer ribbons. There are two likely reasons for this: (1) the Raman signals of single ribbons are too weak to be detected at all or without extended integration times or (2) there are no/very few single ribbons present, only aggregates. In the case of (1), a simple solution is to increase the laser power, however this was found to cause burning of the sample, even with just a few mW of power in some cases. Increasing the size of the ribbons so that they fill more of the laser beam focus could increase the Raman signal from individual ribbons. This approach was tried, but single ribbons still could not be detected. For (2), more optimum conditions for uniform ribbon deposition, e.g. trying different solvents and drying techniques, were investigated, but aggregation persisted.

Although optical microscopy showed mostly aggregates for all GNR samples, occasionally there appeared to be stacks of partially-exfoliated ribbons. The shape of these more ordered aggregates, compared to the more random blob-like shapes of the majority

of aggregates, suggests that these could be stacks of ribbons oriented in a similar direction, thus one might expect there to be some polarisation effects. Indeed, polarised Raman experiments of these types of aggregates typically did show some polarisation-dependent behaviour. A large body of data was collected from many aggregates to allow for any relationships between the appearance of Raman spectra, polarisation behaviour and morphology of the sample to be determined. Changes in the D:G ratios were found to occur for most of the aggregates sampled, as well as changes in the Raman intensity of the D, G and 2D bands. Aggregates that appeared to be more ribbon-like, i.e. smaller and with straighter edges and thus likely to be stacks of ribbons aligned in a similar direction, tended to have D:G polarisation profiles with a single maximum or minimum in the $0^\circ - 180^\circ$ range of polarisation, whereas more random blob-like aggregates tended to have multiple maxima/minima or otherwise no consistent pattern in their D:G profiles. A single max/min between $0^\circ - 180^\circ$ is consistent with ribbons containing reasonably straight edges aligned in a single direction, where polarisation aligned with the ribbon edge direction gives max D band intensity, and that aligned perpendicular to the ribbon edge gives min D band intensity. The observation of clear D:G band fluctuations even in partially aggregated GNRs suggests that most of the D band intensity is coming from the edges, which suggests high quality, low defect ribbons with reasonably straight edges. The position of the D:G profile max/min could also be approximately correlated with the ribbon orientation suggested by the optical microscope image, and the initial incident laser polarisation (at a $\lambda/2$ waveplate rotation of 0°) appeared to be aligned approximately with the Y-axis of the microscope crosshair, as ribbon-like aggregates aligned with this direction tended to have a max D:G ratio near 0°. The position of the D:G max was found to shift for ribbons that appeared to be aligned in different directions, which confirms that the D:G changes are in fact dependent on the ribbon edge direction and are not simply artefacts.

Polarised Raman microscopy of ribbon-like aggregates from samples cut at a range of different widths, both wet- and dry-cut, was used to probe the structure and orientation of edges in ordered GNR aggregates. 488 nm excitation was normally used, to give the minimum laser focus spot size. From the $\cos^2\theta$ functions fit to the polar D:G ratio plots, the $I(D:G)_{min}/I(D:G)_{max}$ ratios could be calculated, and these were found to vary widely between aggregates, ranging from $0.23 - 0.79$. Overall, lower $I(D:G)_{min}/I(D:G)_{max}$ and better $\cos^2\theta$ dependence were obtained for ribbons with larger widths. In many cases, the G band intensity could also be fit with a $\cos^2\theta$ or $\sin^2\theta$ function. Thus, the average edge structure and orientation in a GNR aggregate could be determined by analysis of the polarisation behaviour of both the D and G bands. The details of this method are shown in the following pages for aggregates showing the strongest D and G band polarisation behaviour.

Figure 68 shows polarised Raman data of a small aggregate of 500 nm wet-cut GNR.

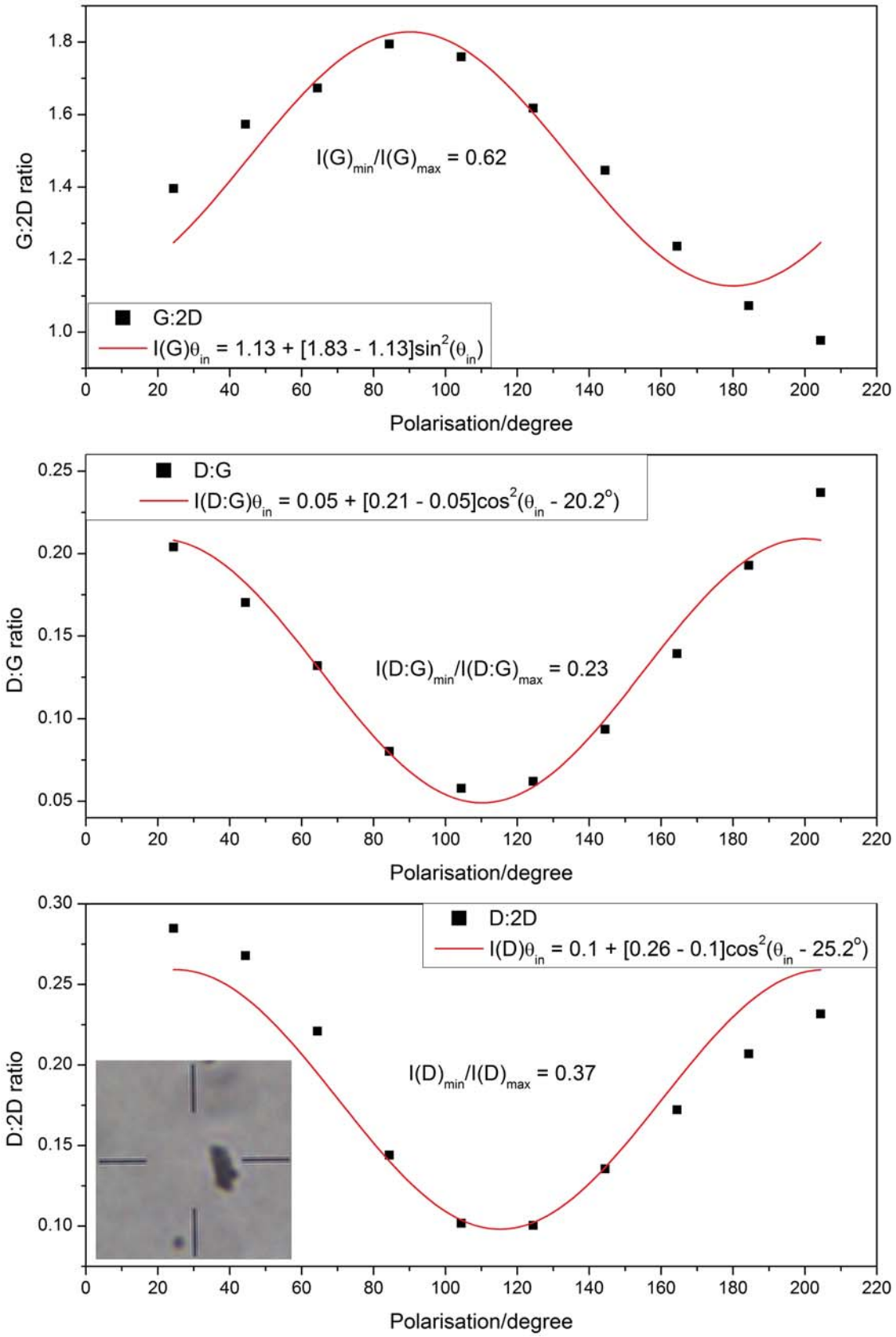

Figure 68: G:2D, D:G and D:2D ratios of 500 nm wet-cut GNR plotted as a function of polarisation. Raman spectra were acquired with 488 nm excitation.

The optical microscope image shows the aggregate positioned to the right of the centre of the crosshair, thus the laser beam should just graze the left edge(s). The D:G ratio shows a strong dependence on polarisation, with a good $cos^2\theta$ fit. The $I(D:G)_{min}/I(D:G)_{max}$ value of 0.23 is comparable to those reported in the literature for polarised Raman studies of edges of single-layer graphene flakes.[99,103] This suggests a high purity and would lead to a tentative assignment as an edge with predominant armchair character. However, the G band also shows a polarisation dependence, though not as strong as the D band, with $I(G)_{min}/I(G)_{max}$ of 0.62. In calculating the G band intensities, they were normalised to that of the 2D band, to correct for fluctuations of the overall Raman intensity throughout the course of the experiment. In contrast to what would be expected for an armchair edge, for which the G band would be expected to exhibit a similar $cos^2\theta$ dependence as the D band, the G band in fact shows a $sin^2\theta$ dependence, indicative of a zigzag edge. Hence, these results suggest an edge (or possibly mutiple edges, as the sample appears to be an aggregate of ribbons) with predominant zigzag geometry, but also with numerous armchair segments. Also, note that the θ_{max} for maximum D band intensity is offset by approximately 20° from the θ_{min} for minimum G band intensity. This would suggest that the armchair segments giving rise to the D band are not predominantly oriented along the average edge direction, i.e. not fully symmetric. If multiple edges are contributing, which is likely the case, this could be adding to this effect even further. The θ_{min} for G band intensity should correspond to the average direction of zigzag segments of all the edges, whereas the θ_{max} of the D band should correspond to the average direction of armchair segments of all the edges. Thus, the overall average edge direction could lie somewhere between θ_{min} for G and θ_{max} for D. For this and the remaining polarised Raman data, the θ_{min} of the G band will arbitrarily be taken as the average edge direction, and the θ_{max} of the D band will be determined relative to the θ_{min} for the G band. It is difficult to accurately determine the average edge direction of the aggregates from the optical microscope images, as the GNRs sampled are aggregates of ribbons with presumably many edges, which may not all be perfectly aligned with one another. This example represents the lowest $I(D:G)_{min}/I(D:G)_{max}$ and $I(G)_{min}/I(G)_{max}$ values found from all of the polarised Raman studies conducted on GNRs in this project. The polarisation data of the D band normalised to the 2D band intensity shows a similar $cos^2\theta$ dependence as the I(D:G) ratio, though with a poorer fit, larger $I(D)_{min}/I(D)_{max}$ and an extra 5° offset from the G band. The differences in $I(D)_{min}/I(D)_{max}$ vs $I(D:G)_{min}/I(D:G)_{max}$ and θ_{max} offset are due to the effects of the G band polarisation. Additional examples of GNR aggregates exhibiting similar polarisation dependences also suggestive of zigzag edge predominance are shown in figures 69 and 70.

Figure 71 shows polarised Raman data of a 100 nm dry-cut aggregate. The polar behaviour of this aggregate is different from the previous ones shown, as the D and G bands both exhibit a $cos^2\theta$ dependence, which is typical of an armchair edge. However,

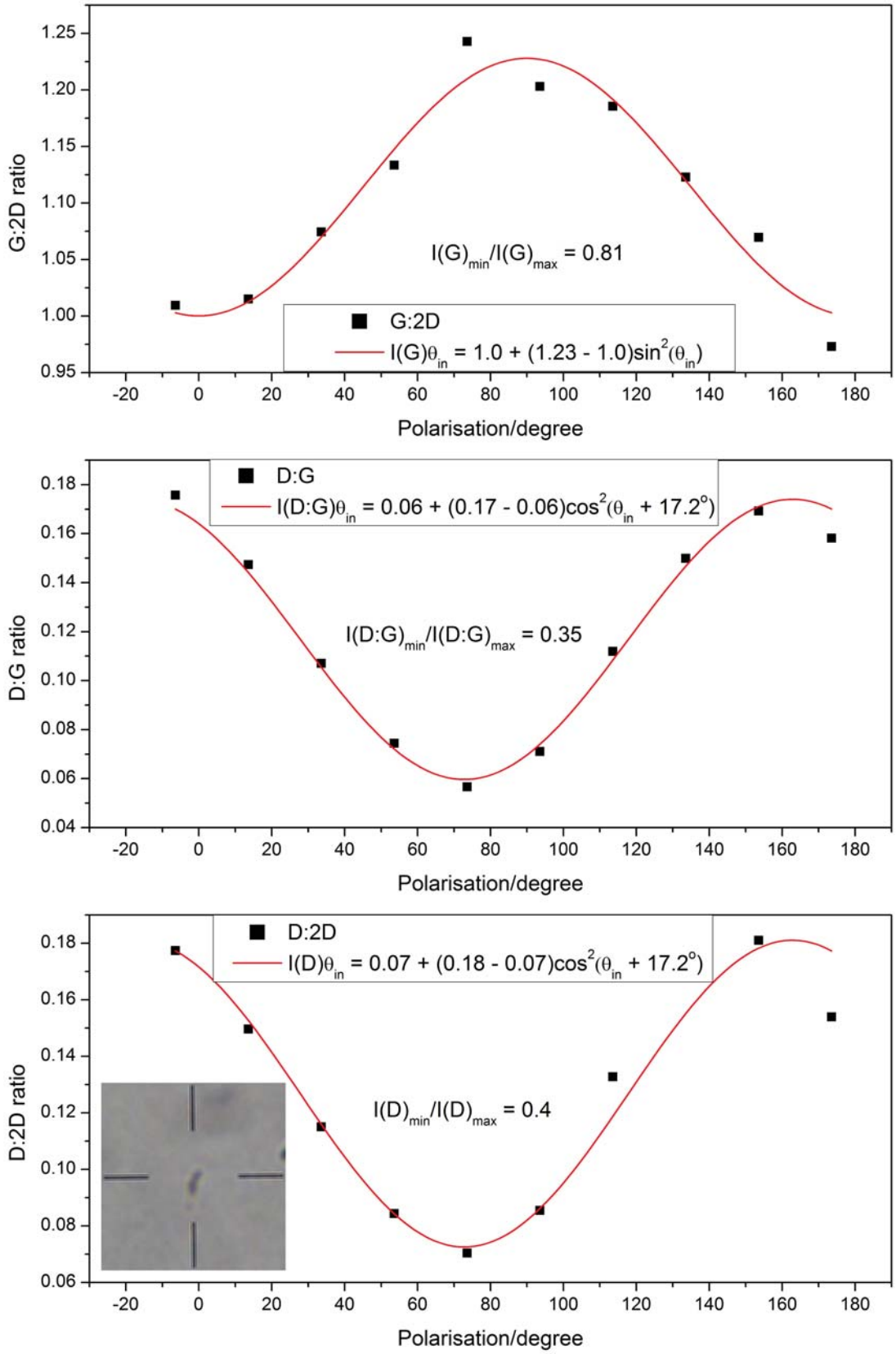

Figure 69: G:2D, D:G and D:2D ratios of 300 nm wet-cut GNR plotted as a function of polarisation. Raman spectra were acquired with 488 nm excitation.

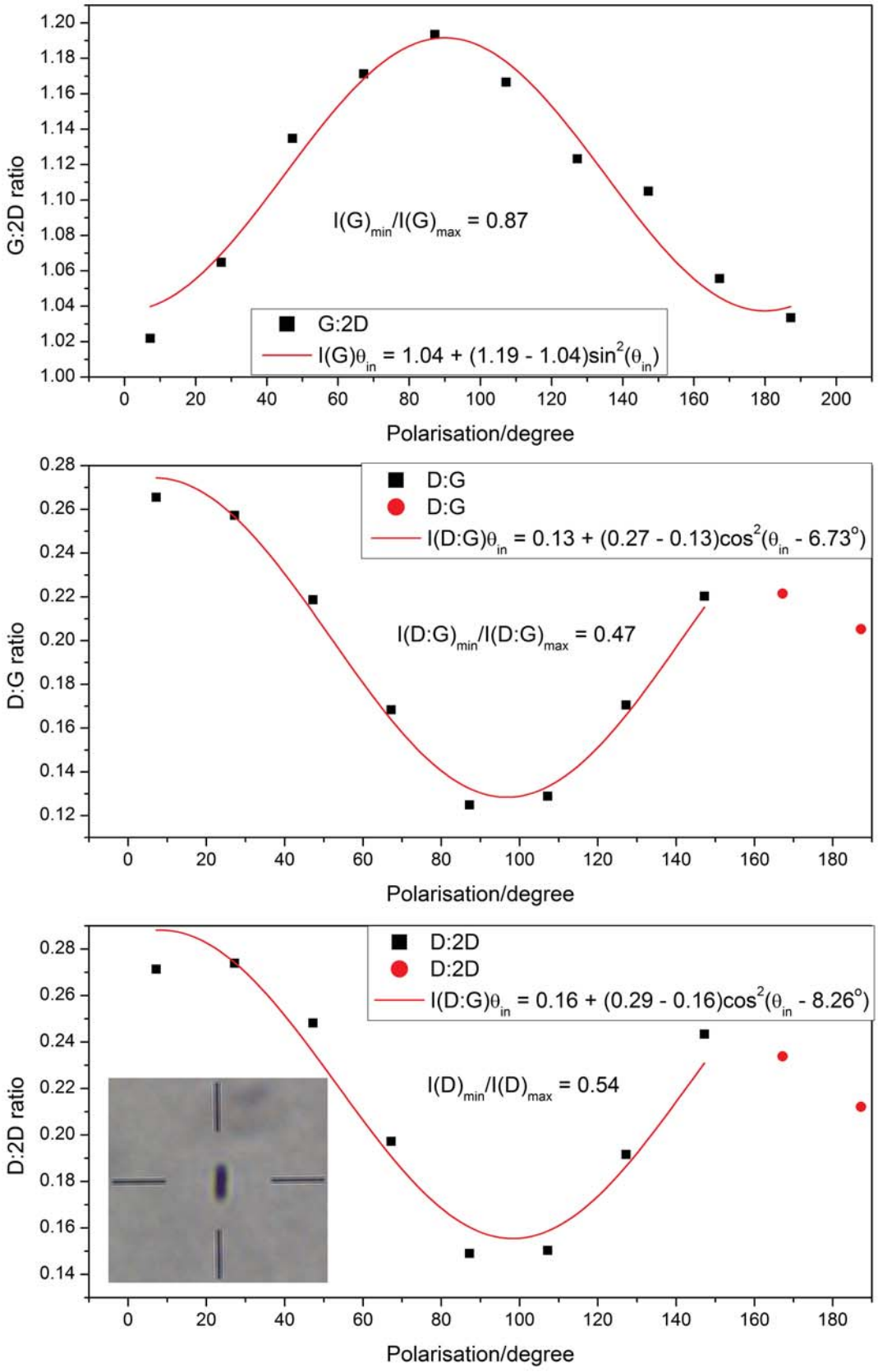

Figure 70: G:2D, D:G and D:2D ratios of 300 nm wet-cut GNR plotted as a function of polarisation. Raman spectra were acquired with 488 nm excitation.

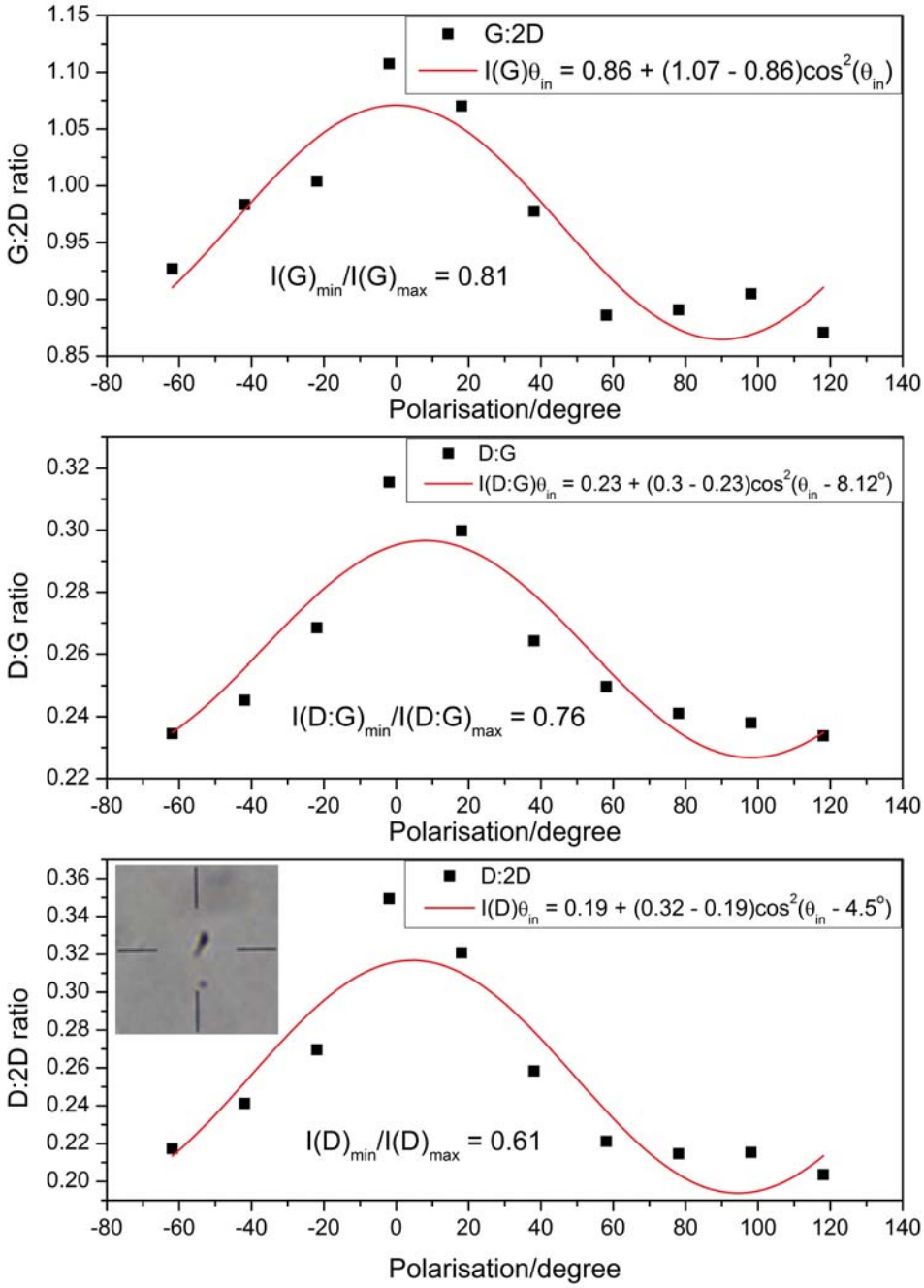

Figure 71: G:2D, D:G and D:2D ratios of 100 nm dry-cut GNR plotted as a function of polarisation. Raman spectra were acquired with 488 nm excitation.

the curve fit is not that good, and $I(D:G)_{min}/I(D:G)_{max}$ is quite high. There are two factors that could be contributing to this: (1) the edges are more disordered, i.e. contain shorter armchair segments and/or a higher proportion of segments not oriented along the average edge direction and/or (2) the aggregate consists of ribbons that are not well aligned.

Not all GNR aggregates sampled exhibited $\cos^2\theta$ or $\sin^2\theta$ dependences for both the D and G bands. Shown in figures 72 through 75 are polarised Raman plots of aggregates that only exhibited either a D or G band polarisation dependence, or no dependence. Further examples can be found in Appendix B.

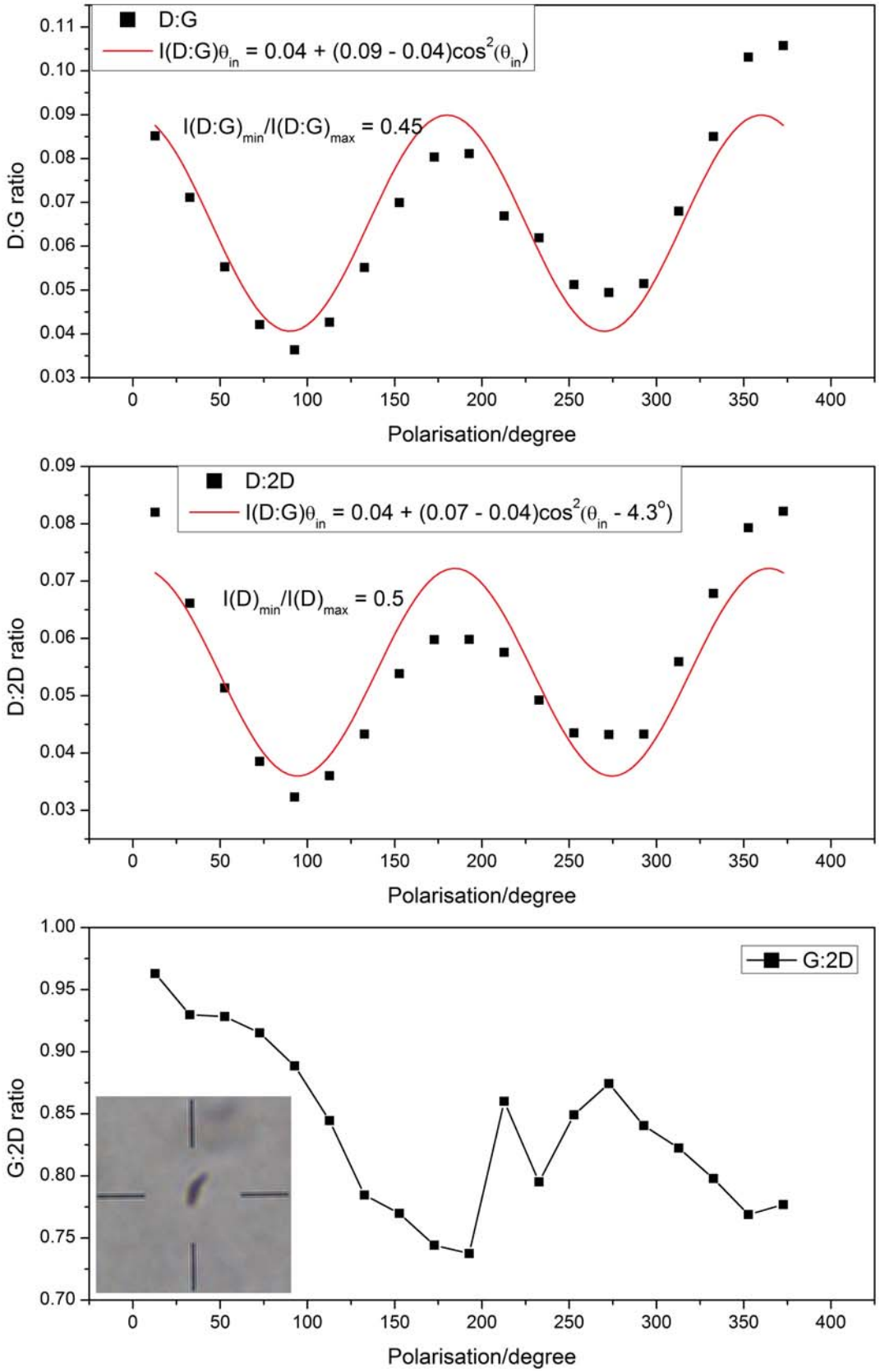

Figure 72: G:2D, D:G and D:2D ratios of 500 nm wet-cut GNR plotted as a function of polarisation. Raman spectra were acquired with 488 nm excitation.

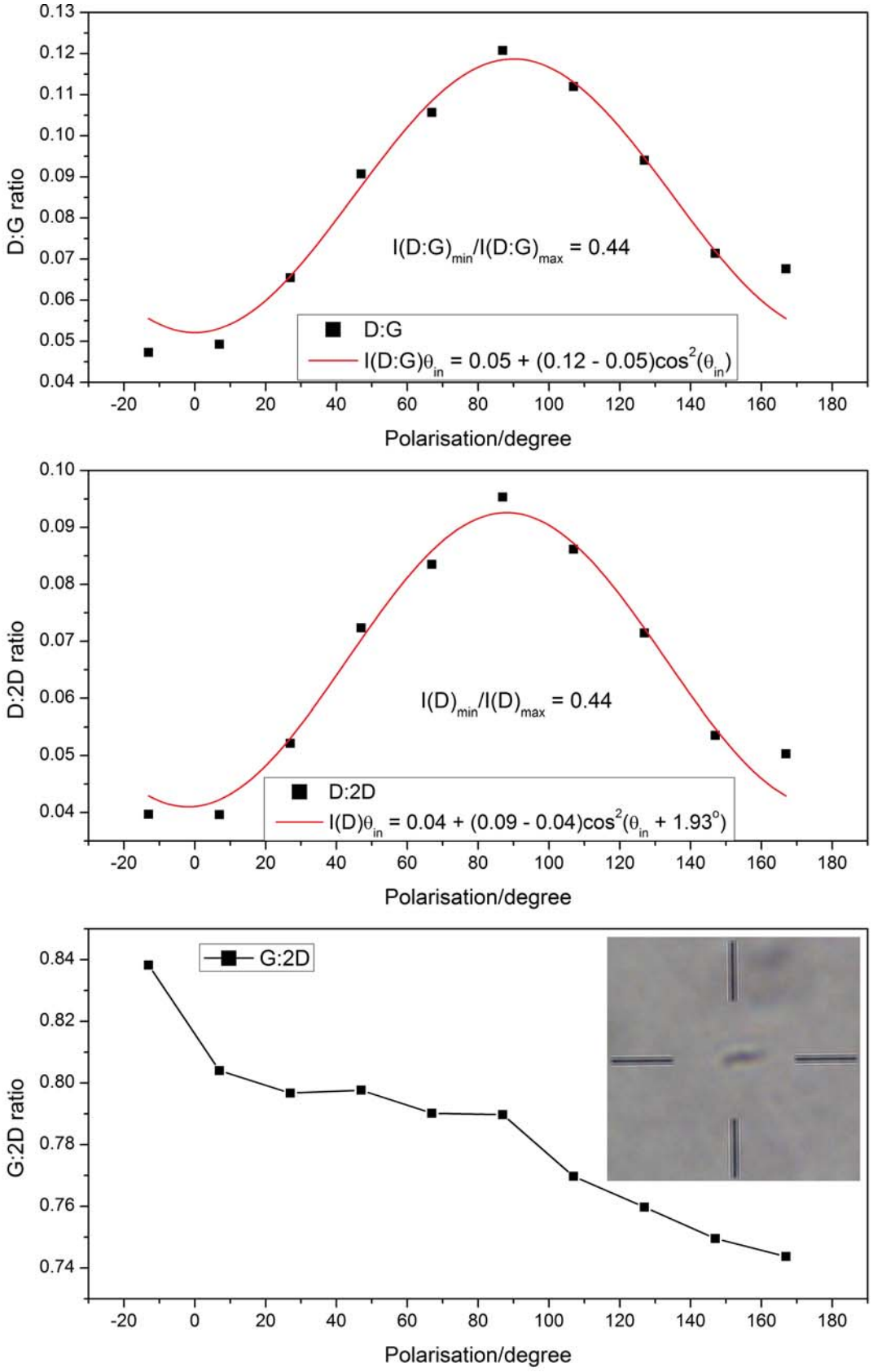

Figure 73: G:2D, D:G and D:2D ratios of 500 nm GNR plotted as a function of polarisation. Raman spectra were acquired with 488 nm excitation.

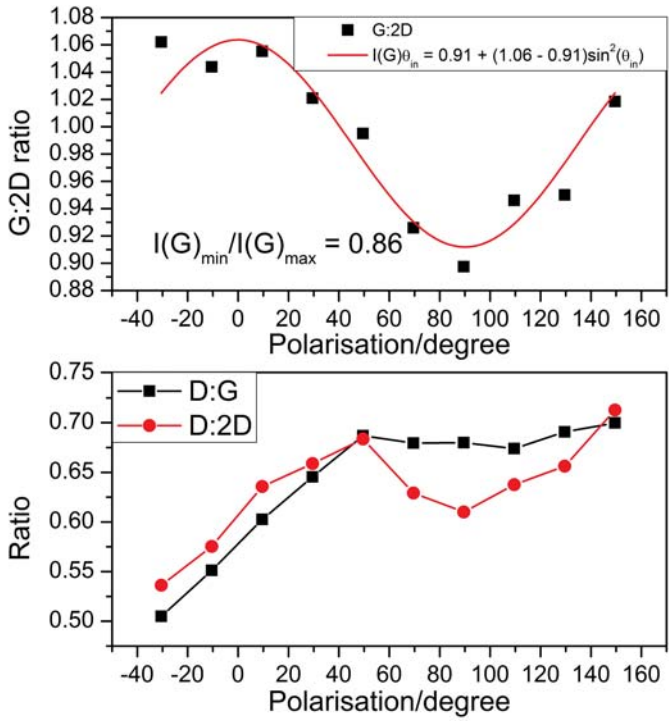

Figure 74: G:2D, D:G and D:2D ratios of 100 nm dry-cut GNR plotted as a function of polarisation. Raman spectra were acquired with 488 nm excitation.

The examples presented here have shown that many GNR aggregates, in which the ribbons are likely not well aligned, still exhibit clear polarisation dependences in many cases (over 30 individual aggregates of a range of widths were sampled in total). This would suggest that the GNRs produced via the nanotomy method are of high quality and contain reasonably ordered and straight edges with mixed segments of armchair and zigzag geometry. The predominance of a $\sin^2\theta$ G band dependence in almost all of the aggregates suggests that ribbons with predominant zigzag geometry are consistently produced in the nanotomy method, which is in agreement with the findings from XPS data reported by Mohanty et al.[83]

The results of these polarised Raman studies have shown that $I(D:G)_{min}/I(D:G)_{max}$ values can vary greatly between GNR aggregates, even those cut at the same width. Additionally, no significant variation in $I(D:G)_{min}/I(D:G)_{max}$ was found for wet- vs dry-cut ribbons. The ribbons for all these samples were microtomed at a relatively high cutting speed (7.5 mm/s). Figures 76 and 77 show polar plots of D:G ratios for wet- and dry-cut 100 nm ribbons cut at a slower speed of 0.8 mm/s. It is apparent that there is a large difference in average $I(D:G)_{min}/I(D:G)_{max}$ for wet- vs dry-cut ribbons, with dry-cut ribbons giving consistently lower $I(D:G)_{min}/I(D:G)_{max}$ values. Furthermore, there is less variation in $I(D:G)_{min}/I(D:G)_{max}$ values for these ribbons cut at the slower speed, particularly for the dry-cut GNRs. Though there is significant variation in average D:G ratios between different samples, the $I(D:G)_{min}/I(D:G)_{max}$ remained quite similar.

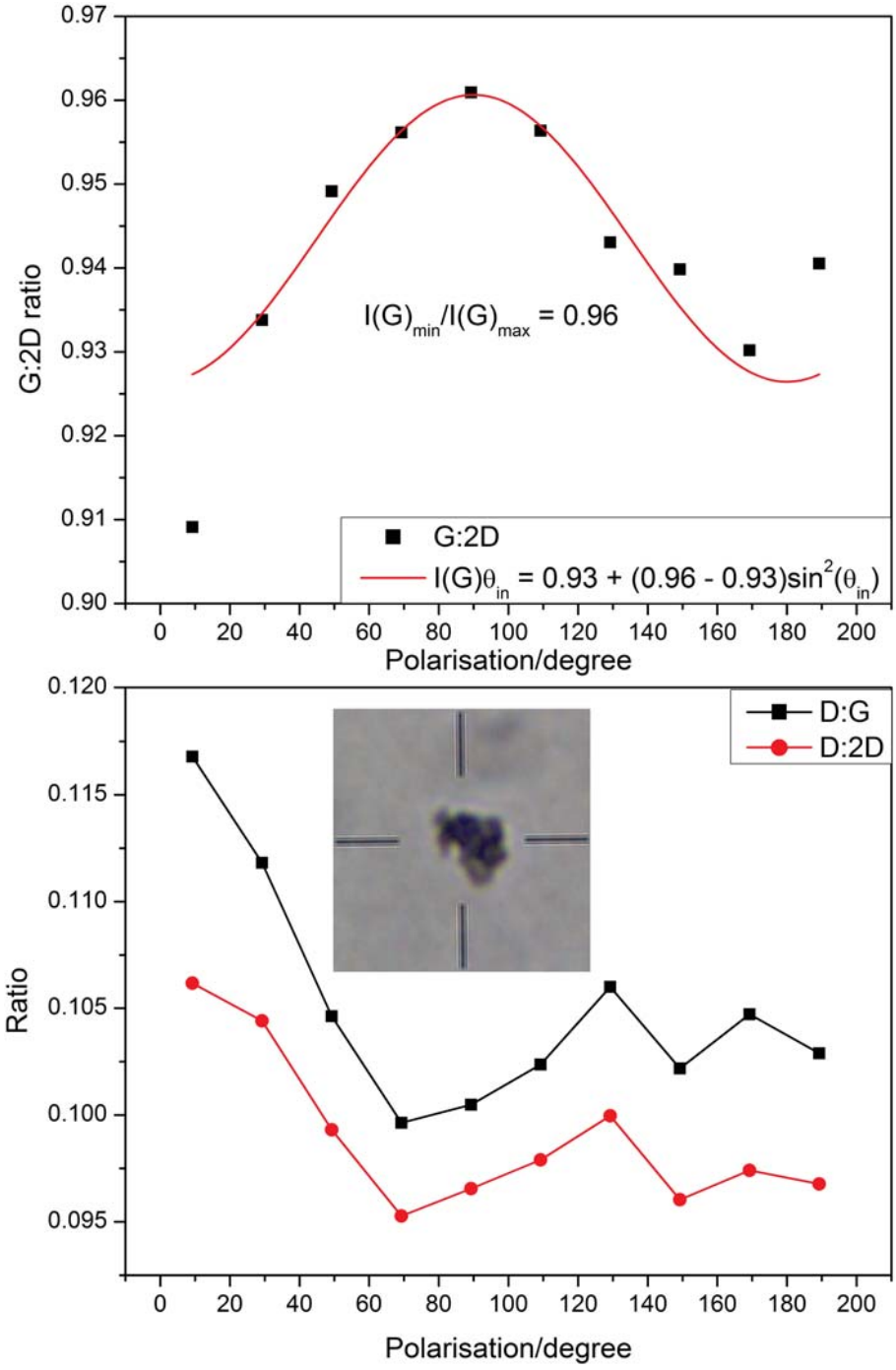

Figure 75: G:2D, D:G and D:2D ratios of 500 nm GNR plotted as a function of polarisation. All Raman spectra were acquired with 488 nm excitation.

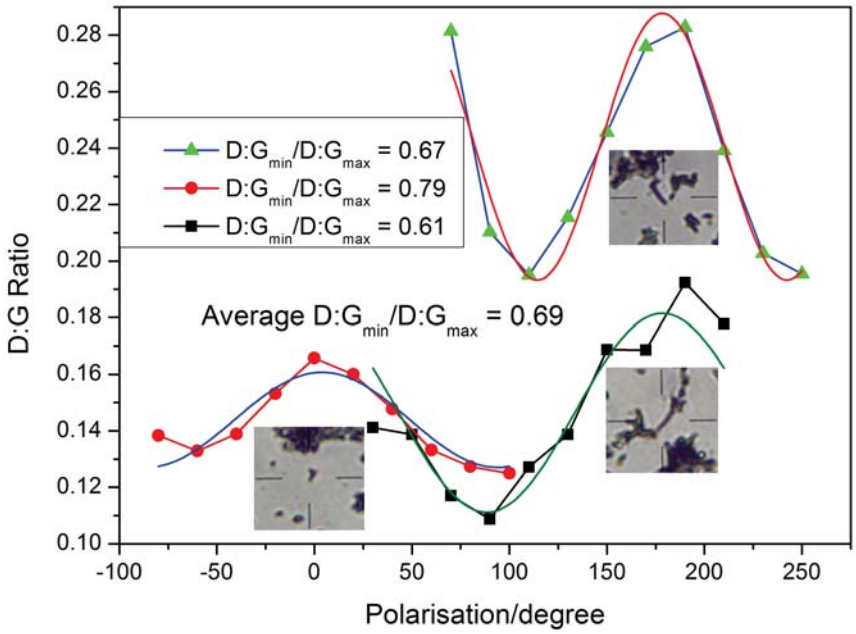

Figure 76: G:2D, D:G and D:2D ratios of 100 nm wet-cut GNR plotted as a function of polarisation. All Raman spectra were acquired with 488 nm excitation.

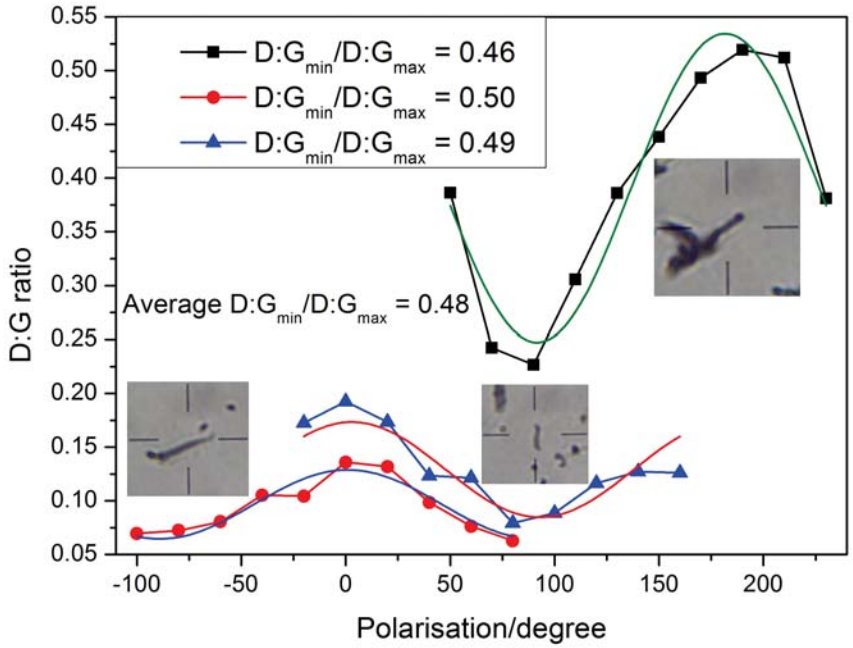

Figure 77: G:2D, D:G and D:2D ratios of 100 nm dry-cut GNR plotted as a function of polarisation. All Raman spectra were acquired with 488 nm excitation.

4.3 Conclusion

Various aspects of the structure of GNRs produced via the nanotomy method have been probed using Raman microscopy, AFM and TEM. AFM and TEM images have revealed high-quality GNRs with relatively straight edges, though aggregation is found to occur persistently. Low-frequency Raman microscopy has confirmed the presence of aggregated ribbons, through probing the interlayer interactions via analysis of both the C and 2D bands. Most importantly, and of most relevence to the edge modification of GNRs, the structure of GNR edges has been characterised via analysis of D:G ratios and polarised Raman microscopy. Analysis of D:G ratios in ribbons cut at different widths revealed an increase in D:G ratio with decreasing ribbon width, similar to the findings by Mohanty et al.[83] These studies have also revealed that cutting the ribbons dry or into water has an effect on the edge structure, manifest as an increase in the D:G ratio for wet-cut ribbons. This would suggest more disordered edges in wet-cut ribbons, or a higher proportion of armchair edges compared to dry-cut ribbons. By studying the polarised behaviour of both the D and G bands, the predominant edge type, degree of disorder/edge misorientation and relative orientation of armchair and zigzag segments was able to be determined. This combined approach has not previously been reported in the literature. Overall, the polarised Raman data suggests a predominance of zigzag edges, which is consistent with the findings of Mohanty et al.[83]

5 Edge Chemistry of Graphene Nanoribbons

5.1 Introduction

To make graphene useful in many electronic applications, a bandgap is required. One way in which this can occur is by confinement of the graphene electronic wave-functions in the lateral dimension, for example in nanoribbons, where the bandgap is determined by the width of the ribbon.[2] In addition to the nanoribbon width, the edge geometry (e.g. zigzag vs armchair) also affects the electronic structure. Bandgap tuning in graphene can also be achieved by chemical functionalisation, which can be covalent or non-covalent. Due to the two-dimensional nature of graphene, chemical doping of this material is limited to edge or surface interactions.[84] However, covalent modification of the graphene basal plane inevitably alters its exceptional electronic and optical properties, hence edge functionalisation, which preserves the pristine graphene electronic structure, is the more desirable strategy. The following sections explore this idea in detail, beginning with a discussion of how the aromaticity in graphene and graphene nanoribbons can be used to explain differences in their chemical reactivity. An overview of the different strategies used for functionalisation of graphene materials is given, which focusses on ways in which graphene edges can be selectively functionalised without modification of the basal plane. Finally, the scope and aims of this chapter are outlined.

5.1.1 Clar Sextet Theory and Graphene Aromaticity

Graphene is composed entirely of sp^2 carbon atoms, thus its valence π electrons dominate its electronic and chemical properties. Clar sextet theory, which is an effective model for π-bonding structure, is thus useful for representing the chemical bonding in graphene.[137] Clar sextet theory is well known for explaining the chemical reactivities of PAHs (polycyclic aromatic hydrocarbons), and can be effectively used to rationalise why PAHs with similar structures can be very different in terms of their chemical stability. Thus, representing graphene as an extended PAH allows the chemical reactivity to be determined from the aromaticity of the PAH system.[138] Clar sextet theory can be used to explain the dependence of band gap and chemical reactivity on the width and edge geometry (i.e. armchair vs zigzag) in GNRs.[137]

The aromaticity, and subsequently chemical reactivity, of graphene can be determined by the combination of all the possible different isomeric Clar formulae.[138] In an infinite graphene sheet, there are three Clar formulae in resonance (see figure 78); each resonance structure has a unit cell with dimensions $\sqrt{3}a \times \sqrt{3}a$.[139] The distribution of electrons and bond lengths is uniform over the entire network, giving the graphene sheet high thermodynamic stability and low chemical reactivity. Upon cutting graphene to produce an edge, a boundary is introduced to what was previously a system with fully delocalised π elec-

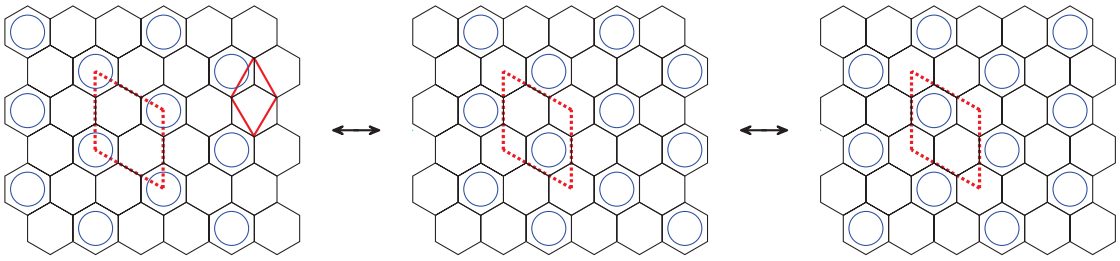

Figure 78: Resonance structures of a graphene sheet. The unit cells of the migrating Clar sextets are marked with dotted red lines, and the unit cell of graphene is marked with solid red lines for comparison. The Clar sextet unit cell length is $\sqrt{3}a$, where a is the length of the graphene unit cell. Figure adapted from Fujii et al.[139]

trons.[96] As a result, the electron distribution for nanographenes and graphene nanoribbons can be quite different from the fully benzenoid structure of an infinite graphene sheet, as the aromaticity is strongly influenced by the edge geometry.[138,139] In fact, three new categories of Clar formulae arise, as shown in figure 79. One of these is the fully benzenoid structure, the most stable form, as found in large-scale graphene. Another is the Kekulé structure, which contains both Clar sextets and olefinic double bonds, the latter of which are localised at either of the two edges for armchair-edged GNRs. The remaining incomplete Clar structure consists of Clar sextets in the inner hexagons, with double bonds localised at both edges. In armchair GNRs, the bandgap exhibits a periodicity with the ribbon width, which matches a similar periodicity in the Clar formulae. This dependence of the Clar structure on the ribbon width can be expressed using the following formulae: w = 3n for fully benzenoid, w = 3n + 1 for Kekulé and w = 3n + 2 for incomplete clar (where n is a positive integer).[137] The Clar formula determines the chemical stability for armchair GNRs, with fully benzenoid structures being the most stable, due to extensive delocalisation of the π electrons. The incomplete Clar structure has greater chemical reactivity than the Kekulé structure, as it has localised double bonds at the edges, whereas

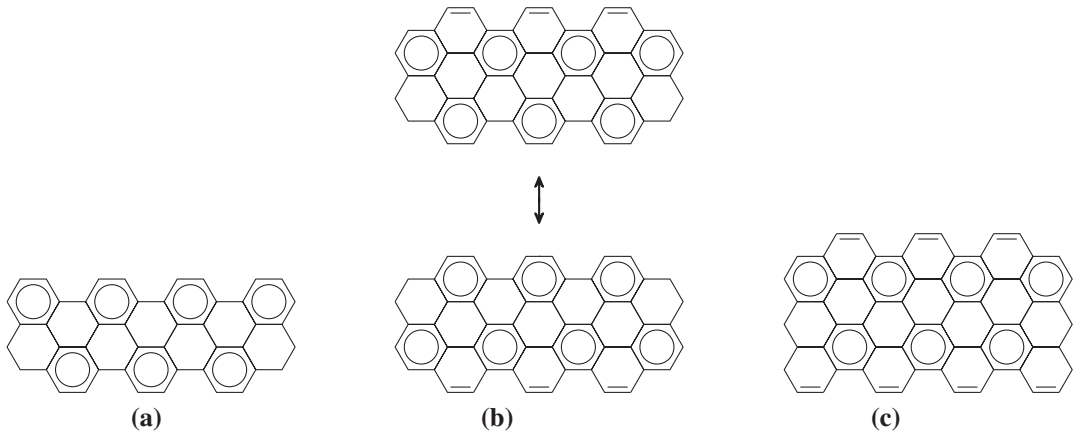

Figure 79: The three different width-dependent Clar formulae for armchair-edged GNRs: (a) fully benzenoid, (b) Kekulé and (c) incomplete Clar. Figure adapted from Schneider et al.[138]

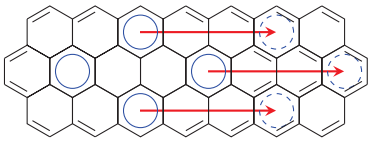

Figure 80: Segment of a zigzag-edged GNR with migration of Clar sextets depicted by red arrows. Figure adapted from Schneider et al.[138]

for the latter the edge double bonds are in resonance with aromatic rings.[138]

Whereas the bandgap is strongly dependent on ribbon width for armchair GNRs, for zigzag GNRs the bandgap is very small for almost all ribbon widths. In zigzag GNRs, the structure is never fully benzenoid, rather the number of Clar sextets is small and these can migrate along the ribbon length to give an infinite number of Clar formulae (see figure 80), giving the GNRs low stability.[137] Thus, the aromaticity of a zigzag GNR is a balance between the extensively delocalised aromatic rings in the lattice and the highly localised and reactive double bonds at the edges.[138] These edge states can be treated as free radicals, as shown in an alternative representation of the Clar structures for zigzag GNRs, in which there is a fully benzenoid structure in the ribbon centre with free radicals at the edges (figure 81).[96] These radicals are delocalised along the edge, giving a partial radical character of 1/6 electron per carbon atom. This partial radical character gives them unique chemical reactivity over the carbon atoms in the basal plane. This is shown in the reaction between a zigzag edge and a H atom, where the BDE (bond dissociation energy) for the newly formed C−H bond is only $\sim 60\%$ of that of a C−H bond formed between H and a molecular carbon radical. The reactivity towards an H radical is in the order

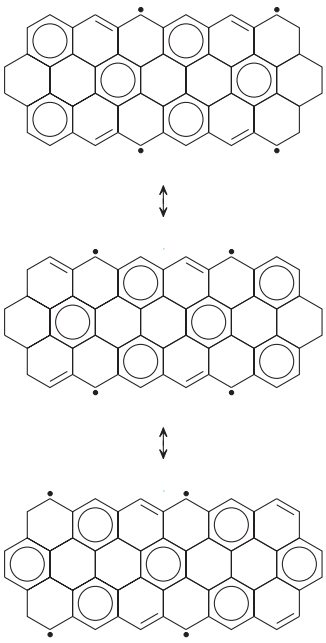

Figure 81: Alternative representation of the Clar structure shown in figure 80. The number of Clar sextets can be increased by having free radicals at the edges. Only three resonance structures are shown here.

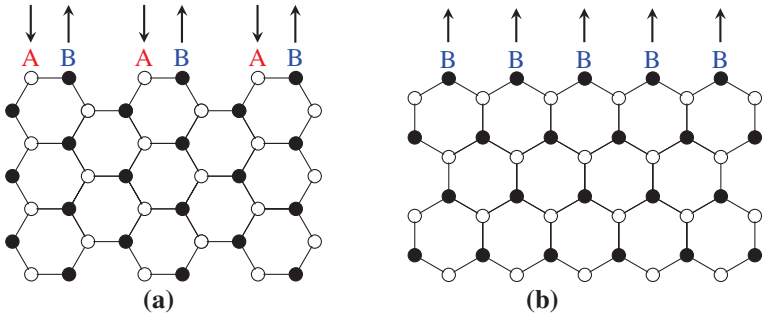

Figure 82: Illustration of the symmetry of A and B sublattices in (a) armchair and (b) zigzag GNRs. The arrows indicate pseudospins. Figure adapted from Fujii et al.[139]

graphene sheet < armchair edge < zigzag edge.

The origin of the edge state in zigzag-terminated edges can also be understood from the effects of the bipartate structure of graphene, which has two independent sublattices A and B in the hexagonal unit cell.[139] Under the tight-binding approximation of π bands in graphene, a linear superposition of the A and B π states form the electronic state. Unlike the armchair edge, which is always terminated by both A and B sublattices in pairs, the zigzag edge is terminated by only A or B atoms (figure 82). This breaks the pseudospin symmetry at the zigzag edge, resulting in a spin polarised edge state.

5.1.2 Functionalisation of Graphene and GNRs

For GNRs to be useful in most electronic applications, they must have bandgaps in the order of 1 eV.[140] As discussed in the previous section, the bandgap of GNRs can be controlled by their width. However, only ribbons with very narrow widths (< 3 nm) have bandgaps in the required range, and the bandgap can be very sensitive to small changes in width; a change of just 0.3 nm can have a large effect on the bandgap. Thus, bandgap tuning via width control alone presents somewhat of a challenge, as it requires very elegant and precise methods of production. However, bandgap tuning in graphene can also be achieved by chemical functionalisation, which can be covalent or non-covalent. Thus, chemical functionalisation, which allows for more controllable tailoring of the electronic properties of GNRs, presents a more favourable alternative to bandgap tuning. Due to the two-dimensional nature of graphene, chemical doping of this material is limited to edge or surface interactions.[84]

Overview of the different strategies for graphene functionalisation

Although graphene is rather inert chemically, there are still numerous possibilities for its functionalisation. The π electron network of graphene can be disrupted in two ways: introduction of defects into the carbon network, or changing sp^2 carbons to sp^3 via covalent bonding.[141] In the first approach, graphene can be substitutionally doped with other

atoms, e.g. nitrogen or boron, to induce n- or p-doping into the sheet, depending on whether the dopant atoms are electrophilic or nucleophilic.[142] Substitution retains the sp^2 character of the basal plane C atoms, however the doping disrupts the continuous cloud of π electrons.[143] Thus, controlling the degree of doping allows for tailoring of the electronic properties of graphene. For nitrogen doping, the electron lone pairs of N atoms are incorporated into the π system of graphene, making it electron rich and giving rise to n-type semiconductor behaviour. N-doped graphene is typically formed during CVD growth by incorporation of the dopant within the carbon lattice, either at the edges or in the basal plane of pristine graphene, or with O atoms in graphene oxide. The second approach involves covalent attachment of functional groups to the sp^2 carbon atoms in the basal plane or at the edges of graphene, changing their hybridisation to sp^3. This is accompanied by loss of a free π electron associated with the sp^2 bond, removing this electron from the π cloud of graphene. This removal of an electronic state can result in introduction of a bandgap by reduction of the carrier density, and the introduction of energy levels in the band structure can shift the behaviour to that of an n-type or p-type semiconductor. Thus, functionalisation can result in substantial changes in the carrier mobility and charge polarity/density of graphene. A large variety of chemical functionalisation strategies have been employed for such purposes, including nucleophilic addition, cycloaddition, free radical addition, Friedel-Crafts acylation and Diels-Alder reactions.[85,86] The relatively high chemical stability of graphene means that highly reactive compounds are usually required for covalent functionalisation. Reactions involving diazonium compounds, nitrenes, carbenes and arynes have all shown to be highly successful in the functionalisation of graphene.[90]

Diazonium chemistry is of particular interest, as it is one of the most prevalent methods applied to the functionalisation of graphene. The mechanism commonly used to explain the covalent functionalisation of graphene with aryldiazonium salts is given in figure 83.[144] This involves electron transfer from graphene to the aryldiazonium cation, which releases N_2 to form an aryl radical. A covalent bond is then formed between the aryl radical and a carbon atom in the graphene lattice, changing its hybridisation from sp^2 to sp^3. Aryl radical formation by reduction of the diazonium salt is the rate-limiting step in the reaction, and this rate is determined by the overlap of the graphene electronic DOS and the unoccupied DOS of the diazonium salt. Though diazonium functionalisation of graphene is commonly attributed to this mechanism, one study has shown that direct reaction of graphene with the diazonium cation to form $-$N=N$-$ linkages can also occur in addition to aryl radical grafting.[145]

The substrate on which the graphene is supported has been shown to have a large effect on its reactivity towards diazonium compounds, with a SiO_2 substrate giving more than a 10-fold increase in attached functional groups for monolayer graphene on SiO_2 compared to the top layer of HOPG, as shown by Raman D:G ratios.[88] Additionally,

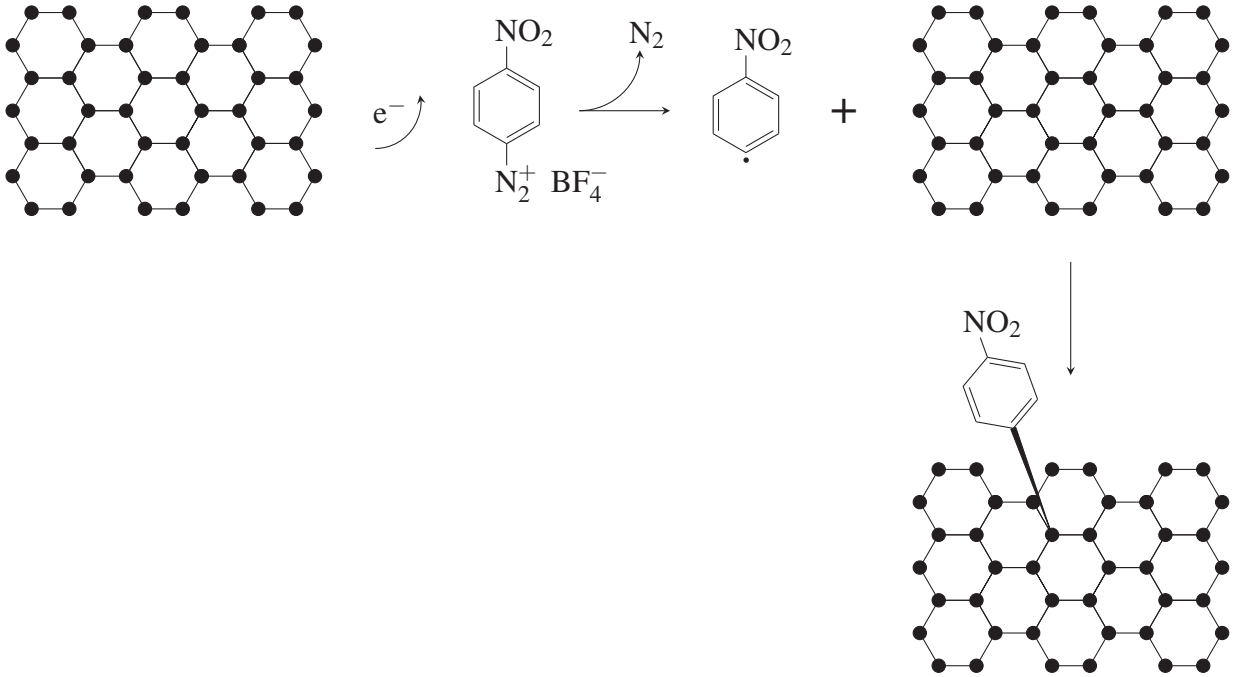

Figure 83: Mechanism for covalent functionalisation of graphene with diazonium salts via aryl radical formation. Figure adapted from Paulus et al.[144]

monolayer graphene was found to be far more reactive than bi- or multi-layer graphene on SiO_2. This enhanced reactivity was attributed to the induction of electron and hole puddles by ionised impurities in the SiO_2, which shift the local Dirac point above or below the Fermi energy, respectively. This results in local areas of increased reactivity on the graphene layer in direct contact with the SiO_2, thus little change in reactivity occurs for bi- and multi-layer graphene, as the top layer, which is the only layer exposed to the diazonium salt solution, is screened from the charged impurities by the underlying layers. The reactivity of graphene towards diazonium salts was also found to vary for other types of substrates.[144] Similar to SiO_2, Al_2O_3 gave higher reactivity, while lower reactivity was observed on OTS (octadecyltrichlorosilane) and hBN (hexagonal boron nitride).

Graphene oxide (GO) presents another approach to graphene functionalisation, as it is decorated with an abundance of oxygen-containing functional groups, including hydroxyl, carboxyl, carbonyl and epoxy groups.[142] Additionally, the large surface area of the material means that all functional groups are readily available for reaction.[146] These functionalities can be targeted with common organic reactions such as condensation, nucleophilic substitution, electrophilic substitution and addition reactions.[143] For example, sulfanilic acid can undergo amidation with carbodiimide-activated carboxyl groups of GO to provide a negative charge, or cysteamine to provide thiol groups for attachment to nanoparticles.[146]

Tailoring of the electronic properties of graphene can also be achieved by non-covalent functionalisation, for example by adsorption of organic or inorganic molecules to the graphene basal plane to alter the electronic properties of the material via interaction with

the sp^2 hybridised carbon atoms.[2] Physisorption and $\pi - \pi$ interactions do not disrupt the sp^2 nature of the basal plane, however they can alter the electronic properties by doping and creating scattering sites by enhancement of the graphene electric field by the molecular dipole moment.[143] Investigations on doping graphene using organic molecules for charge-transfer have received growing interest.[84] Adsorption of aromatic molecules to the graphene basal plane allows for controllable doping of the material via charge-transfer, while largely preserving its high electron mobility.

Edge-specific functionalisation

Covalent modification of the graphene basal plane inevitably alters its exceptional electronic properties. In contrast, edge functionalisation, which largely preserves the aromatic structure of the basal plane, presents a more desirable strategy to manipulating the electronic and chemical properties of graphene.[84,138] In addition to the effects of ribbon width and edge geometry on the electronic properties of GNRs, as discussed earlier, aromaticity considerations also show that the edge chemistry influences the band-gap, thus edge functionalisation should be a useful tool for band-gap tuning.[147] Edge functionalisation of graphene can also be used to impart additional desirable attributes, such as improved solubility.[138]

An important consideration in functionalisation of graphene edges is whether significant reaction with the basal plane can be prevented, i.e. whether a reaction can be edge-selective. There are several ways in which selectivity can be achieved, and three main routes are described here. Firstly, the carbon atoms at the edges of graphene are known to be generally more reactive than the basal plane, which in itself provides a reasonable level of selectivity.[87–90] Graphene edges are frequently reported to be more reactive to diazonium chemistry than the basal plane.[88,138,144] This can be attributed to higher overlap between electronic DOS at graphene edges and unoccupied electronic states of the aryl radical, as well as the edges being able to better accommodate the strain induced upon C atoms changing from sp^2 to tetrahedral sp^3 hybridisation.

The second approach to edge selectivity is to limit exposure of the basal plane to the functionalising reagant, leaving only the edges available for reaction. There are several reports of selective functionalisation of graphite edges, followed by exfoliation to produce functionalised graphenes.[91–93] For example, selective functionalisation of the edges of graphite via the diazonium route has been achieved using 4-bromophenyl radicals, which are too bulky to intercalate between the graphene layers.[138]

Finally, selectivity can be achieved by tailoring reactions to functional groups already present at the edges. In this case, many of the simple click chemistry-type organic reactions commonly used for the functionalisation of GO could be applied to graphene edges containing similar oxygen functionalities. A variation on this approach is to target the highly reactive dangling bonds produced by C−C bond cleavage during mechanical frac-

turing for selective edge functionalisation. An example of this is ball-milling of graphite in the presence of gases such as hydrogen, carbon dioxide and sulfur trioxide to give graphene nanoplatelets edge-functionalised with hydrogen, carboxylic acid and sulfonic acid groups, respectively.[148]

The chirality of graphene edges presents a possible additional level of selectivity, as zigzag and armchair edges exhibit different chemical reactivities. As discussed earlier, zigzag GNRs have unpaired π electrons distributed along the edge carbon atoms, giving them partial radical character.[118] These localised states are not present in armchair edges, giving zigzag edge carbon atoms unique chemical reactivity. Additionally, the formation energy for the attachment of functional groups to single zigzag edge carbon atoms is lower than that for armchair edges.[95] This is due to structural deformation of the armchair edge that occurs upon addition of functional groups to single edge carbon atoms, which arises as a result of steric hindrance between the functional group and the hydrogen atom attached to the neighbouring edge carbon atom. This structural deformation does not occur for zigzag edges. Zigzag and armchair GNRs are predicted to have different reactivities towards diazonium salts, due to differences in the rate of electron transfer to form the aryl radical.[144] For armchair GNRs, the transfer rate increases overall with the ribbon width, though it also follows the aromaticity patterns. Zigzag GNRs have higher overall reactivity due to increased DOS overlapping with the empty states of the diazonium salt, and the electron transfer rate shows the opposite trend to armchair GNRs, with a decrease for increasing width. This is due to the charge localisation at zigzag edges having a greater contribution for narrower ribbons. These differences could allow for the selective functionalisation of zigzag vs armchair GNRs. There are also certain types of functionalisation reactions that could be selective for armchair edges over zigzag edges, for example the Diels-Alder reaction. Computational studies have predicted that certain Diels-Alder reactions with armchair edges are much more favourable than with zigzag edges or the basal plane.[94,149,150]

5.1.3 Characterisation of Functionalised Graphene Edges

The ability to characterise chemically functionalised graphene edges is an important consideration. The low carbon edge:basal ratio of GNRs presents a challenge in distinguishing the chemical and physical structure of the edges from the basal plane.[138] Thus, any methods that will allow for this differentiation must be sensitive to the edge. Such methods can include STM (scanning tunnelling microscopy), TEM, XPS, ζ-potential measurements, cyclic voltammetry, FTIR and Raman spectroscopy. STM (and TEM) can provide images of the edge and basal plane of graphene at atomic resolution. For zigzag GNRs, STM allows the edge states to be investigated, due to localisation of the p_z electrons at the zigzag edge increasing the tunneling current, thus making the zigzag edges appear visibly brighter in the STM images. Since the edge states are sensitive to chemical mod-

ifications, STM can thus be used to probe the chemical, as well as physical, structure of zigzag edges. However, methods such as STM, TEM, and XPS have rather stringent requirements for sample preparation and thus may not always be suitable for all sample types, for example for samples where aggregation may be a problem. However, even relatively simple techniques with more flexible sample requirements can be used to detect edge functionalisation in GNRs and small graphene flakes. In one study, FTIR was able to clearly distinguish between graphene flakes modified with different edge functional groups, with XPS used to confirm these results.[148] This, and other examples, show that FTIR, while a relatively simple technique, can be very useful for detecting the attachment of functional groups to graphene, even at the low levels expected for selective edge functionalisation.

Raman spectroscopy has been used extensively in characterising the atomic and electronic structure of graphene. The change in hybridisation of sp^2 carbon atoms to sp^3 upon chemical functionalisation can be probed using Raman spectroscopy via changes in the relative intensity and polarisation-dependent behaviour of the D band. Prior to functionalisation, the D band of GNRs will exhibit a dependence on polarisation, as most of the D band intensity arises from the edges. After functionalisation of the basal plane, however, the intensity of the D band will increase and the overall polarisation dependence will be lost or dramatically reduced, as the newly generated sp^3 carbon atoms in the basal plane will now contribute the most D band intensity. For example, changes in the behaviour of Raman D:G ratios have been used to prove that graphene edges are functionalised by diazonium salts to a significantly higher degree than the basal plane.[88] Thus, Raman spectroscopy is a useful tool for comparing the reactivity of the edges relative to the basal plane. While Raman spectroscopy may not be sensitive enough to detect signals from low levels of attached functional groups, variations such as SERS, TERS and resonance-enhanced Raman can dramatically improve sensitivity. Raman can also be used to study doping in graphene, due to blue- and red-shifting of the G and 2D peaks upon p- and n-type doping (e.g. upon oxidation or amination), respectively. The relative ratios of the G and 2D band intensities can also change with functionalisation. For example, diazotisation of graphene with different groups has been shown to result in decreased I_{2D}/I_G ratios for both n- and p-doping.[144]

5.1.4 Scope and Aims

This chapter explores the selective functionalisation of the edges of graphene nanoribbons produced via the mechanical fracturing method described in the previous chapter. Polarised Raman analysis has shown that, on average, the edges tend to have mixed armchair and zigzag geometry, with somewhat of a predominance of zigzag segments. For this reason, edge chirality-based selectivity was not studied in this project, as this would require a more elegant method of GNR production. Instead, the goal was to investigate

whether selectivity could be achieved by the three approaches outlined in the previous section: (1) exploiting the higher reactivity of the edges over the basal plane, (2) preventing exposure of the basal plane to the functionalising reagent by performing the reaction prior to exfoliation of the ribbons and (3) targeting chemical groups already present at the edges for functionalisation.

The first sets of reactions presented are those targeted at hydroxyl and carboxyl groups at the edges of GNRs. During the mechanical fracturing microtomy process, C−C bonds are broken by mechanical force, resulting in reactive carbon species at the broken edges. These will rapidly react with anything nearby, in this case with gases in the air, to produce, presumably, a variety of largely oxygen-containing groups at the nanoribbon edges. These will likely be a mixture of ketones, carboxylic acids, alcohols, epoxides, etc. Simple esterification and amidation reactions were performed on these edge functional groups, involving the use of carbodiimides for the activation of carboxyls.

The second set of reactions involved diazonium-based functionalisation of edges. The relative reactivity of the edges and basal plane were investigated by performing the reactions on ribbons both prior to and post exfoliation, to determine whether limiting exposure of the basal plane would result in a higher degree of edge selectivity.

Characterisation of the functionalised GNR samples presented the largest challenge out of all the experimental work, as the persisting problem of ribbon aggregation and poor stability in most solvents, combined with the minute quantities of sample that could be produced, dramatically limited the techniques that could be used for characterisation. FTIR and Raman spectroscopy (including SERS) were the main techniques used, as these were able to accommodate, and derive useful information from, at least partially aggregated samples. FTIR microscopy, in particular, was found to be very useful in identifying signals from the attached functional groups, as it allowed for the sampling of small, densely aggregated samples. Raman spectroscopy by analysis of D:G ratios was useful in determining whether functionalisation had been limited to the edges without modification of the basal plane.

5.2 Results and Discussion

The mechanical fracturing technique used for GNR production results in ribbons dispersed in a solution rather than on a substrate as is common with CVD methods for graphene production. Unlike GO, which readily forms stable dispersions in water, GNRs are much more hydrophobic and thus much more difficult to stabilise in solution. Dispersions of ribbons were found to aggregate quite quickly even after periods of prolonged sonication, and this presented a problem for reactions that required several hours for completion. To keep the ribbons stabilised, reactions were required to be performed under mild sonication in an ultrasonic bath, which limited the types of reactions that could be performed based on their required experimental conditions. For this reason, the reactions studied here were limited to those that could be run near room temperature or in an ice bath. Detailed descriptions of the experimental methods can be found in chapter 3.

The low proportion of carbon atoms at the GNR edges available for reaction was important to keep in mind when characterising the samples as it could lead to sensitivity issues. Calculations of the approximate numbers of edge carbon atoms per 100 C atoms of the basal plane are useful to provide an idea of the approximate degree of edge functionalisation expected with the GNRs used in this study, and for GNRs of 100, 50 and 20 nm width, these values were calculated to be approximately 0.2, 0.45 and 1.2, respectively. Details of how these values were calculated are given in Appendix A. In these experiments, the majority of reactions were performed on ribbons with a width of 20 nm (except for the initial ester coupling reactions, for which ribbons of 100 nm width were used), which is the minimum width that can be obtained with the microtome, in order to maximise the number of possible edge sites for reaction.

The following sections are organised as follows: firstly, the three main routes followed for edge functionalisation are presented, namely ester coupling, amide coupling and aryldiazonium grafting. FTIR and Raman spectra are included in the results as the main characterisation techniques and used to show whether the reactions were likely successful and whether they were edge selective. Some additional characterisation techniques are then presented, namely SERS and Terahertz spectroscopy, which support the Raman and FTIR analysis and provide some additional useful evidence for functionalisation.

5.2.1 Ester Coupling

The first strategy for edge functionalisation of GNRs involved targeting edge OH groups for reaction with carboxylic acid-containing compounds for ester bond formation. $NaBH_4$ was used to reduce edge carbonyl groups to maximise the number of OH groups. The functionalising reaction involves the following steps (figure 84): (1) activation of the COOH group of the functionalising molecule with EDC and DMAP and (2) reaction of the resulting activated ester (AE) with a GNR edge OH group to form an ester bond. This

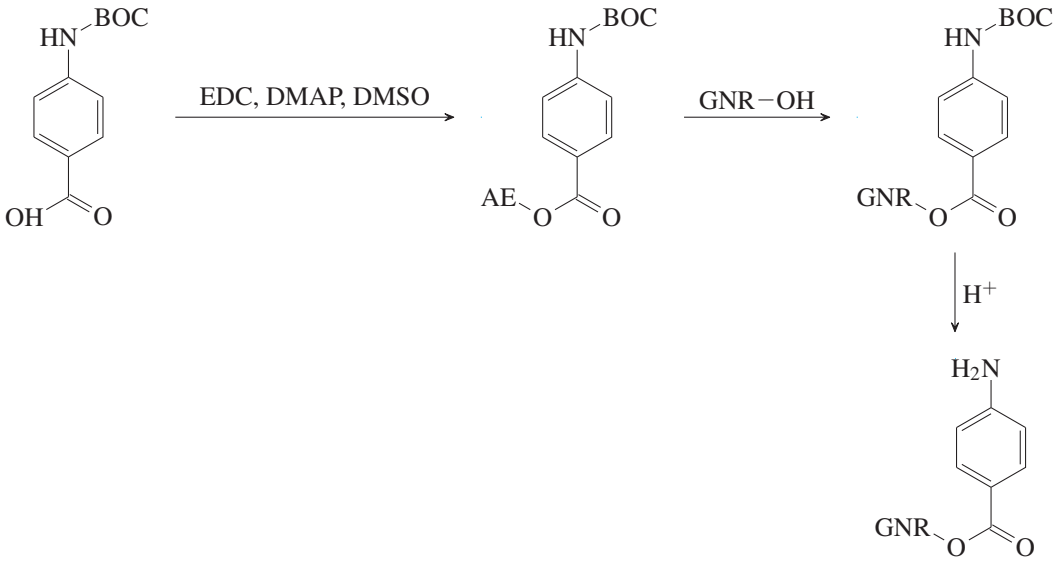

Figure 84: Reaction scheme for functionalisation of GNRs with 4-aminobenzoic acid via EDC/DMAP ester bond formation.

reaction was used with 4-aminobenzoic acid (4-ABA), 4-nitrobenzoic acid (4-NBA) and Rhodamine B (RhB) (see figure 85).

Due to the low edge:basal ratio of the GNRs cut via the nanotomy method, the viability of functionalisation via ester bond formation was also tested on GO, which contains a much higher proportion of oxygen-containing functional groups. GO was functionalised with Rhodamine B (RhB) and 4-nitrobenzoic acid (4-NBA), which both contain carboxyl groups for reaction with OH groups on the GO to form ester linkages. Since RhB is a dye that is strongly light-absorbing in the visible region, it was reasoned that this could make it easier to detect in the Raman due to fluorescence or resonance enhancement effects. Likewise, the nitro group of 4-NBA should be strongly absorbing in the IR measurements. The IR spectra of GO and GO functionalised with 4-NBA and RhB are shown in figure 86. The broad bands at approximately 1115, 1398 and 1615 cm^{-1} in GO, which can be attributed to C−O and C=O vibrations of various oxygen functionalities, are strongly reduced upon functionalisation. The spectrum of 4-NBA-GO has only broad bands in the $1300 - 1500\ cm^{-1}$ region instead of the strong, sharp ones expected for the nitro group.

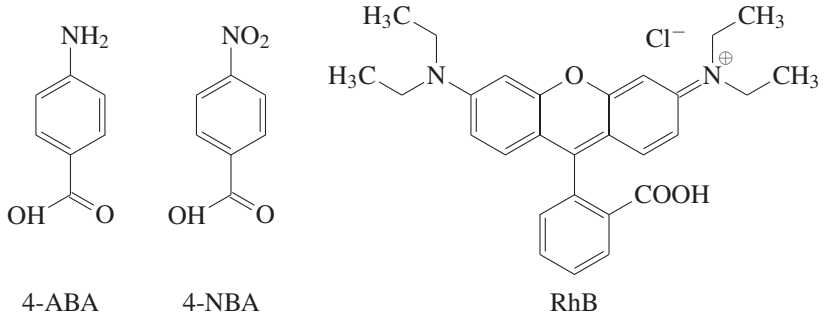

Figure 85: Chemical structures of the modifiers used in the ester coupling reactions.

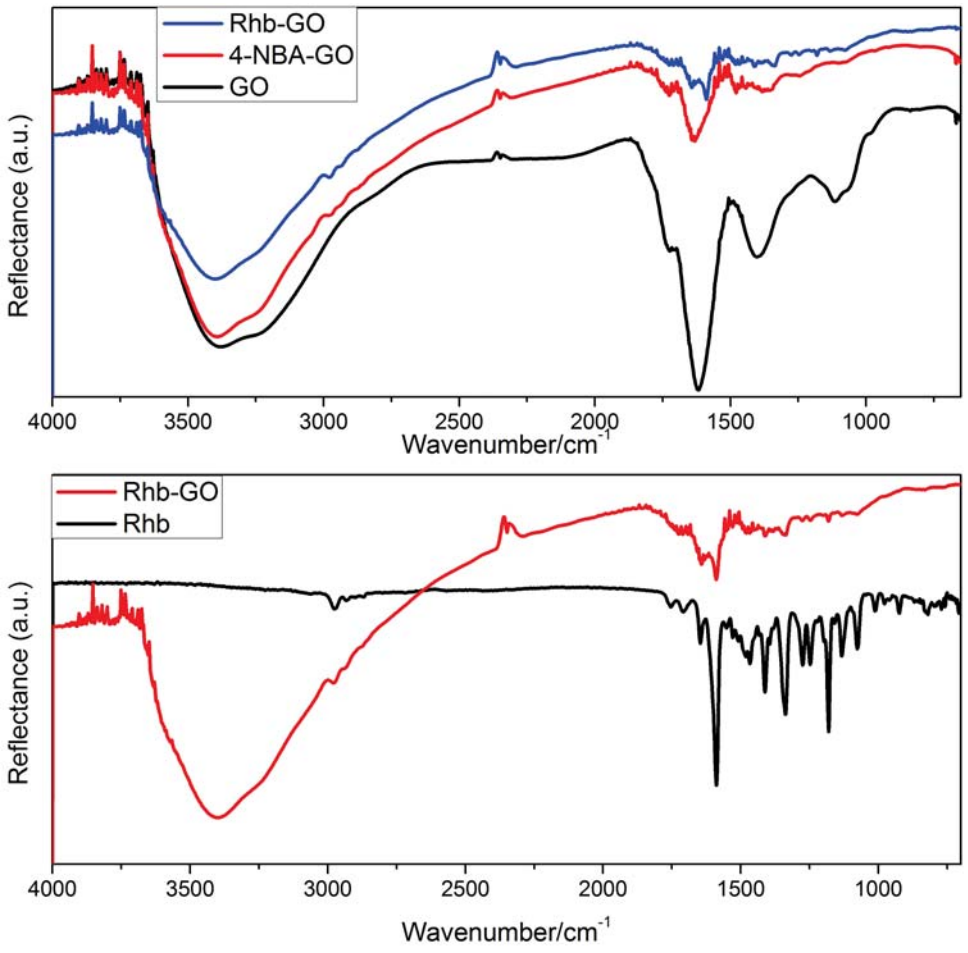

(a)

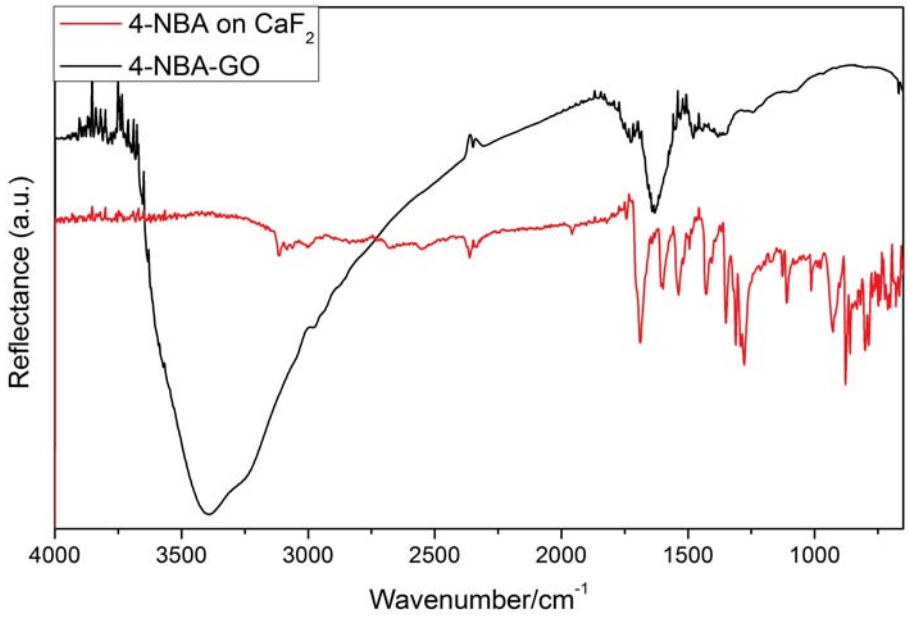

(b)

Figure 86: FTIR microscope spectra of unmodified GO and GO functionalised with Rhb and 4-NBA.

The spectrum of RhB-GO has strong bands that clearly match the spectrum of RhB. The IR spectrum of 4-NBA-GO is also compared with the spectrum of the functionalising reagent. There are no clear matches of peaks between the free and functionalised samples.

Raman spectra of the modified and unmodified GO samples are given in figure 87. This preliminary data was recorded with 785 nm excitation, which is far from the absorption maximum of Rhodamine B. However, visible brief flashes of fluorescence were observed as the RhB-GO sample was scanned across the laser focus, but these seemed to bleach/quench very quickly, so were not captured in the Raman spectra. The Raman spectra of the functionalised and un-functionalised GO samples all appear very similar with no apparent extra peaks from the attached groups. The D band appears broad and intense and the D:G ratio is high for all samples, characteristic of a high degree of sp^3 hybridisation in the graphene basal plane.

Figure 88 shows the Raman spectra of GNR, GNR reduced with $NaBH_4$, and reduced GNR (r-GNR) functionalised with 4-aminobenzoic acid (4-ABA). The spectra shown are the average of several scans for each sample, with 532 nm excitation. Immediately apparent is the difference in the intensity of the D band. This increases quite significantly in the order GNR $<$ r-GNR $<$ f-GNR. It is not too clear why the D band intensity should change with edge reduction and functionalisation. As discussed in the previous chapter, sample heterogeneity has been a problem in obtaining consistent D:G ratios, even in densely aggregated samples. Thus it is possible that the D:G ratio differences observed here are simply due to this heterogeneity, however, the differences do appear to be quite significant. Furthermore, the distributions of D:G ratios used in calculating the averages

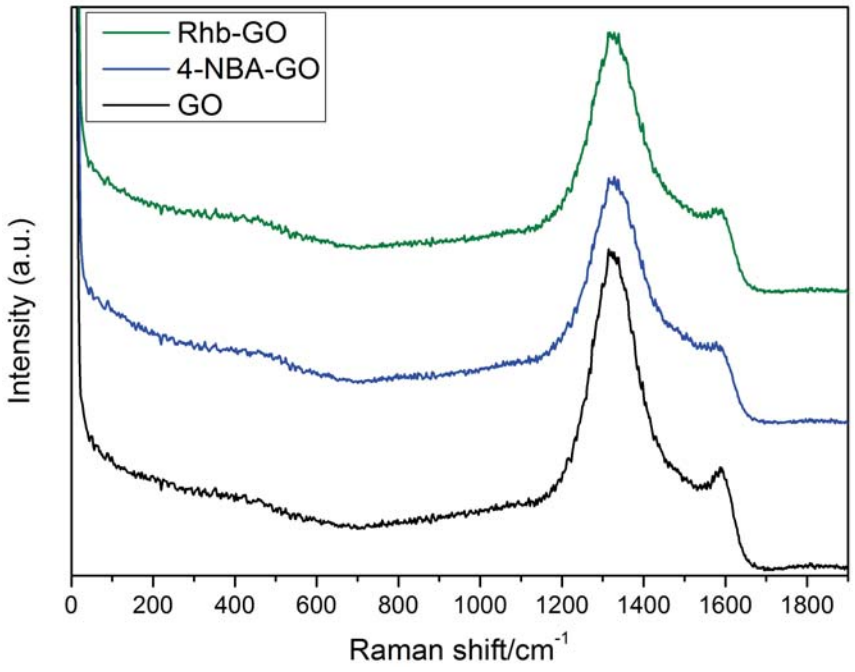

Figure 87: Raman spectra of GO and modified GO samples acquired with 785 nm excitation.

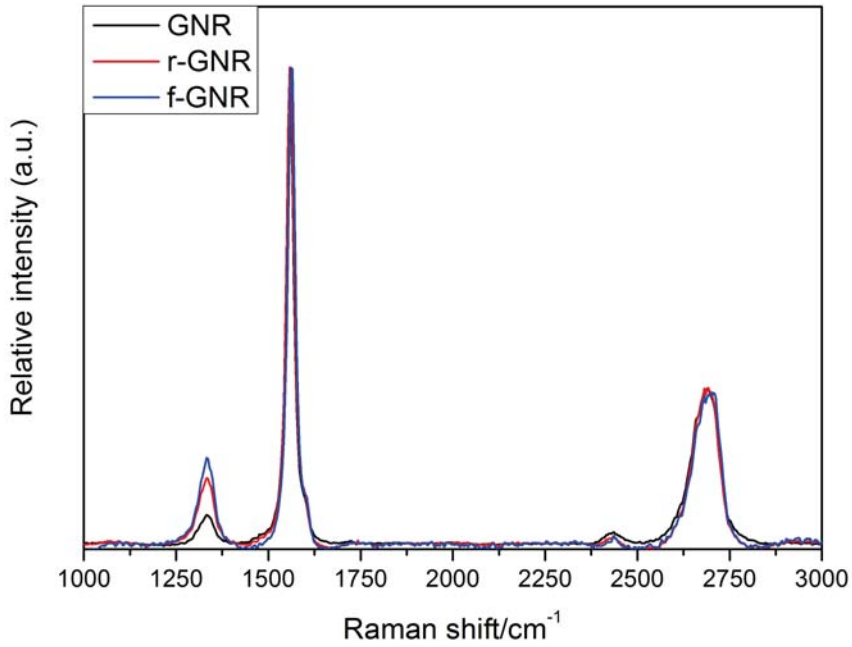

Figure 88: Raman spectra of as-cut GNR, GNR reduced with $NaBH_4$ and GNR modified with 4-ABA. Spectra were acquired with 532 nm excitation. Each spectrum shown is actually the average of five spectra taken at different positions on the sample. The spectra have been normalised to the intensity of the G band.

for each sample did not overlap significantly, which would suggest that the differences are indeed due to real differences between samples. Other than the D band differences, the spectra appear very similar with no Raman bands unique to any of the samples.

Shown in figure 89 are the FTIR spectra of a new batch of r-GNR samples, includ-

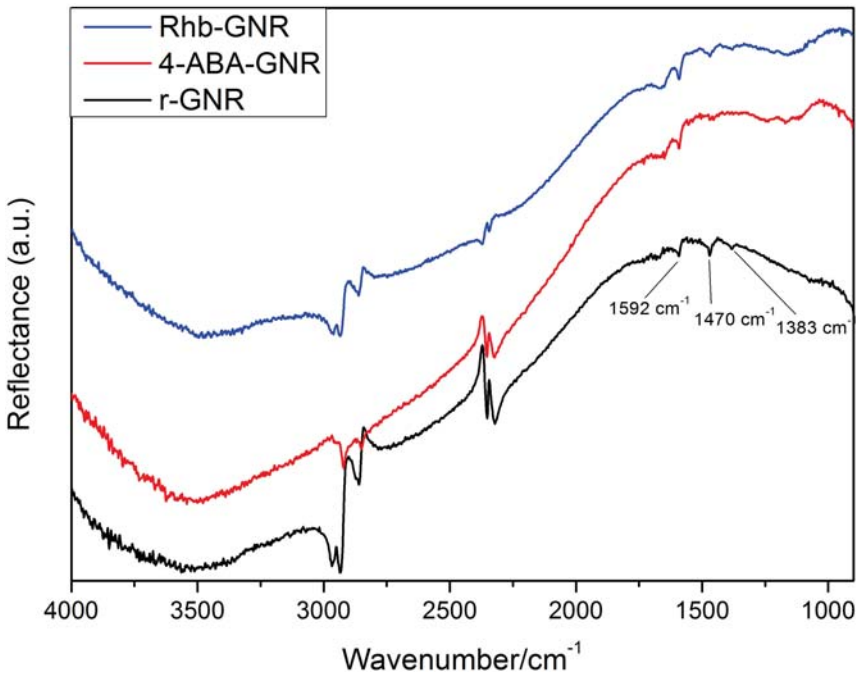

Figure 89: ATR-FTIR spectra of r-GNR, 4-ABA-GNR and RhB-GNR.

ing those edge-functionalised with 4-ABA and RhB. Weak bands around 1650 cm^{-1} are present in all the spectra, which have been assigned to the vibrational mode of adsorbed water molecules on graphene.[148] Interestingly, r-GNR and RhB-GNR have bands around 1470 and 1383 cm^{-1} that are absent for 4-ABA-GNR. There are few other differences in the spectra.

Raman spectra of the same samples are shown in figure 90. Though there are no apparent differences in the appearance of Raman bands between the different samples, there is definitely a higher background in RhB that suggests fluorescence. This background did not diminish after further purification, suggesting that it could indeed be due to RhB attached to the GNR edges or otherwise RhB strongly adsorbed to the graphene basal plane. Additionally, there are some differences in D:G ratios with the f-GNR samples both consistently giving higher D:G ratios than the r-GNR sample.

In the experiments described so far, GNRs with 100 nm width were used in all the functionalisation reactions. This gives a rather low ratio of edge:basal carbon atoms, which could explain the difficulty in detecting differences between unmodified and edge-functionalised samples via Raman and FTIR so far. Additionally, there were problems with ribbon aggregation and settling out during the reaction, which could further reduce the degree of successful functionalisation. Thus, the next steps were to work on improving the degree of edge functionalisation to allow for easier detection, namely by reducing the ribbon width and introducing gentle sonication during the reactions to keep the ribbons fully dispersed.

GNRs, chopped from an HOPG block at 50 nm width, were reduced with $NaBH_4$

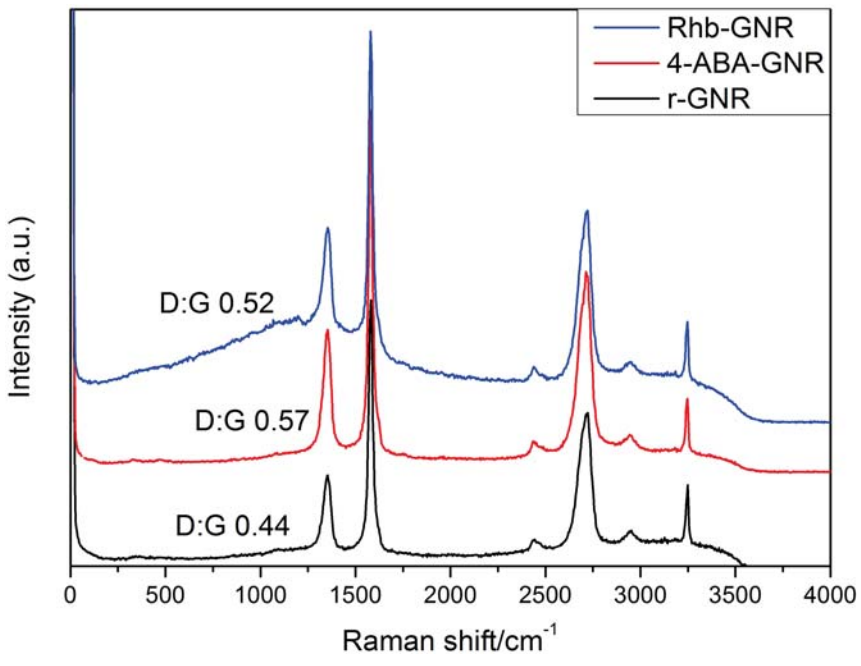

Figure 90: Raman spectra of the samples in figure 89 acquired with 532 nm excitation. The spectra shown are the average of several spectra for each sample.

prior to functionalisation with 4-ABA and RhB. The Raman and FTIR spectra of the series of ribbons are given in figures 91 and 92, respectively. A control for the RhB-GNR was prepared to determine whether the fluorescence observed in the Raman spectrum of the previous RhB-GNR sample was due to residual RhB in the ribbons solution or from RhB attached to the graphene. This control was prepared by mixing r-GNR with the same concentration of RhB as used for functionalisation, followed by purification. The Raman spectra show very few differences between the various ribbon samples. The only substantial difference observed is in the spectrum of RhB-GNR, which has a weak fluorescence background. This background was barely observed in the RhB control sample, hence it is possible that it could be coming from dye molecules attached to the graphene. There are only minor variations in D:G ratios between samples, with the RhB-GNR and control sample giving slightly higher D:G ratios than the other samples. Similarly, there are no significant differences between the FTIR spectra of the samples, except that the RhB-GNR appears to have a very weak possible peak at ~ 1730 cm^{-1}. This band is in the range for a C=O stretch and does not appear in the IR spectrum of RhB, hence is not due to unattached dye molecules and thus could be due to the formation of an ester bond with the graphene via the EDC coupling reaction. However, the signal-to-noise ratio is so low that it is inconclusive as to whether this is actually a real peak or not. Combined with the Raman data though, this could indicate successful functionalisation.

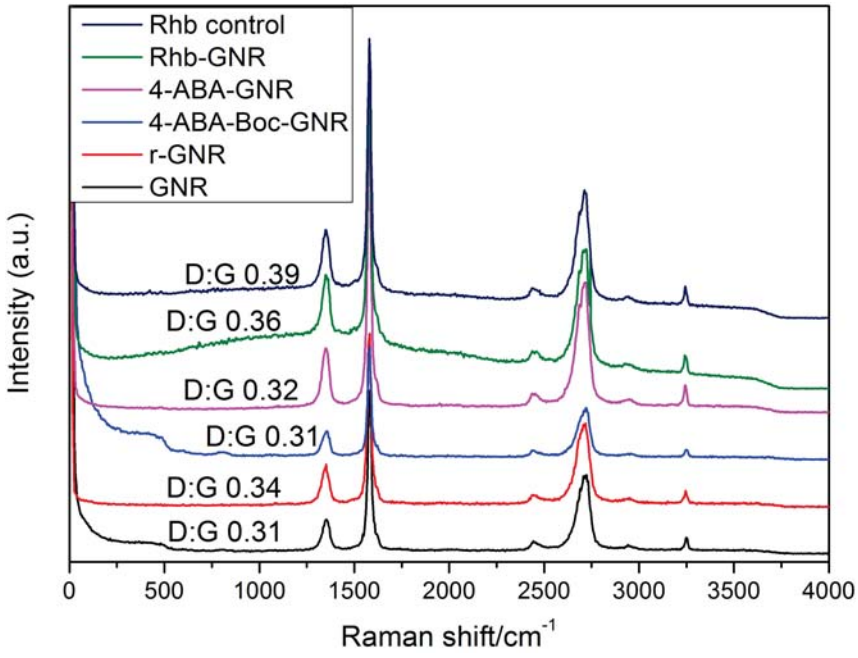

Figure 91: Raman spectra of 50 nm modified and unmodified GNR samples acquired with 532 nm excitation.

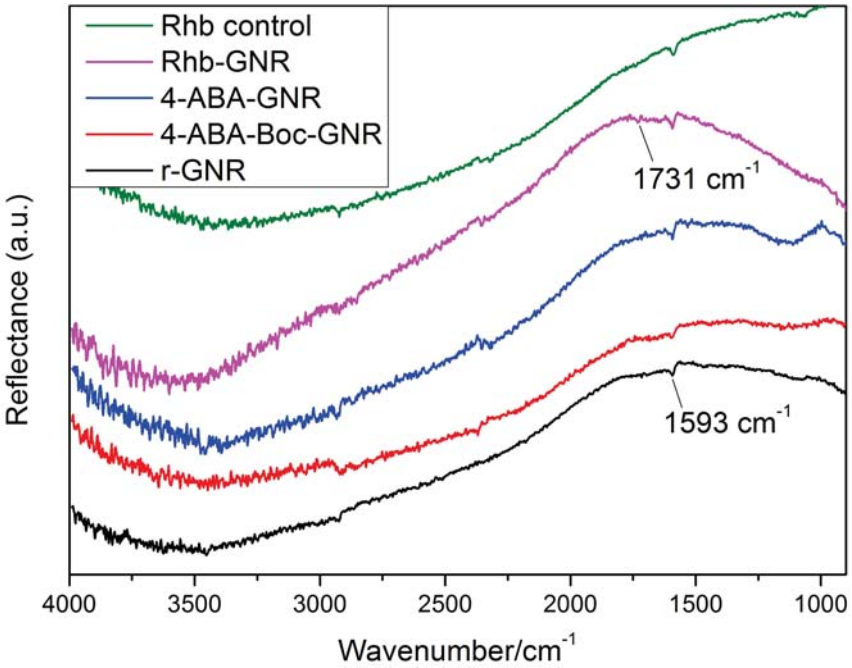

Figure 92: ATR-FTIR spectra of 50 nm r-GNR with various edge modifications.

5.2.2 Amide Coupling

The previous section explored reactions targeted to edge hydroxyl groups of GNRs. However, it is likely that the edges also contain a significant proportion of carboxyl groups. Thus, the next strategy was to target these groups for amidation reactions. The sulfate or sulfonic acid group is a good candidate for edge functionalisation as it is strongly acidic and thus easily deprotonated within a wide pH range ($3 - 10$) to yield a negative charge.[151] Numerous procedures are detailed in the literature for the sulfonation of graphene oxide. A common approach employs diazonium chemistry using the diazo salt of sulfanilic acid.[146,151–156] Other methods include EDC/NHS coupling through the formation of an amide bond between the amino group of sulfanilic acid and carboxyl/epoxide groups of GO[157], and sulfonation by fuming sulfuric acid[158–161]. A procedure for the sulfation of GO (as opposed to sulfonation) involves substitution of epoxy and/or OH groups attached to the graphene with sulfate groups via treatment with fuming sulfuric acid.[162]

A general procedure for the edge-functionalisation of GNRs via an amidation reaction was adapted from established methods for the sulfonation of graphene oxide.[146,157] This was applied to sulfonation of GNR edge COOH groups, employing the EDC/NHS coupling system for amide bond formation. The role of EDC and NHS in the amide coupling reaction is shown in figure 93. The role of EDC/NHS is to activate the carboxyl group to make it more electrophilic and thus more susceptible to attack by the primary amine. Upon addition of the carboxyl OH group across one of the double bonds of the carbodiimide EDC, the activated O-acylurea is formed.[163] This intermediate can react directly with the primary amine, however it is not very stable and can undergo rearrangement via intramolecular acyl transfer to yield an N-acylurea, as shown in figure 94. Hence, NHS is included to compete with this reaction and form a more stable intermediate that can react with the primary amine to form an amide bond.

The EDC/NHS amide coupling method was tested on graphene oxide which has an abundance of oxygen-containing groups, including carboxylic acids. This method was derived from the procedure given by Zhang et al.[157] for the sulfonation of GO via reaction

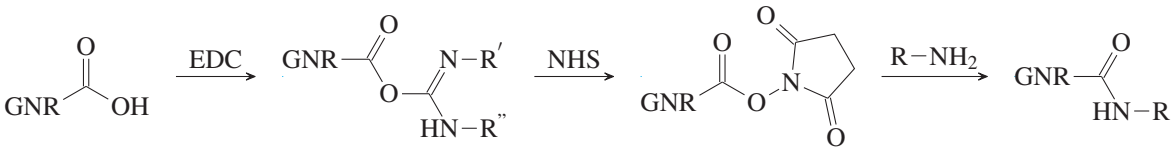

Figure 93: Reaction scheme for the amidation of GNR COOH groups.

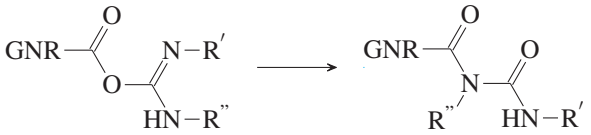

Figure 94: Rearrangement of the O-acylurea intermediate to form an N-acylurea.

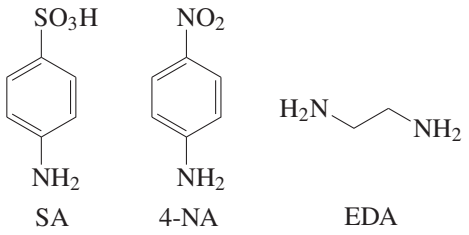

Figure 95: Chemical structures of the modifiers used in the amide coupling reactions.

of COOH groups with sulfanilic acid (SA) (see figure 95), a study that employed FTIR spectroscopy to prove the introduction of SA functional groups onto the GO sheet and XPS analysis to show a clear shift from carboxyl groups to amide linkages, confirming that these SA groups were covalently grafted. IR spectra of GO and GO functionalised with sulfanilic acid and 4-nitroaniline using a similar EDC/NHS amide coupling method are shown in figure 96. For both SA and 4-NA, functionalisation introduces new bands in the spectrum. A group of bands in the region $1000-1200$ cm^{-1} are apparent in the spectrum of the sulfonated sample, which are absent in the other samples. These bands show excellent agreement with the literature for sulfonated graphene oxide[146,157]. These bands occur at $\sim$ 1211, 1177 (S-phenyl stretch), 1122 (asymmetric SO_3 stretch), 1031 (symmetric SO_3 stretch) and 1008 (in-plane C-H bending) cm^{-1}. For 4-NA, however, the new bands are much more broad, contrary to the sharp, intense nitro bands that would be expected. These broad, noisy bands appear in the region $1300-1500$ cm^{-1}, which is the correct region for the nitro stretch. Weak bands at 2856, 2929 and 2971 cm^{-1} are visible in both functionalised samples and are likely due to aromatic C$-$H vibrations. The clear changes in the spectrum of GO upon reaction with SA and 4-NA provide good evidence to suggest covalent functionalisation. Raman spectra of the GO and f-GO samples are given in figure 97. The Raman spectra of the functionalised and unmodified GO samples all appear very similar with no apparent extra peaks from the attached groups. The D band appears broad and intense and the D:G ratio is high for all samples, characteristic of a high degree of sp^3 hybridisation in the graphene basal plane.

Figures 98 and 99 show IR spectra of GNRs functionalised with SA by the same procedure. Figure 98a shows the spectra of numerous SA-GNR samples from separate batches, and the consistent appearance of the same peaks in all the spectra proves the reliability and reproducibility of the method for edge functionalisation. The sulfonated ribbons show consistent, substantial changes from the spectra of the unfunctionalised control samples (figure 98b), and the peaks match those of SA-GO very well (figure 99a). Figure 99b shows the similarities and differences between the spectra of SA and SA-GNR. The lack of peaks in the IR spectra of control samples (same reaction conditions but with the omission of EDC and NHS) suggests covalent attachment over non-covalent adsorption. This is very good evidence for the success of the functionalisation reaction and would thus suggest that carboxyl groups do indeed have a significant presence at

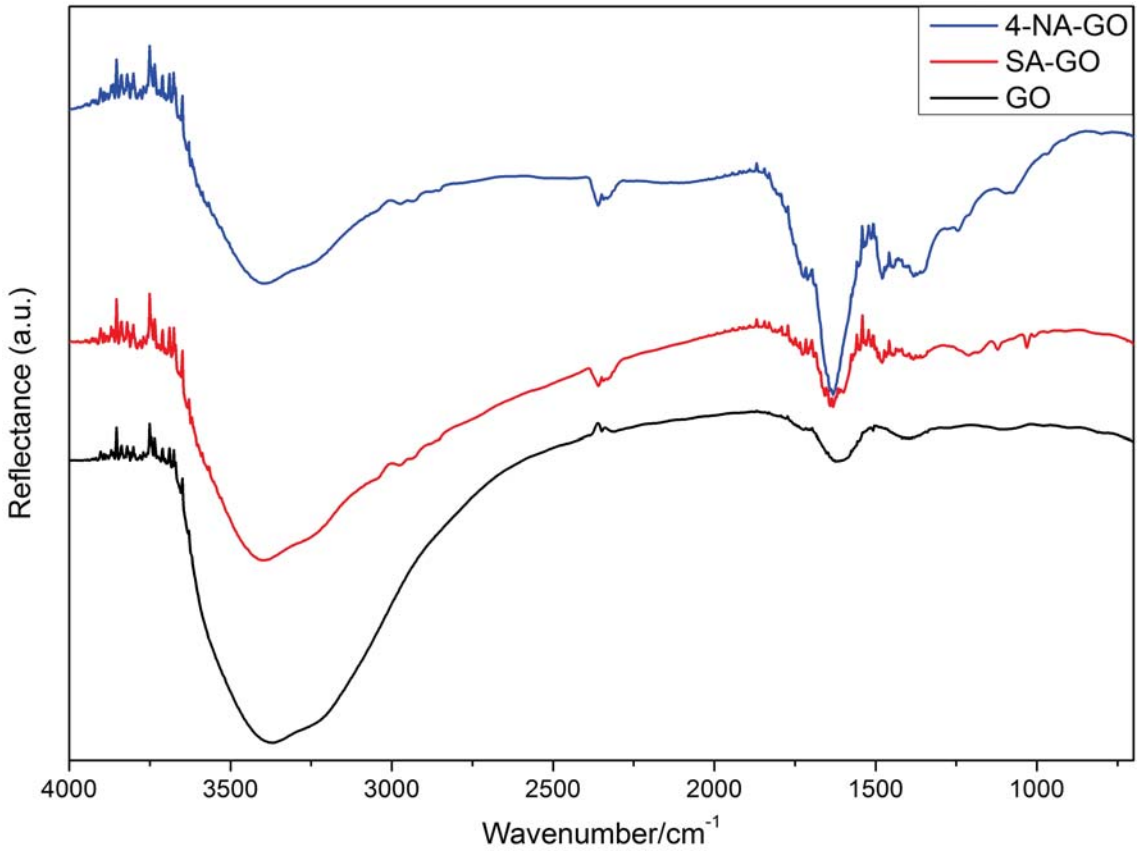

Figure 96: FTIR microscope reflectance spectra of GO and GO modified with SA and 4-NA.

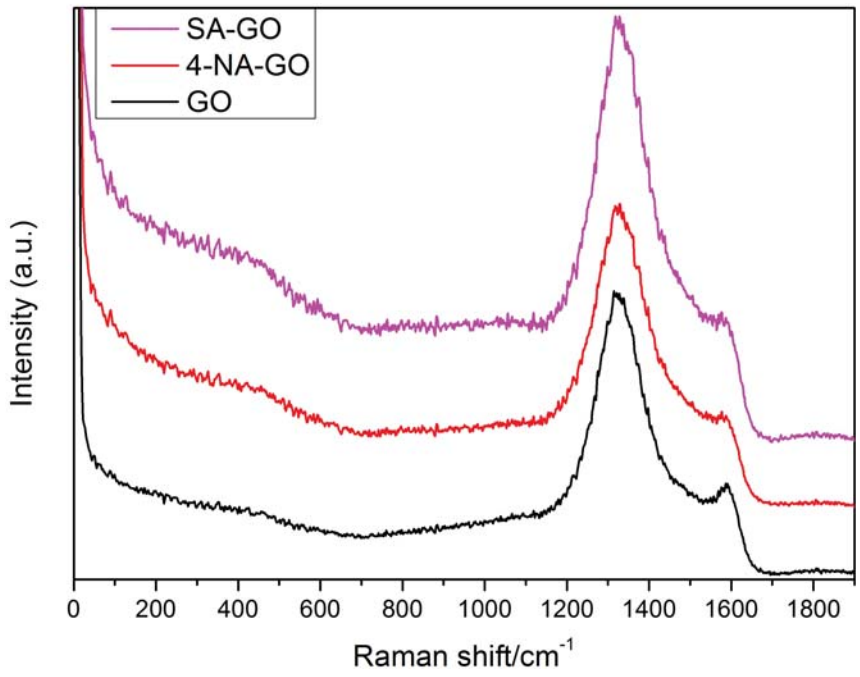

Figure 97: Raman spectra of GO and f-GO samples acquired with 785 nm excitation.

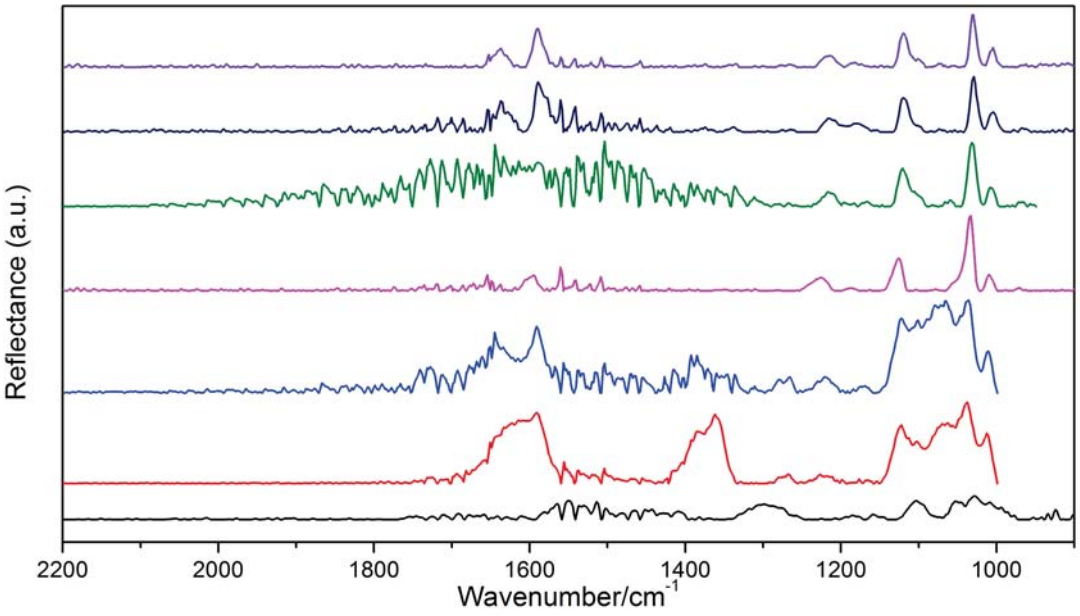

(a)

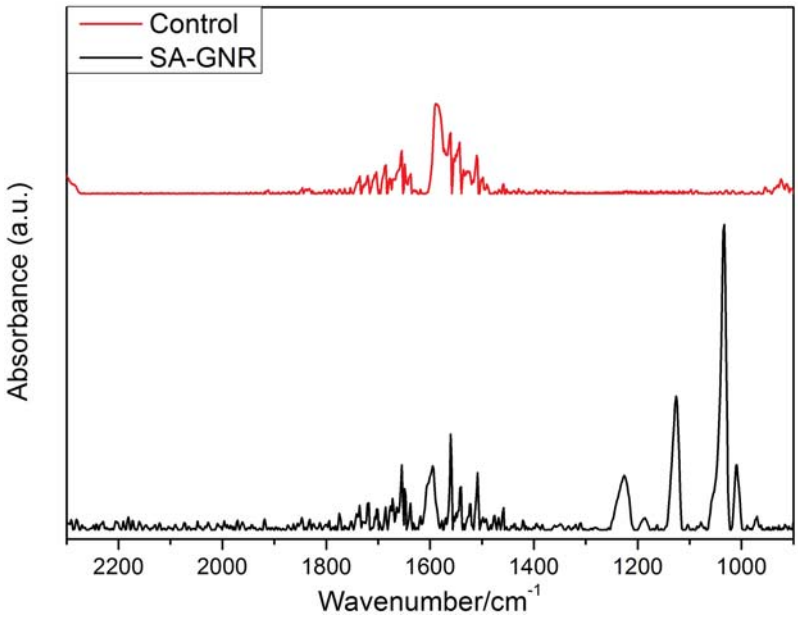

(b)

Figure 98: FTIR microscope spectra of multiple SA-GNR samples produced from different batches of 20 nm and 50 nm GNRsof SA-GNR (a) and comparison of SA-GNR and control sample (b). The IR spectra of GNR samples were taken in reflectance mode, and were Kramers-Kronig transformed and baseline subtracted.

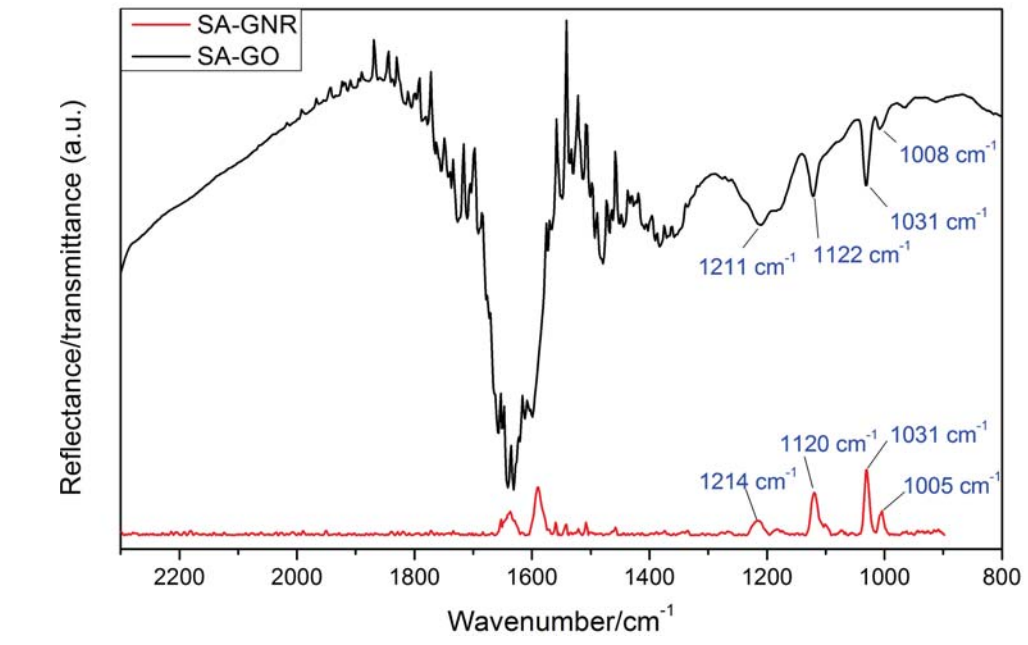

(a)

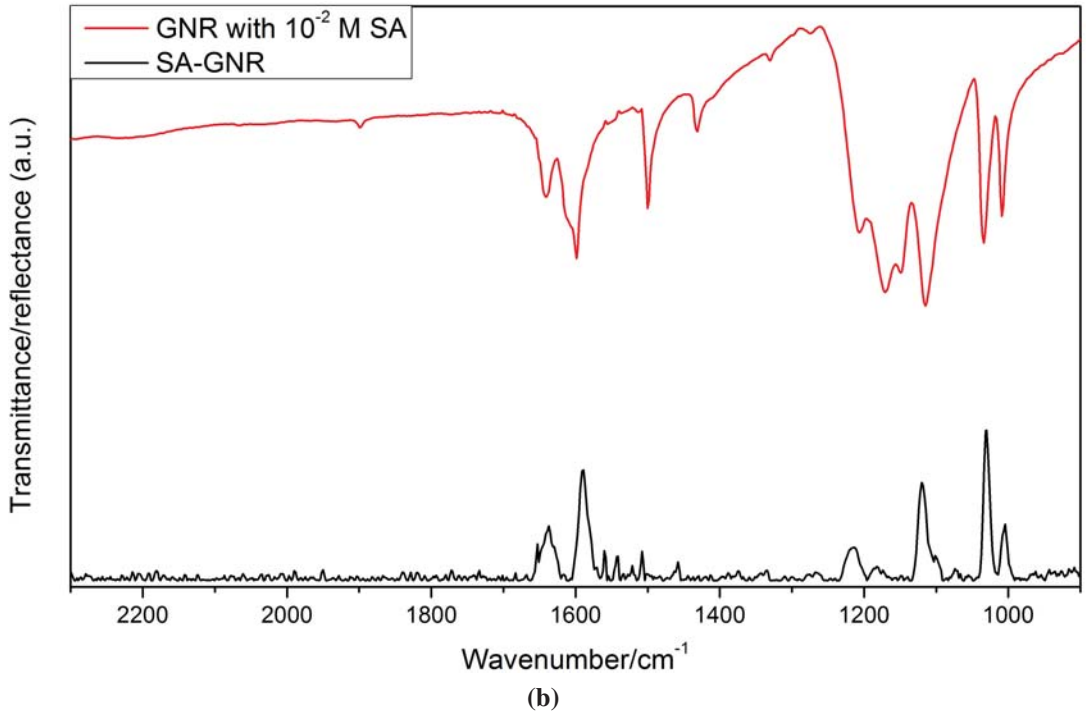

(b)

Figure 99: (a) Comparison of SA-GO and SA-GNR FTIR spectra. (b) Comparison of transmission mode spectrum of SA with spectrum of SA-GNR. The IR spectra of GNR samples were taken in reflectance mode, and were Kramers-Kronig transformed and baseline subtracted.

the edges of GNRs. The Raman spectra of the SA-modified samples are given in figure 100. Unlike for the samples modified via functionalisation of edge OH groups, these samples do not show any increase in D:G ratio upon functionalisation, which confirms that functionalisation is restricted to the edge groups, leaving the pristine basal plane intact.

FTIR analysis of sulfanilic acid-modified GNRs via the EDC/NHS method has given evidence of edge functionalisation. Following this, GNRs with other primary amine-containing modifiers were prepared and the IR spectra of the GNR samples functionalised with these modifiers are given in figure 101. These include 4-nitroaniline (4-NA) and ethyelenediamine (EDA), which is a good candidate as it has a second primary amine available for providing positive charge or undergoing further modification. The IR spectrum of 4-NA-GNR shown in figure 101a displays several prominent peaks between $\sim 900 - 1200$ cm^{-1} that are absent in the spectrum of the unmodified sample. However, these did not show up consistently for different batches of functionalised GNRs and the expected strong nitro peaks are also not apparent, although there is a high level of water vapour background in the region where these peaks would be expected to appear. The IR spectrum of GNRs modified with EDA shown in figure 101b affords very little evidence of successful functionalisation, with no obvious peaks belonging to the attached EDA, however the background is rather noisy, particularly in the region around $1300 - 1700$ cm^{-1} due to residual water vapour. Shown in figure 101c is the IR spectrum of EDA-GNR further modified with RhB via ester bond formation between the free amine group of EDA-GNR and the carboxyl group of RhB. Similarly to EDA-GNR, no strong peaks characteristic of RhB are visible in the spectrum. Shown in figure 102 are the Raman

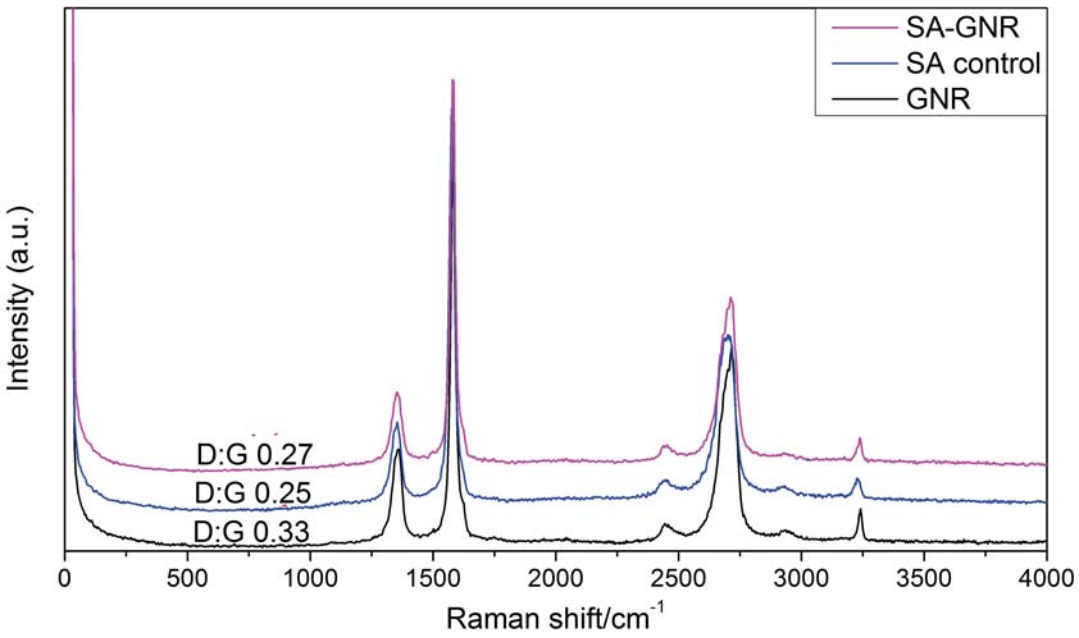

Figure 100: Raman spectra of 20 nm GNR samples acquired with 532 nm excitation.

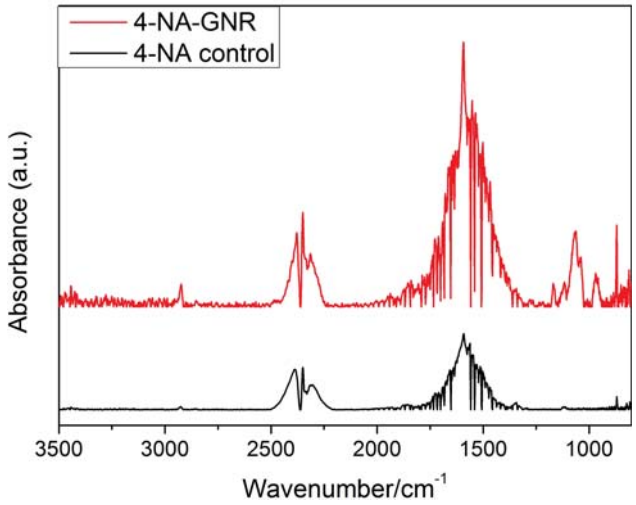

(a)

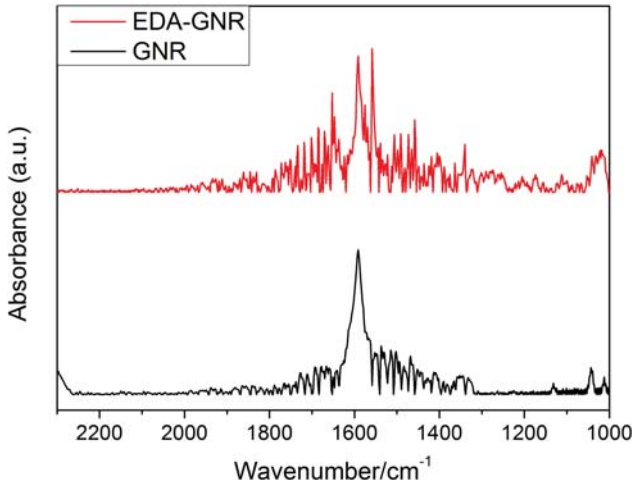

(b)

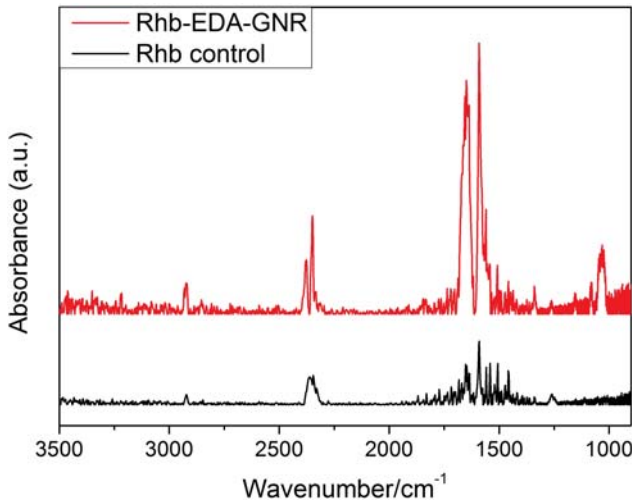

(c)

Figure 101: FTIR microscope spectra of 20 nm f-GNR. The IR spectra were taken in reflectance mode, and were Kramers-Kronig transformed and baseline subtracted. Note that the strong bands around 2600-2700 cm^{-1} are due to CO_2 absorptions.

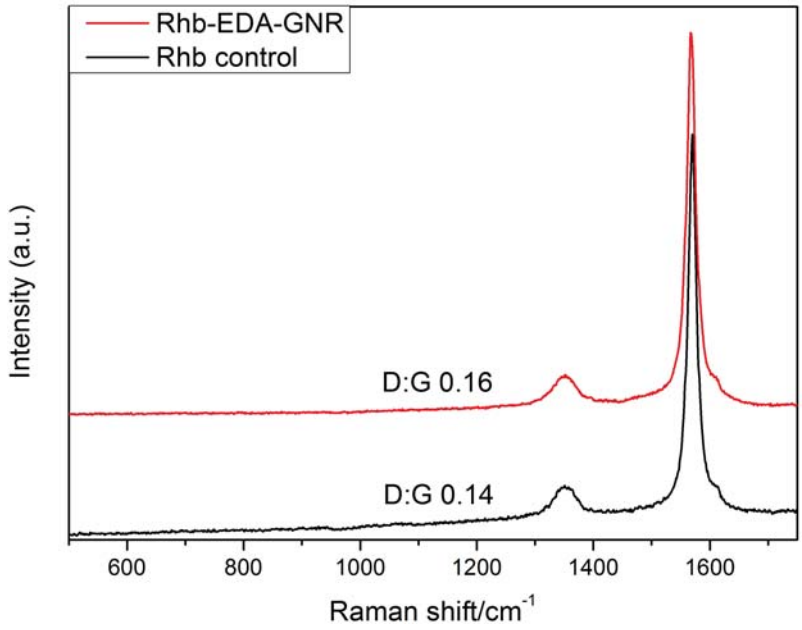

Figure 102: Raman spectra acquired with 488 nm excitation. Spectra shown are the average of several spectra for each sample.

spectra of RhB-EDA-GNR and the control sample for comparison. The spectra of the two samples appear almost identical with very little change in the D:G ratio.

5.2.3 Diazonium Chemistry

So far, edge specificity has been achieved using reactions tailored to specific oxygen-containing groups on the graphene edge (alcohols and carboxylic acids). Another approach to edge-selective functionalisation of GNRs is to use a more non-specific type of reaction that exploits the higher comparative reactivity of the edges to achieve edge specific functionalisation. This may allow for a higher density of edge functional groups to be attained. Furthermore, analysis of D:G ratios from Raman spectroscopy should allow for the determination of the relative edge:basal plane reactivity to the functionalising reagents. Specificity can be further enforced by limiting the exposure of the basal plane so that only the edges are available for reaction. This can be done by performing the reaction prior to exfoliation of the ribbons. It was reasoned that diazonium chemistry would be a good option for this as previous studies have shown that this is effective in grafting aryl groups, such as nitrophenyl, to graphene.[145]

GNRs were modified with the BF_4^- diazonium salts of 4-nitroaniline and sulfanilic acid, using a procedure adapted from the method reported by Downard et al.[141] Solutions of the diazonium salts were mixed with either pre-sonicated solutions of GNRs or solutions of GNBs as cut directly from an HOPG block without exfoliation. For the GNR solutions, the reactions were run under mild sonication, and for the GNB solutions, under stirring. Figure 103 shows the FTIR microscope spectra of several samples of GNRs modified with sulfophenyl (SP) groups via the diazonium route. The spectra are reasonably consistent between samples, with the peaks at $\sim$ 1034 and 1005 cm^{-1}, indicative of the SP group[146], appearing in all spectra. The intensity of the peaks is rather low for all

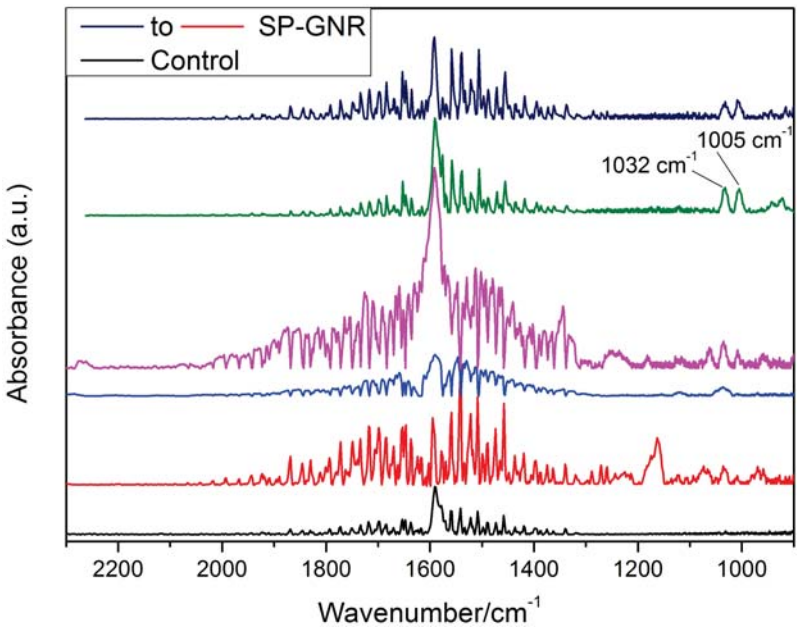

Figure 103: FTIR microscope spectra of 20 nm GNR modified with SP groups. The IR spectra were taken in reflectance mode, and were Kramers-Kronig transformed and baseline subtracted.

samples, suggesting possibly a lower degree of functionalisation than that attained via the amidation route.

FTIR spectra of GNRs modified with the diazonium salt of 4-NA are given in figure 104. Figure 104a shows spectra of ribbons modified after exfoliation, in which the diazonium salt is not prevented from interacting with the basal plane. Peaks at ~ 1350 and 1525 cm^{-1} are present in the spectra of all modified samples, which are in excellent

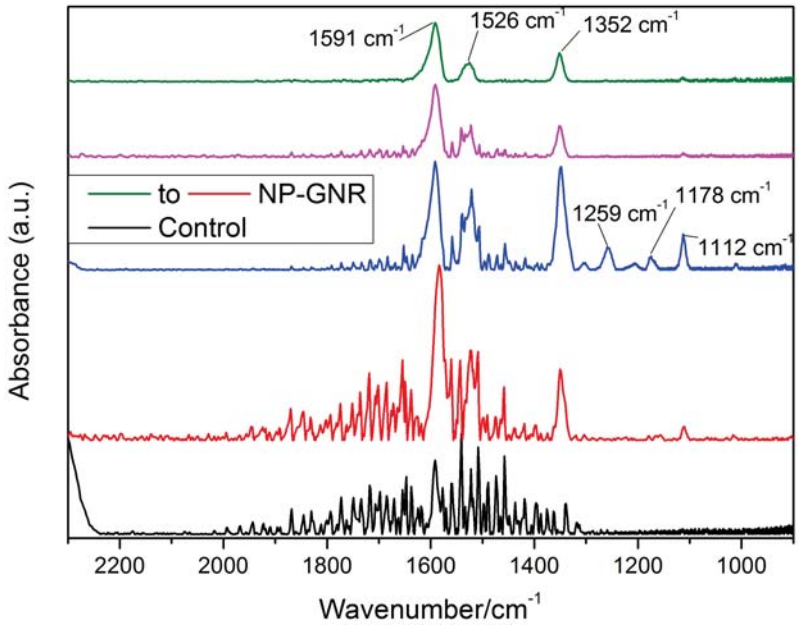

(a)

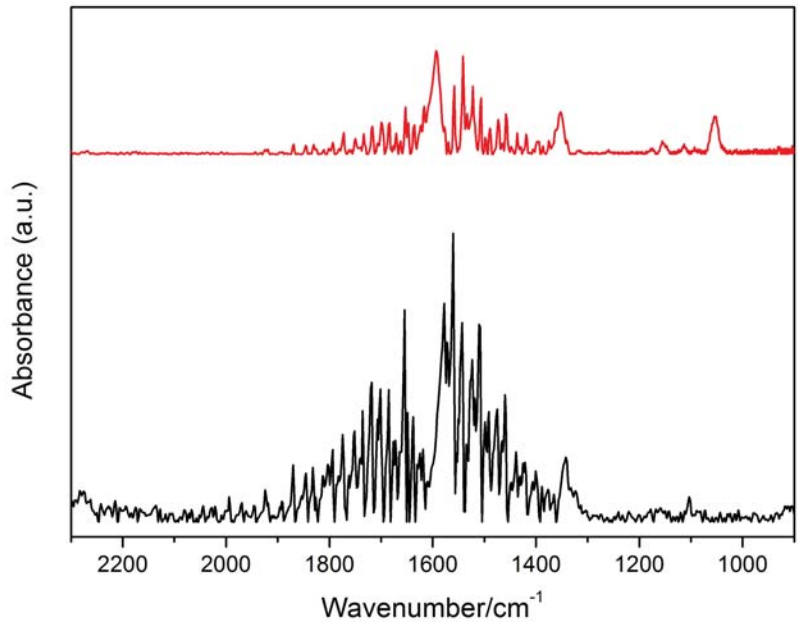

(b)

Figure 104: FTIR microscope spectra of 20 nm GNR modified with NP groups (a) with exfoliation and (b) without exfoliation. The IR spectra were taken in reflectance mode and were Kramers-Kronig transformed and baseline subtracted.

agreement with the results reported by Downard et al.[145] for the aryldiazonium modification of CVD few-layer graphene with nitrophenyl (NP) groups. These results suggest successful grafting of NP to GNRs. The peaks at 1350 and 1525 cm^{-1} can be assigned to symmetric and asymmetric stretching modes of the nitro group, respectively. Additional, weaker bands below 1300 cm^{-1} appear in some of the spectra at lower intensity. These are the bands at $\sim$ 1260, 1180 and 1110 cm^{-1}, which have also been reported in the study on aryldiazonium modification of CVD graphene.[145] Figure 104b shows FTIR spectra of GNBs modified with NP groups without pre-exfoliation. The nitro bands are notably weaker than in the exfoliated samples, indicating a lower degree of functionalisation. This is likely due to reduced exposure of the basal plane limiting functionalisation to the edges, and suggests that ribbon stacking in GNBs is effective in preventing reaction with the basal plane sp^2 carbon atoms.

Raman microscopy is a useful tool for investigating the reactivity of aryldiazonium ions with the edge and basal plane carbon atoms, as the D:G ratio is sensitive to the level of sp^3 carbon atoms. Figure 105 shows the Raman spectra of SP-GNR and NP-GNR samples produced via the diazonium route. Although no features from the introduced modifiers are observed in any of the spectra, the D:G ratios show some interesting results. Both SP and NP modification of exfoliated GNRs result in only minor changes in D:G ratios, suggesting that functionalisation occurs predominantly at the edges. Furthermore, no increase in D:G ratio is observed between reactions with un-exfoliated GNBs and exfoliated GNRs (figure 106), suggesting that greater exposure of the basal plane does not necessarily result in a higher detectable level of functionalisation of the basal plane. This would suggest that functionalisation is limited almost exclusively to the edges of GNRs. This may seem contrary to the FTIR results, which suggested that exfoliation leads to a higher degree of functionalisation. However, this can be explained by considering that exfoliation could also serve to increase the edge exposure, leading to a higher degree of edge functionalisation without increasing reaction with the basal plane.

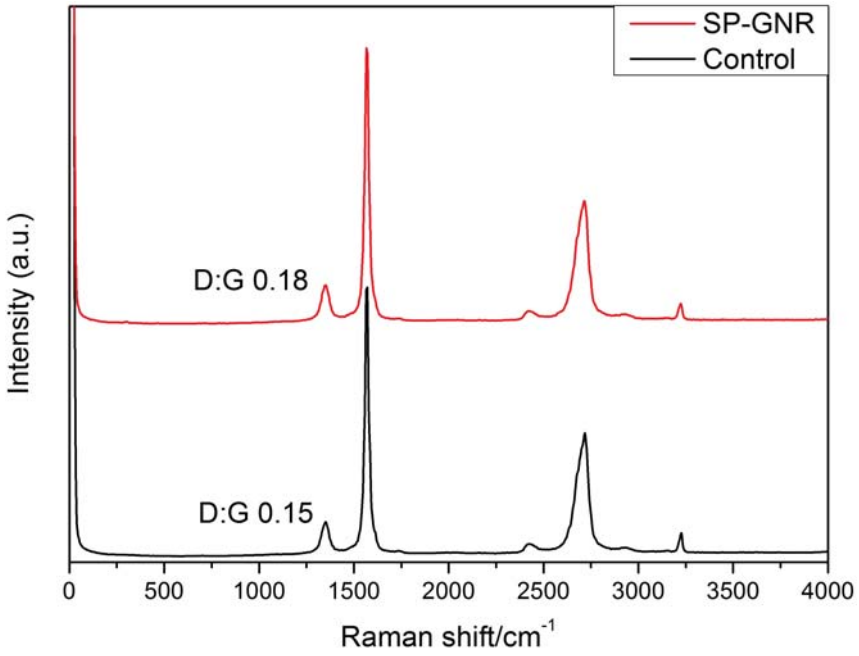

(a)

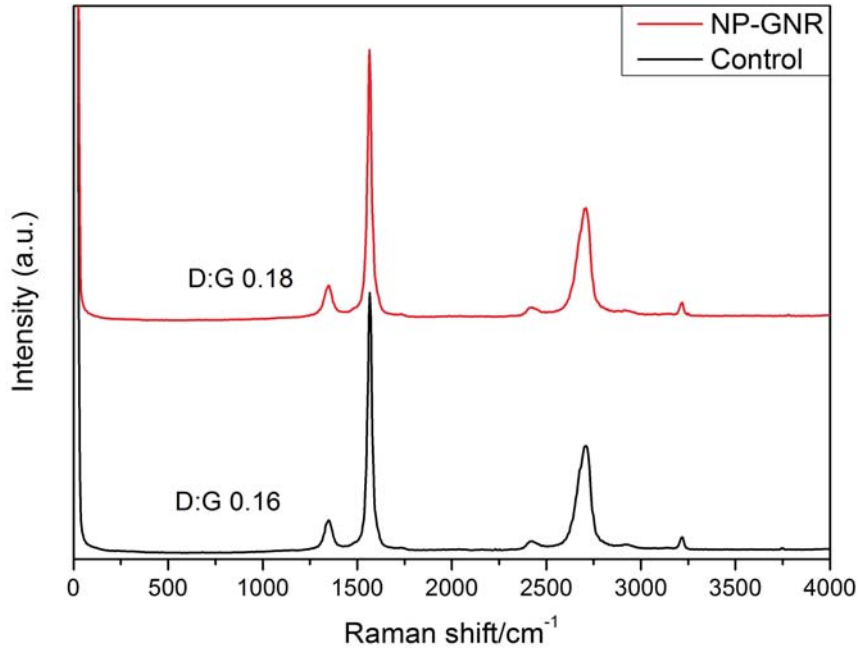

(b)

Figure 105: Raman spectra of 20 nm GNR modified with (a) SP and (b) NP groups. Spectra were acquired with 488 nm excitation. All spectra shown are the average of several spectra for each sample.

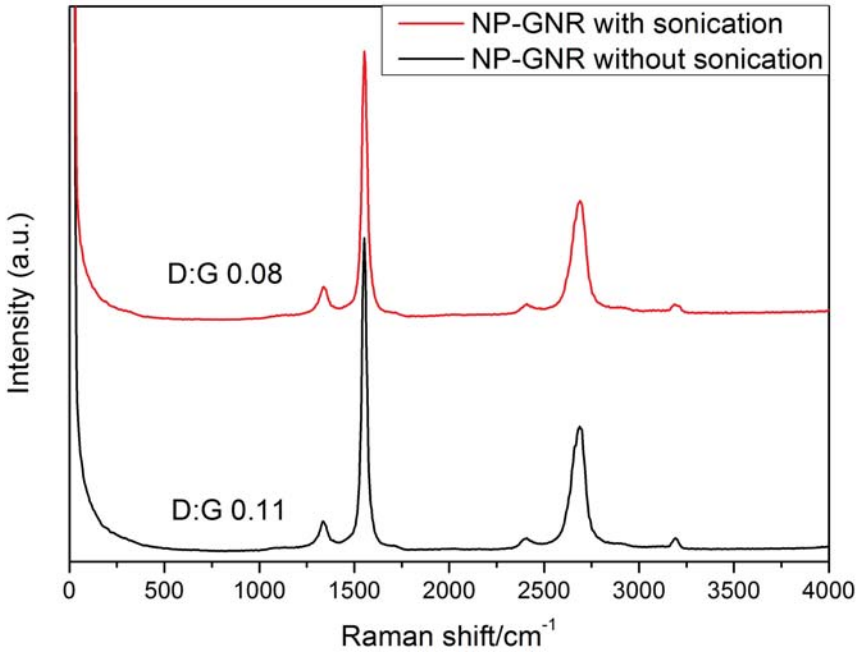

(a)

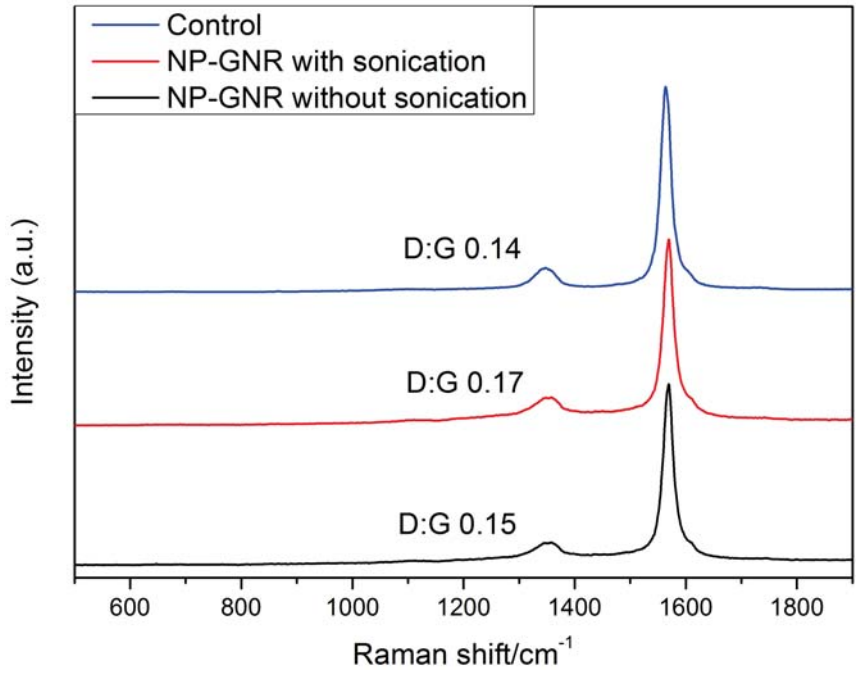

(b)

Figure 106: Comparison Raman spectra of 20 nm GNR modified NP groups, with and without sonication. Spectra were acquired with 488 nm excitation. All spectra shown are the average of several spectra for each sample.

5.2.4 SERS

As shown in the previous sections, non-enhanced Raman microscopy is not sensitive enough to detect GNR edge functional groups directly through signals from the groups themselves, rather it is only useful for distinguishing reactions at the edge from reactions in the basal plane via changes in carbon atom hybridisation. Thus, SERS presents a more sensitive adaptation of normal Raman that should allow for the edge groups to be probed directly via enhancement of their Raman signals. This technique has some challenges experimentally, as a suitable roughened metal substrate is required for providing enhancement of the electric field, and this substrate must be compatible with the strongly hydrophobic GNRs. The first attempt at producing such a substrate was based on a procedure for the formation of superhydrophobic surfaces[164], which involved depositing a rough metal coating of Ag or Au onto a polished Cu or Zn surface via immersion of a metal into a solution of $AgNO_3$ or $HAuCl_4$, followed by SAM formation with a perfluorinated alkanethiol. The result is a superhydrophobic surface that mimics the lotus leaf in its water-repelling nature. The same roughened, nanostructured metal surface that helps to give these materials their superhydrophobic nature should also be ideal for providing the SPR (surface plasmon resonance) enhancement in SERS experiments. A trial run with Ag and Au superhydrophobic subtrates prepared by this method was performed to see if they could provide SERS enhancement for a thin layer of GNRs. However, no substantial SERS enhancement was found, and the substrate gave a high level of scattering background in the Raman spectra that nullified any enhancement effects.

In a second approach, Ag nanoparticles (Agnps) synthesised by the method by Kitaev et al.[115] were used to provide SERS enhancement of GNRs on a quartz substrate. This simple, yet elegant method for Agnp production allows for tailoring of the size and shape of the nanoparticles, thus enabling the SPR frequency to be controlled.[116] The nps were mixed with solutions of GNRs and deposited onto a quartz substrate, which is an ideal substrate as it has almost no background in its Raman spectrum. However, the nps are prepared with sodium citrate caps to stabilise them, thus they are hydrophilic and would be expected to have low affinity for GNRs. This problem was overcome by sonicating the GNRs in a solution of CTAB, which stabilises the ribbons and provides a positive charge, giving them a much greater affinity for the negatively charged Agnps.

The SERS spectrum for a dilute solution of Rhodamine 6G (R6G) mixed with Agnps and dried onto a quartz substrate is given in figure 107a. This test sample has strong Raman bands even at a dye concentration of 10^{-8} M, indicating strong SERS enhancement by the Agnps. Figure 107b shows SERS spectra of NP-GNR produced via the diazo route. The spectra shown were taken as 1 second ”snapshots” and show strongly varying Raman peaks, which tended to pop up and disappear. Longer integration times resulted in averaging of all the peaks to produce a spectrum with two broad humps centred around 1300

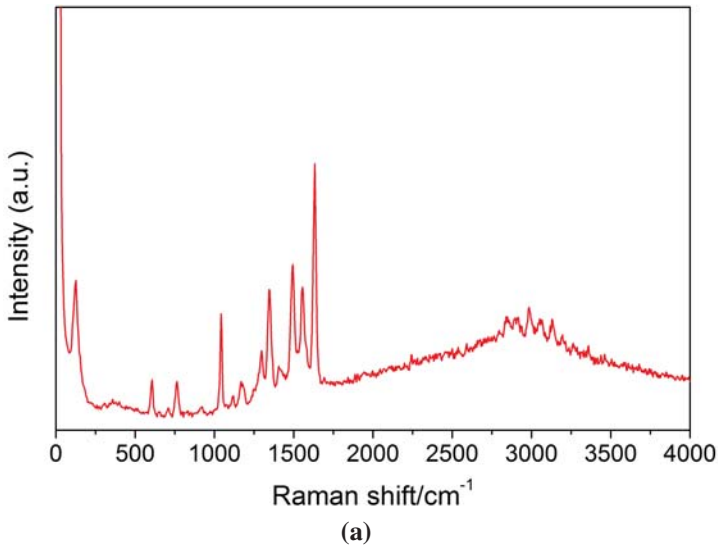

(a)

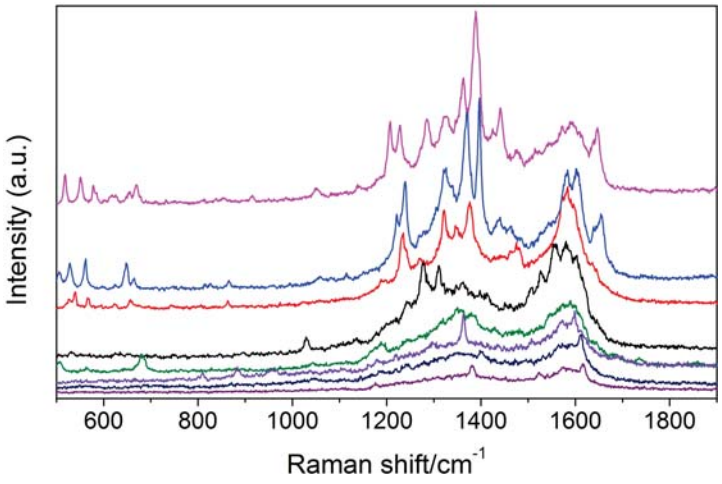

(b)

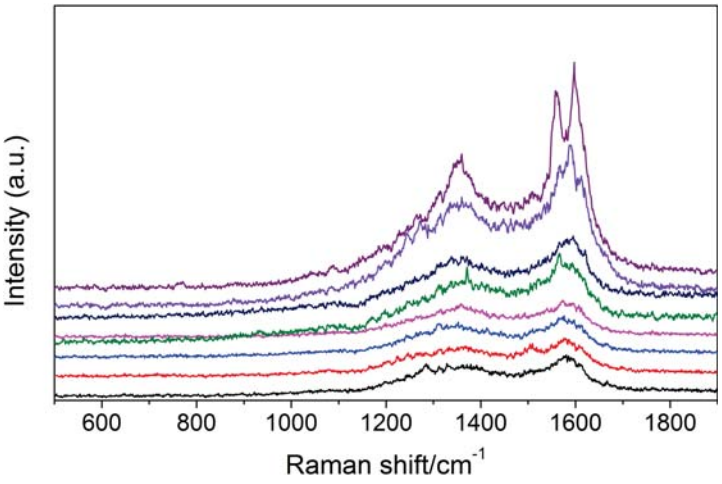

(c)

Figure 107: SERS spectra acquired with 488 nm excitation. (a) Spectrum of a solution 10^{-8} M R6G mixed with Agnps and dried on quartz. (b) Spectra of NP-GNR exfoliated in CTAB solution, mixed with Agnps and dried onto quartz. (c) Spectra of unmodified GNR exfoliated in CTAB solution, mixed with Agnps and dried onto quartz

and 1500 cm^{-1}, which can be attributed to the Agnps. For comparison, the SERS spectrum of unmodified GNR as a control sample is shown in figure 107c. Significantly fewer sharp SERS bands are observed in this control, suggesting that the numerous peaks observed in figure 107b are likely to be due to attached NP groups, as all other experimental conditions were the same.

Figure 108 shows a similar SERS experiment done with RhB-EDA-GNR (GNR functionalised with EDA via amidation, followed by further functionalisation of amine groups with RhB via amidation). Numerous SERS peaks are observed in the spectrum of the functionalised sample, and like NP-GNR, these peaks are transient with the SERS spectrum constantly changing. The control sample also shows several strong SERS peaks, suggesting that traces of the functionalising reagents may still be present after purification.

In a second batch of NP-GNR samples, the SERS spectra obtained were found to be much more stable with repeat measurements over longer integration times giving consistent spectra (although the overall SERS intensity does change), as shown in figure 109. Numerous SERS peaks are observed in the spectra, and to confirm that these bands are not simply due to traces of unreacted 4-nitrobenzene diazonium ions or 4-nitroaniline, the Raman spectrum of 4-NA is included for comparison and this shows different bands than the modified GNR samples. This confirms that the strong SERS bands observed in the modified samples can be attributed to attached NP groups with good confidence. This shows good agreement with the FTIR and Raman results presented in the previous section.

In this study, SERS has provided some useful, though in some cases somewhat tenuous, data to complement the previous FTIR and Raman results. Obtaining reproducible, consistent spectra is a familiar problem with SERS, and in only one case (figure 109) were reproducible spectra obtained for a f-GNR sample. Similarly, the FTIR and Raman results already presented provide only weak evidence of functionalisation when considered individually, however it is only when all the data is considered collectively that a convincing argument for successful edge modification emerges.

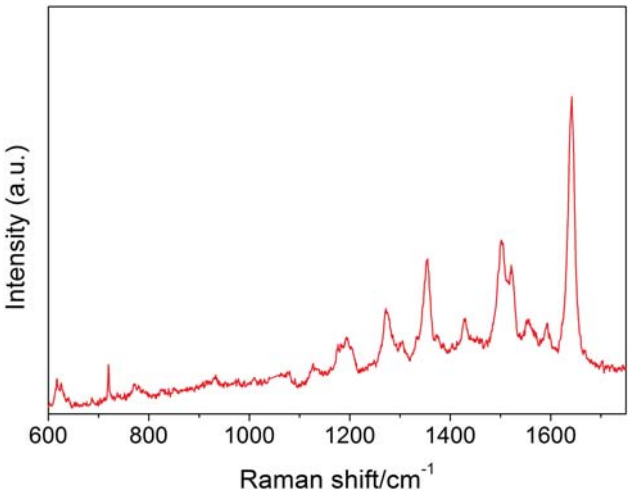

(a)

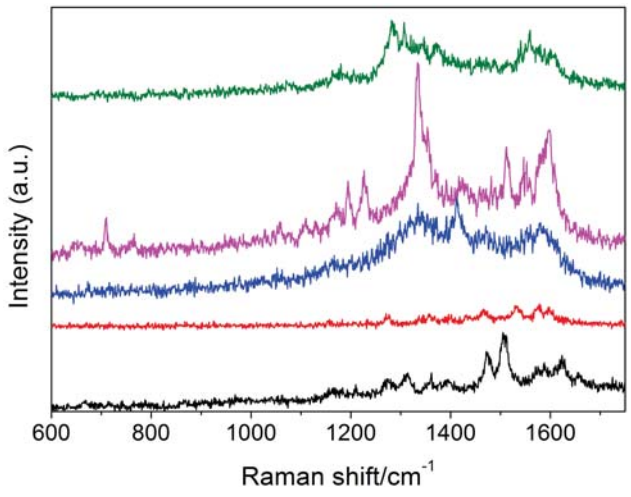

(b)

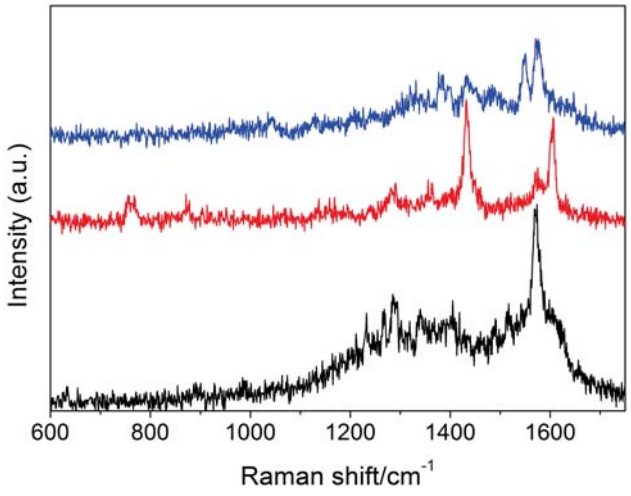

(c)

Figure 108: SERS spectra acquired with 532 nm excitation. (a) Spectrum of Rhodamine B. (b) Spectra of RhB-EDA-GNR. (c) Spectra of RhB control GNR sample.

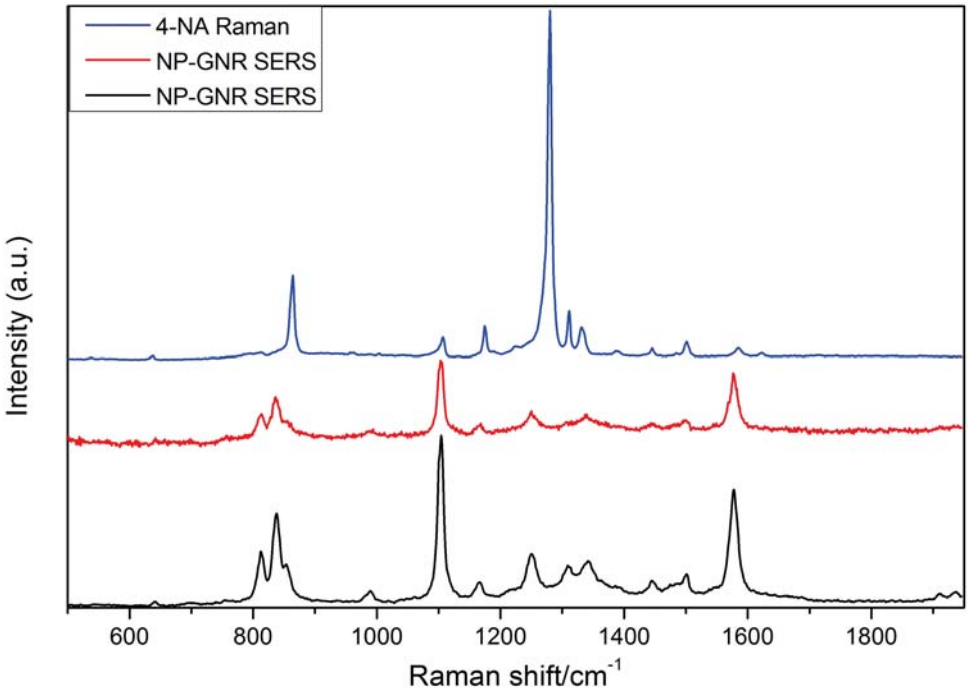

Figure 109: Raman and SERS spectra of 4-NA and NP-GNR samples acquired with 488 nm excitation.

5.2.5 THz Spectroscopy

THz spectroscopy, also known as far-infrared (far-IR) spectroscopy, is a powerful and sensitive tool for detecting the vibrations of weak bonds in crystals, such as hydrogen bonds.[165,166] It was reasoned that THz spectroscopy could be useful in probing the possible interactions between GNR edge functional groups able to participate in intermolecular bonds, particularly hydrogen bonds whose vibrational frequencies typically lie in the far-IR, and could provide valuable additional data to the FTIR results already obtained. For this reason, the Far-IR beamline at the Australian Synchrotron was employed to probe the interactions between the edges of functionalised GNRs. As well as being a useful tool for identifying the presence of edge groups containing hydrogen bond donor/acceptor groups, this could also have important implications into how these interactions might be used to control self-assembly.

The ratio of edge:basal plane carbon atoms in GNRs of 20 nm width is approximately 1:100, thus sensitivity to any modifications of the edges was expected to be low and any differences in far-IR spectra expected to be small, if detectable. It was reasoned that a large library of ribbons with a variety of different edge modifications would be needed to detect any small differences and correlate them with changes in edge structure and chemistry. This library of ribbons consisted of unmodified ribbons, reduced ribbons and ribbons edge-modified with a variety of different groups able to participate in hydrogen-bonding interactions (intramolecular and intermolecular). Figure 110 shows some of these edge modifications. The multi-carboxylated molecules TMA (trimesic acid) and BTB (benzene 1,3,5-tribenzoic acid) were used to increase the edge density of COOH groups for hydrogen-bonding interactions and further modification, in an effort to boost any possible vibrational signals in the far-IR. Ribbons modified with hydrogen-bond donor or acceptor groups would be expected to participate in hydrogen bonding interactions under the right conditions (e.g. pH). To investigate this, triethylamine and trifluoroacetic acid were added to some samples to convert carboxylic acids and amines to their salts for comparison.

Time constraints as a result of technical issues with sample preparation prevented data from the whole library of samples from being acquired, and in fact only about a third of the samples were run. Far-IR spectroscopy is a rather unfamiliar characterisation method, and GNRs are not at all typical of the types of samples usually analysed with this technique, thus the preparation methods had to be worked out mostly ad hoc. This involved identifying the best choice of acquisition mode (ATR vs transmission), choice of substrate and means of depositing the sample onto the substrate, and a fair amount of time was spent optimising these factors so that quality data could be obtained.

Figure 111 shows the most promising data acquired from samples prepared on polyethylene wedges for transmission mode. The spectra of unmodified and reduced ribbons are

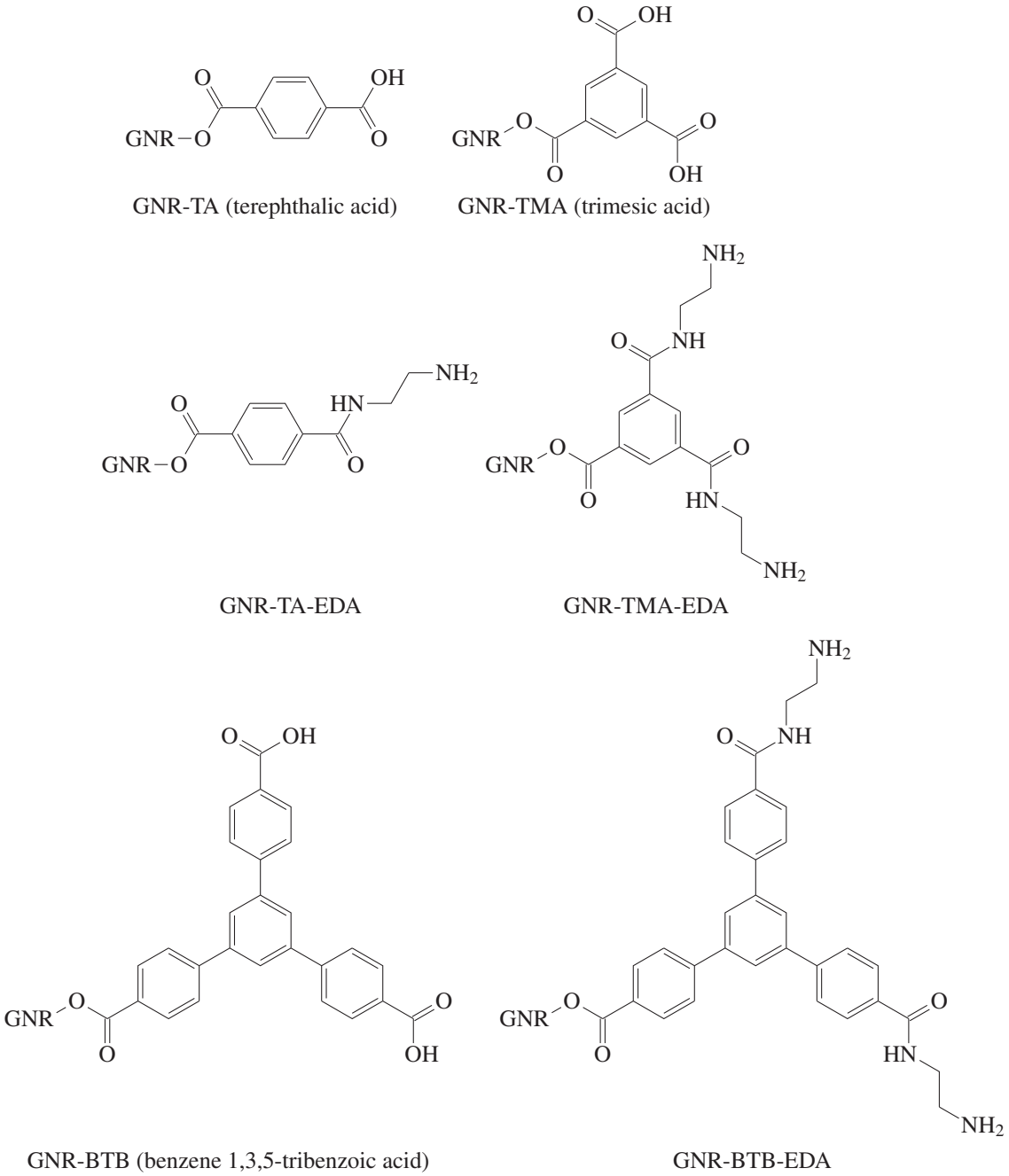

Figure 110: GNRs edge-functionalised with various combinations of multi-carboxylated molecules and ethylenediamine.

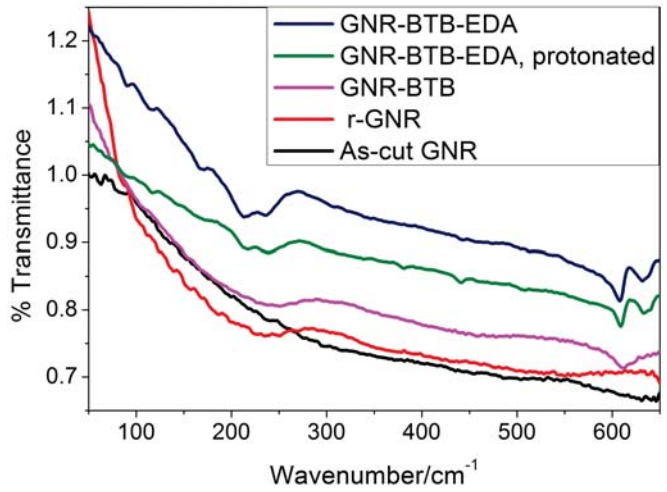

(a)

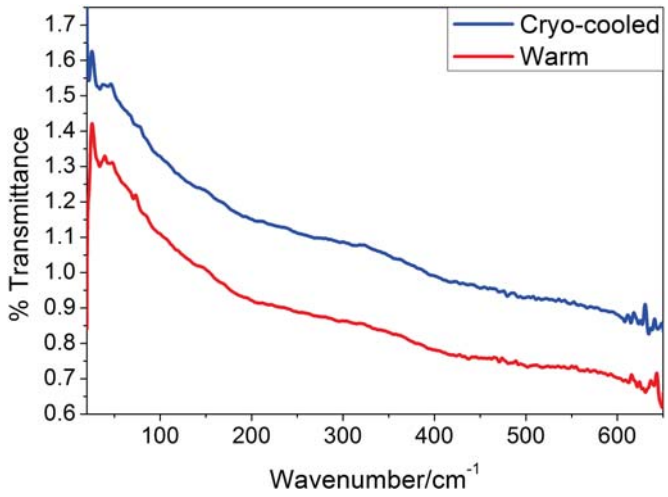

(b)

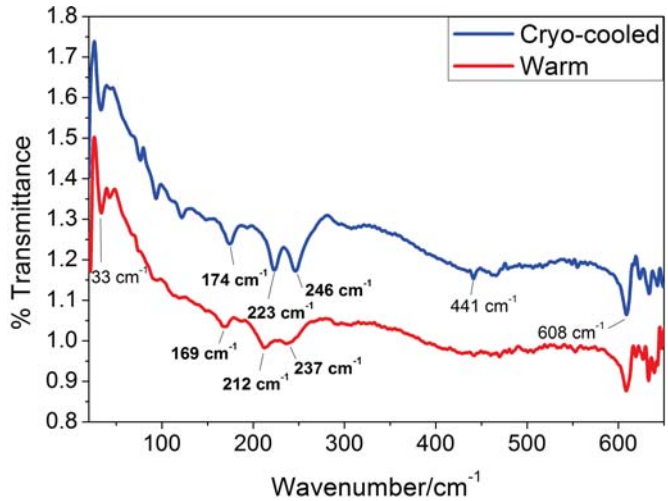

(c)

Figure 111: Far-IR spectra of 20 nm GNR with various edge modifications. (a) Spectra of unmodified GNR, GNR reduced with $NaBH_4$ and r-GNR modified with BTB and EDA. (b) Spectra of GNR-BTB, with and without cryo-cooling. (c) Spectra of GNR-BTB-EDA, with and without cryo-cooling.

featureless, as were the spectra of many of the modified ribbon samples not shown, the only differences being small changes in the shape of the baseline (figure 111a). Ribbons functionalised with BTB and EDA were the only samples that displayed any features in their Far-IR spectra. Interestingly, the spectral features of these samples show little change upon the addition of small amounts of acid for amine protonation.

To investigate whether the bands are real spectral features, Far-IR spectra of GNR-BTB and GNR-BTB-EDA samples cooled in a cryostat were run, as shown in figure 111b and 111c. THz vibrations can be sensitive to temperature and the observation of a temperature dependence is often indicative of weak bonds.[165] For low-frequency vibrational modes, generally, as the temperature decreases the number of peaks increases, the frequencies shift and the peaks become narrower. This behaviour is due to a decrease in thermal populations with temperature, where broadening is reduced by having the majority of oscillators occupying the lowest energy level at low temperature. Thus, it is expected that upon cooling, the vibrational bands should sharpen and narrow, making them and other possible bands with low S:N more apparent. For GNR-BTB, the spectrum undergoes very little change upon cooling and the weak band at 610 cm^{-1} that is present in figure 111a is not apparent in either the warm or cryo-cooled spectrum, though this could be due to the cryostat chamber windows reducing the single beam intensity by a factor of two, thereby reducing the S:N for a band that already has very low S:N. The spectra of GNR-BTB-EDA are the most interesting. There are significant changes in the appearance of the spectrum upon cooling, with sharpening of many of the bands, as well as shifting of the bands at 169, 212 and 237 cm^{-1} to higher frequency upon cryo-cooling.

Although only limited data was acquired at the Synchrotron, the Far-IR work described here has led to the establishment of methodologies for acquiring Far-IR spectra from GNR samples, which is the first of its kind. Thus, the results and procedures established in this work provide a basis for a more detailed investigation in the future. Obtaining spectra from a library of samples with small, sequential and precisely controlled differences could allow for assignment of vibrational bands, and computational studies could also be employed to assist in this.

5.3 Conclusion

In summary, edge-specific functionalisation of GNR edges was investigated through three main routes: (1) coupling of edge hydroxyl groups with small carboxyl-terminated molecules via ester bond formation, (2) coupling of edge carboxyl groups with small primary amine-terminated molecules via amide bond formation and (3) aryl grafting of sulfophenyl and nitrophenyl groups via diazonium reactions. In the first approach, modification of GNRs cut at a width of 100 nm did not afford any evidence of modification, as shown by Raman and FTIR spectroscopy. Ribbons cut at a width of 50 nm did show some, albeit weak, evidence of functionalisation in their Raman and FTIR spectra, and THz spectroscopy of modified 20 nm GNRs gave substantial evidence of weak, non-covalent interactions between edge functional groups containing primary amines. In this case, successful observation of peaks in the spectra could, in part, be attributed to the multicarboxylated molecule BTB used to increase the density of edge COOH groups for reaction with the amine modifier. Thus, there is reasonable combined evidence for the presence of hydroxyl groups (and groups that can be converted to hydroxyl groups upon $NaBH_4$ reduction) at the edges of GNRs produced via the mechanical fracturing technique, and that these groups can be targeted for covalent modification via ester bond formation.

In the second approach, GNRs were cut at a narrower width of 20 nm in an attempt to increase the relative proportion of edge groups available for reaction. FTIR and Raman data have given good and reproducible evidence for edge-specific modification with sulfanilic acid, with the results showing excellent agreement with well-established methods for SA functionalisation of GO. The sharpness and intensity of these bands in the IR spectrum of SA-GO could explain why they would be visible in the spectrum of SA-GNR, despite the inherent low sensitivity of FTIR spectroscopy. Attempts to functionalise GNRs with other amine-containing modifiers did not afford such strong evidence of attachment, though this could be due to the low sensitivity of FTIR and problems with water vapour background in regions where IR bands are expected to occur. Nevertheless, successful reaction of SA suggests that carboxyl groups have a significant presence at the edges of GNRs.

Finally, good evidence of the edge-selectivity of aryldiazonium modification of GNRs with SP and NP groups has been obtained by FTIR, Raman and SERS spectroscopy. Behaviour of Raman D:G ratios and intensity of IR bands has suggested that functionalisation is restricted almost exclusively, as far as detection allows, to the edges of GNRs, regardless of whether the ribbons are modified in their exfoliated state or as stacked GNBs. This indicates that the reactivity of the graphene basal plane is very low in solution, as opposed to on a substrate such as SiO_2 [88], and that modification of GNRs in solution could be key to the selectivity.

6 Conclusion and Future Perspectives

The work presented in this thesis explored new avenues in the production, characterisation and functionalisation of graphene nanoribbons. GNRs were produced using the unique and novel technique of nanotomy-based mechanical fracturing developed by Mohanty et el.[83], a method that allowed for the production of high-quality, low defect ribbons. A Raman microscope with low-frequency (THz) and polarised Raman capabilities was specifically developed for the characterisation of GNRs, using a simple microscope platform to build a low-cost but highly versatile instrument with capabilities for characterising a large variety of samples. Despite persistent problems with stability and aggregation of ribbons, AFM, TEM and Raman analysis has revealed high-quality GNRs with relatively straight edges. In particular, Raman microscopy has proved to be especially invaluable, with analysis of Raman D:G ratios revealing a difference between cutting ribbons dry or into water, with the lower D:G ratios for dry-cut ribbons suggesting that these may be of a higher quality. In addition, polarised Raman studies of the D and G bands were used to determine the predominant nanoribbon edge type, degree of disorder and relative orientation of armchair and zigzag segments in small, ordered aggregates of GNRs. Overall, these studies suggest a predominance of zigzag edges. Another main objective of the project was to develop methods for the selective edge-functionalisation of the GNRs produced, and this was investigated via three main routes; ester coupling, amide coupling and aryldiazonium grafting. Characterisation by IR spectroscopy/microscopy, Raman & SERS microscopy and Far-IR spectroscopy have provided good combined evidence for success in each approach, collectively presenting a convincing argument for the successful, selective modification of the edges of GNRs.

The structural characterisation of graphene nanoribbons presented here focused largely on their average characteristics, particularly in the Raman experiments. The reasons for this were two-fold: (1) the aggregation problem made it difficult to isolate single ribbons and (2) limitation of the laser focus spot size (i.e. diffraction limit) to a minimum of a few hundred nm. AFM and TEM images have shown that individual, separated ribbons do occur amongst the aggregates, however, therefore in the case of Raman microscopy it is the inherent low sensitivity of the technique that makes it difficult to detect the weak signals from individual ribbons, especially considering that these would only fill part of the laser focus spot (particularly for ribbons with widths down to 20 nm). To overcome these limitations, Raman extensions such as an AFM/Raman combination or TERS (Tip-Enhanced Raman Spectroscopy) could be applied. A combination of AFM and Raman microscopy built into the same instrument could allow for direct correlation of a Raman spectrum with an AFM image. This could be done by simply mounting a tip-moving AFM onto the Raman microscope stage. A tip-moving, rather than a sample-moving, AFM is required so that the sample would not move in the laser focal point as the AFM

image is scanned. The AFM tip would interact with the sample placed face-side-up above the microscope objective, while the Raman spectra could be collected from the bottom side of the sample. Another extension of Raman microscopy is TERS, which involves the use of a sharp plasmonic metal tip to create a single, localised hotspot. By positioning the tip very close to the sample surface, the part of the sample close to the tip will experience surface enhancement, while other parts of the sample will not. This could greatly improve the spatial resolution of the microscope far above the diffraction limit, depending on the tip dimensions, which can be of the order of nanometres. The morphology of the tip is critical in determining in its ability to sustain surface plasmon hotspots, and though this can be difficult to control, electrochemical procedures could be an effective solution. Combining the TERS approach with a piezo stage for moving the sample in small incremental steps could allow for Raman mapping experiments, where a Raman map of the sample is constructed from the spectrum obtained at each step (pixel).

The chemistry used in this project for the edge-functionalisation of GNRs was chosen partly for its compatibility with the required experimental conditions and small sample volumes, however it is by no means an exhaustive list of all the possible chemistries that could be applied. As discussed in chapter 5, many of the techniques in the literature for the functionalisation of GO can also be applied to the edges of GNRs produced here, due to the similarity of oxygen-containing groups. There is an additional, and somewhat novel, possibility that is of particular interest in light of this project; that is performing the cutting of ribbons in a controlled atmosphere to obtain selectively edge-functionalised ribbons in situ. For example, housing the microtome in a gas-filled chamber, for example CO_2, could result in the formation of GNRs with a high degree of edge COOH groups. The inspiration for this idea is based on the work by Jeon et al.[148], in which graphite was ball-milled in a chamber filled with gases such as hydrogen, carbon dioxide and sulfur trioxide to give graphene nanoplatelets edge-functionalised with hydrogen, carboxylic acid and sulfonic acid groups, respectively.

The purpose of GNR edge functionalisation was to provide a means for directing the layer-by-layer assembly of individual ribbons. Although it was eventually determined that it would be unrealistic to include this advanced stage in the scope of this project, it is still useful to describe here what this could involve in future directions. As AFM, TEM and Raman analysis has shown, the GNRs produced after exfoliation of GNBs are of a high quality and are at least several microns in length. For unmodified GNRs, assembly would likely occur in a disordered manner to produce aggregates of interlacing ribbons, rather than ordered, aligned stacks of ribbons akin to the GNBs from which they were produced. In fact, this is exactly what has been observed throughout the experimental work; the persistent aggregation problem. This assembly is driven by van der Waals and $\pi - \pi$ interactions, which display little or no preference between edge and basal plane interactions. However, when the nanoribbon edges contain functional groups, the assem-

bly could become driven predominantly by the formation of electrostatic interactions or hydrogen bonds - forces significantly stronger than the typical van der Waals and $\pi - \pi$ interactions between graphene sheets. It is proposed that by mixing GNRs with different and complementary edge functional groups, that selective interactions between the edge functionalities should drive assembly of GNRs in an ordered and non-random fashion. This will also allow for the production of multi-layered GNRs with alternating edge functionalities. Since the edge functional groups can alter the electronic properties of the GNRs, this could allow for selective doping of individual GNRs within the multi-layer GNR stack.

The results presented in this thesis have shown that there is considerable variation in the width of GNRs produced by the mechanical fracturing technique. Self-assembly of GNRs would require that the ribbons have homogeneously distributed widths and edge smoothness, which would either require more elegant and precise methods of production, or otherwise refinement of the nanotomy method to allow for better control over the cutting direction and alignment of the diamond knife relative to the HOPG planes, which could lead to smoother edges with controlled armchair/zigzag geometry and more homogeneous widths. Control over the ribbon length would also be important, so that the ribbons can interact over their full lengths without self-folding/aggregation of dangling ends. Mohanty et al. have shown that the nanotomy process can be used to control the length of GNRs to give graphene nanosquares.[83] Thus, there is the possibility of being able to control the ribbon length using a similar approach. For self-assembly of GNRs to be directed by the edge functional groups, interactions between the edges need to be highly thermodynamically favourable so that they will dominate over the van der Waals and $\pi - \pi$ interactions that drive aggregation. This clearly requires a minimum ratio of edge groups to basal carbon atoms, which has likely not yet been achieved in the work presented here. Thus, control over the length of the GNRs to produce graphene nanorectangles could be one effective means to increase the edge:basal ratio, and the lengths could be gradually increased to determine at which point aggregation takes over and what combination of ribbon length, width and density/type of functional groups is required for edge interactions to lead to controlled self-assembly.

Molecular dynamics (MD) simulations have been reported for the study of the mechanism of GNR aggregation in solution and the effects of edge functionalisation on the self-assembly.[167,168] These simulations were used to determine how polymeric side chains grafted to the edges of GNRs affected their aggregation behaviour, as well as to study the aggregation pathway for H-terminated ribbons. The results of these studies showed that the main energy barrier to aggregation involves expulsion of the last solvent layer, and that the height of this barrier (in potentials of mean force (PMF) curves) is sensitive to the type and density of edge functional groups, as well as the type of solvent. The simulations also showed that when two ribbons come together to aggregate, they will at

first try to minimise their surface area overlap due to steric repulsion[169] with the solvent layer, and will actually contact at the edges first, which then facilitates rapid exclusion of the solvent layer, allowing the ribbons to fully aggregate and align along their lengths to maximise contact. This shows that edge interactions are important for aggregation even in H-terminated ribbons, thus these studies have important and interesting implications for future studies of GNR self-assembly driven by edge interactions.

Another means to tailor the electronic properties of GNR composites and produce charge-separation is by electron/hole doping upon the introduction of intercalating electron-donating or electron-accepting molecules between the graphene layers, where the nature of the intercalating molecules can be used to finely control the degree and type of doping. Again, edge functionalities on GNRs would direct the layer-by-layer assembly of GNR composites, this time including intercalating molecules between the layers, which will interact with the graphene basal plane via van der Waals and $\pi - \pi$ interactions. These composites will have the appearance of GNR sandwich-type structures, with electron-donating or -withdrawing molecules sandwiched between GNRs. The intercalating molecules to be investigated could be aromatic organic molecules with electron-accepting or -donating properties, for example HATN (hexaazatriphenylene), TCNQ (7,7,8,8-tetracyanoquinodimethane), and perfluorinated aromatic molecules such as F4-TCNQ (2,3,5,6-tetrafluoro-7,7,8,8-tetracyanoquinodimethane).

The experimental techniques for the assembly of GNRs and GNR composites could involve the sequential build-up of layers by exposure of previous layers to a solution containing the next layer – be it a differently functionalised GNR or intercalating molecule. If the first GNRs for each composite are immobilised onto a suitable substrate (e.g. silanised silica or freshly-cleaved mica), subsequent layers could be built up by sequential exposure to solutions containing the different layers, with rinsing in between to remove excess material – i.e. a repeated dip-and-rinse procedure. Multi-layered GNR composites could also be produced in solution by mixing two solutions, each containing GNRs with complementary functional groups, where the thickness of the alternating-layer structures could be controlled by the concentrations of the two GNR solutions.

7 Bibliography

1. Novoselov K; Geim A; Morozov S; Jiang D; Zhang Y; Dubonos S; Grigorieva I and Firsov A, Electric field effect in atomically thin carbon films. *Science* 306(5696), **2004**, 666–669.

2. Lv R and Terrones M, Towards new graphene materials: Doped graphene sheets and nanoribbons. *Mater. Lett.* 78, **2012**, 209–218.

3. Bao Q and Loh KP, Graphene Photonics, Plasmonics, and Broadband Optoelectronic Devices. *ACS Nano* 6(5), **2012**, 3677–3694.

4. Fang Z; Liu Z; Wang Y; Ajayan PM; Nordlander P and Halas NJ, Graphene-Antenna Sandwich Photodetector. *Nano. Lett.* 12(7), **2012**, 3808–3813.

5. Geim AK and Novoselov KS, The rise of graphene. *Nat. Mater.* 6(3), **2007**, 183–191.

6. Venables J; Spiller G and Hanbucken M, Nucleation and Growth of Thin-Films. *Rep. Prog. Phys.* 47(4), **1984**, 399–459.

7. Evans JW; Thiel PA and Bartelt MC, Morphological evolution during epitaxial thin film growth: Formation of 2D islands and 3D mounds. *Surf. Sci. Rep.* 61(1-2), **2006**, 1–128.

8. Mermin N, Crystalline Order in 2 Dimensions. *Phys. Rev.* 176(1), **1968**, 250–254.

9. Meyer JC; Geim AK; Katsnelson MI; Novoselov KS; Booth TJ and Roth S, The structure of suspended graphene sheets. *Nature* 446(7131), **2007**, 60–63.

10. Berger C; Song Z; Li T; Li X; Ogbazghi A; Feng R; Dai Z; Marchenkov A; Conrad E; First P and de Heer W, Ultrathin epitaxial graphite: 2D electron gas properties and a route toward graphene-based nanoelectronics. *J. Phys. Chem. B.* 108(52), **2004**, 19912–19916.

11. Berger C; Song Z; Li X; Wu X; Brown N; Naud C; Mayou D; Li T; Hass J; Marchenkov AN; Conrad EH; First PN and de Heer WA, Electronic confinement and coherence in patterned epitaxial graphene. *Science* 312(5777), **2006**, 1191–1196.

12. Zhang Y; Tan Y; Stormer H and Kim P, Experimental observation of the quantum Hall effect and Berry's phase in graphene. *Nature* 438(7065), **2005**, 201–204.

13. Katsnelson MI; Novoselov KS and Geim AK, Chiral tunnelling and the Klein paradox in graphene. *Nat. Phys.* 2(9), **2006**, 620–625.

14. Novoselov K; Jiang D; Schedin F; Booth T; Khotkevich V; Morozov S and Geim A, Two-dimensional atomic crystals. *Proc. Natl. Acad. Sci. U.S.A.* 102(30), **2005**, 10451–10453.

15. Lotya M; Hernandez Y; King PJ; Smith RJ; Nicolosi V; Karlsson LS; Blighe FM; De S; Wang Z; McGovern IT; Duesberg GS and Coleman JN, Liquid Phase Production of Graphene by Exfoliation of Graphite in Surfactant/Water Solutions. *J. Am. Chem. Soc.* 131(10), **2009**, 3611–3620.

16. Hernandez Y; Nicolosi V; Lotya M; Blighe FM; Sun Z; De S; McGovern IT; Holland B; Byrne M; Gun'ko YK; Boland JJ; Niraj P; Duesberg G; Krishnamurthy S; Goodhue R; Hutchison J; Scardaci V; Ferrari AC and Coleman JN, High-yield production of graphene by liquid-phase exfoliation of graphite. *Nat. Nanotechnol.* 3(9), **2008**, 563–568.

17. Khan U; O'Neill A; Lotya M; De S and Coleman JN, High-Concentration Solvent Exfoliation of Graphene. *Small* 6(7), **2010**, 864–871.

18. Dresselhaus M and Dresselhaus G, Intercalation compounds of graphite. *Adv. Phys.* 51(1), **2002**, 1–186.

19. Soldano C; Mahmood A and Dujardin E, Production, properties and potential of graphene. *Carbon* 48(8), **2010**, 2127–2150.

20. Li X; Zhang G; Bai X; Sun X; Wang X; Wang E and Dai H, Highly conducting graphene sheets and Langmuir-Blodgett films. *Nat. Nanotechnol.* 3(9), **2008**, 538–542.

21. Wu J; Pisula W and Muellen K, Graphenes as potential material for electronics. *Chem. Rev.* 107(3), **2007**, 718–747.

22. Yang X; Dou X; Rouhanipour A; Zhi L; Raeder HJ and Muellen K, Two-dimensional graphene nanoribbons. *J. Am. Chem. Soc.* 130(13), **2008**, 4216–4217.

23. Yan X; Cui X and Li Ls, Synthesis of Large, Stable Colloidal Graphene Quantum Dots with Tunable Size. *J. Am. Chem. Soc.* 132(17), **2010**, 5944–5945.

24. Land T; Michely T; Behm R; Hemminger J and Comsa G, STM investigation of single layer graphite structures produced on Pt(111) by hydrocarbon decomposition. *Surf. Sci.* 264(3), **1992**, 261–270.

25. Nagashima A; Nuka K; Itoh H; Ichinokawa T; Oshima C and Otani S, Electronic states of monolayer graphite formed on TiC(111) surface. *Surf. Sci.* 291(1-2), **1993**, 93–98.

26. Ohta T; Bostwick A; Seyller T; Horn K and Rotenberg E, Controlling the electronic structure of bilayer graphene. *Science* 313(5789), **2006**, 951–954.

27. Park S; An J; Jung I; Piner RD; An SJ; Li X; Velamakanni A and Ruoff RS, Colloidal Suspensions of Highly Reduced Graphene Oxide in a Wide Variety of Organic Solvents. *Nano Lett.* 9(4), **2009**, 1593–1597.

28. Rafiee MA; Rafiee J; Wang Z; Song H; Yu ZZ and Koratkar N, Enhanced Mechanical Properties of Nanocomposites at Low Graphene Content. *ACS Nano* 3(12), **2009**, 3884–3890.

29. Shao Y; Wang J; Engelhard M; Wang C and Lin Y, Facile and controllable electrochemical reduction of graphene oxide and its applications. *J. Mater. Chem.* 20(4), **2010**, 743–748.

30. Weiss NO; Zhou H; Liao L; Liu Y; Jiang S; Huang Y and Duan X, Graphene: An Emerging Electronic Material. *Adv. Mater.* 24(43), **2012**, 5782–5825.

31. Mayorov AS; Gorbachev RV; Morozov SV; Britnell L; Jalil R; Ponomarenko LA; Blake P; Novoselov KS; Watanabe K; Taniguchi T and Geim AK, Micrometer-Scale Ballistic Transport in Encapsulated Graphene at Room Temperature. *Nano. Lett.* 11(6), **2011**, 2396–2399.

32. Novoselov K; Geim A; Morozov S; Jiang D; Katsnelson M; Grigorieva I; Dubonos S and Firsov A, Two-dimensional gas of massless Dirac fermions in graphene. *Nature* 438(7065), **2005**, 197–200.

33. Jiang Z; Zhang Y; Tan YW; Stormer HL and Kim P, Quantum Hall effect in graphene. *Solid State Commun.* 143(1-2), **2007**, 14–19.

34. Morozov S; Novoselov K; Schedin F; Jiang D; Firsov A and Geim A, Two-dimensional electron and hole gases at the surface of graphite. *Phys. Rev. B* 72(20), **2005**, 201401.

35. Partoens B and Peeters FM, From graphene to graphite: Electronic structure around the K point. *Phys. Rev. B* 74(7), **2006**, 075404.

36. Li B; Cao X; Ong HG; Cheah JW; Zhou X; Yin Z; Li H; Wang J; Boey F; Huang W and Zhang H, All-Carbon Electronic Devices Fabricated by Directly Grown Single-Walled Carbon Nanotubes on Reduced Graphene Oxide Electrodes. *Adv. Mater.* 22(28), **2010**, 3058–3061.

37. Hong SW; Du F; Lan W; Kim S; Kim HS and Rogers JA, Monolithic Integration of Arrays of Single-Walled Carbon Nanotubes and Sheets of Graphene. *Adv. Mater.* 23(33), **2011**, 3821–3826.

38. Lee SK; Kim BJ; Jang H; Yoon SC; Lee C; Hong BH; Rogers JA; Cho JH and Ahn JH, Stretchable Graphene Transistors with Printed Dielectrics and Gate Electrodes. *Nano. Lett.* 11(11), **2011**, 4642–4646.

39. De Arco LG; Zhang Y; Schlenker CW; Ryu K; Thompson ME and Zhou C, Continuous, Highly Flexible, and Transparent Graphene Films by Chemical Vapor Deposition for Organic Photovoltaics. *ACS Nano.* 4(5), **2010**, 2865–2873.

40. Lee YY; Tu KH; Yu CC; Li SS; Hwang JY; Lin CC; Chen KH; Chen LC; Chen HL and Chen CW, Top Laminated Graphene Electrode in a Semitransparent Polymer Solar Cell by Simultaneous Thermal Annealing/Releasing Method. *ACS Nano.* 5(8), **2011**, 6564–6570.

41. Wang Y; Tong SW; Xu XF; Oezyilmaz B and Loh KP, Interface Engineering of Layer-by-Layer Stacked Graphene Anodes for High-Performance Organic Solar Cells. *Adv. Mater.* 23(13), **2011**, 1514–1518.

42. Kim RH; Bae MH; Kim DG; Cheng H; Kim BH; Kim DH; Li M; Wu J; Du F; Kim HS; Kim S; Estrada D; Hong SW; Huang Y; Pop E and Rogers JA, Stretchable, Transparent Graphene Interconnects for Arrays of Microscale Inorganic Light Emitting Diodes on Rubber Substrates. *Nano Lett.* 11(9), **2011**, 3881–3886.

43. Han TH; Lee Y; Choi MR; Woo SH; Bae SH; Hong BH; Ahn JH and Lee TW, Extremely efficient flexible organic light-emitting diodes with modified graphene anode. *Nat. Photonics* 6(2), **2012**, 105–110.

44. Zhu J; Sharma YK; Zeng Z; Zhang X; Srinivasan M; Mhaisalkar S; Zhang H; Hng HH and Yan Q, Cobalt Oxide Nanowall Arrays on Reduced Graphene Oxide Sheets with Controlled Phase, Grain Size, and Porosity for Li-Ion Battery Electrodes. *J. Phys. Chem. C* 115(16), **2011**, 8400–8406.

45. Wang H; Yang Y; Liang Y; Cui LF; Casalongue HS; Li Y; Hong G; Cui Y and Dai H, LiMn1-xFexPO4 Nanorods Grown on Graphene Sheets for Ultrahigh-Rate-Performance Lithium Ion Batteries. *Angew. Chem. Int. Ed.* 50(32), **2011**, 7364–7368.

46. Huang X; Zeng Z; Fan Z; Liu J and Zhang H, Graphene-Based Electrodes. *Adv. Mater.* 24(45), **2012**, 5979–6004.

47. Wang Z; Zhang J; Yin Z; Wu S; Mandler D and Zhang H, Fabrication of nanoelectrode ensembles by electrodepositon of Au nanoparticles on single-layer graphene oxide sheets. *Nanoscale* 4(8), **2012**, 2728–2733.

48. Wang T; Zhang S; Mao C; Song J; Niu H; Jin B and Tian Y, Enhanced electrochemiluminescence of CdSe quantum dots composited with graphene oxide and chitosan for sensitive sensor. *Biosens. Bioelectron.* 31(1), **2012**, 369–375.

49. Loh KP; Tong SW and Wu J, Graphene and Graphene-like Molecules: Prospects in Solar Cells. *J. Am. Chem. Soc.* 138(4), **2016**, 1095–1102.

50. Bonaccorso F; Sun Z; Hasan T and Ferrari AC, Graphene photonics and optoelectronics. *Nat. Photonics* 4(9), **2010**, 611–622.

51. Wang X; Zhi L and Muellen K, Transparent, conductive graphene electrodes for dye-sensitized solar cells. *Nano Lett.* 8(1), **2008**, 323–327.

52. Singh E and Nalwa HS, Graphene-Based Dye-Sensitized Solar Cells: A Review. *Sci. Adv. Mater.* 7(10, SI), **2015**, 1863–1912.

53. Kavan L; Yum JH and Graetzel M, Optically Transparent Cathode for Dye-Sensitized Solar Cells Based on Graphene Nanoplatelets. *ACS Nano* 5(1), **2011**, 165–172.

54. Kavan L; Yum JH; Nazeeruddin MK and Graetzel M, Graphene Nanoplatelet Cathode for Co(III)/(II) Mediated Dye-Sensitized Solar Cells. *ACS Nano* 5(11), **2011**, 9171–9178.

55. Chen L; Guo CX; Zhang Q; Lei Y; Xie J; Ee S; Guai G; Song Q and Li CM, Graphene Quantum-Dot-Doped Polypyrrole Counter Electrode for High-Performance Dye-Sensitized Solar Cells. *ACS Appl. Mater. Interfaces* 5(6), **2013**, 2047–2052.

56. Zhu Y; Sun Z; Yan Z; Jin Z and Tour JM, Rational Design of Hybrid Graphene Films for High-Performance Transparent Electrodes. *ACS Nano* 5(8), **2011**, 6472–6479.

57. Ahmad I; Khan U and Gun'ko YK, Graphene, carbon nanotube and ionic liquid mixtures: towards new quasi-solid state electrolytes for dye sensitised solar cells. *J. Mater. Chem.* 21(42), **2011**, 16990–16996.

58. Yuan S; Tang Q; He B and Zhao Y, Multifunctional graphene incorporated conducting gel electrolytes in enhancing photovoltaic performances of quasi-solid-state dye-sensitized solar cells. *J. Power Sources* 260, **2014**, 225–232.

59. Yan X; Cui X; Li B and Li Ls, Large, Solution-Processable Graphene Quantum Dots as Light Absorbers for Photovoltaics. *Nano Lett.* 10(5), **2010**, 1869–1873.

60. Ji Z; Wu R; Adamska L; Velizhanin KA; Doorn SK and Sykora M, In Situ Synthesis of Graphene Molecules on TiO2: Application in Sensitized Solar Cells. *ACS Appl. Mater. Interfaces* 6(22), **2014**, 20473–20478.

61. Zhang Y; Zhang N; Tang ZR and Xu YJ, Graphene Transforms Wide Band Gap ZnS to a Visible Light Photocatalyst. The New Role of Graphene as a Macromolecular Photosensitizer. *ACS Nano* 6(11), **2012**, 9777–9789.

62. Liu Y; Yuan L; Yang M; Zheng Y; Li L; Gao L; Nerngchamnong N; Nai CT; Sangeeth CSS; Feng YP; Nijhuis CA and Loh KP, Giant enhancement in vertical conductivity of stacked CVD graphene sheets by self-assembled molecular layers. *Nat. Commun.* 5, **2014**, 5461.

63. Celis A; Nair MN; Taleb-Ibrahimi A; Conrad EH; Berger C; de Heer WA and Tejeda A, Graphene nanoribbons: fabrication, properties and devices. *J. Phys. D: Appl. Phys.* 49(14), **2016**, 143001.

64. Nakada K; Fujita M; Dresselhaus G and Dresselhaus M, Edge state in graphene ribbons: Nanometer size effect and edge shape dependence. *Phys. Rev. B* 54(24), **1996**, 17954–17961.

65. Wakabayashi K; Fujita M; Ajiki H and Sigrist M, Electronic and magnetic properties of nanographite ribbons. *Phys. Rev. B* 59(12), **1999**, 8271–8282.

66. Pisani L; Chan JA; Montanari B and Harrison NM, Electronic structure and magnetic properties of graphitic ribbons. *Phys. Rev. B* 75(6), **2007**, 064418.

67. Yazyev OV, Emergence of magnetism in graphene materials and nanostructures. *Rep. Prog. Phys.* 73(5), **2010**, 056501.

68. Son YW; Cohen ML and Louie SG, Half-metallic graphene nanoribbons. *Nature* 444(7117), **2006**, 347–349.

69. Bai J; Duan X and Huang Y, Rational Fabrication of Graphene Nanoribbons Using a Nanowire Etch Mask. *Nano Lett.* 9(5), **2009**, 2083–2087.

70. Liu G; Wu Y; Lin YM; Farmer DB; Ott JA; Bruley J; Grill A; Avouris P; Pfeiffer D; Balandin AA and Dimitrakopoulos C, Epitaxial Graphene Nanoribbon Array Fabrication Using BCP-Assisted Nanolithography. *ACS Nano* 6(8), **2012**, 6786–6792.

71. Bryan SE; Yang Y and Murali R, Conductance of Epitaxial Graphene Nanoribbons: Influence of Size Effects and Substrate Morphology. *J. Phys. Chem. C* 115(20), **2011**, 10230–10235.

72. Hwang WS; Zhao P; Tahy K; Nyakiti LO; Wheeler VD; Myers-Ward RL; Eddy CR Jr; Gaskill DK; Robinson JA; Haensch W; Xing HG; Seabaugh A and Jena D, Graphene nanoribbon field-effect transistors on wafer-scale epitaxial graphene on SiC substrates. *APL Materials* 3(1), **2015**, 011101.

73. Vo TH; Shekhirev M; Kunkel DA; Morton MD; Berglund E; Kong L; Wilson PM; Dowben PA; Enders A and Sinitskii A, Large-scale solution synthesis of narrow graphene nanoribbons. *Nat. Commun.* 5, **2014**, 3189.

74. Jia X; Hofmann M; Meunier V; Sumpter BG; Campos-Delgado J; Romo-Herrera JM; Son H; Hsieh YP; Reina A; Kong J; Terrones M and Dresselhaus MS, Controlled Formation of Sharp Zigzag and Armchair Edges in Graphitic Nanoribbons. *Science* 323(5922), **2009**, 1701–1705.

75. Xie L; Wang H; Jin C; Wang X; Jiao L; Suenaga K and Dai H, Graphene Nanoribbons from Unzipped Carbon Nanotubes: Atomic Structures, Raman Spectroscopy, and Electrical Properties. *J. Am. Chem. Soc.* 133(27), **2011**, 10394–10397.

76. Kosynkin DV; Higginbotham AL; Sinitskii A; Lomeda JR; Dimiev A; Price BK and Tour JM, Longitudinal unzipping of carbon nanotubes to form graphene nanoribbons. *Nature* 458(7240), **2009**, 872–877.

77. Kumar P; Yamijala SSRKC and Pati SK, Optical Unzipping of Carbon Nanotubes in Liquid Media. *J. Phys. Chem. C* 120(30), **2016**, 16985–16993.

78. Campos LC; Manfrinato VR; Sanchez-Yamagishi JD; Kong J and Jarillo-Herrero P, Anisotropic Etching and Nanoribbon Formation in Single-Layer Graphene. *Nano Lett.* 9(7), **2009**, 2600–2604.

79. Doessel L; Gherghel L; Feng X and Muellen K, Graphene Nanoribbons by Chemists: Nanometer-Sized, Soluble, and Defect-Free. *Angew. Chem. Int. Ed.* 50(11), **2011**, 2540–2543.

80. Kato T and Hatakeyama R, Site- and alignment-controlled growth of graphene nanoribbons from nickel nanobars. *Nat. Nanotechnol.* 7(10), **2012**, 651–656.

81. Sokolov AN; Yap FL; Liu N; Kim K; Ci L; Johnson OB; Wang H; Vosgueritchian M; Koh AL; Chen J; Park J and Bao Z, Direct growth of aligned graphitic nanoribbons from a DNA template by chemical vapour deposition. *Nat. Commun.* 4, **2013**, 2402.

82. Martin-Fernandez I; Wang D and Zhang Y, Direct Growth of Graphene Nanoribbons for Large-Scale Device Fabrication. *Nano Lett.* 12(12), **2012**, 6175–6179.

83. Mohanty N; Moore D; Xu Z; Sreeprasad TS; Nagaraja A; Rodriguez AA and Berry V, Nanotomy-based production of transferable and dispersible graphene nanostructures of controlled shape and size. *Nat. Commun.* 3, **2012**, 844.

84. Wang X; Xu JB; Xie W and Du J, Quantitative Analysis of Graphene Doping by Organic Molecular Charge Transfer. *J. Phys. Chem. C.* 115(15), **2011**, 7596–7602.

85. Chua CK and Pumera M, Covalent chemistry on graphene. *Chem. Soc. Rev.* 42(8), **2013**, 3222–3233.

86. Sarkar S; Bekyarova E and Haddon RC, Chemistry at the Dirac Point: Diels-Alder Reactivity of Graphene. *Accounts Chem. Res.* 45(4), **2012**, 673–682.

87. Acik M and Chabal YJ, Nature of Graphene Edges: A Review. *Jpn. J. Appl. Phys.* 50(7), **2011**, 070101.

88. Sharma R; Baik JH; Perera CJ and Strano MS, Anomalously Large Reactivity of Single Graphene Layers and Edges toward Electron Transfer Chemistries. *Nano. Lett.* 10(2), **2010**, 398–405.

89. Jin Z; McNicholas TP; Shih CJ; Wang QH; Paulus GLC; Hilmer A; Shimizu S and Strano MS, Click Chemistry on Solution-Dispersed Graphene and Monolayer CVD Graphene. *Chem. Mater.* 23(14), **2011**, 3362–3370.

90. Park J and Yan M, Covalent Functionalization of Graphene with Reactive Intermediates. *Accounts Chem. Res.* 46(1), **2013**, 181–189.

91. Kim KS; Jeon IY; Ahn SN; Kwon YD and Baek JB, Edge-functionalized graphene-like platelets as a co-curing agent and a nanoscale additive to epoxy resin. *J. Mater. Chem.* 21(20), **2011**, 7337–7342.

92. Chattopadhyay J; Mukherjee A; Hamilton CE; Kang J; Chakraborty S; Guo W; Kelly KF; Barron AR and Billups WE, Graphite epoxide. *J. Am. Chem. Soc.* 130(16), **2008**, 5414–5415.

93. Sun Z; Kohama Si; Zhang Z; Lomeda JR and Tour JM, Soluble graphene through edge-selective functionalization. *Nano. Res.* 3(2), **2010**, 117–125.

94. Denis PA, Organic Chemistry of Graphene: The Diels-Alder Reaction. *Chem-Eur. J.* 19(46), **2013**, 15719–15725.

95. Lee H, Preferential functionalization on zigzag graphene nanoribbons: first-principles calculations. *J. Phys-Condens. Mat.* 22(35), **2010**, 352205.

96. Jiang De; Sumpter BG and Dai S, Unique chemical reactivity of a graphene nanoribbon's zigzag edge. *J. Chem. Phys.* 126(13), **2007**, 134701.

97. Cao Y; Osuna S; Liang Y; Haddon RC and Houk KN, Diels-Alder Reactions of Graphene: Computational Predictions of Products and Sites of Reaction. *J. Am. Chem. Soc.* 135(46), **2013**, 17643–17649.

98. Malard LM; Pimenta MA; Dresselhaus G and Dresselhaus MS, Raman spectroscopy in graphene. *Phys. Rep.* 473(5-6), **2009**, 51–87.

99. Casiraghi C; Hartschuh A; Qian H; Piscanec S; Georgi C; Fasoli A; Novoselov KS; Basko DM and Ferrari AC, Raman Spectroscopy of Graphene Edges. *Nano. Lett.* 9(4), **2009**, 1433–1441.

100. Sasaki Ki; Tokura Y and Sogawa T, The Origin of Raman D Band: Bonding and Antibonding Orbitals in Graphene. *Crystals* 3(1), **2013**, 120–140.

101. You Y; Ni Z; Yu T and Shen Z, Edge chirality determination of graphene by Raman spectroscopy. *Appl. Phys. Lett.* 93(16), **2008**, 163112.

102. Ferrari AC and Basko DM, Raman spectroscopy as a versatile tool for studying the properties of graphene. *Nat. Nanotechnol.* 8(4), **2013**, 235–246.

103. Cong C; Yu T and Wang H, Raman Study on the G Mode of Graphene for Determination of Edge Orientation. *ACS Nano* 4(6), **2010**, 3175–3180.

104. Tan PH; Han WP; Zhao WJ; Wu ZH; Chang K; Wang H; Wang YF; Bonini N; Marzari N; Pugno N; Savini G; Lombardo A and Ferrari AC, The shear mode of multilayer graphene. *Nat. Mater.* 11(4), **2012**, 294–300.

105. Lee WH; Park J; Sim SH; Lim S; Kim KS; Hong BH and Cho K, Surface-Directed Molecular Assembly of Pentacene on Monolayer Graphene for High-Performance Organic Transistors. *J. Am. Chem. Soc.* 133(12), **2011**, 4447–4454.

106. Ikeda Y; Ishihara Y; Moriwaki T; Kato E and Terada K, A Novel Analytical Method for Pharmaceutical Polymorphs by Terahertz Spectroscopy and the Optimization of Crystal Form at the Discovery Stage. *Chem. Pharm. Bull.* 58(1), **2010**, 76–81.

107. Carriere JT and Havermeyer F, Ultra-low frequency Stokes and anti-Stokes Raman spectroscopy at 785nm with volume holographic grating filters. In *Biomedical Vibrational Spectroscopy V: Advances In Research And Industry*, *Proceedings of SPIE*, vol. 8219, ed. MahadevanJansen, A and Petrich, W, SPIE, SPIE-Int Soc Optical Engineering, 1000 20th St, PO Box 10, Bellingham, WA 98227-0010 USA, **2012**, Conference on Biomedical Vibrational Spectroscopy V - Advances in Research and Industry, San Francisco, CA, JAN 21-22, 2012.

108. Lebedkin S; Blum C; Stuerzi N; Hennrich F and Kappes MM, A low-wavenumber-extended confocal Raman microscope with very high laser excitation line discrimination. *Rev. Sci. Instrum.* 82(1), **2011**, 013705.

109. Rapaport A; Roussel B; Reich HJ; Adar F; Glebov A; Mokhun O; Smirnov V and Glebov L, Very Low Frequency Stokes and Anti-Stokes Raman Spectra Accessible with a Single Multichannel Spectrograph and Volume Bragg Grating Optical Filters. In *XXII International Conference on Raman Spectroscopy*, *AIP Conference Proceedings*, vol. 1267, ed. Champion, PM and Ziegler, LD, NE Univ; Boston Univ & Photon Ctr; Horiba Sci; Thermo Sci; Bruker Opt, Amer Inst Physics, 2 Huntington Quadrangle, Ste 1no1, Melville, NY 11747-4501 USA, **2010**, pp. 808–809, 22nd International Conference on Raman Spectroscopy, Boston, MA, AUG 08-13, 2010.

110. Moser C and Havermeyer F, Ultra-narrow-band tunable laserline notch filter. *Appl. Phys B-Lasers. O.* 95(3), **2009**, 597–601.

111. Moser C and Havermeyer F, Compact Raman spectrometer system for low frequency spectroscopy. In *Optical Components and Materials Vii*, *Proceedings of SPIE-The International Society for Optical Engineering*, vol. 7598, ed. Jiang, S and Digonnet, MJF and Glesener, JW and Dries, JC, SPIE, SPIE-Int Soc Optical Engineering, 1000 20th St, PO Box 10, Bellingham, WA 98227-0010 USA, **2010**, Conference on Optical Components and Materials VII, San Francisco, CA, JAN 26-28, 2010.

112. Tsurumi A; Naito Y and Iwata K, Construction of Multichannel Low-Frequency Raman Microspectrometer of Spectral Coverage to 20 cm(-1) with Gratings Formed in Glass Plates. In *XXII International Conference on Raman Spectroscopy*, *AIP Conference Proceedings*, vol. 1267, ed. Champion, PM and Ziegler, LD, NE Univ; Boston Univ & Photon Ctr; Horiba Sci; Thermo Sci; Bruker Opt, Amer Inst Physics, 2 Huntington Quadrangle, Ste 1no1, Melville, NY 11747-4501 USA, **2010**, pp. 792–793, 22nd International Conference on Raman Spectroscopy, Boston, MA, AUG 08-13, 2010.

113. Barden S; Arns J and Colburn W, Volume-phase holographic gratings and their potential for astronomical applications. In *Optical Astronomical Instrumentation, Pts 1 And 2*, *Proceedings of the Society of Photo-optical Instrumentation Engineers (SPIE)*, vol. 3355, ed. DOdorico, S, SPIE; European So Observ; Amer Astron Soc; Astron Soc Pacific; Canadian Astron Soc, SPIE-Int Soc Optical Engineering, 1000 20th St, Po Box 10, Bellingham, Wa 98227-0010 USA, **1998**, pp. 866–876, SPIE Optical Astronomical Instrumentation Conference, KONA, HI, MAR 26-28, 1998.

114. O'Neill A; Khan U; Nirmalraj PN; Boland J and Coleman JN, Graphene Dispersion and Exfoliation in Low Boiling Point Solvents. *J. Phys. Chem. C.* 115(13), **2011**, 5422–5428.

115. Frank AJ; Cathcart N; Maly KE and Kitaev V, Synthesis of Silver Nanoprisms with Variable Size and Investigation of Their Optical Properties: A First-Year Undergraduate Experiment Exploring Plasmonic Nanoparticles. *J. Chem. Educ.* 87(10), **2010**, 1098–1101.

116. Cathcart N; Frank AJ and Kitaev V, Silver nanoparticles with planar twinned defects: effect of halides for precise tuning of plasmon resonance maxima from 400 to $>$ 900 nm. *Chem. Commun.* (46), **2009**, 7170–7172.

117. Li X; Wang X; Zhang L; Lee S and Dai H, Chemically derived, ultrasmooth graphene nanoribbon semiconductors. *Science* 319(5867), **2008**, 1229–1232.

118. Jiang De; Sumpter BG and Dai S, Unique chemical reactivity of a graphene nanoribbon's zigzag edge. *J. Chem. Phys.* 126(13), **2007**, 134701.

119. Tuinstra F and Koenig J, Raman Spectrum of Graphite. *J. Chem. Phys.* 53(3), **1970**, 1126–1130.

120. Vidano R and Fischbach D, New Lines in the Raman Spectra of Carbons and Graphite. *J. Am. Ceram. Soc.* 61(1-2), **1978**, 13–17.

121. Nemanich R and Solin S, Observation of an anomolously sharp feature in the 2nd order Raman spectrum of graphite. *Solid State Commun.* 23(7), **1977**, 417–420.

122. Nemanich R and Solin S, First- and second-order Raman scattering from finite-size crystals of graphite. *Phys. Rev. B* 20(2), **1979**, 392–401.

123. Vidano R; Fischbach D; Willis L and Loehr T, Observation of Raman band shifting with excitation wavelength for carbons and graphites. *Solid State Commun.* 39(2), **1981**, 341–344.

124. Pocsik I; Hundhausen M; Koos M and Ley L, Origin of the D peak in the Raman spectrum of microcrystalline graphite. *J. Non-Cryst. Solids* 227(B), **1998**, 1083–1086, 17th International Conference on Amorphous and Microcrystalline Semiconductors - Science and Technology (ICAMS 17), BUDAPEST, HUNGARY, AUG 25-29, 1997.

125. Thomsen C and Reich S, Double resonant Raman scattering in graphite. *Phys. Rev. Lett.* 85(24), **2000**, 5214–5217.

126. Krauss B; Nemes-Incze P; Skakalova V; Biro LP; von Klitzing K and Smet JH, Raman Scattering at Pure Graphene Zigzag Edges. *Nano Lett.* 10(11), **2010**, 4544–4548.

127. Sasaki Ki; Yamamoto M; Murakami S; Saito R; Dresselhaus MS; Takai K; Mori T; Enoki T and Wakabayashi K, Kohn anomalies in graphene nanoribbons. *Phys. Rev. B* 80(15), **2009**, 155450.

128. Sasaki Ki; Saito R; Wakabayashi K and Enoki T, Identifying the Orientation of Edge of Graphene Using G Band Raman Spectra. *J. Phys. Soc. Jpn.* 79(4), **2010**, 044603.

129. Tsurumi J; Saito Y and Verma P, Evaluation of the interlayer interactions of few layers of graphene. *Chem. Phys. Lett.* 557, **2013**, 114–117.

130. Tommasini M; Castiglioni C and Zerbi G, Raman scattering of molecular graphenes. *Phys. Chem. Chem. Phys.* 11(43), **2009**, 10185–10194.

131. Peticolas W; Nafie L; Stein P and Fanconi B, Quantum Theory of the Intensities of Molecular Vibrational Spectra. *J. Chem. Phys.* 52(3), **1970**, 1576–1584.

132. Coleman JN, Liquid Exfoliation of Defect-Free Graphene. *Accounts Chem. Res.* 46(1), **2013**, 14–22.

133. Lotya M; King PJ; Khan U; De S and Coleman JN, High-Concentration, Surfactant-Stabilized Graphene Dispersions. *ACS Nano* 4(6), **2010**, 3155–3162.

134. Vadukumpully S; Paul J and Valiyaveettil S, Cationic surfactant mediated exfoliation of graphite into graphene flakes. *Carbon* 47(14), **2009**, 3288–3294.

135. Smith RJ; Lotya M and Coleman JN, The importance of repulsive potential barriers for the dispersion of graphene using surfactants. *New J. Phys.* 12, **2010**, 125008.

136. Nishinakagawa R; Matsuda K; Arai T; Sawada A and Terashima T, Raman spectroscopy investigations of chemically derived zigzag edge graphene nanoribbons. *AIP Adv.* 3(9), **2013**, 092111.

137. Wu D; Gao X; Zhou Z and Chen Z, *Understanding Aromaticity of Graphene and Graphene Nanoribbons by the Clar Sextet Rule*. John Wiley & Sons, Ltd, **2013**, pp. 29–49, URL `http://dx.doi.org/10.1002/9781118691281.ch3`.

138. Bellunato A; Tash HA; Cesa Y and Schneider GF, Chemistry at the Edge of Graphene. *ChemPhysChem* 17(6), **2016**, 785–801.

139. Fujii S and Enoki T, Nanographene and Graphene Edges: Electronic Structure and Nanofabrication. *Acc. Chem. Res.* 46(10), **2013**, 2202–2210.

140. Martin-Martinez FJ; Fias S; Van Lier G; De Proft F and Geerlings P, Electronic Structure and Aromaticity of Graphene Nanoribbons. *Chem. Eur. J.* 18(20), **2012**, 6183–6194.

141. Brooksby PA; Farquhar AK; Dykstra HM; Waterland MR and Downard AJ, Quantum Capacitance of Aryldiazonium Modified Large Area Few-Layer Graphene Electrodes. *J. Phys. Chem. C* 119(46), **2015**, 25778–25785.

142. Georgakilas V; Otyepka M; Bourlinos AB; Chandra V; Kim N; Kemp KC; Hobza P; Zboril R and Kim KS, Functionalization of Graphene: Covalent and Non-Covalent Approaches, Derivatives and Applications. *Chem. Rev.* 112(11), **2012**, 6156–6214.

143. Sreeprasad TS and Berry V, How Do the Electrical Properties of Graphene Change with its Functionalization? *Small* 9(3), **2013**, 341–350.

144. Paulus GLC; Wang QH and Strano MS, Covalent Electron Transfer Chemistry of Graphene with Diazonium Salts. *Acc. Chem. Res.* 46(1, SI), **2013**, 160–170.

145. Farquhar AK; Dykstra HM; Waterland MR; Downard AJ and Brooksby PA, Spontaneous Modification of Free-Floating Few-Layer Graphene by Aryldiazonium Ions: Electrochemistry, Atomic Force Microscopy, and Infrared Spectroscopy from Grafted Films. *J. Phys. Chem. C* 120(14), **2016**, 7543–7552.

146. Chen G; Zhai S; Zhai Y; Zhang K; Yue Q; Wang L; Zhao J; Wang H; Liu J and Jia J, Preparation of sulfonic-functionalized graphene oxide as ion-exchange material and its application into electrochemiluminescence analysis. *Biosens. Bioelectron.* 26(7), **2011**, 3136–3141.

147. Martin-Martinez FJ; Fias S; Van Lier G; De Proft F and Geerlings P, Tuning aromaticity patterns and electronic properties of armchair graphene nanoribbons with chemical edge functionalisation. *Phys. Chem. Chem. Phys.* 15(30), **2013**, 12637–12647.

148. Jeon IY; Choi HJ; Jung SM; Seo JM; Kim MJ; Dai L and Baek JB, Large-Scale Production of Edge-Selectively Functionalized Graphene Nanoplatelets via Ball Milling and Their Use as Metal-Free Electrocatalysts for Oxygen Reduction Reaction. *J. Am. Chem. Soc.* 135(4), **2013**, 1386–1393.

149. Bian S; Scott AM; Cao Y; Liang Y; Osuna S; Houk KN and Braunschweig AB, Covalently Patterned Graphene Surfaces by a Force-Accelerated Diels-Alder Reaction. *J. Am. Chem. Soc.* 135(25), **2013**, 9240–9243.

150. Seo JM; Jeon IY and Baek JB, Mechanochemically driven solid-state Diels-Alder reaction of graphite into graphene nanoplatelets. *Chem. Sci.* 4(11), **2013**, 4273–4277.

151. Si Y and Samulski ET, Synthesis of water soluble graphene. *Nano Lett.* 8(6), **2008**, 1679–1682.

152. Chien HC; Tsai LD; Huang CP; Kang Cy; Lin JN and Chang FC, Sulfonated graphene oxide/Nafion composite membranes for high-performance direct methanol fuel cells. *Int. J. Hydrogen Energy* 38(31), **2013**, 13792–13801.

153. Shen Y and Chen B, Sulfonated Graphene Nanosheets as a Superb Adsorbent for Various Environmental Pollutants in Water. *Environ. Sci. Technol.* 49(12), **2015**, 7364–7372.

154. Hou H; Hu X; Liu X; Hu W; Meng R and Li L, Sulfonated graphene oxide with improved ionic performances. *Ionics* 21(7), **2015**, 1919–1923.

155. Coskun E; Zaragoza-Contreras EA and Salavagione HJ, Synthesis of sulfonated graphene/polyaniline composites with improved electroactivity. *Carbon* 50(6), **2012**, 2235–2243.

156. Zhao G; Jiang L; He Y; Li J; Dong H; Wang X and Hu W, Sulfonated Graphene for Persistent Aromatic Pollutant Management. *Adv. Mater.* 23(34), **2011**, 3959–3963.

157. Zhang L; Shi T; Wu S and Zhou H, Sulfonated graphene oxide: the new and effective material for synthesis of polystyrene-based nanocomposites. *Colloid Polym. Sci.* 291(9), **2013**, 2061–2068.

158. Liu F; Sun J; Zhu L; Meng X; Qi C and Xiao FS, Sulfated graphene as an efficient solid catalyst for acid-catalyzed liquid reactions. *J. Mater. Chem.* 22(12), **2012**, 5495–5502.

159. Hung TF; Wang B; Tsai CW; Tu MH; Wang GX; Liu RS; Tsai DP; Lo MY; Shy DS and Xing XK, Sulfonation of graphene nanosheet-supported platinum via a simple thermal-treatment toward its oxygen reduction activity in acid medium. *Int. J. Hydrogen Energy* 37(19), **2012**, 14205–14210.

160. Choi BG; Park H; Yang MH; Jung YM; Lee SY; Hong WH and Park TJ, Microwave-assisted synthesis of highly water-soluble graphene towards electrical DNA sensor. *Nanoscale* 2(12), **2010**, 2692–2697.

161. Garg B; Bisht T and Ling YC, Sulfonated graphene as highly efficient and reusable acid carbocatalyst for the synthesis of ester plasticizers. *RSC Adv.* 4(100), **2014**, 57297–57307.

162. Liu J; Xue Y and Dai L, Sulfated Graphene Oxide as a Hole-Extraction Layer in High-Performance Polymer Solar Cells. *J. Phys. Chem. Lett.* 3(14), **2012**, 1928–1933.

163. Sam S; Touahir L; Andresa JS; Allongue P; Chazalviel JN; Gouget-Laemmel AC; de Villeneuve CH; Moraillon A; Ozanam F; Gabouze N and Djebbar S, Semiquantitative Study of the EDC/NHS Activation of Acid Terminal Groups at Modified Porous Silicon Surfaces. *Langmuir* 26(2), **2010**, 809–814.

164. Larmour IA; Bell SEJ and Saunders GC, Remarkably simple fabrication of superhydrophobic surfaces using electroless galvanic deposition. *Angew. Chem. Int. Ed.* 46(10), **2007**, 1710–1712.

165. Takahashi M, Terahertz Vibrations and Hydrogen-Bonded Networks in Crystals. *Crystals* 4(2), **2014**, 74–103.

166. Li R; Zeitler JA; Tomerini D; Parrott EPJ; Gladden LF and Day GM, A study into the effect of subtle structural details and disorder on the terahertz spectrum of crystalline benzoic acid. *Phys. Chem. Chem. Phys.* 12(20), **2010**, 5329–5340.

167. Saathoff JD and Clancy P, Simulation of Graphene Nanoribbon Aggregation and Its Mediation by Edge Decoration. *J. Phys. Chem. B* 119(13), **2015**, 4766–4776.

168. Saathoff JD and Clancy P, Effect of edge-functionalization on the ease of graphene nanoribbon aggregation in solvent. *Carbon* 115, **2017**, 154–161.

169. Shih CJ; Lin S; Strano MS and Blankschtein D, Understanding the Stabilization of Liquid-Phase-Exfoliated Graphene in Polar Solvents: Molecular Dynamics Simulations and Kinetic Theory of Colloid Aggregation. *J. Am. Ceram. Soc.* 132(41), **2010**, 14638–14648.

170. Tummala NR; Grady BP and Striolo A, Lateral confinement effects on the structural properties of surfactant aggregates: SDS on graphene. *Phys. Chem. Chem. Phys.* 12(40), **2010**, 13137–13143.

8 Appendix A

8.1 Calculation for Monolayer Coverage of SDS on GNRs

Calculation for a GNR sample size $\sim 2 \times 10^{-9}$ GNRs, ribbon length 5 μm and width 100 nm.

Surface area per GNR: $2 \times (5000 \text{ nm} \times 100 \text{ nm}) = 10^6 \text{ nm}^2$

Total surface area: $(8 \times 10^4) \times (10^6 \text{ nm}^2) = 8 \times 10^{17} \text{ nm}^2$

Surface coverage of SDS $\sim$ 1 molecule per nm^2 for monolayer coverage.[170] Thus, 8×10^{17} nm^2 SDS molecules are required for surface coverage, or 1.3×10^{-6} mol SDS. In a 0.5 mL solution, this corresponds to a surfactant concentration of 0.0011 M.

8.2 Estimation of Edge:Basal Carbon Ratios in GNRs

The ratio of edge carbons per 100 basal plane carbons are calculated for GNRs with widths 100 nm, 50 nm and 20 nm. As shown in figure 112, there is one edge C atom per 0.246 nm length of edge for zigzag GNRs, and 2 edge C atoms per 0.426 nm of edge for armchair GNRs. The results of these calculations are summarised in table 6, which shows the results for zigzag and armchair-edged GNRs of different widths. Due to the ribbons likely having mixed zigzag/armchair geometry at the edges, the average expected values of these disordered ribbons are also included.

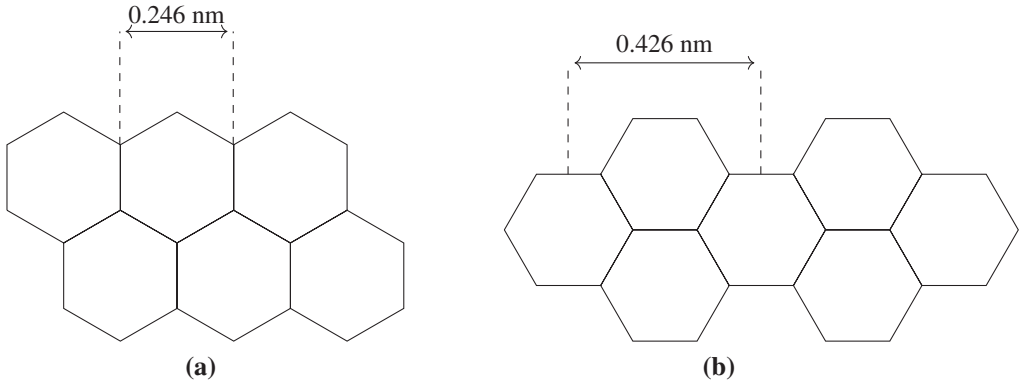

Figure 112: Edge unit cells for segments of (a) zigzag and (b) armchair GNRs.

Table 6: Calculated numbers of edge C atoms per 100 basal C atoms in GNRs.

	Zigzag	**Armchair**	**Average**
100 nm	0.21	0.25	0.23
50 nm	0.43	0.50	0.46
20 nm	1.08	1.25	1.17

9 Appendix B

9.1 Additional AFM images

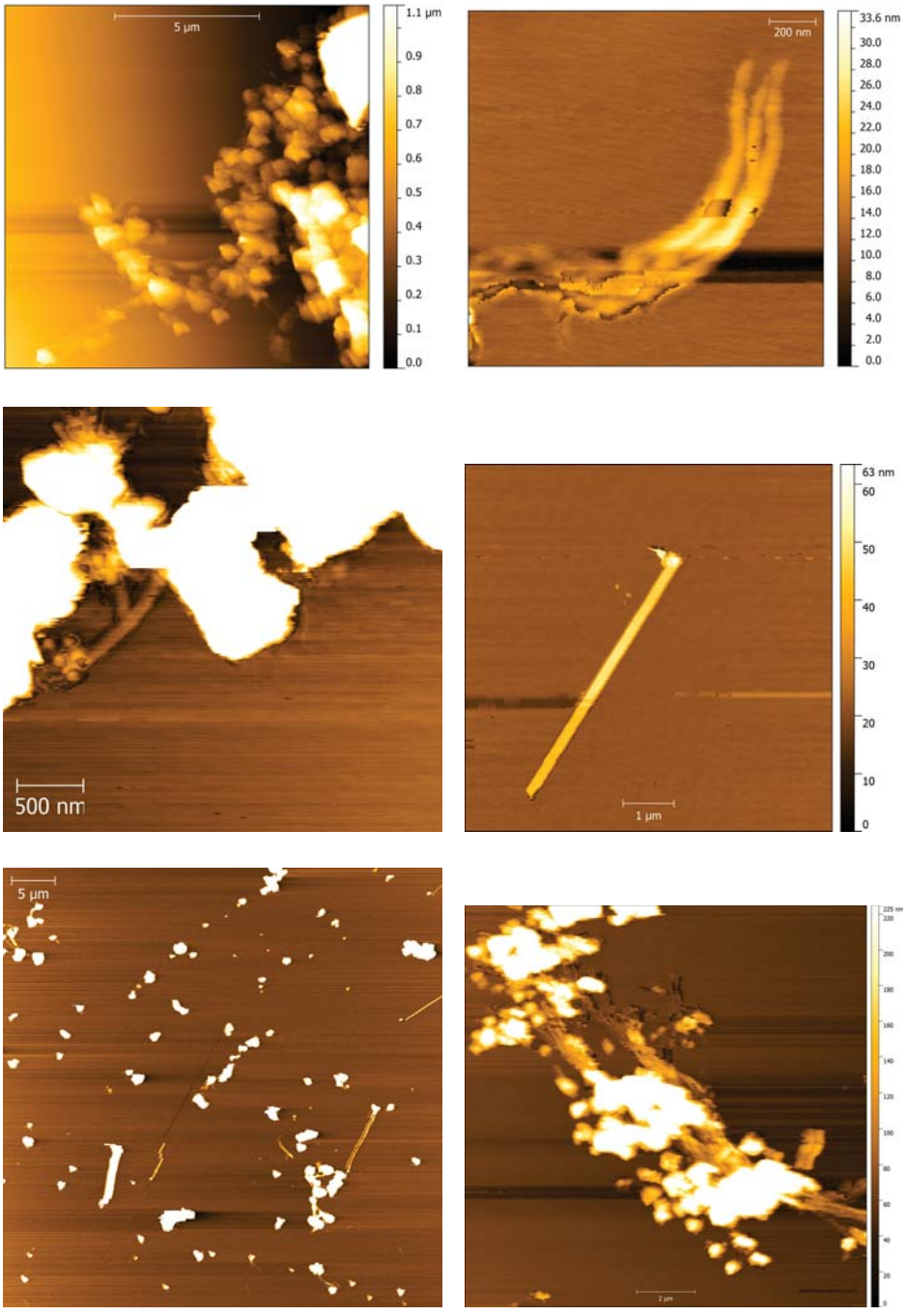

Figure 113: AFM images of GNRs cut at 100 nm width, showing numerous aggregates with some single-layer and few-layer ribbons.

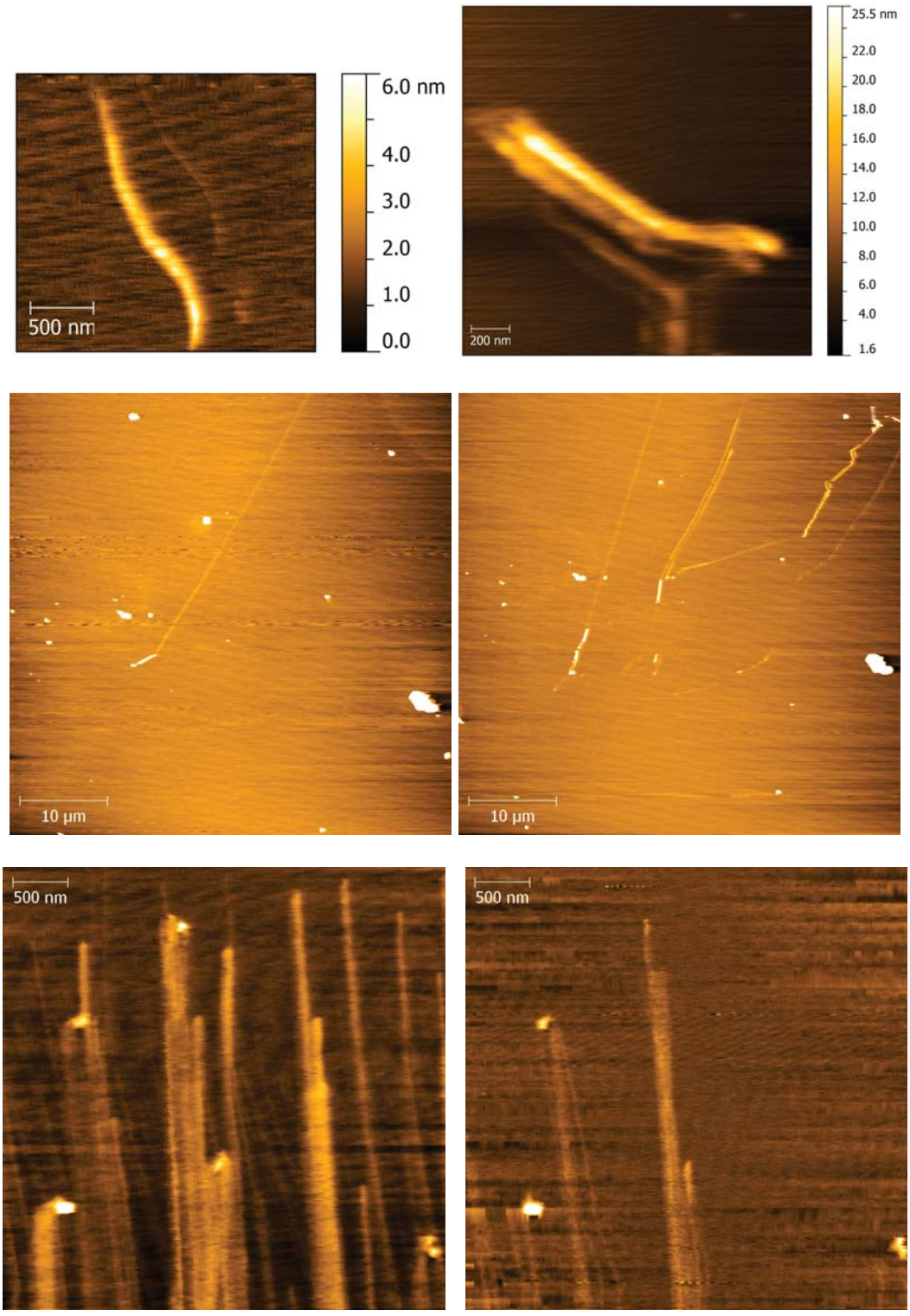

Figure 114: Figure 113 continued

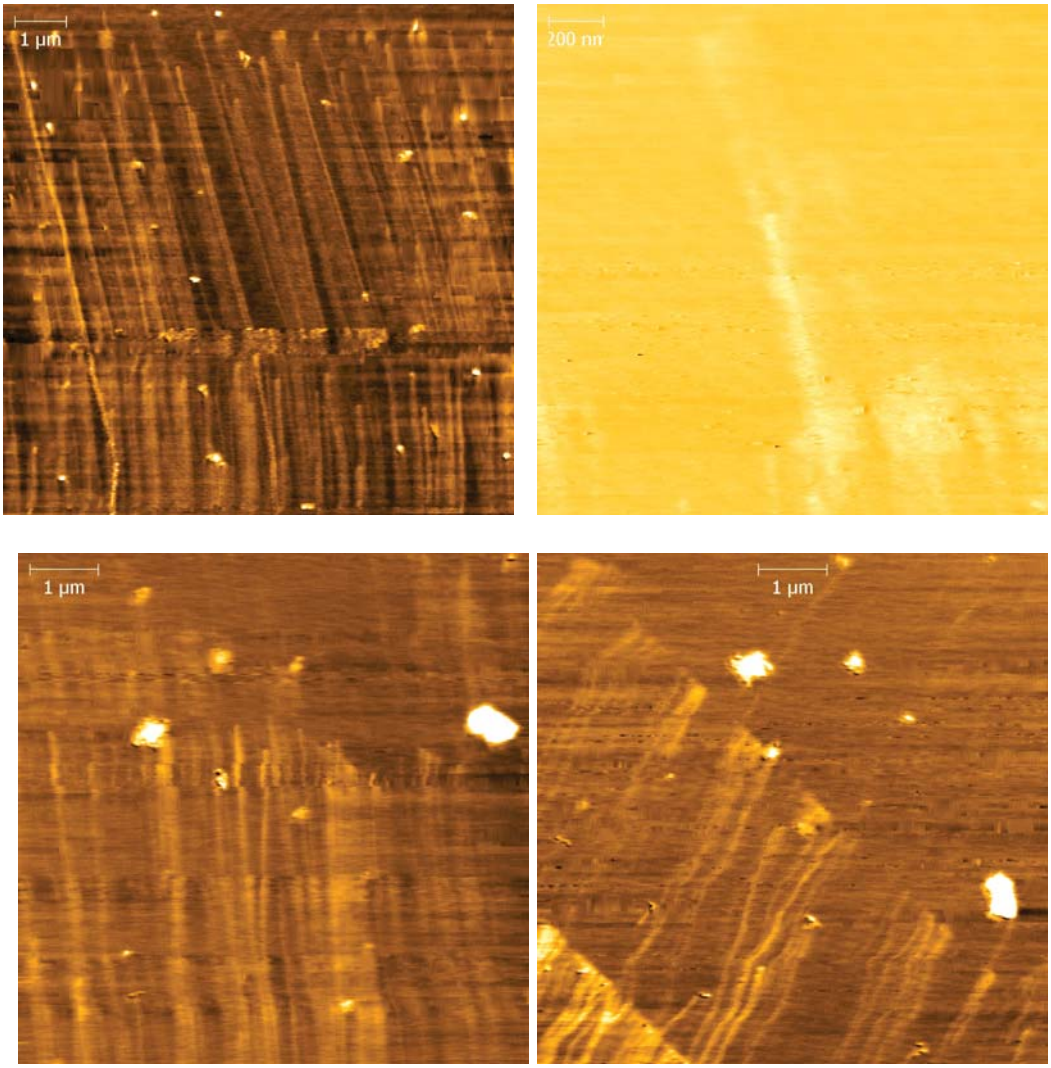

Figure 115: Figure 113 continued

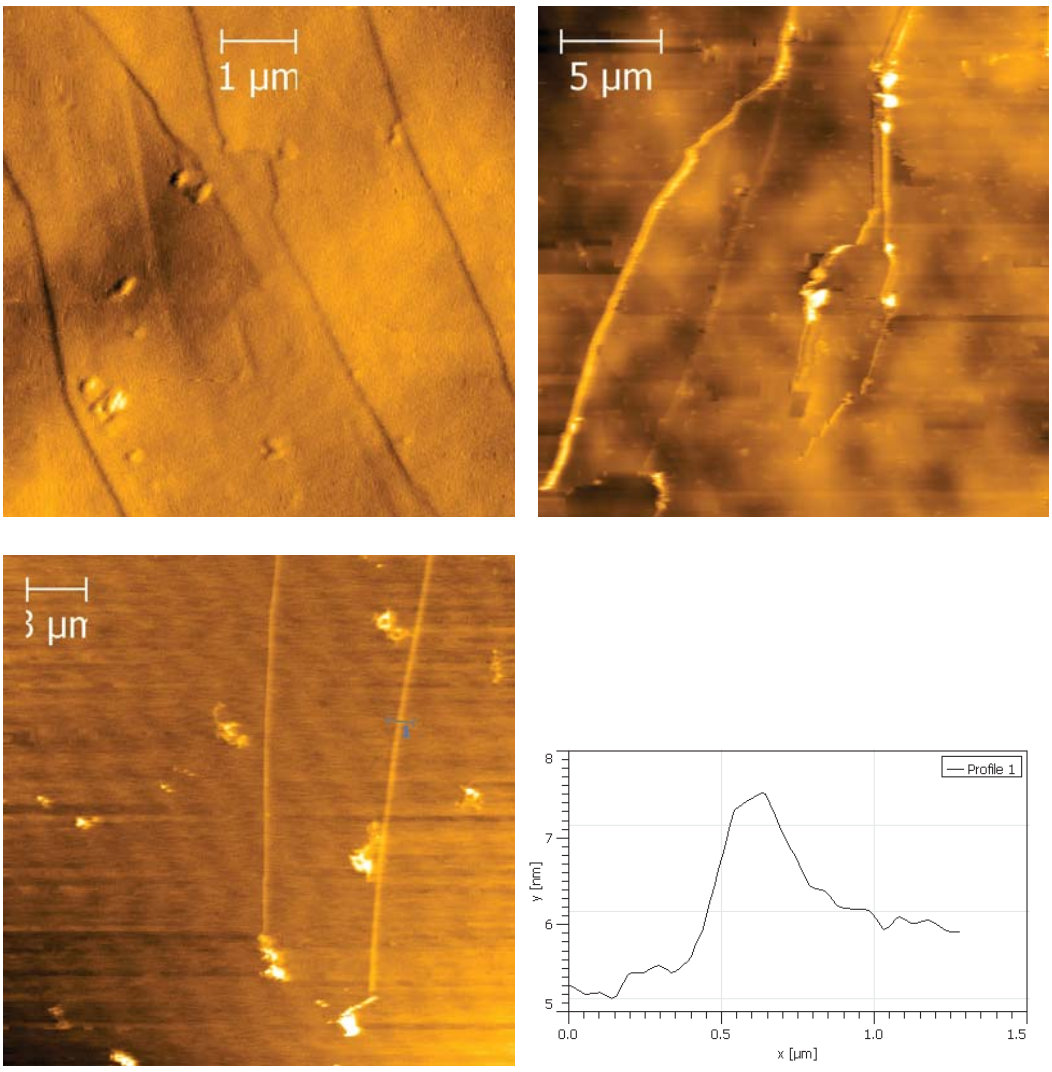

Figure 116: 100 nm GNRs on an HOPG substrate.

9.2 Additional TEM images

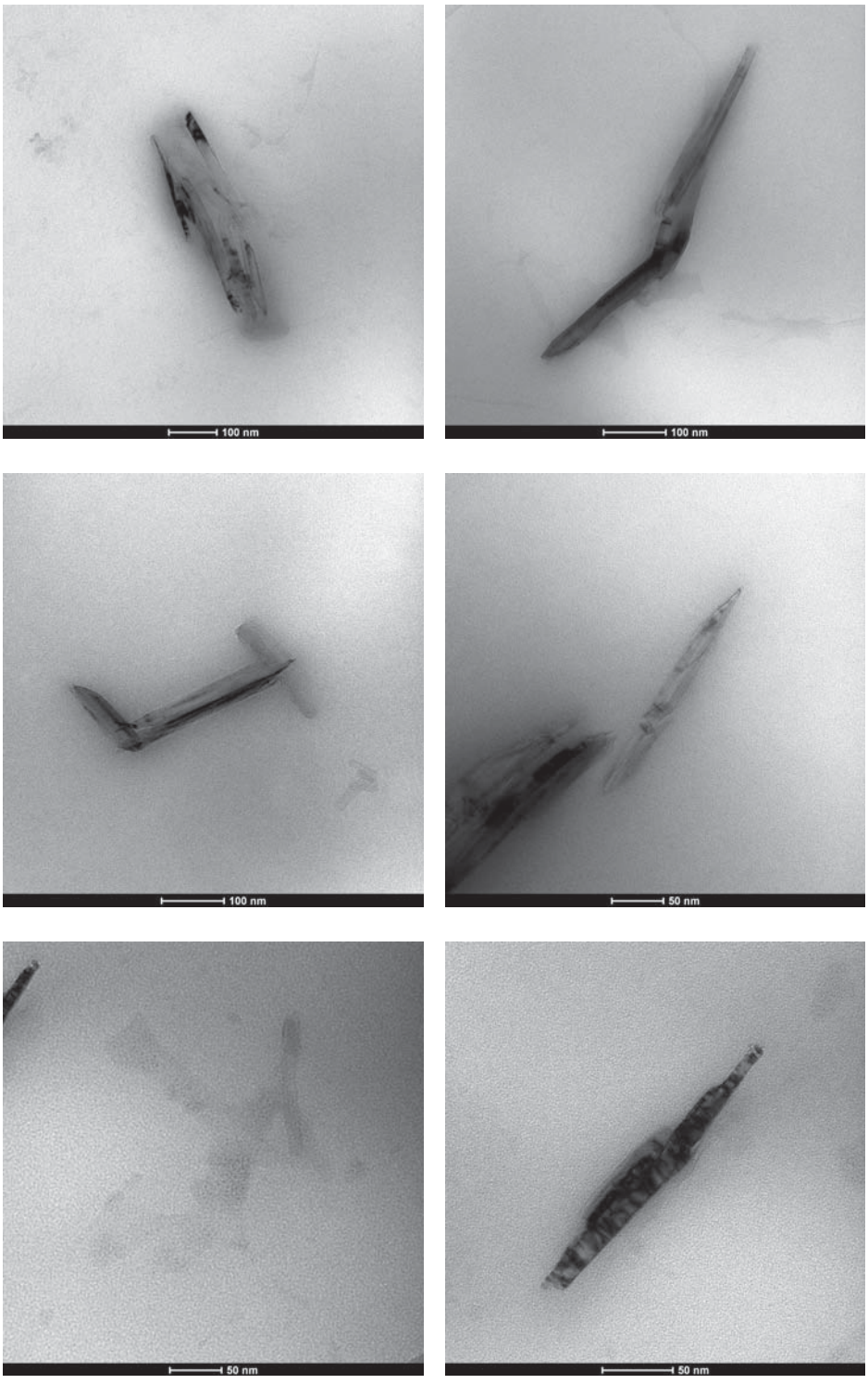

Figure 117: TEM images of 20 nm GNRs.

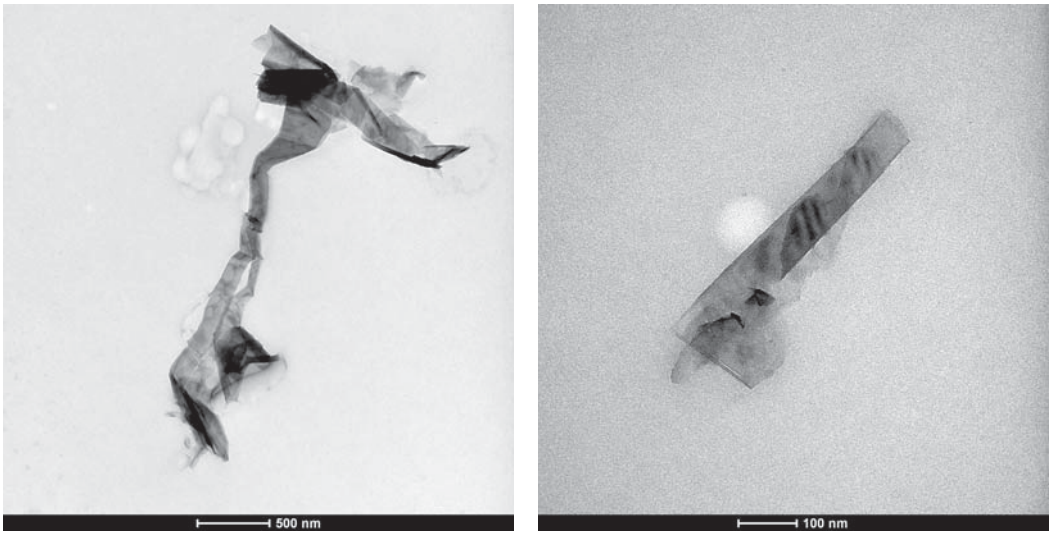

Figure 118: Figure 117 continued.

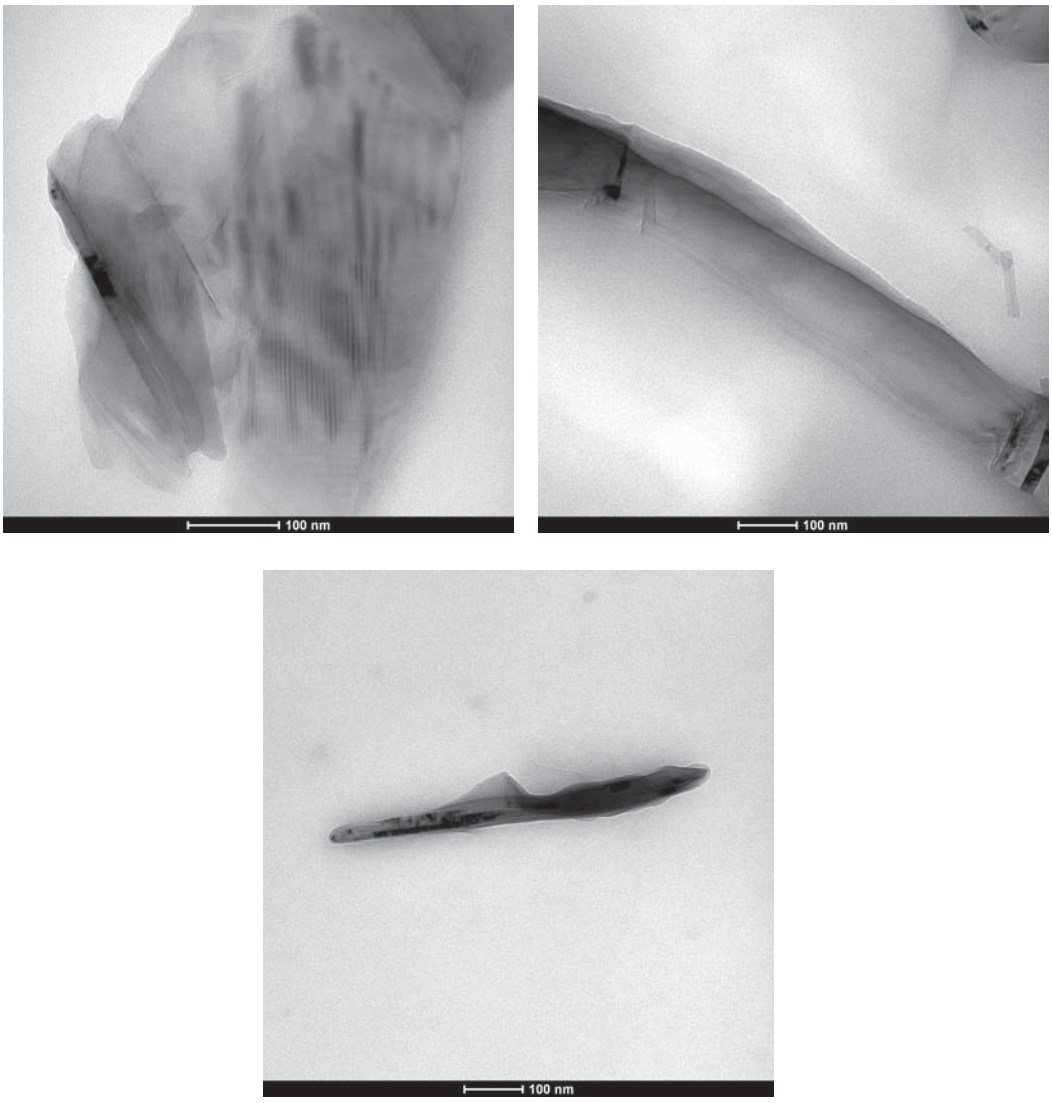

Figure 119: TEM images of 50 nm GNRs.

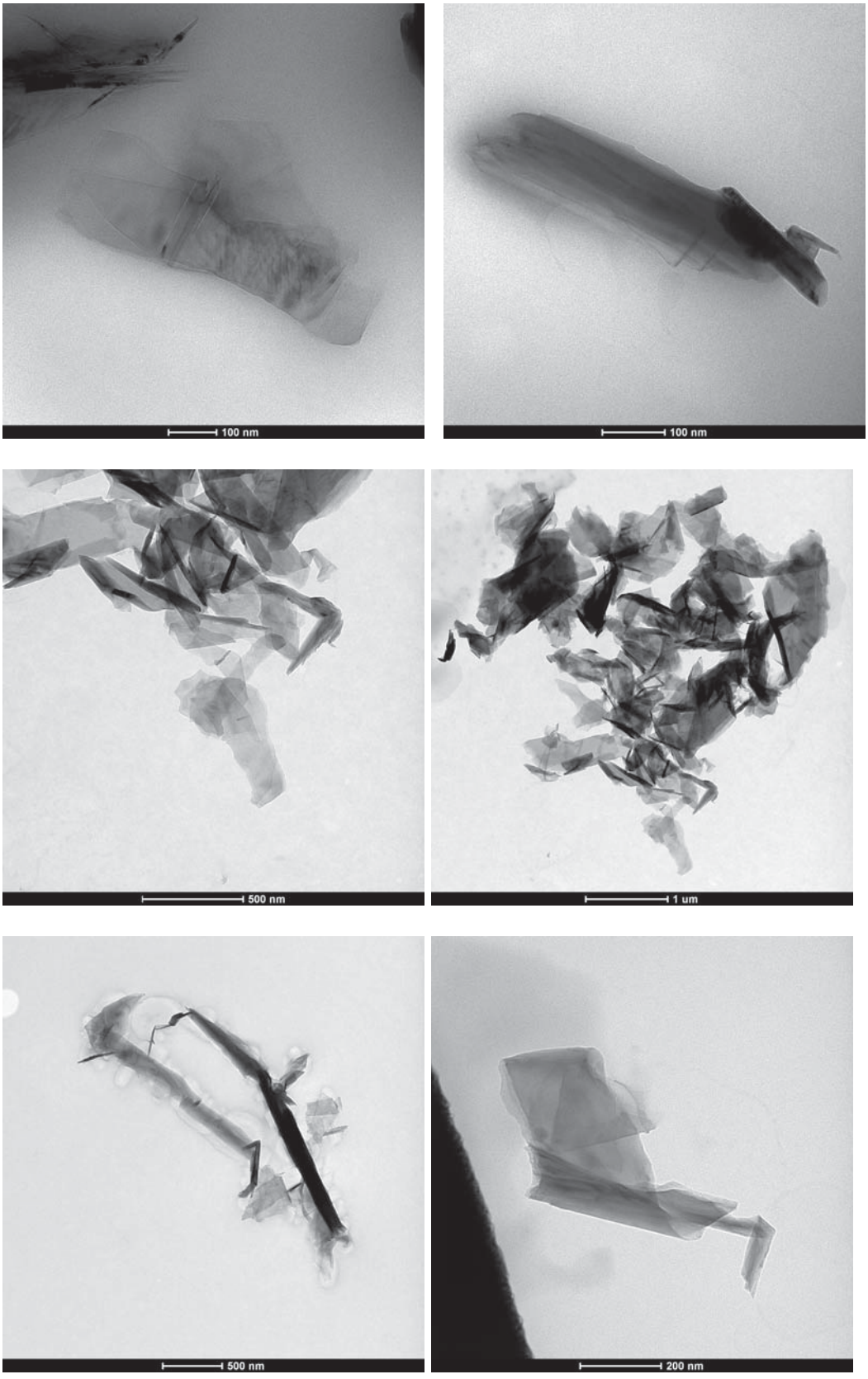

Figure 120: TEM images of 100 nm GNRs.

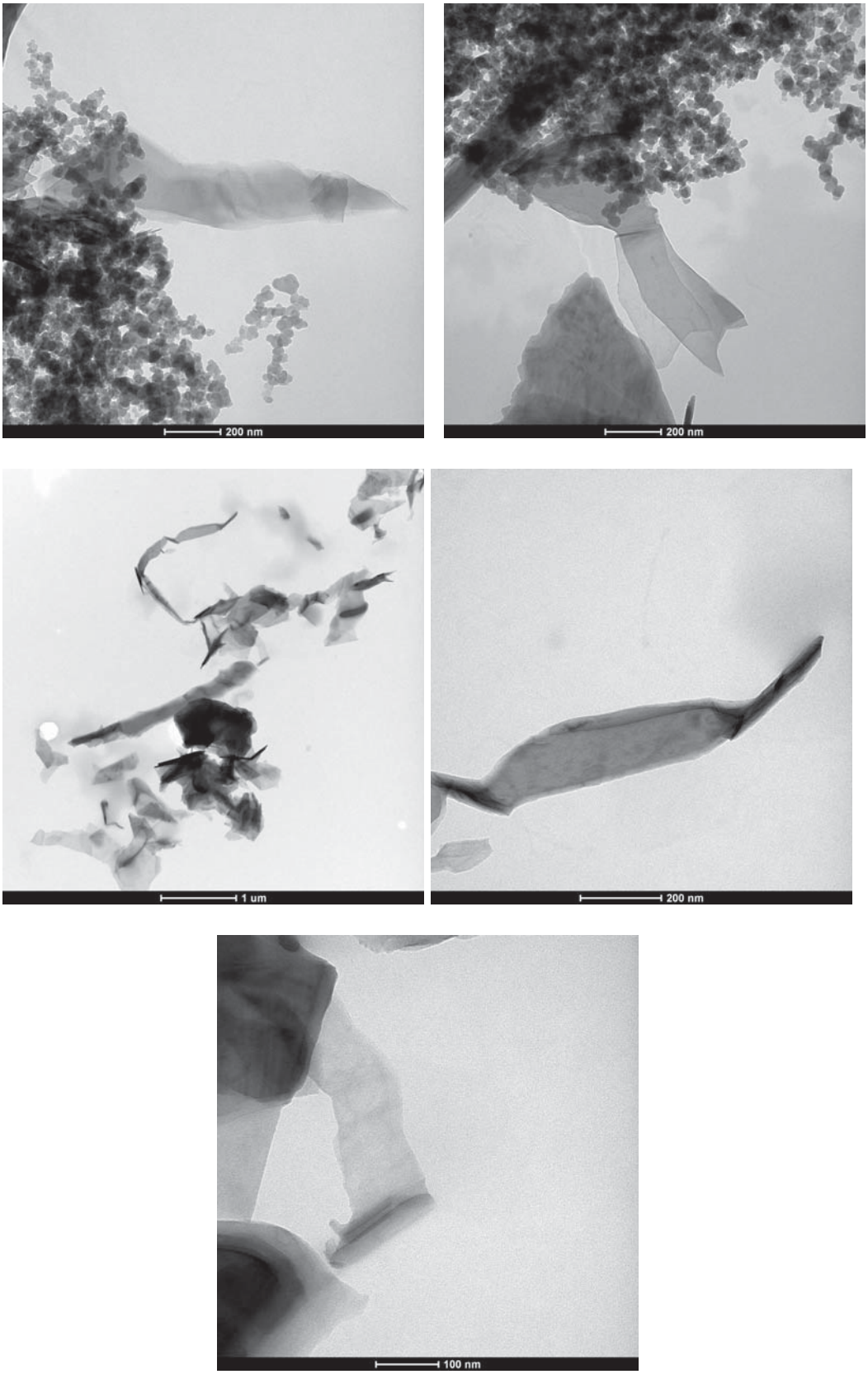

Figure 121: Figure 120 continued.

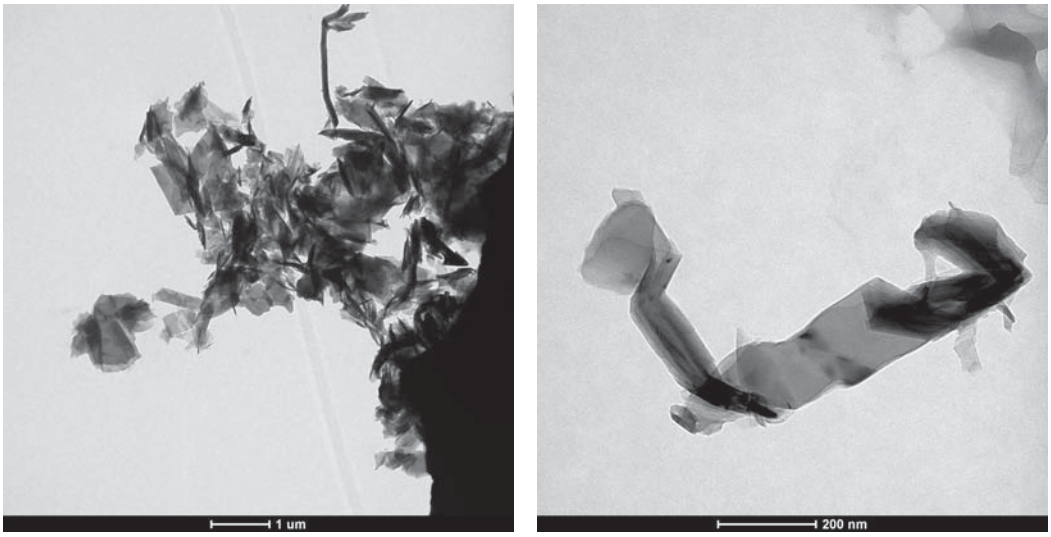

Figure 122: Figure 120 continued.

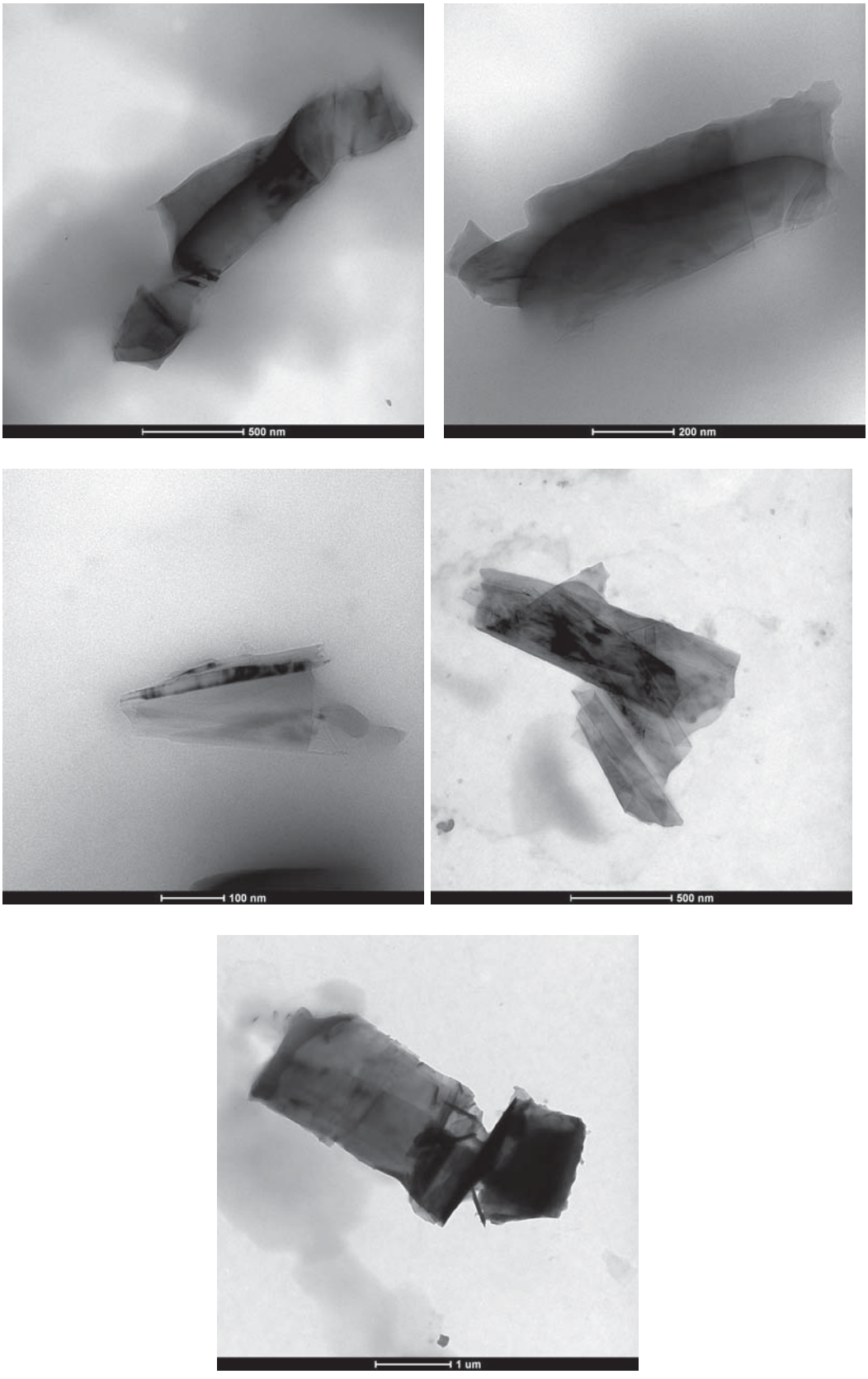

Figure 123: TEM images 0f 300 nm GNRs.

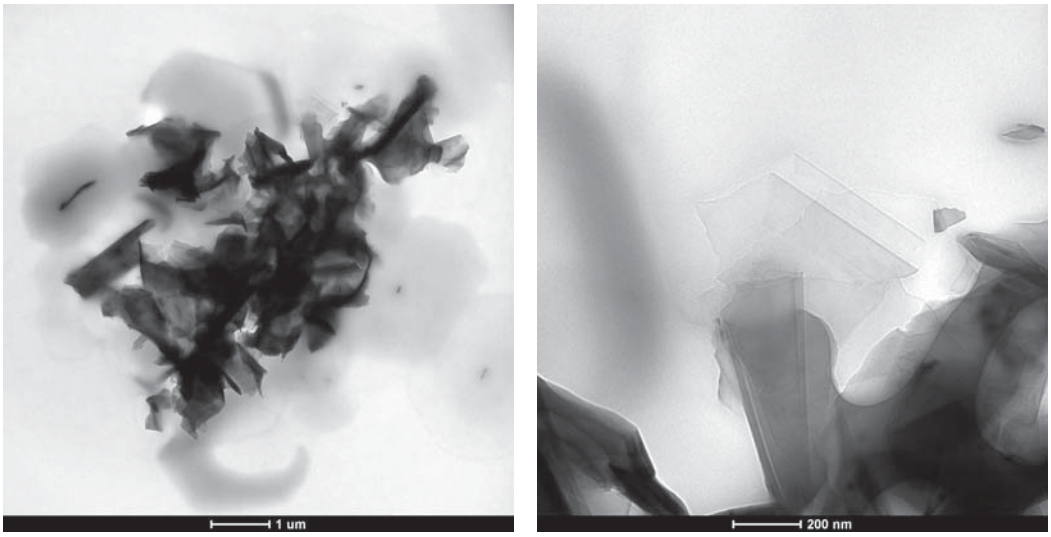

Figure 124: TEM images 0f 500 nm GNRs.

9.3 Additional Raman data

9.3.1 HOPG

Figure 125 compares the Raman spectra of the edge side of an HOPG block, the smooth side of an HOPG block and a disordered graphite sheet. Given in figure 126 are polarised Raman spectra of the smooth face and cut edge sides of the HOPG block. The input laser beam was linearly polarised. For the smooth face side of HOPG, without a linear polariser in the path of the scattered beam, the background is quite high and there is no evidence of a D band, suggesting a largely defect- and edge-free sample area. With a linear polariser in the scattered beam path, the G band shows a polarisation dependence, with $I(G)_{min}$ occurring with the polariser set perpendicular to the input polarisation, and $I(G)_{max}$ occurring with parallel polarisation. With parallel polarisation, the background intensity is also greatly reduced, revealing a low intensity D band. For the edge side of HOPG, a similar effect is seen. The D band at the edge side is much more intense than at the face, as expected, as is the D' band. The shear bands are visible in both edge and face spectra.

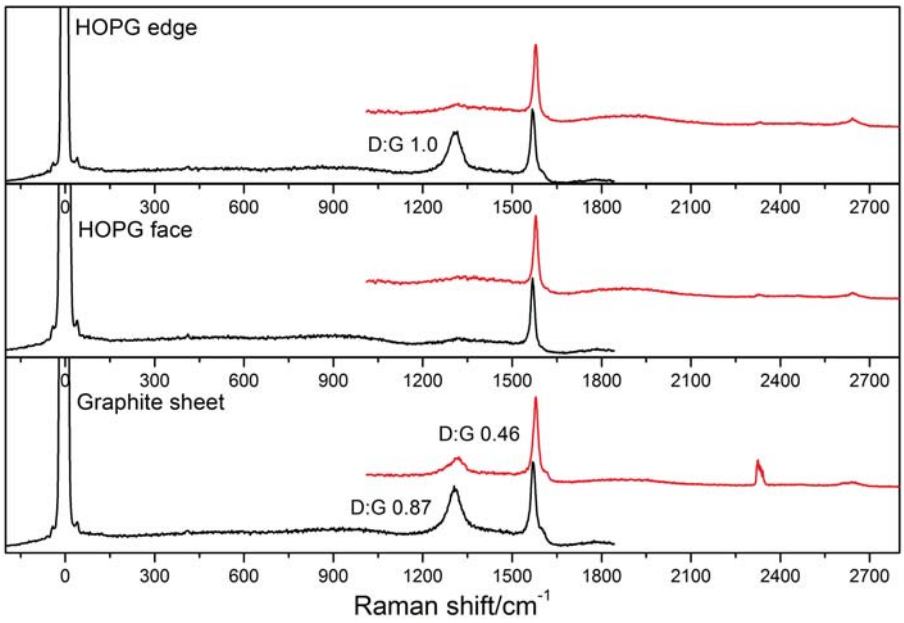

Figure 125: Raman spectra of HOPG basal plane, edge of HOPG block and disordered graphite sheet. Spectra were acquired with 785 nm excitation.

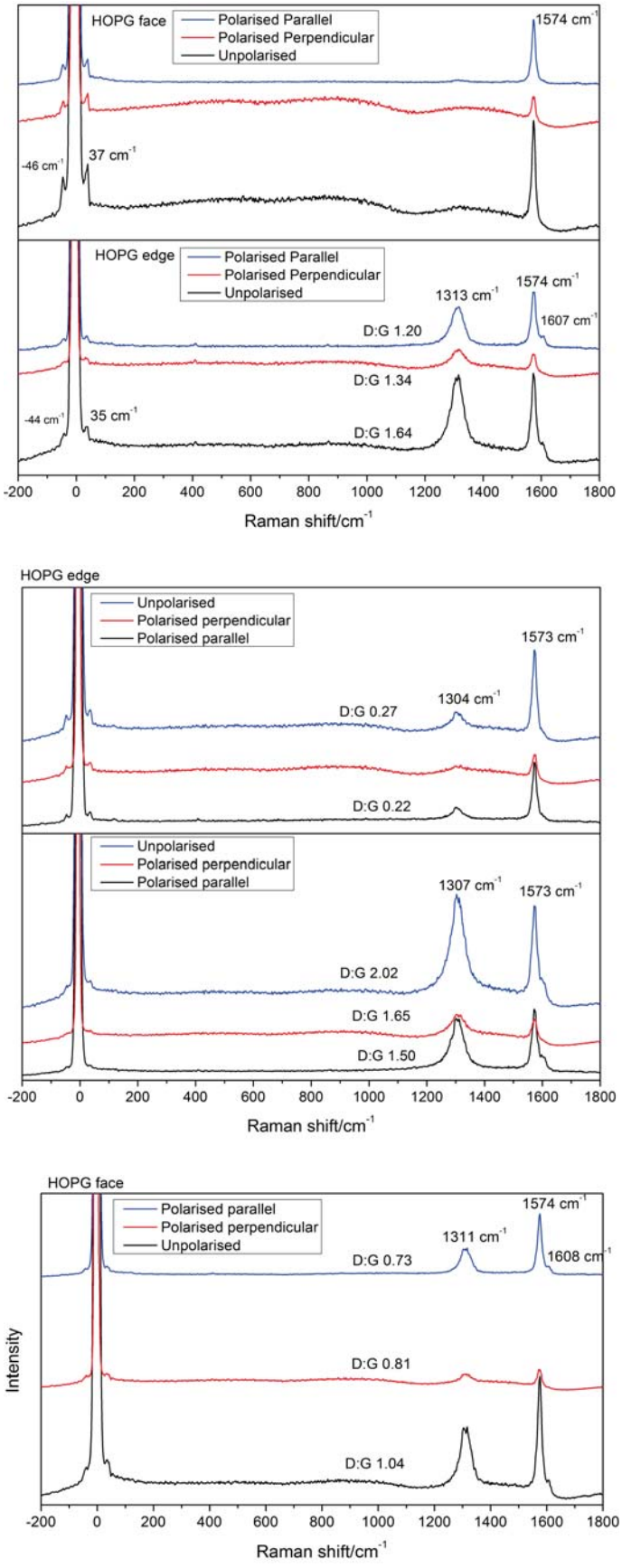

Figure 126: Raman spectra at various positions on the edge and face sides of an HOPG block. Raman spectra were acquired with 785 nm excitation. For the polarised spectra, a linear polariser was used in the scattered beam path.

9.3.2 Graphene test samples

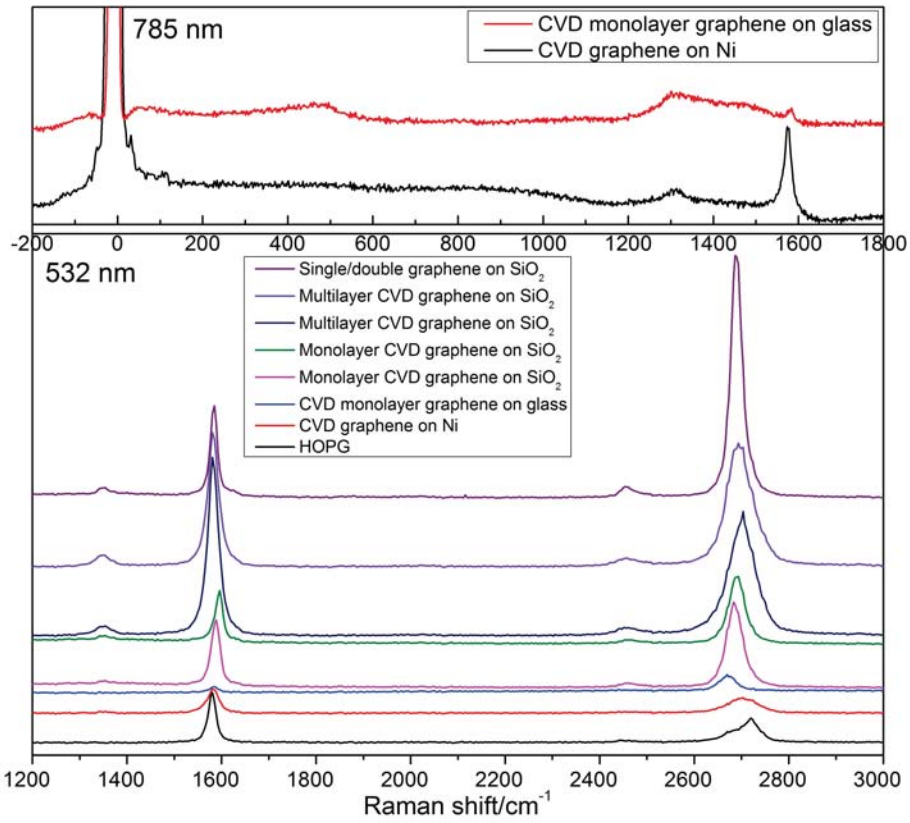

Figure 127: Raman spectra of various graphene samples. Spectra were acquired with 785 nm and 532 nm excitation.

9.3.3 GNRs

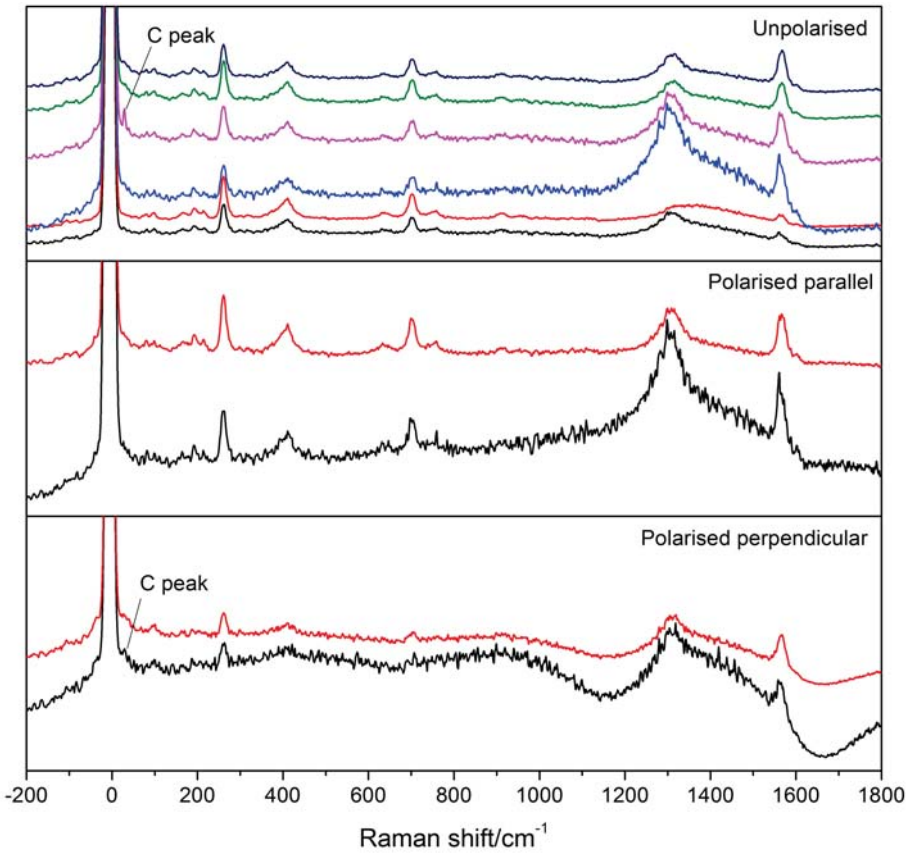

Figure 128: Raman spectra of 100 nm GNR on a mica substrate. Spectra were acquired with 532 nm excitation. The non-graphene peaks in the spectra are due to the mica substrate. For the polarised spectra, a linear polariser was used in the scattered beam path.

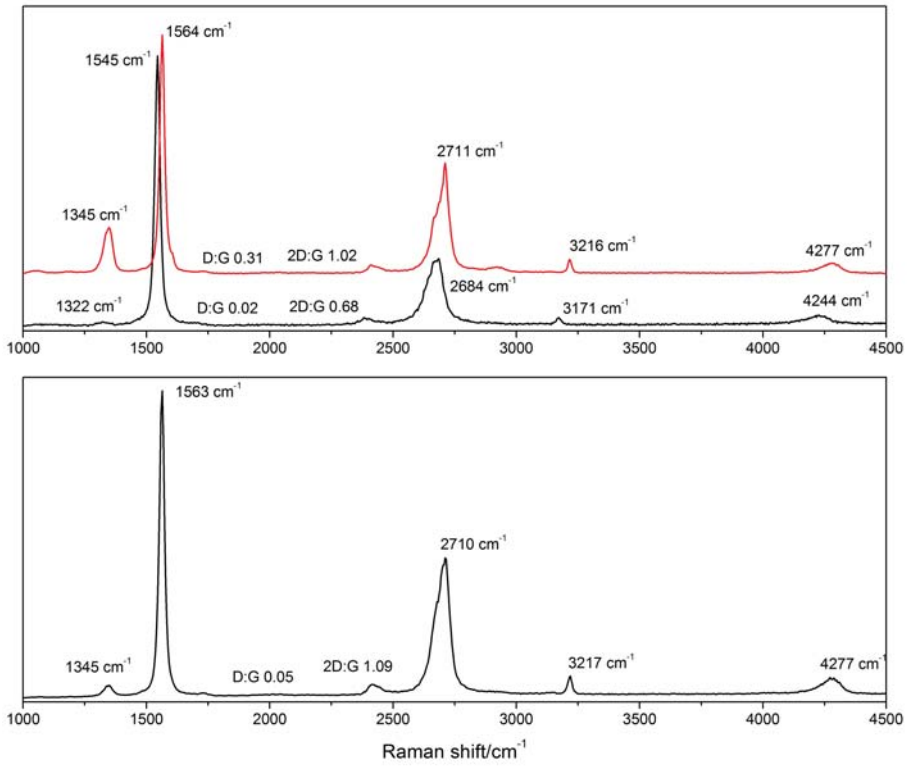

Figure 129: Raman spectra of small 500 nm wet-cut GNR aggregates. Spectra were acquired with 532 nm excitation.

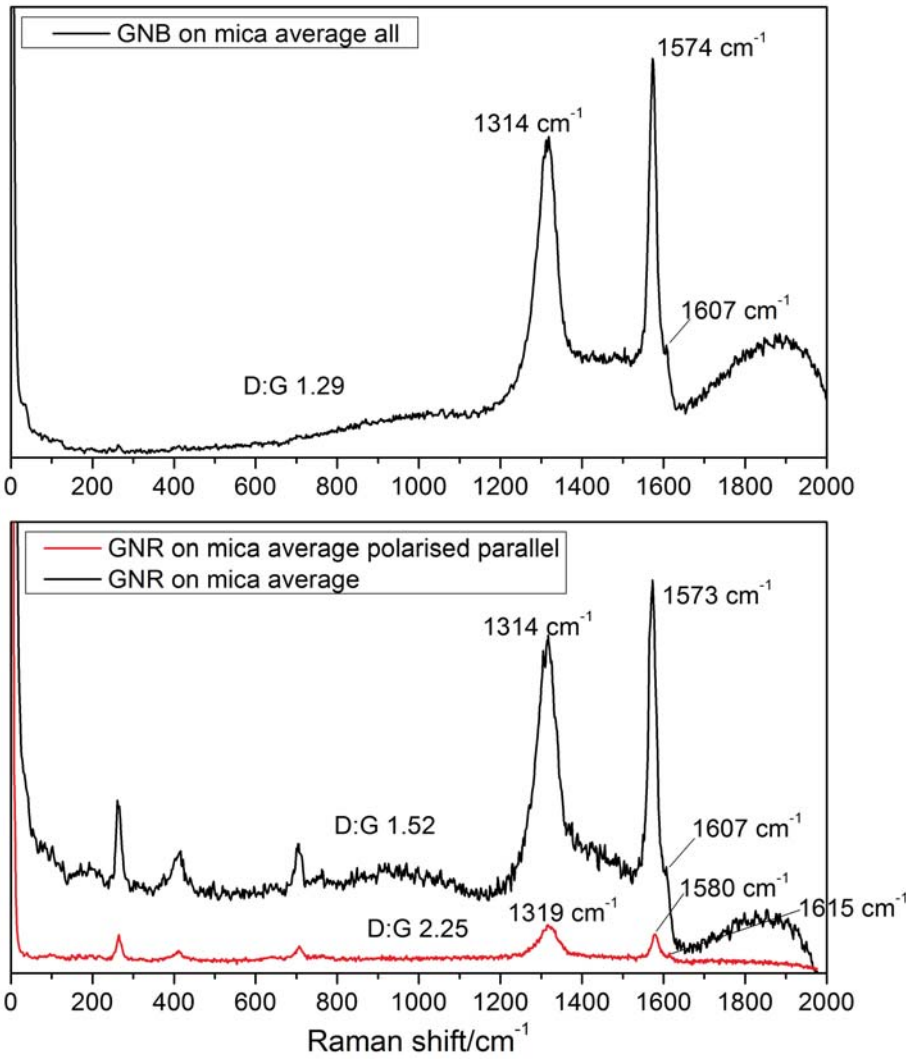

Figure 130: Spectra of unexfoliated 100 nm GNBs transferred directly onto mica after microtomy (top) and dispersed onto mica following exfoliation (bottom). Raman spectra were acquired with 785 nm excitation. For the polarised spectra, a linear polariser was used in the scattered beam path.

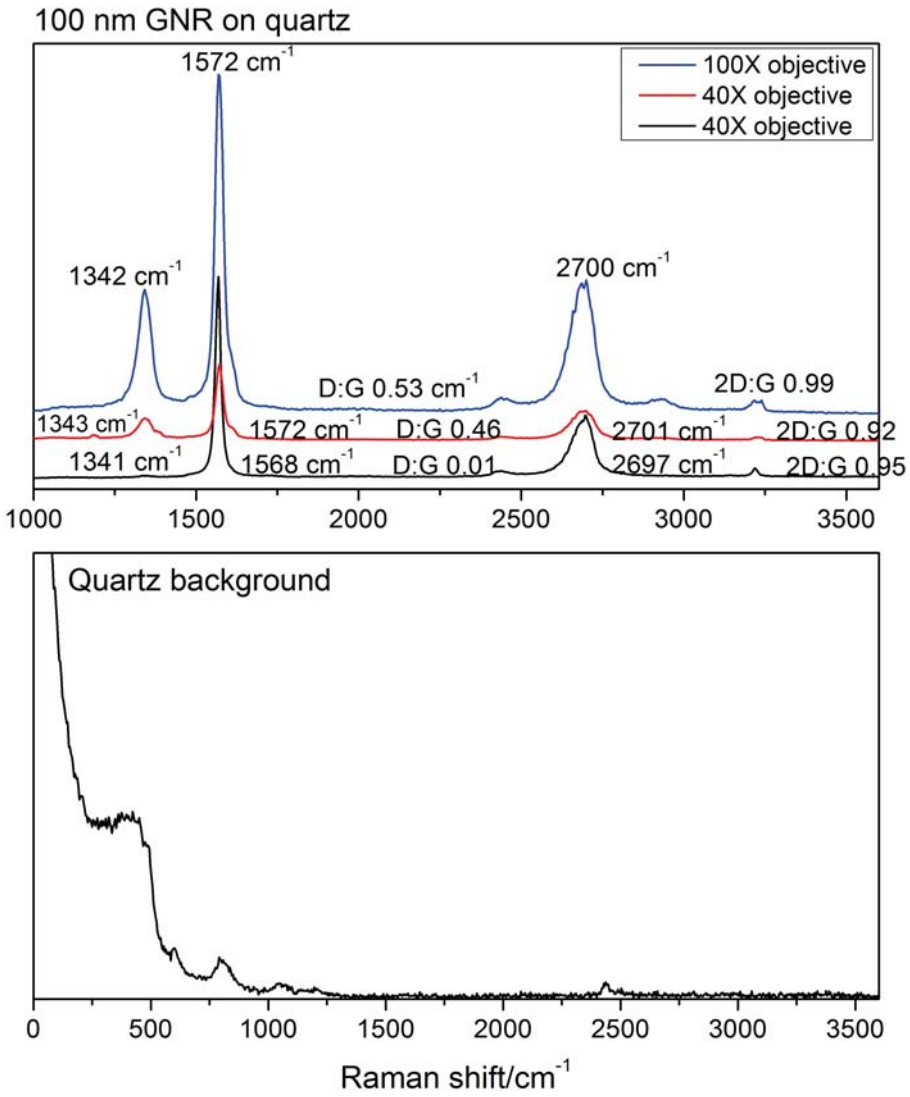

Figure 131: Raman spectra of 100 nm GNRs on a quartz substrate. Spectra were acquired with 532 nm excitation. Laser power approx 20 mW.

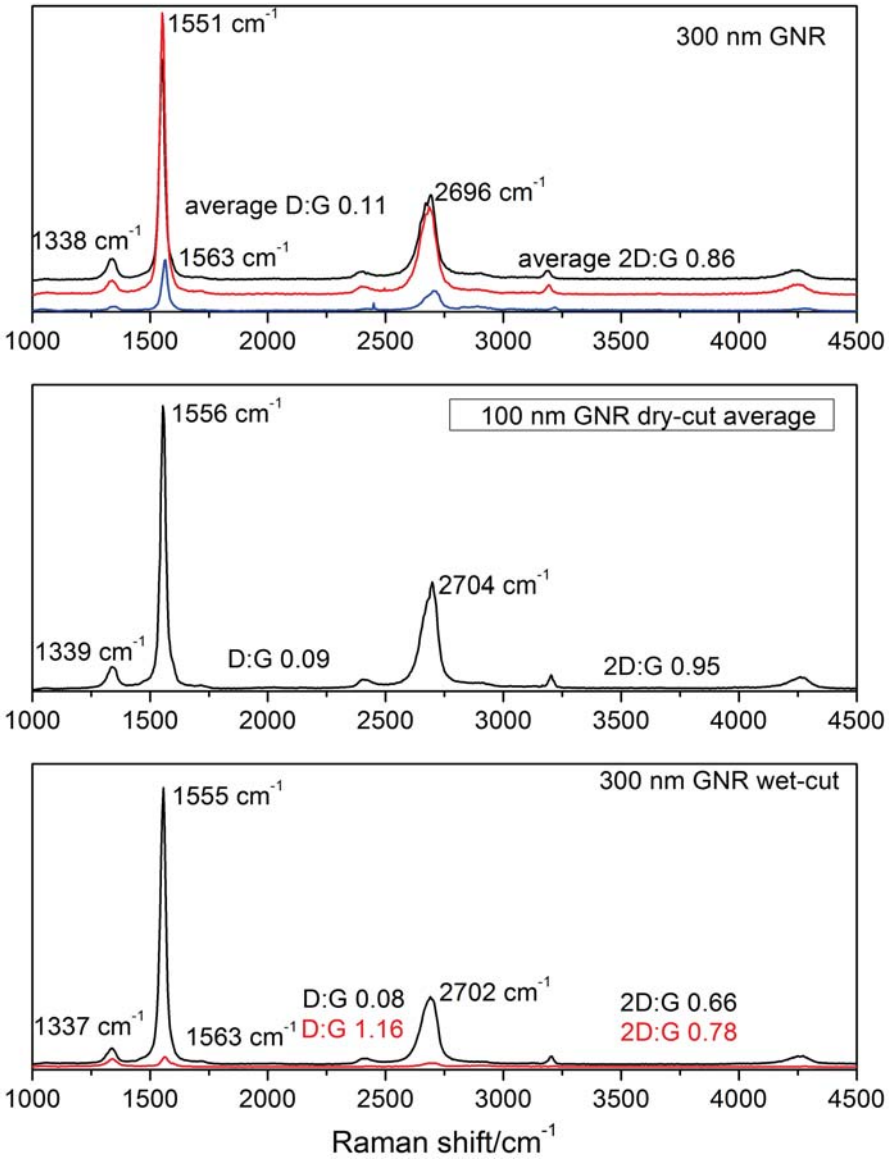

Figure 132: Raman spectra of GNR samples on quartz substrates. Spectra were acquired with 488 nm excitation.

9.3.4 Polarised Raman

HOPG and graphene test samples

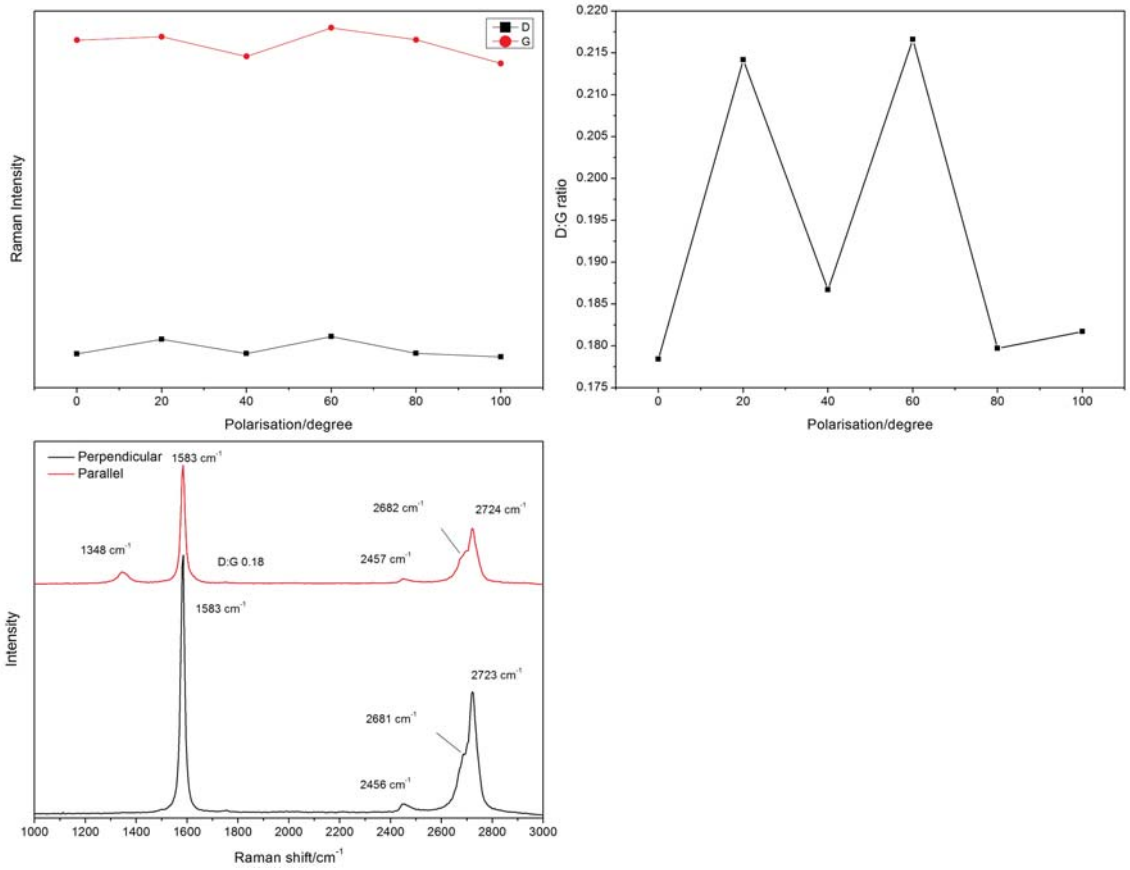

Figure 133: Polarised Raman analysis of HOPG. Spectra were acquired with 532 nm excitation.

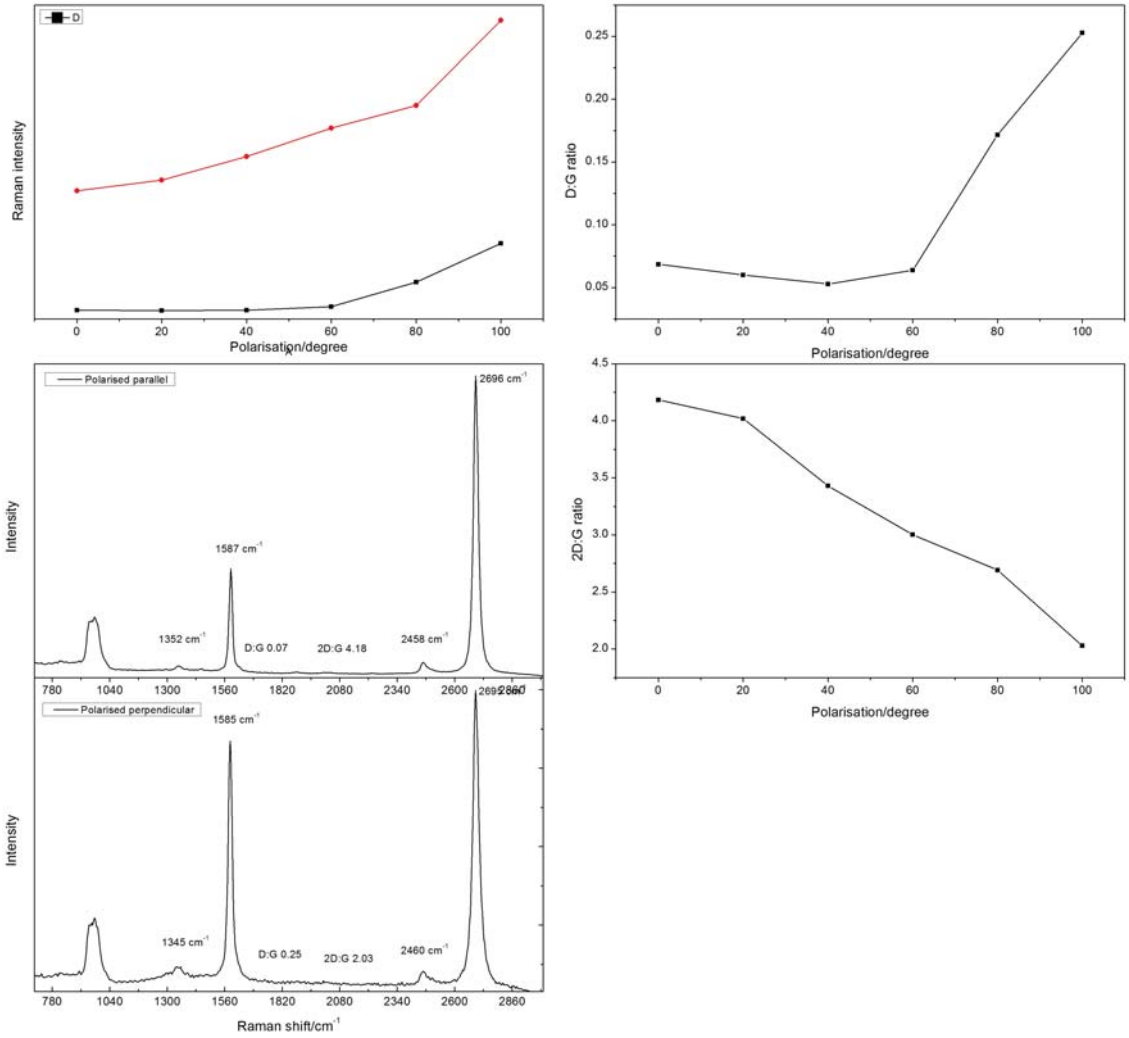

Figure 134: Polarised Raman analysis of single/double graphene on SiO_2. Spectra were acquired with 532 nm excitation.

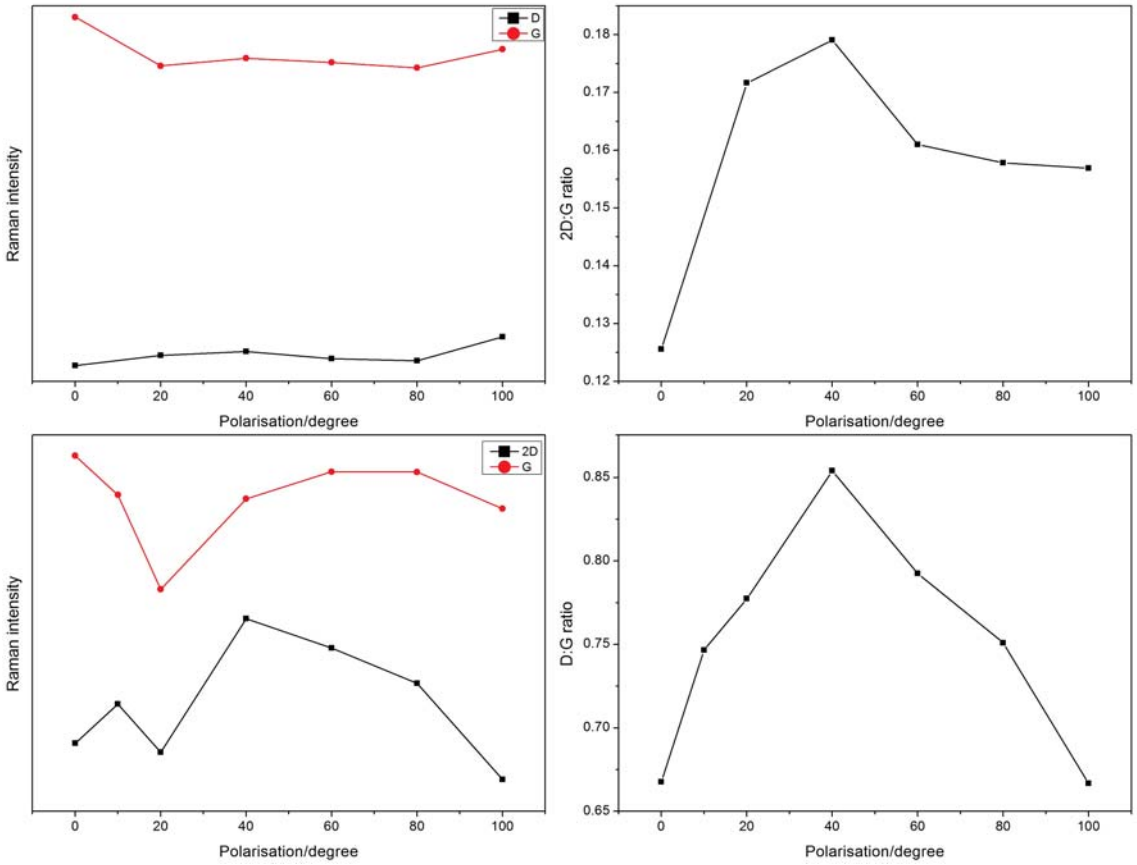

Figure 135: Polarised Raman analysis of single/double graphene on Ni. Spectra were acquired with 532 nm excitation.

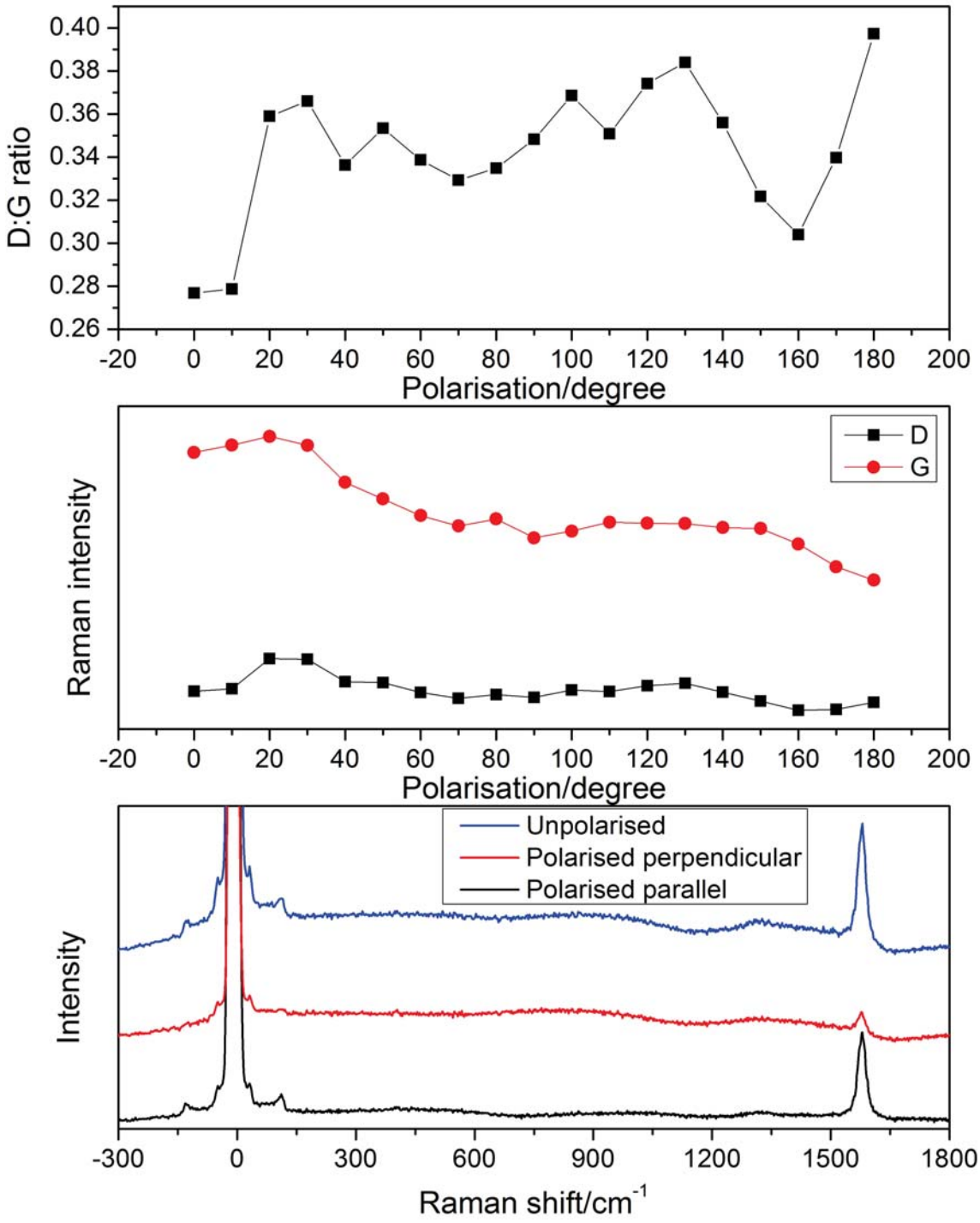

Figure 136: Polarised Raman analysis of CVD graphene on Ni. Spectra were acquired with 532 nm excitation.

GNRs

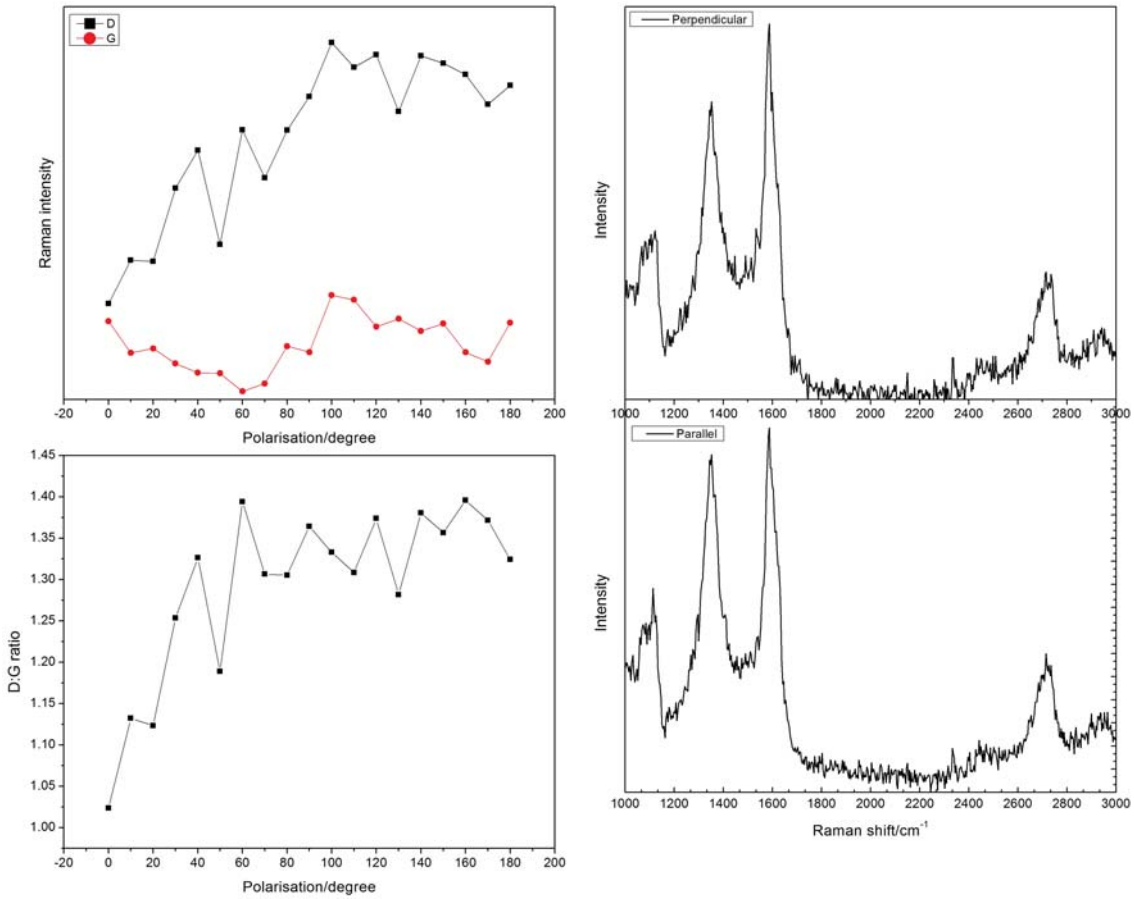

Figure 137: Polarised Raman analysis of 100 nm GNR on mica. Spectra were acquired with 532 nm excitation.

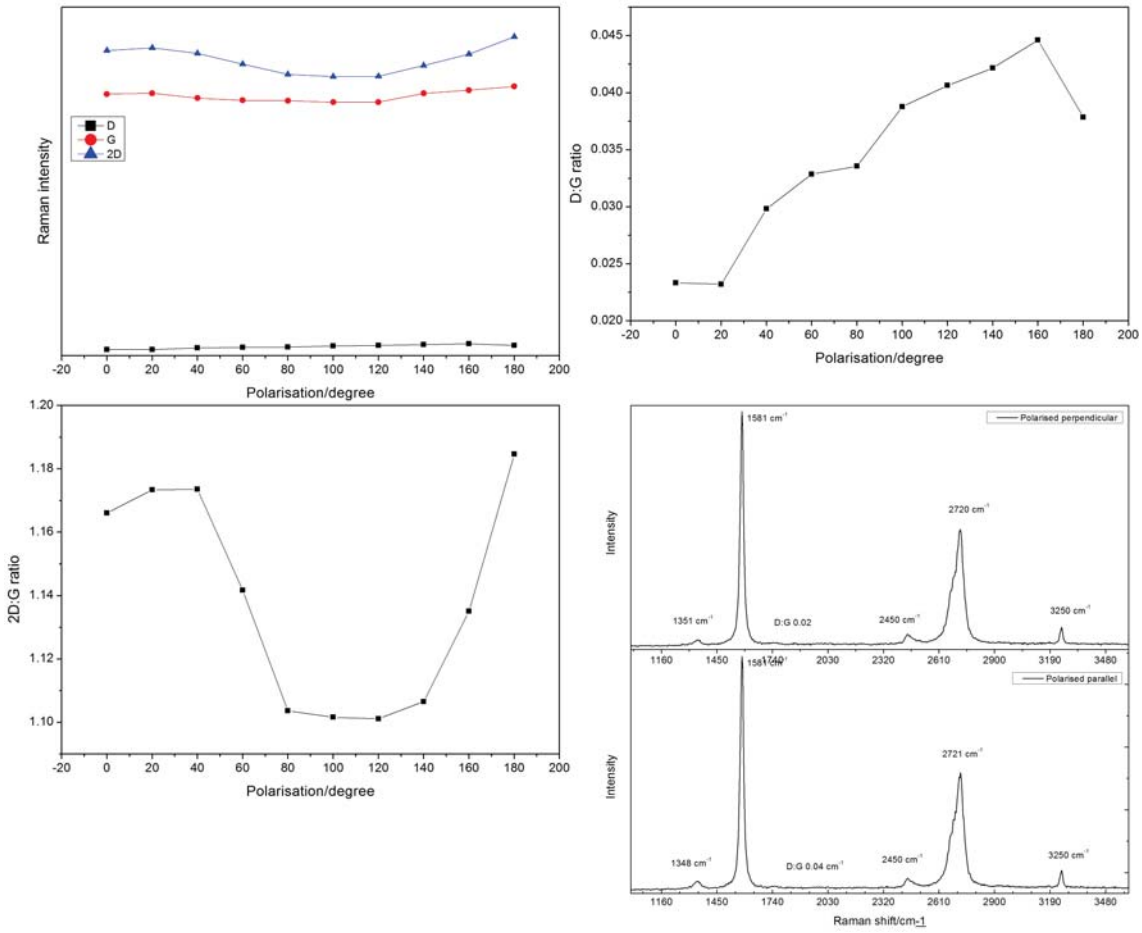

Figure 138: Polarised Raman analysis of 200 nm GNR on HOPG. Spectra were acquired with 532 nm excitation.

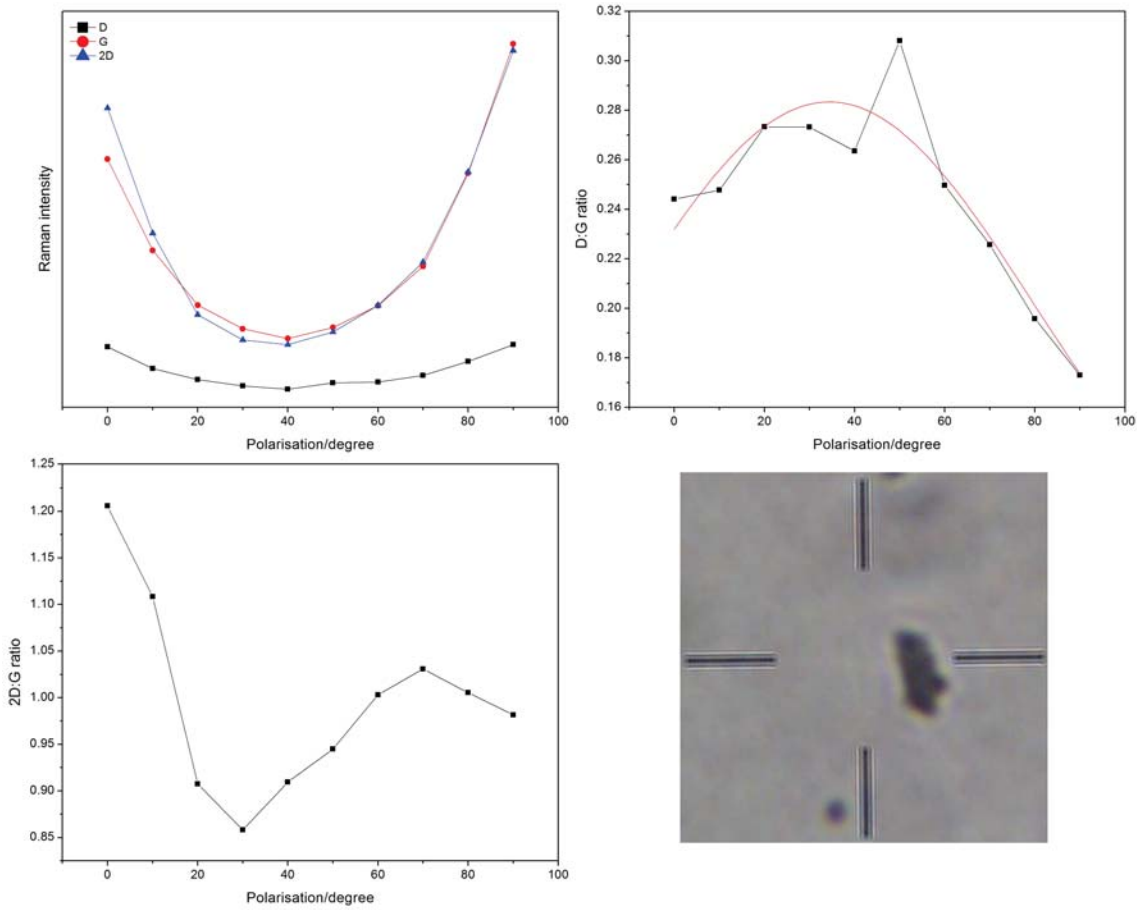

Figure 139: Polarised Raman analysis of 500 nm wet-cut GNR on quartz. Spectra were acquired with 532 nm excitation.

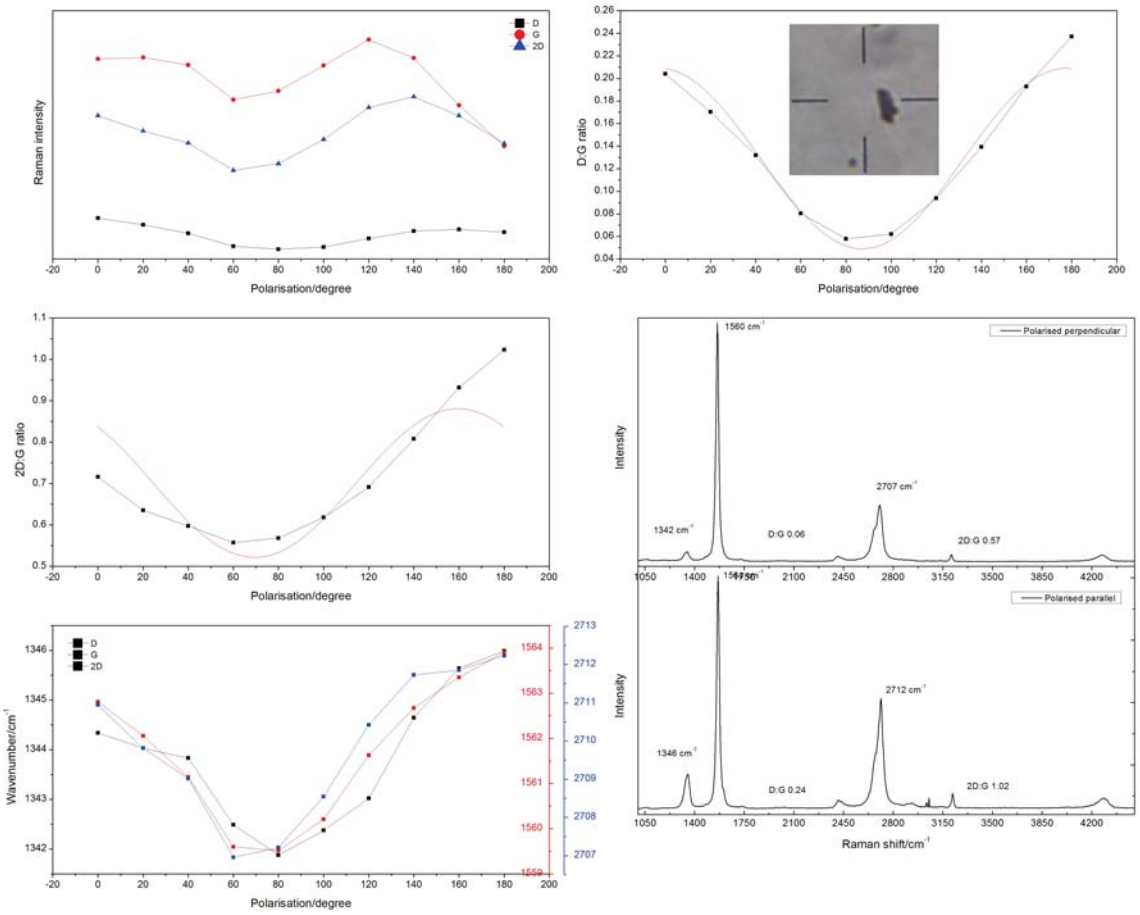

Figure 140: Polarised Raman analysis of 500 nm wet-cut GNR on quartz. Spectra were acquired with 532 nm excitation.

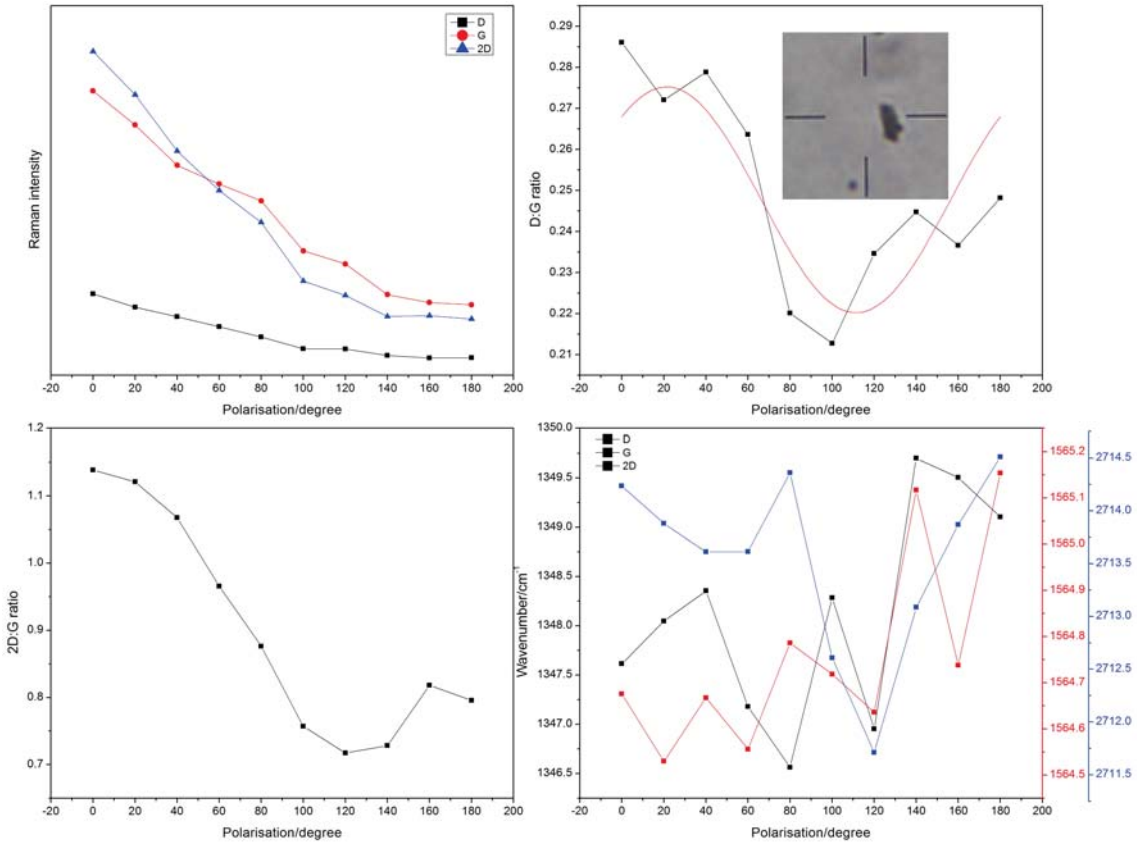

Figure 141: Polarised Raman analysis of 500 nm wet-cut GNR on quartz. Spectra were acquired with 532 nm excitation.

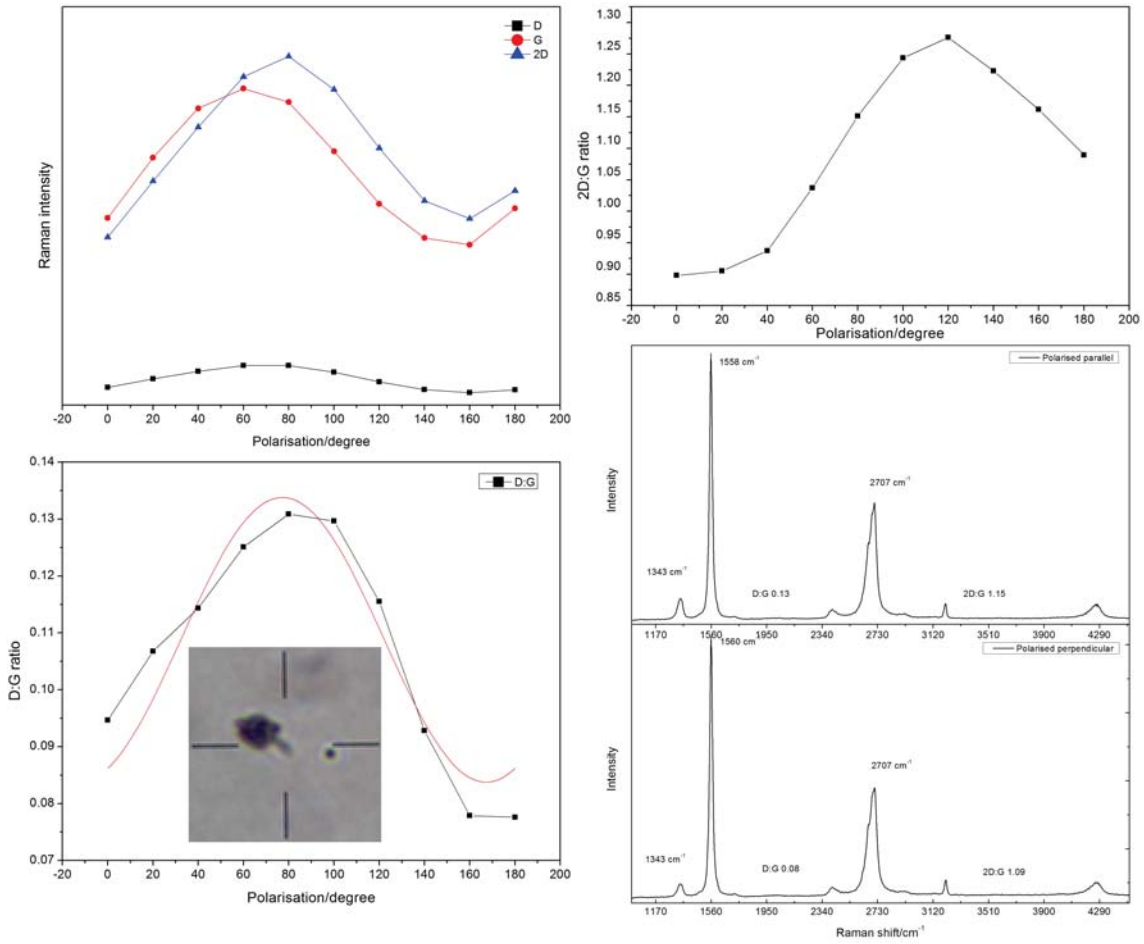

Figure 142: Polarised Raman analysis of 500 nm wet-cut GNR on quartz. Spectra were acquired with 532 nm excitation.

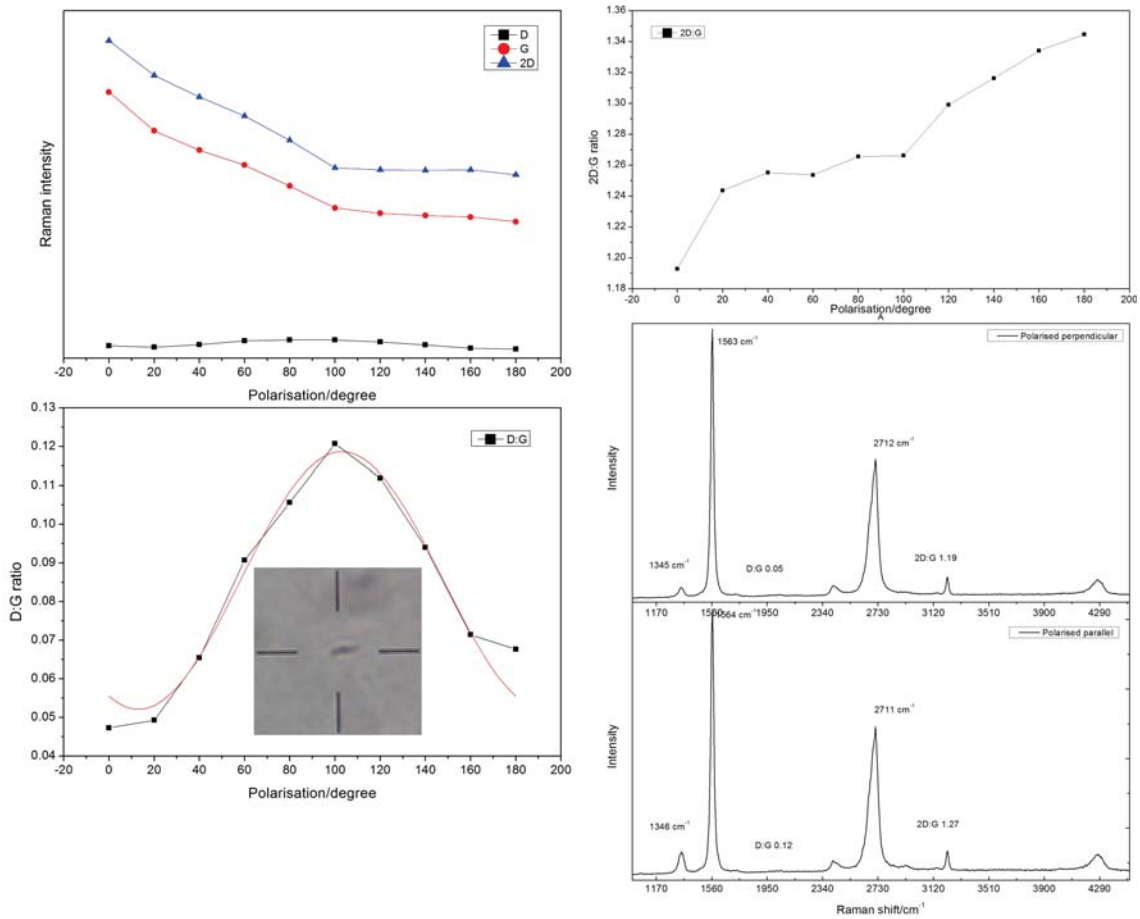

Figure 143: Polarised Raman analysis of 500 nm wet-cut GNR on quartz. Spectra were acquired with 532 nm excitation.

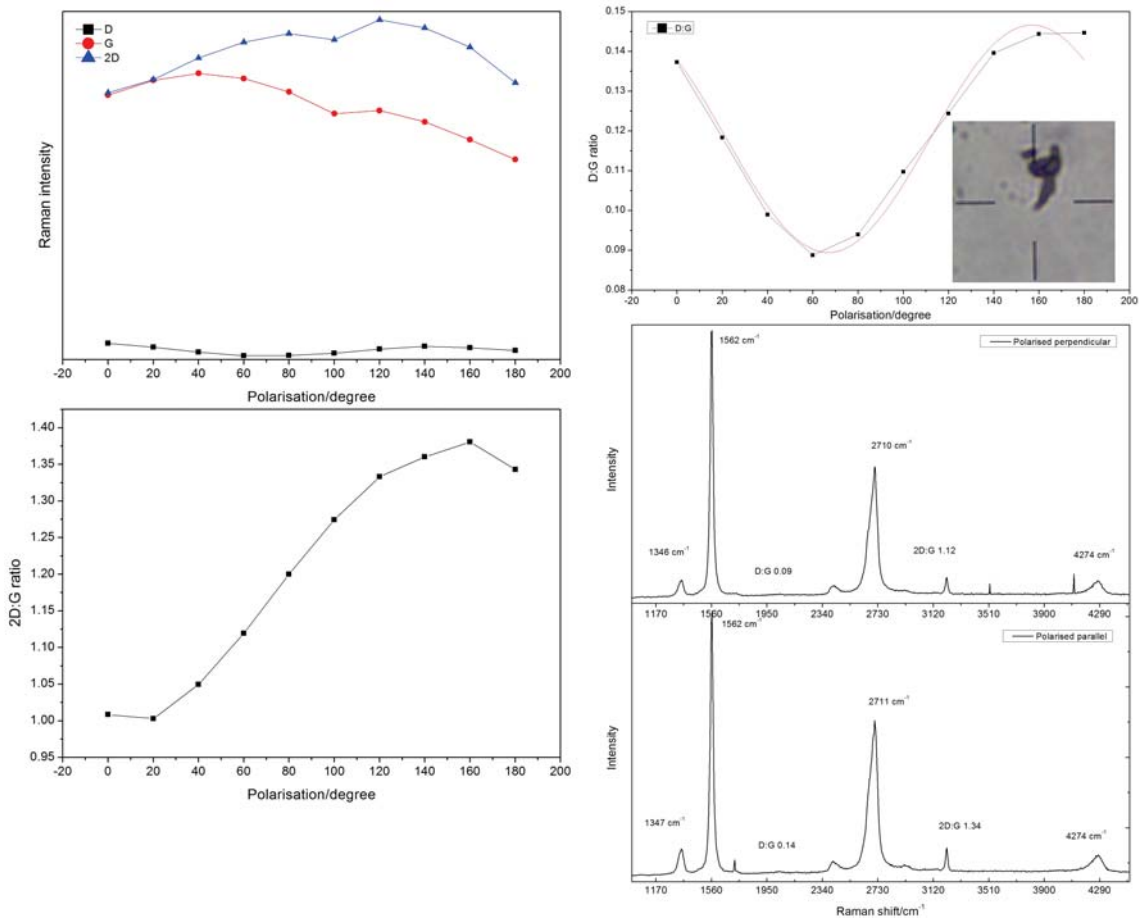

Figure 144: Polarised Raman analysis of 300 nm wet-cut GNR on quartz. Spectra were acquired with 488 nm excitation.

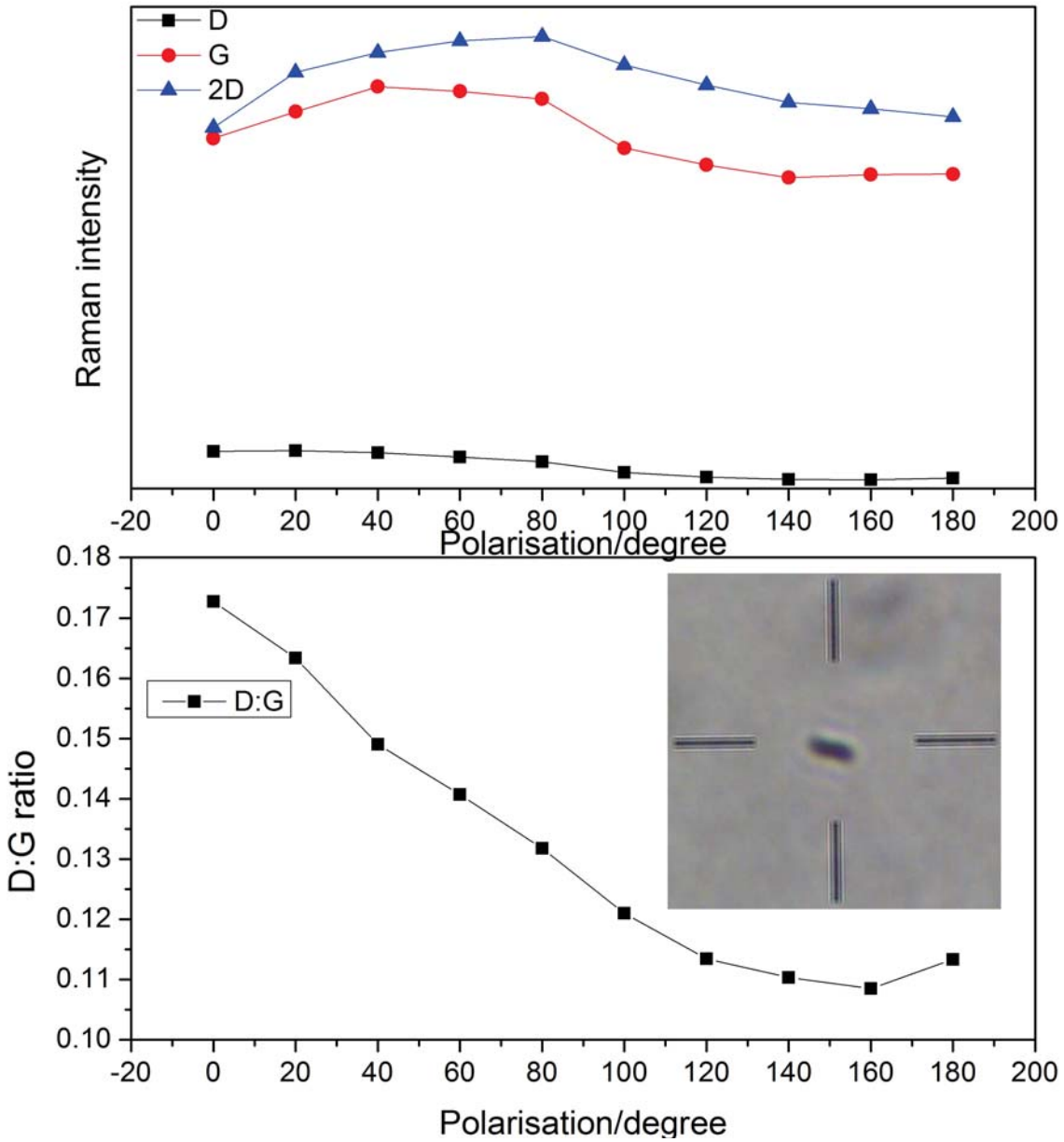

Figure 145: Polarised Raman analysis of 300 nm wet-cut GNR on quartz. Spectra were acquired with 488 nm excitation.

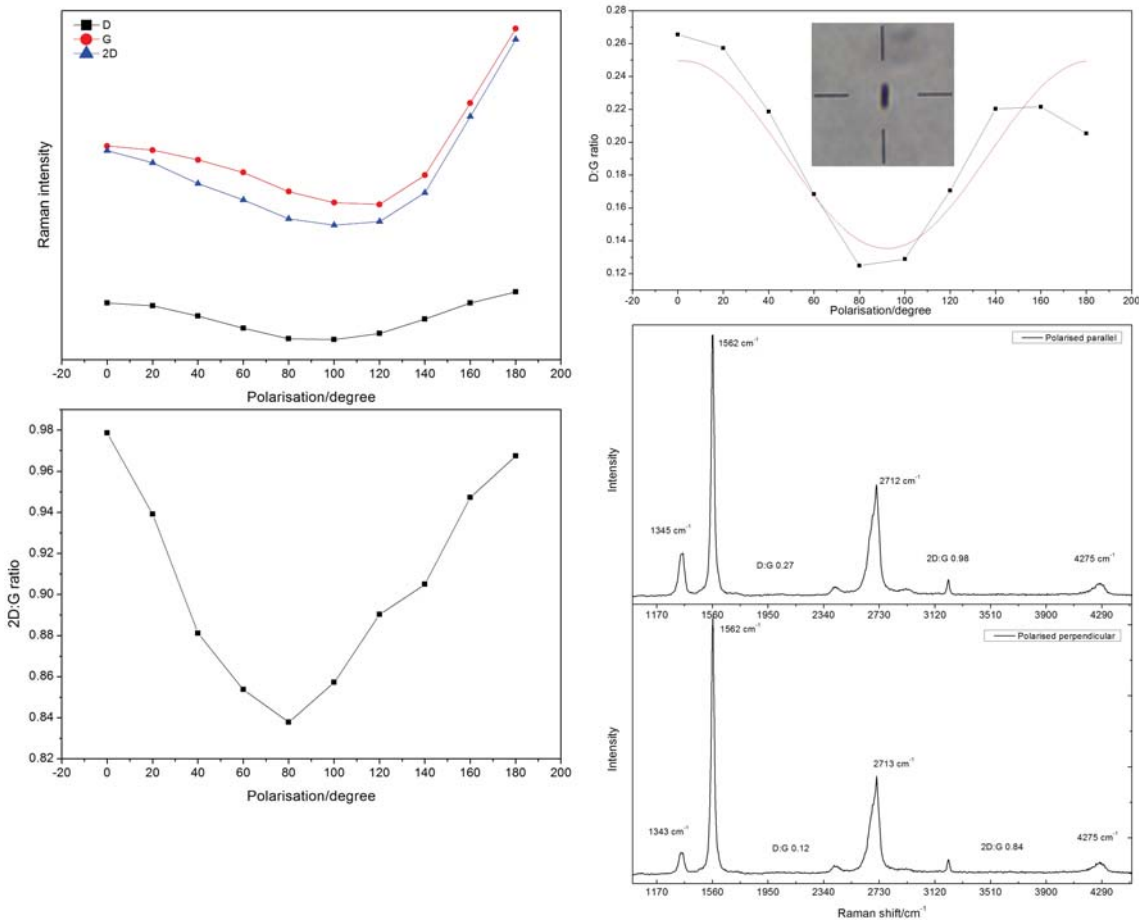

Figure 146: Polarised Raman analysis of 300 nm wet-cut GNR on quartz. Spectra were acquired with 488 nm excitation.

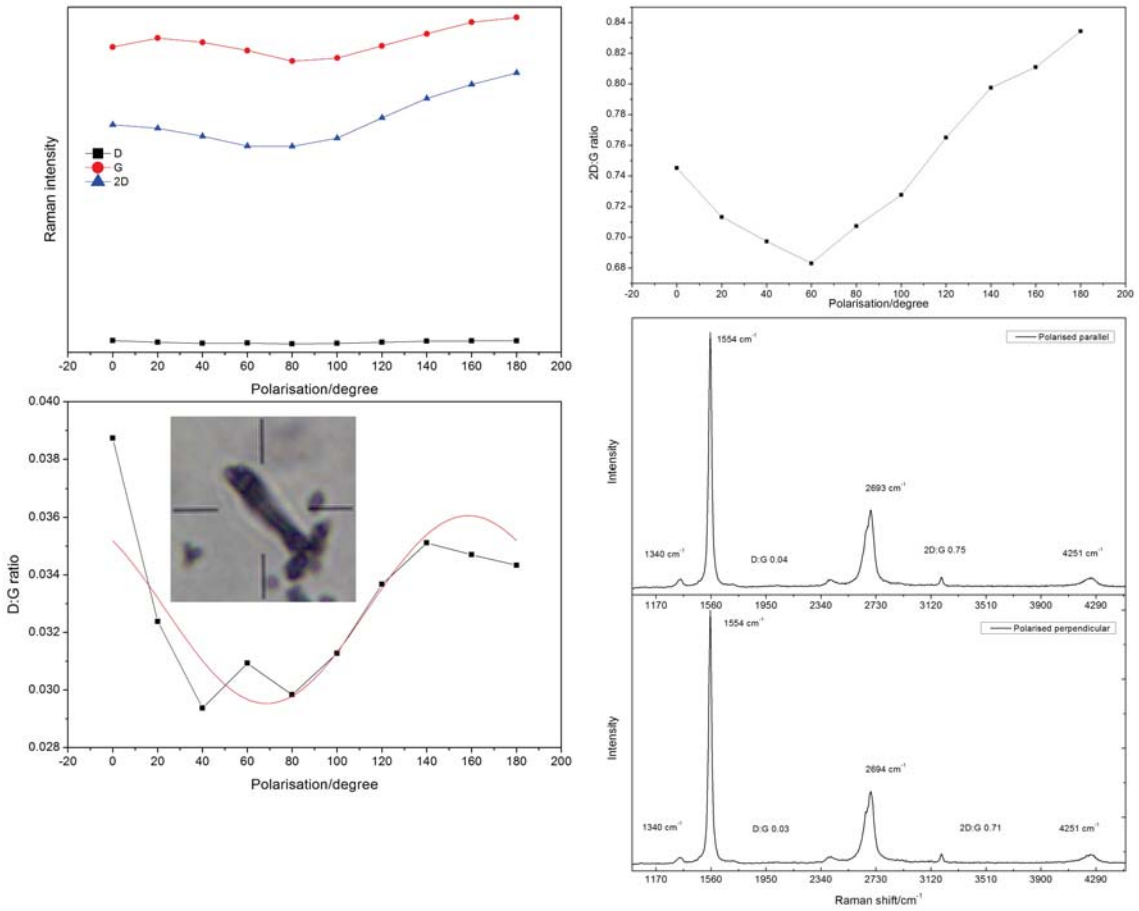

Figure 147: Polarised Raman analysis of 300 nm wet-cut GNR on quartz. Spectra were acquired with 488 nm excitation.

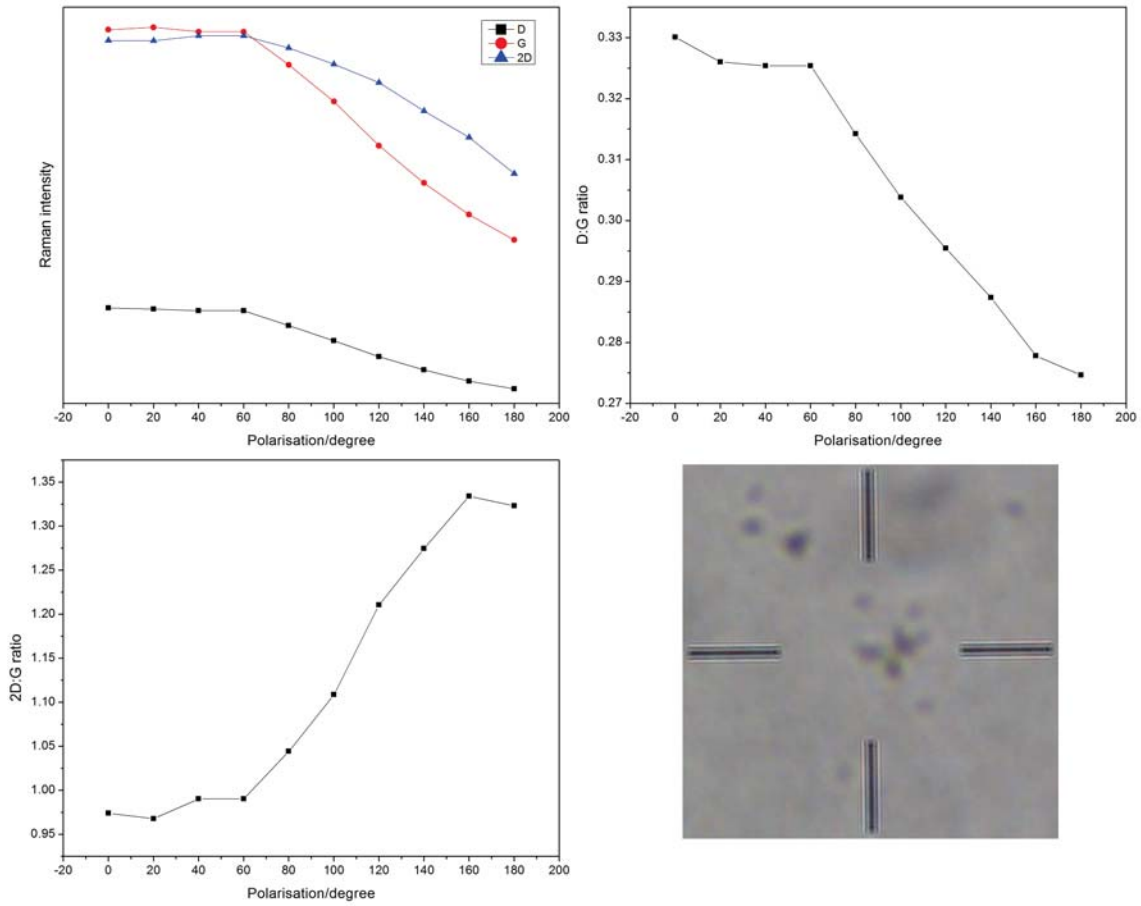

Figure 148: Polarised Raman analysis of 500 nm wet-cut GNR on quartz. Spectra were acquired with 488 nm excitation.

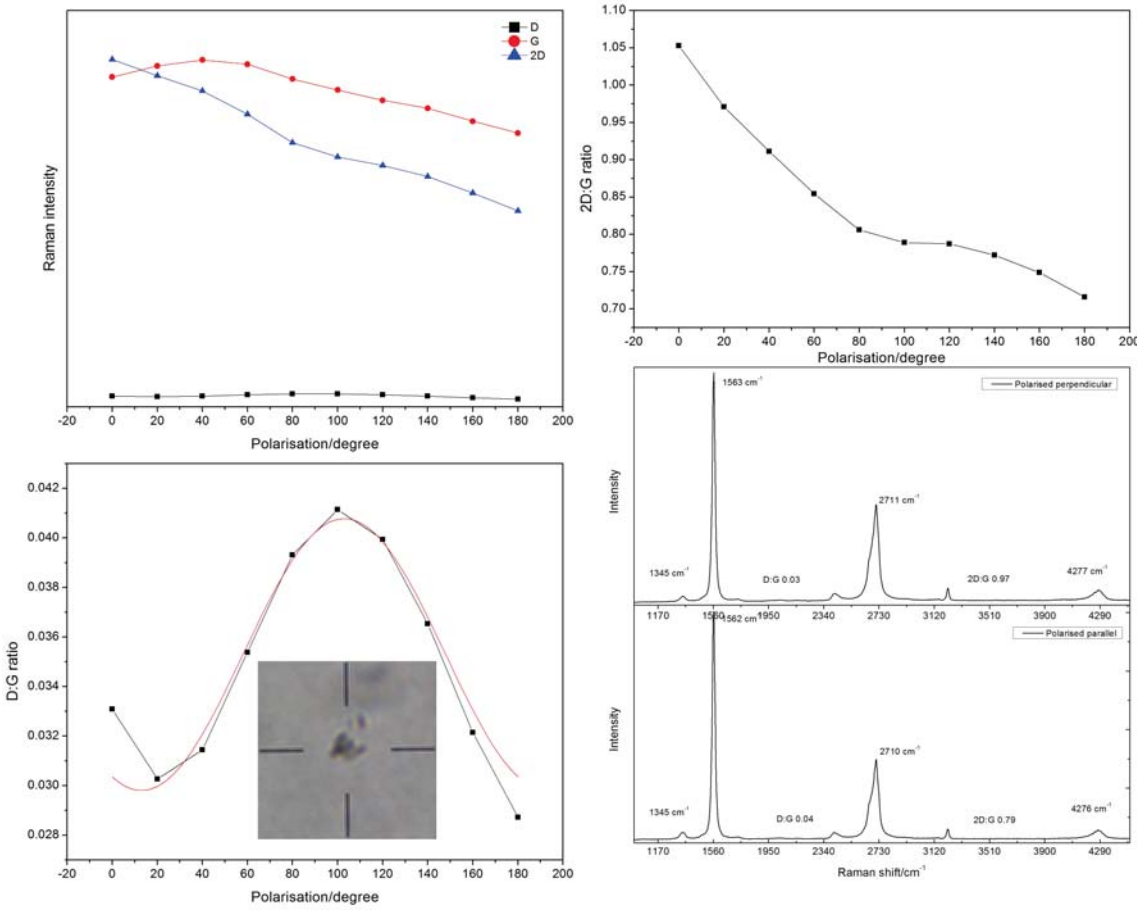

Figure 149: Polarised Raman analysis of 500 nm wet-cut GNR on quartz. Spectra were acquired with 488 nm excitation.

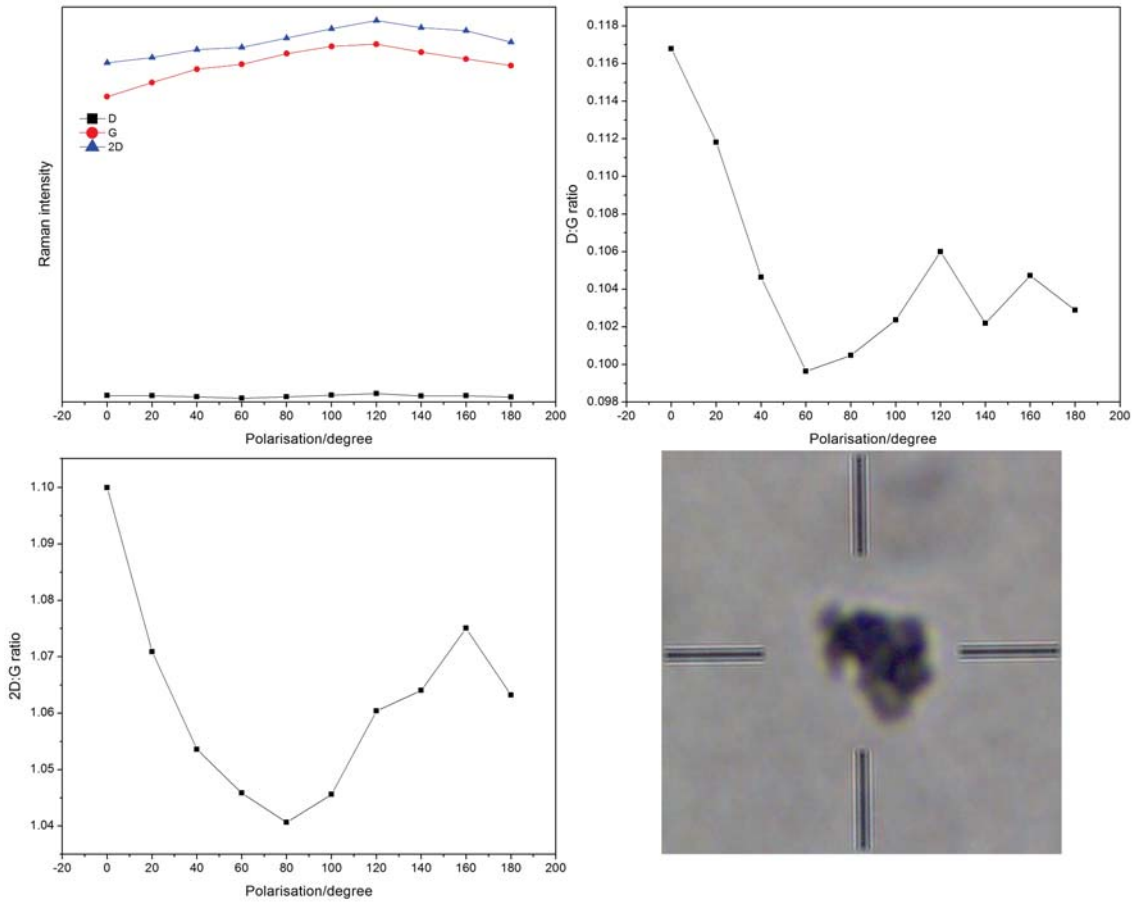

Figure 150: Polarised Raman analysis of 500 nm wet-cut GNR on quartz. Spectra were acquired with 488 nm excitation.

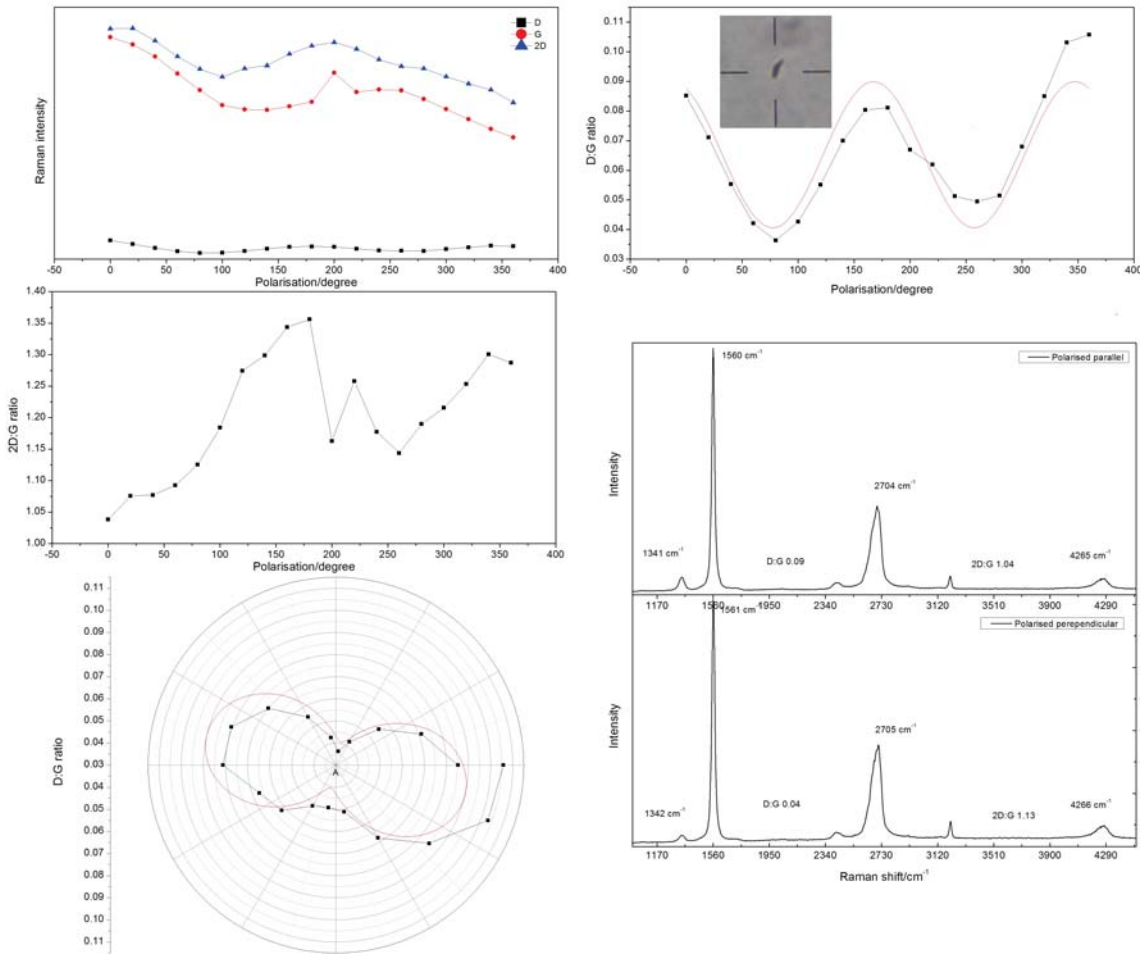

Figure 151: Polarised Raman analysis of 500 nm wet-cut GNR on quartz. Spectra were acquired with 488 nm excitation.

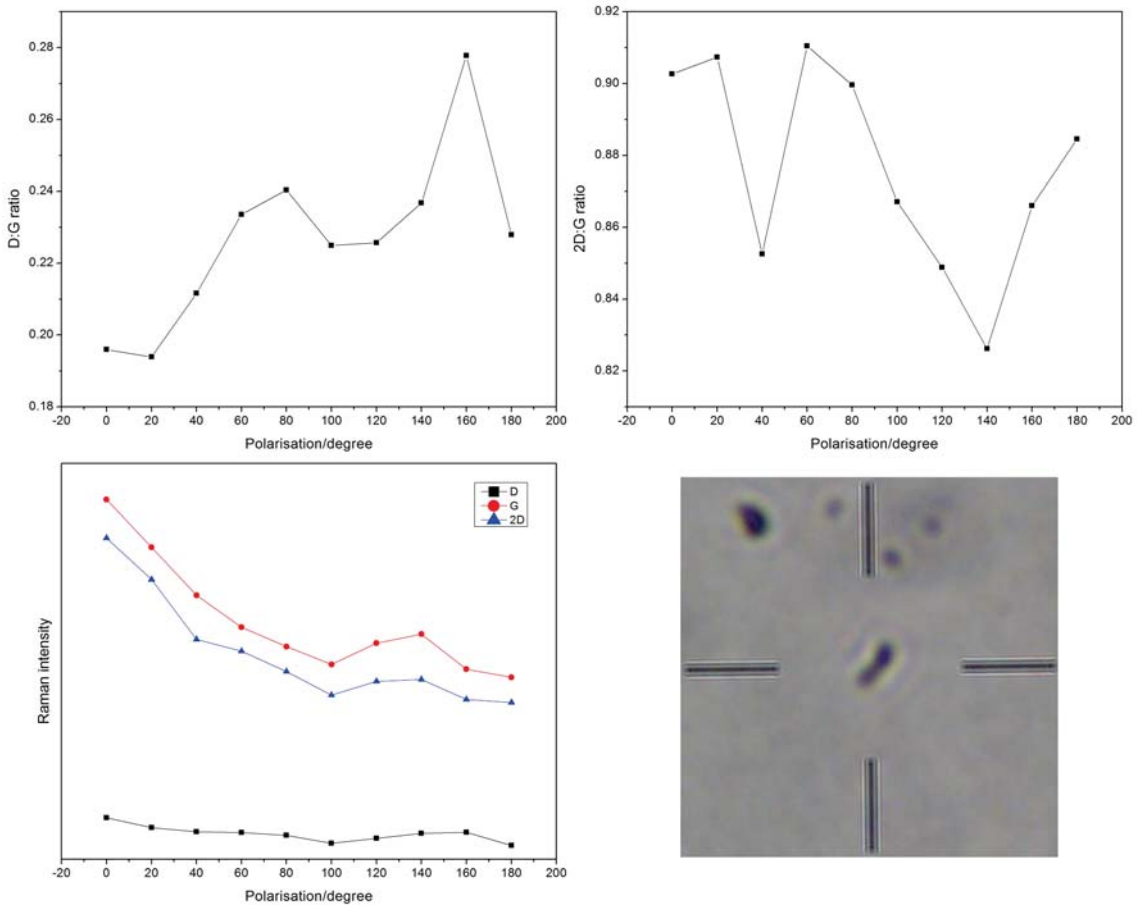

Figure 152: Polarised Raman analysis of 20 nm dry-cut GNR on quartz. Spectra were acquired with 488 nm excitation.

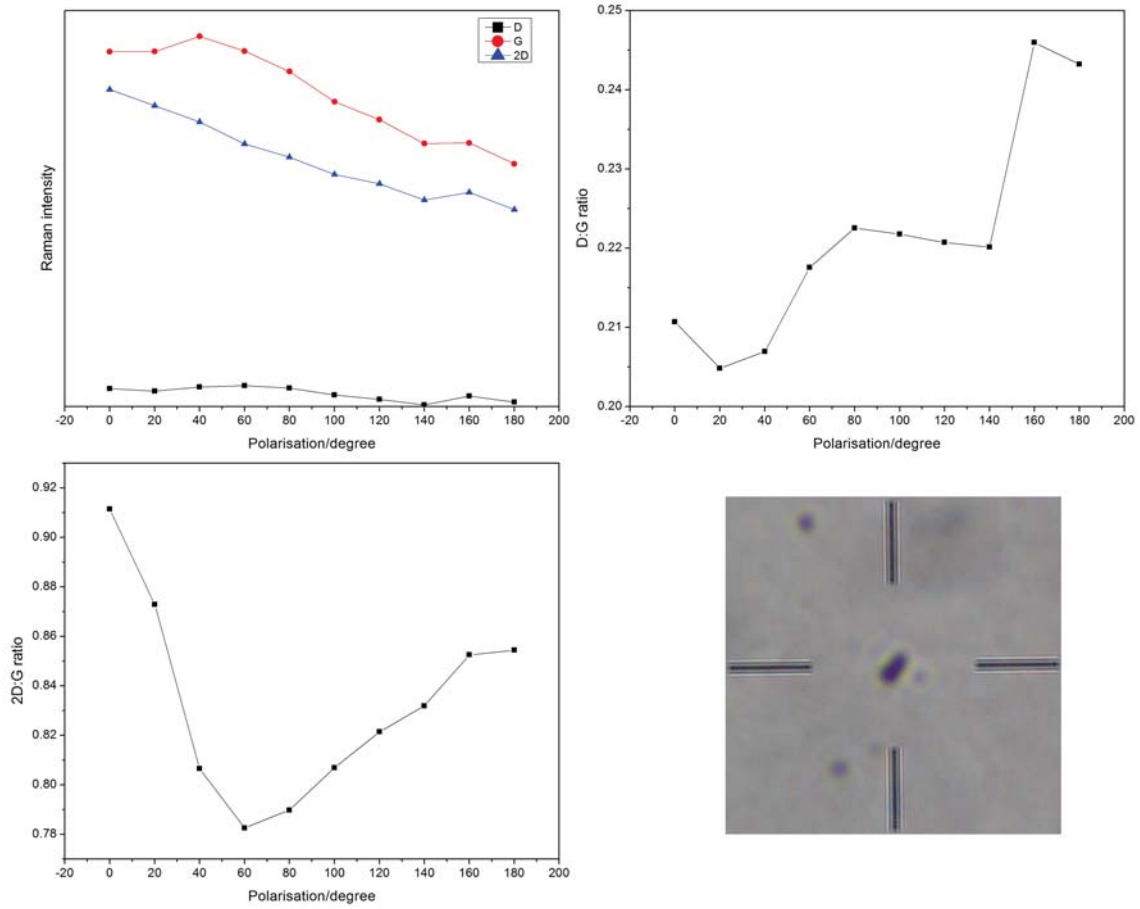

Figure 153: Polarised Raman analysis of 20 nm dry-cut GNR on quartz. Spectra were acquired with 488 nm excitation.

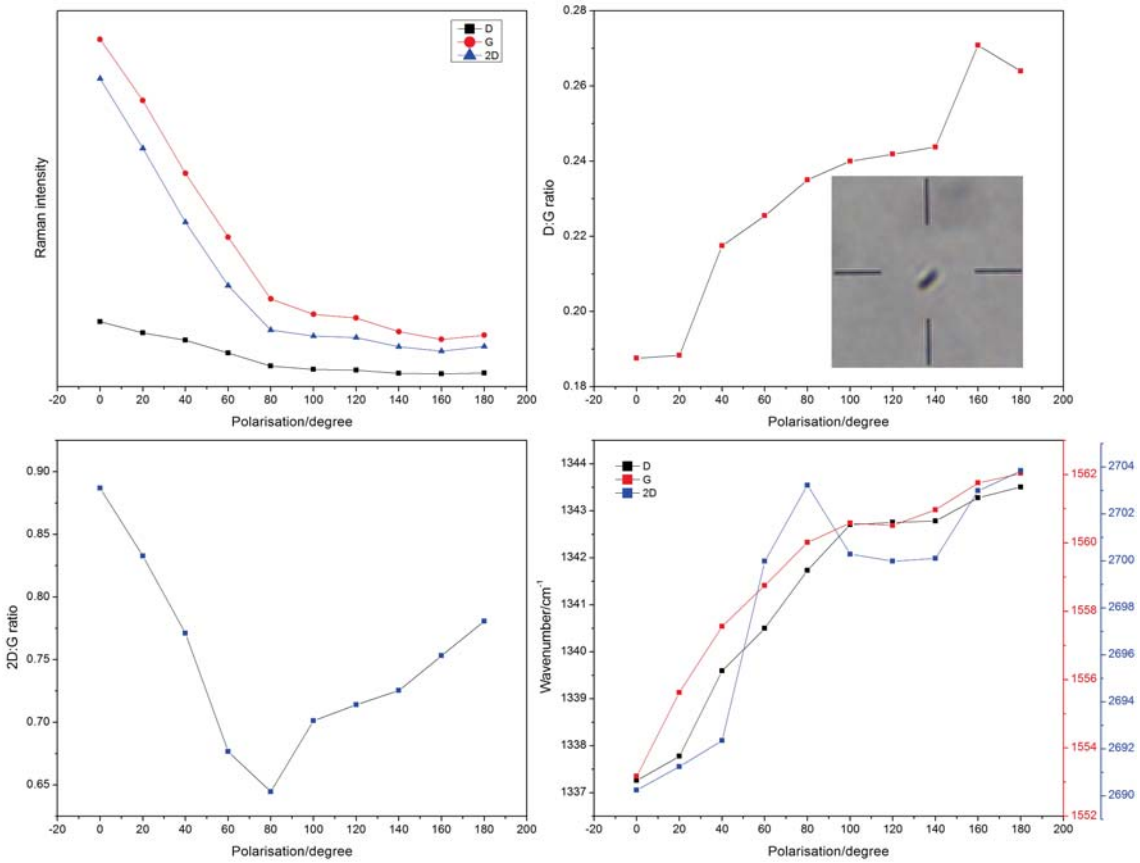

Figure 154: Polarised Raman analysis of 50 nm dry-cut GNR on quartz. Spectra were acquired with 488 nm excitation.

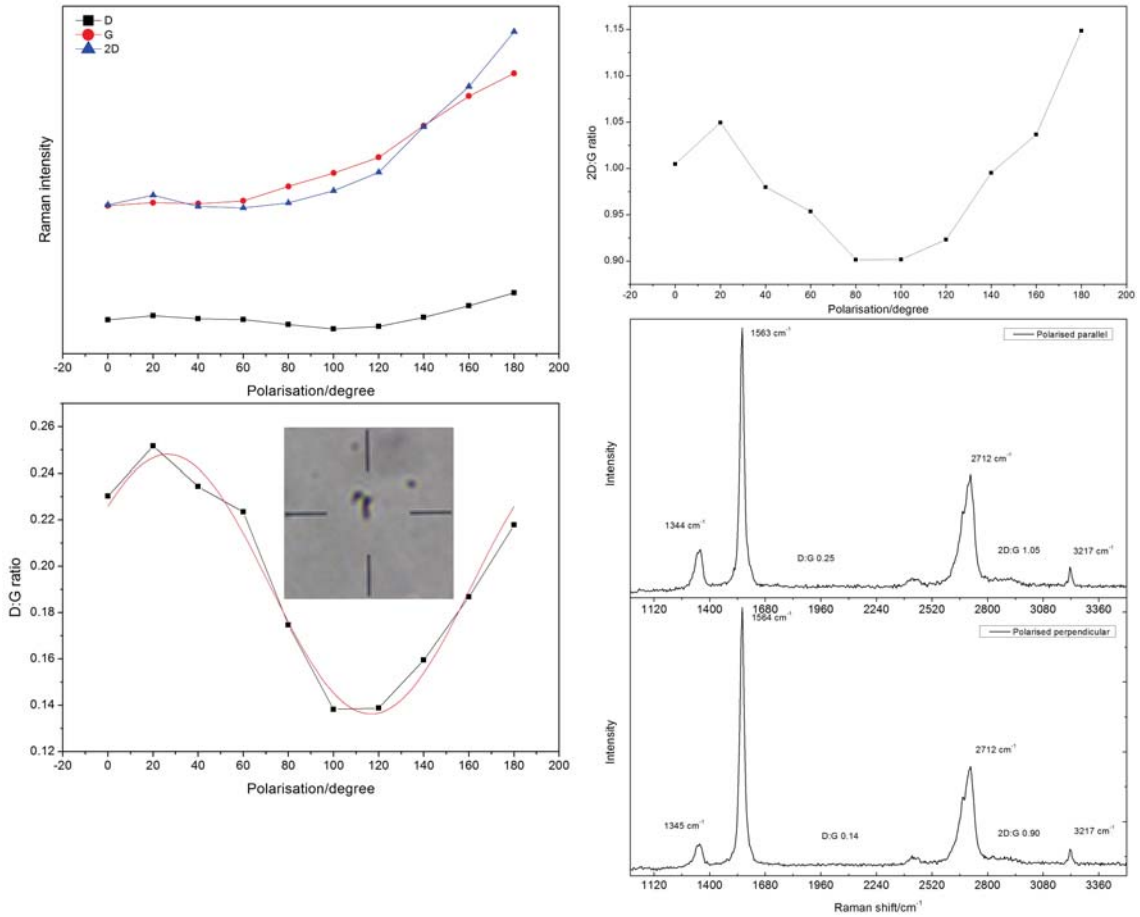

Figure 155: Polarised Raman analysis of 50 nm dry-cut GNR on quartz. Spectra were acquired with 488 nm excitation.

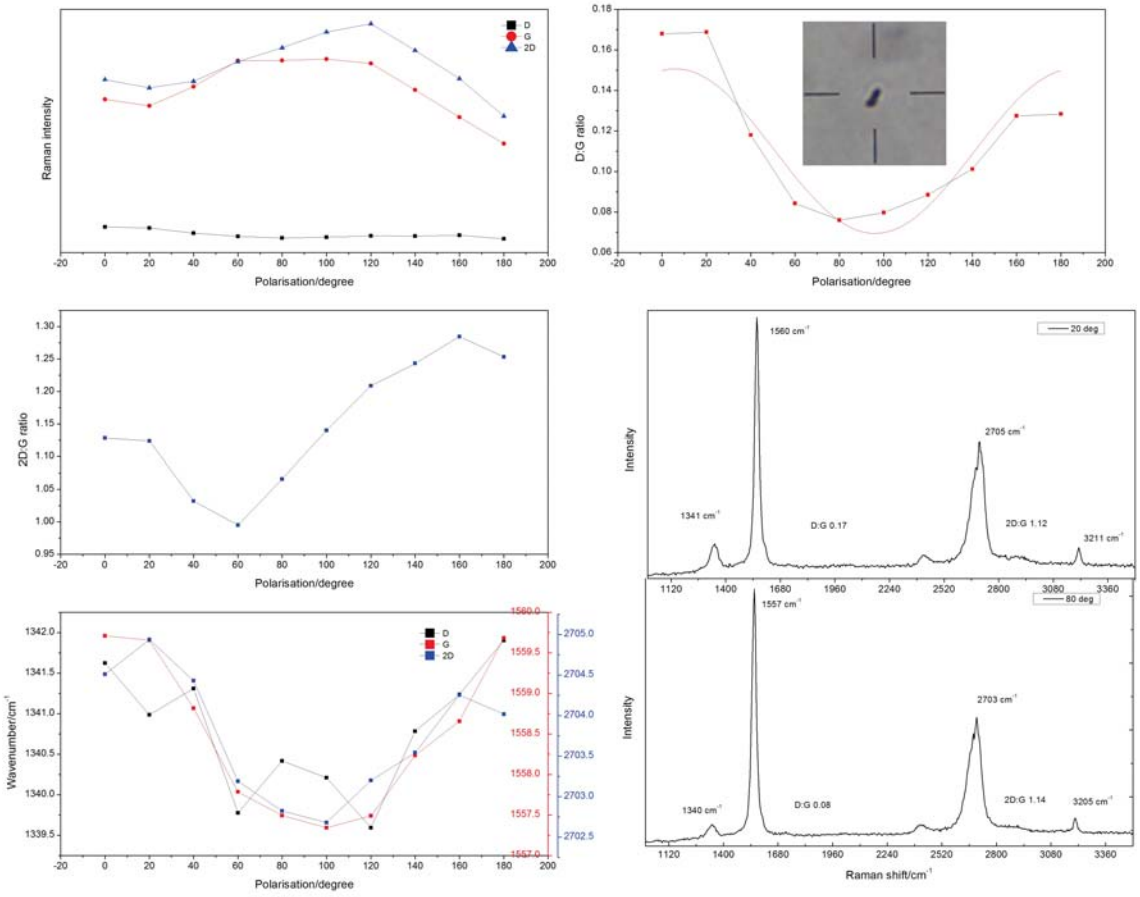

Figure 156: Polarised Raman analysis of 100 nm dry-cut GNR on quartz. Spectra were acquired with 488 nm excitation.

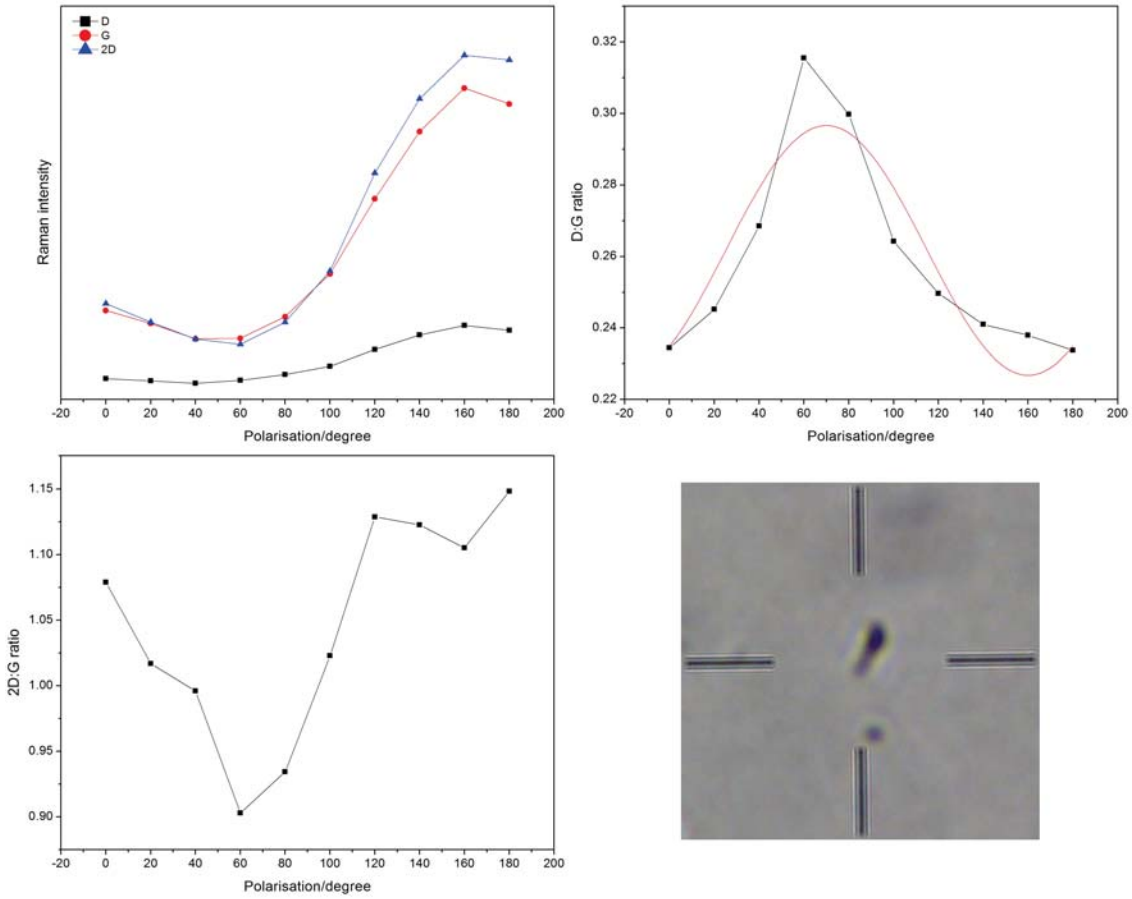

Figure 157: Polarised Raman analysis of 100 nm dry-cut GNR on quartz. Spectra were acquired with 488 nm excitation.

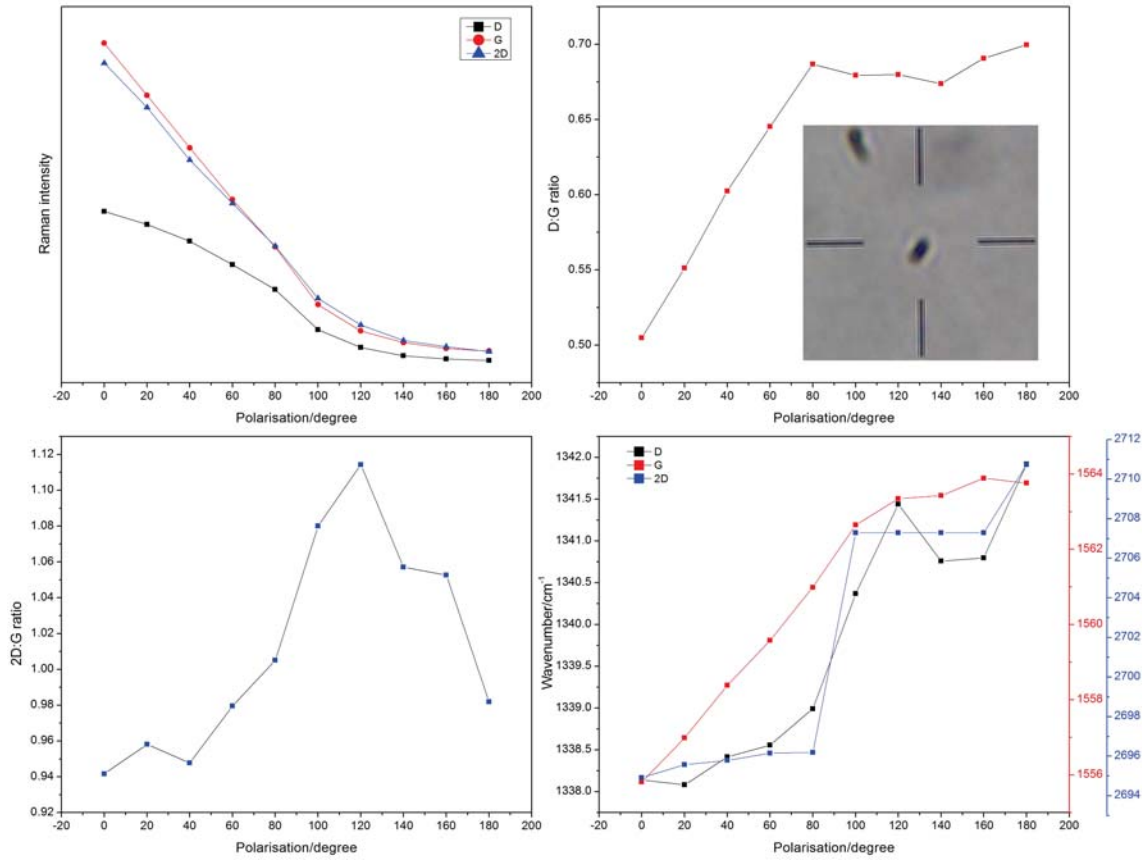

Figure 158: Polarised Raman analysis of 100 nm dry-cut GNR on quartz. Spectra were acquired with 488 nm excitation.

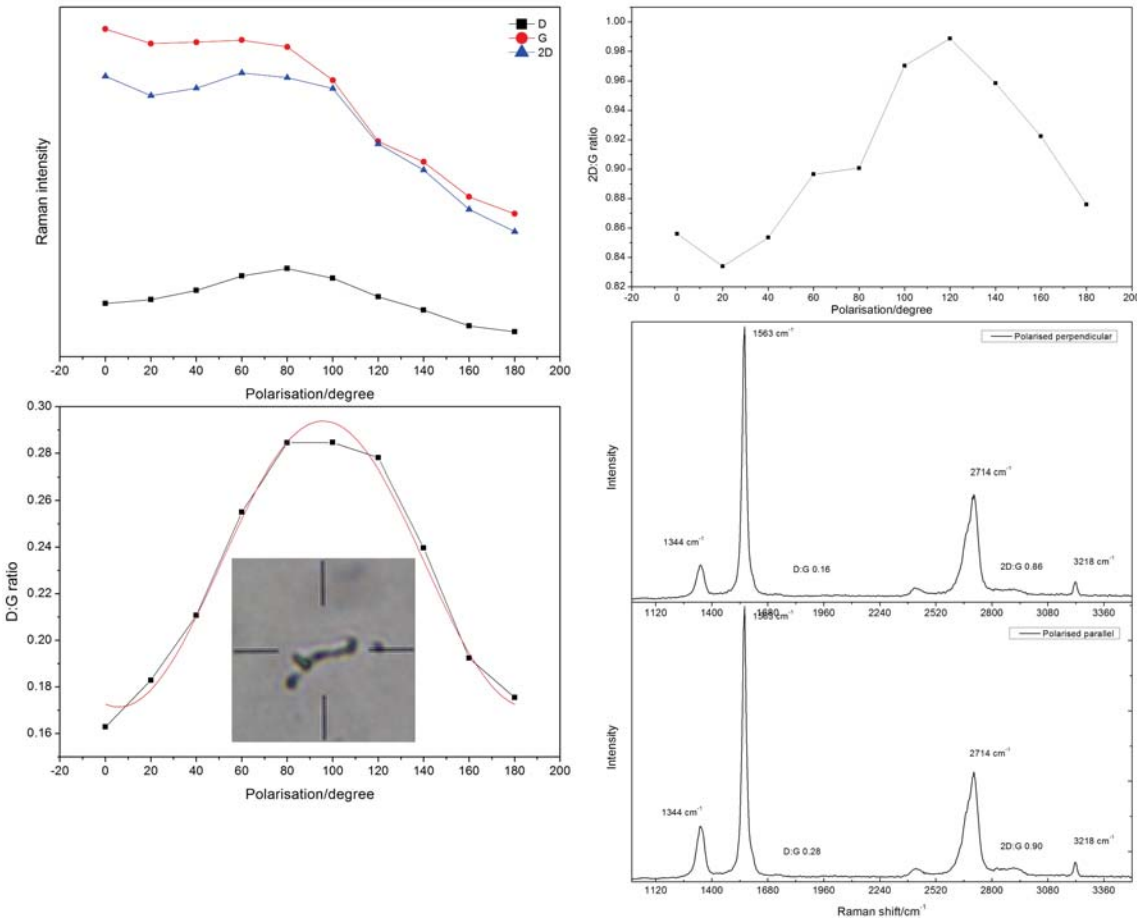

Figure 159: Polarised Raman analysis of 300 nm dry-cut GNR on quartz. Spectra were acquired with 488 nm excitation.

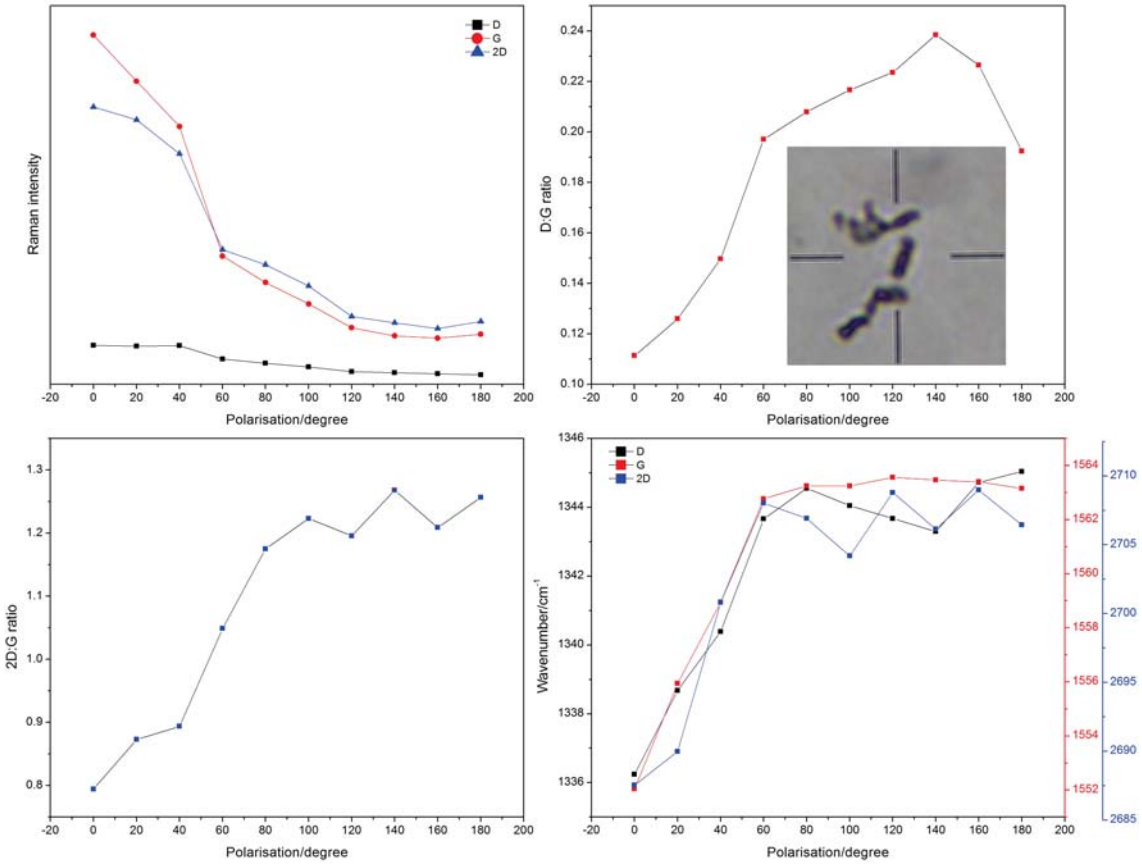

Figure 160: Polarised Raman analysis of 300 nm dry-cut GNR on quartz. Spectra were acquired with 488 nm excitation.

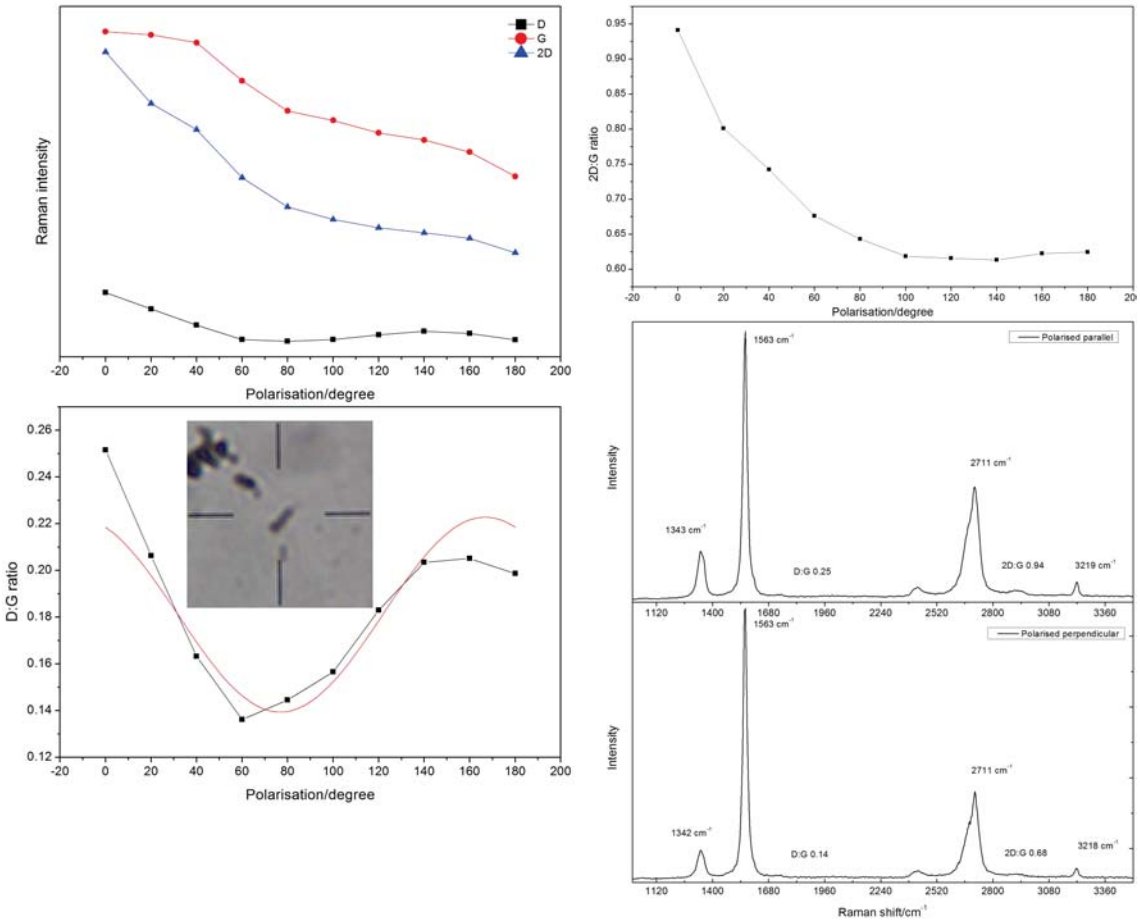

Figure 161: Polarised Raman analysis of 500 nm dry-cut GNR on quartz. Spectra were acquired with 488 nm excitation.

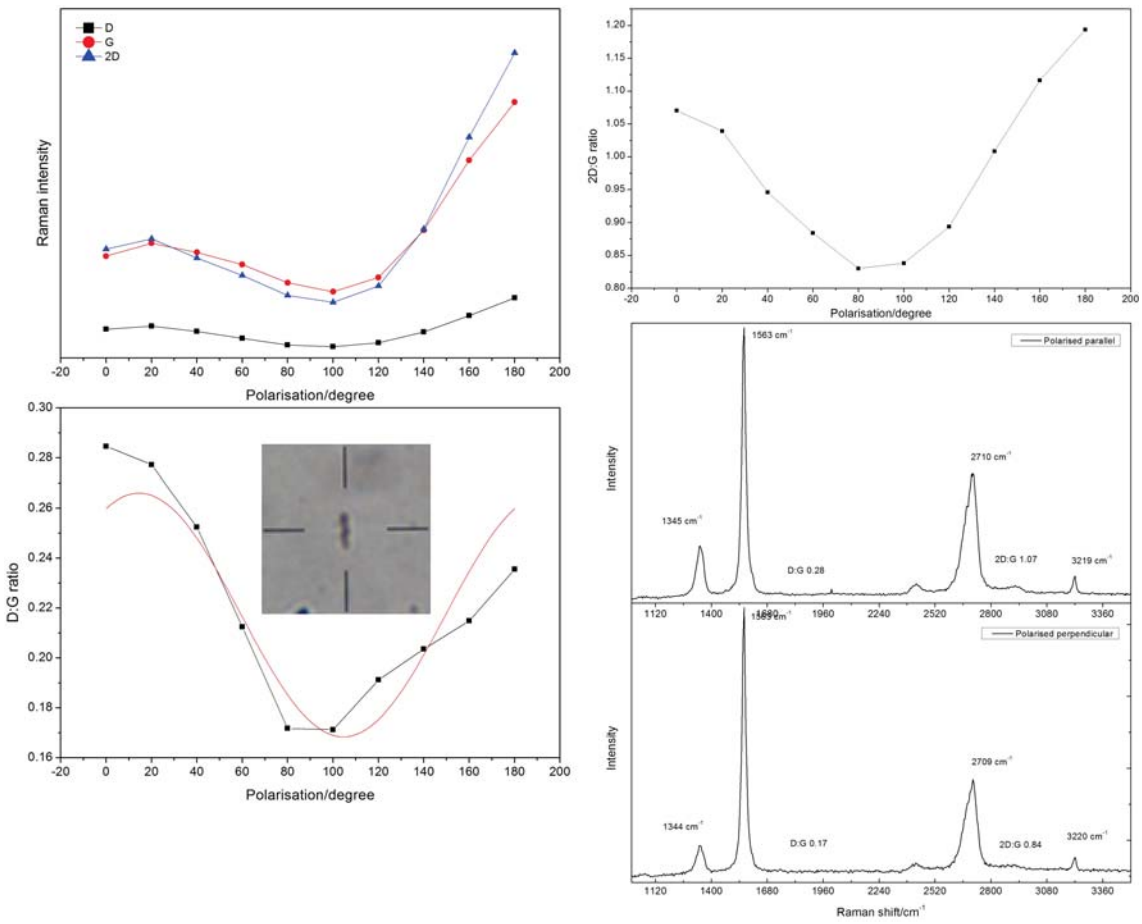

Figure 162: Polarised Raman analysis of 500 nm dry-cut GNR on quartz. Spectra were acquired with 488 nm excitation.

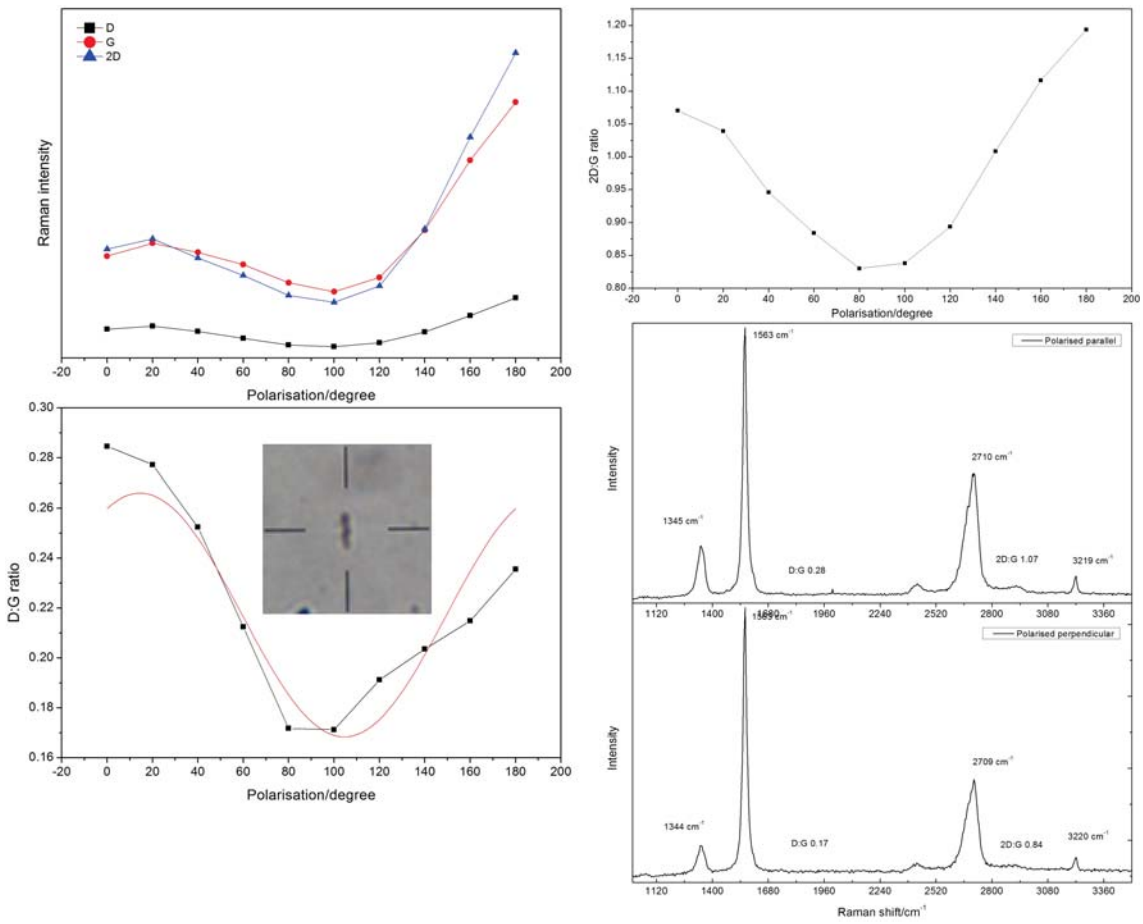

Figure 163: Polarised Raman analysis of 500 nm dry-cut GNR on quartz. Spectra were acquired with 488 nm excitation.

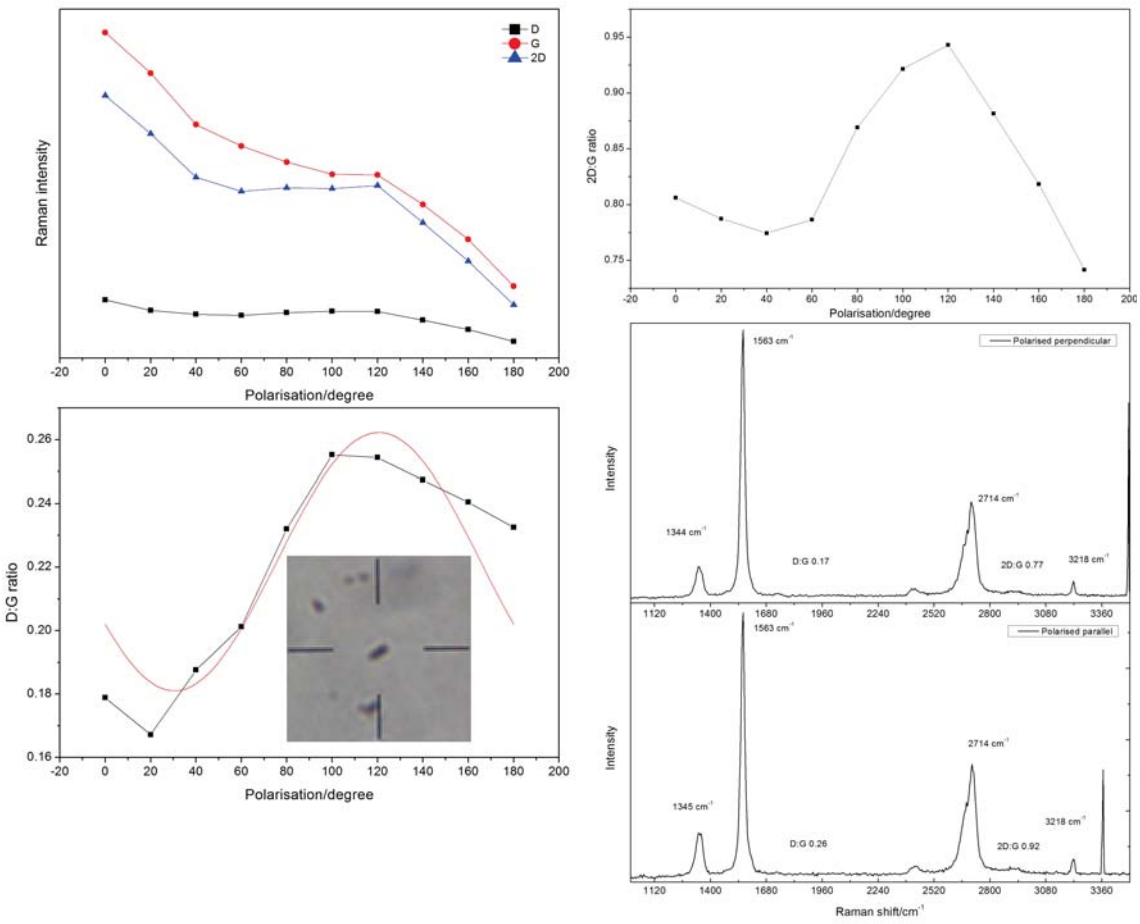

Figure 164: Polarised Raman analysis of 20 nm wet-cut GNR on quartz. Spectra were acquired with 488 nm excitation.

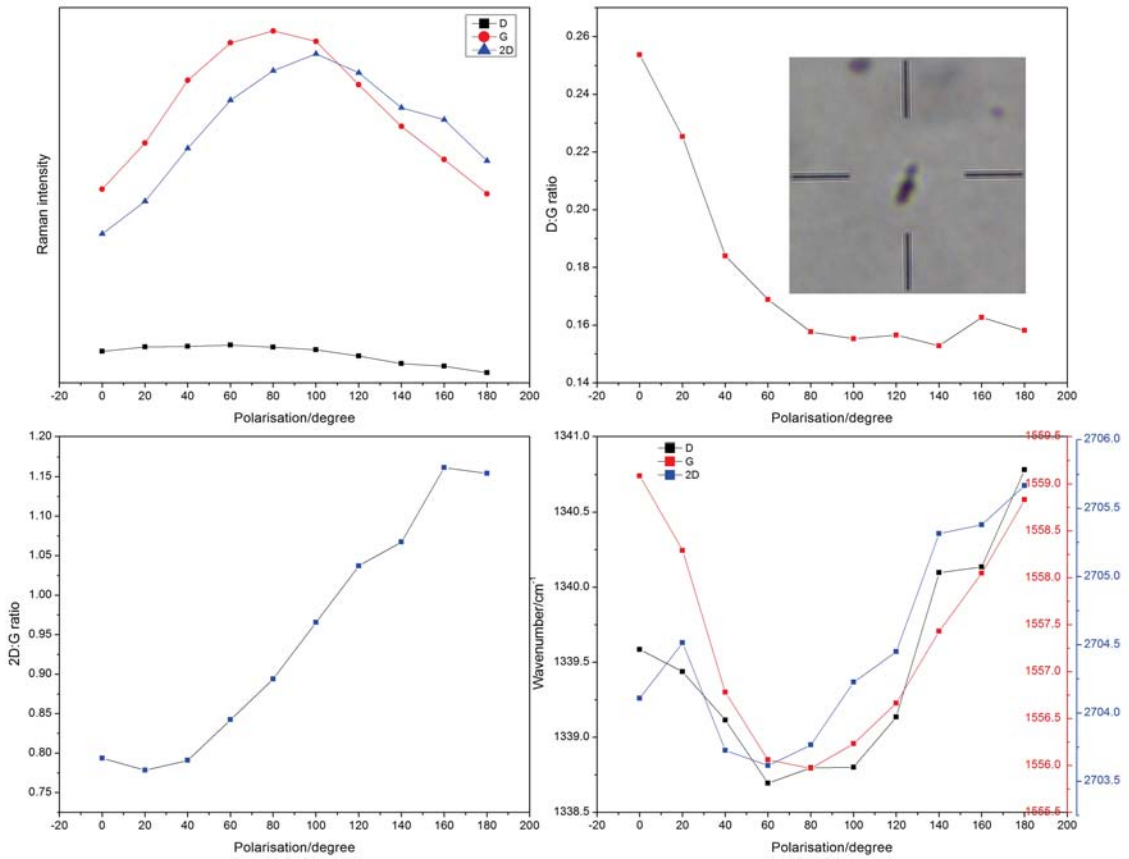

Figure 165: Polarised Raman analysis of 20 nm wet-cut GNR on quartz. Spectra were acquired with 488 nm excitation.

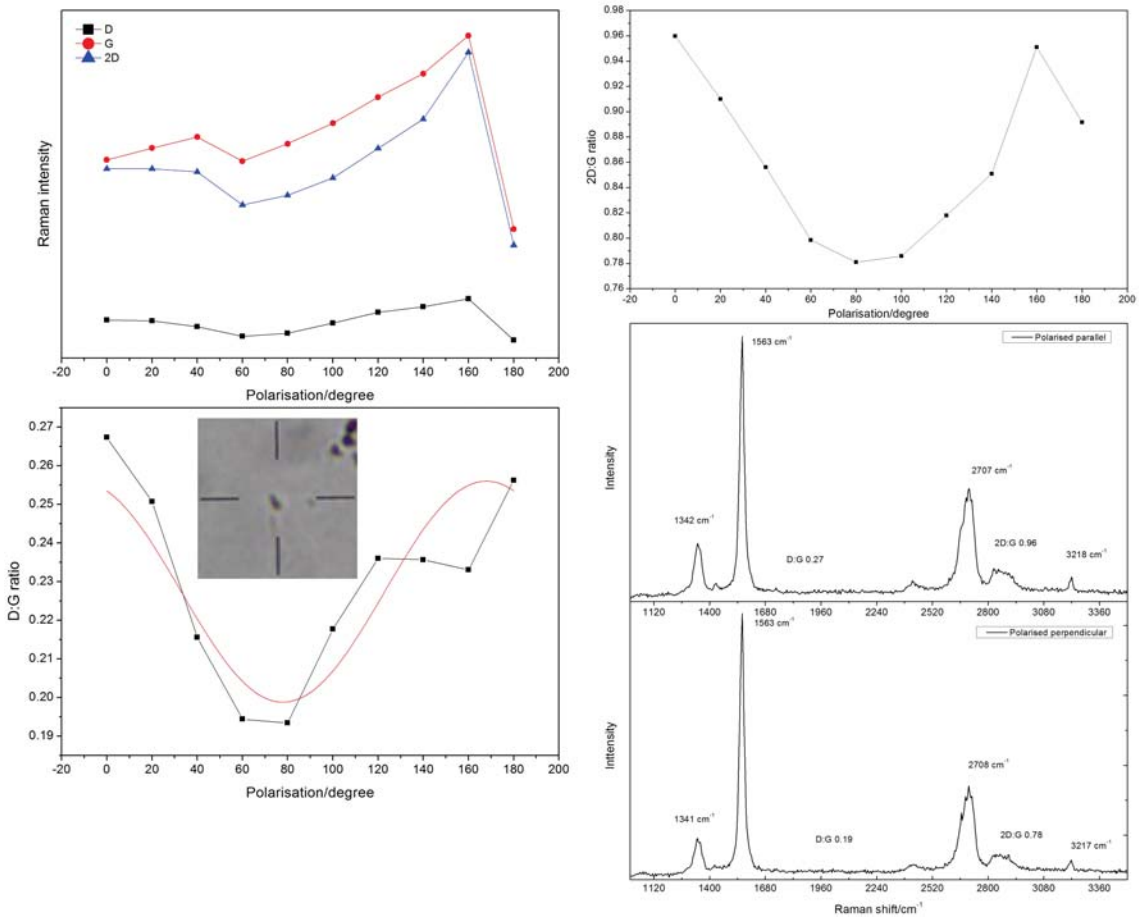

Figure 166: Polarised Raman analysis of 50 nm wet-cut GNR on quartz. Spectra were acquired with 488 nm excitation.

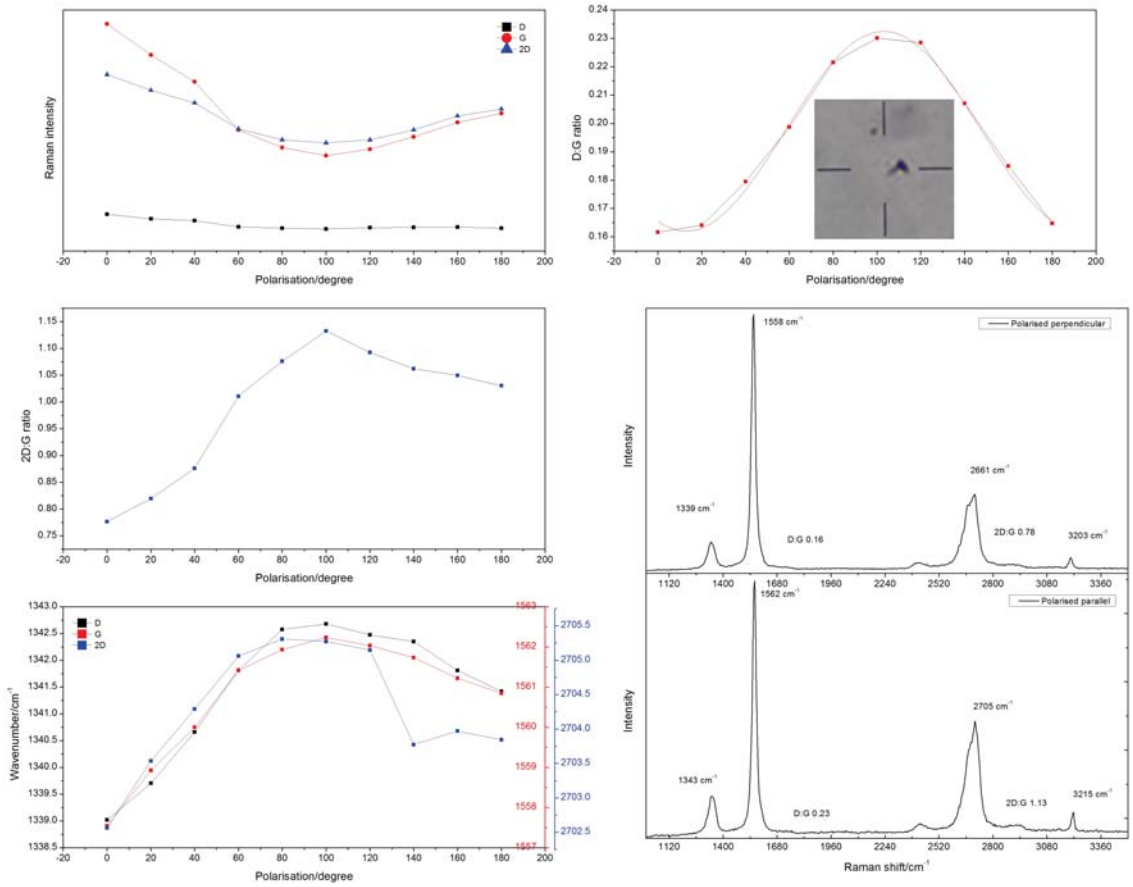

Figure 167: Polarised Raman analysis of 50 nm wet-cut GNR on quartz. Spectra were acquired with 488 nm excitation.

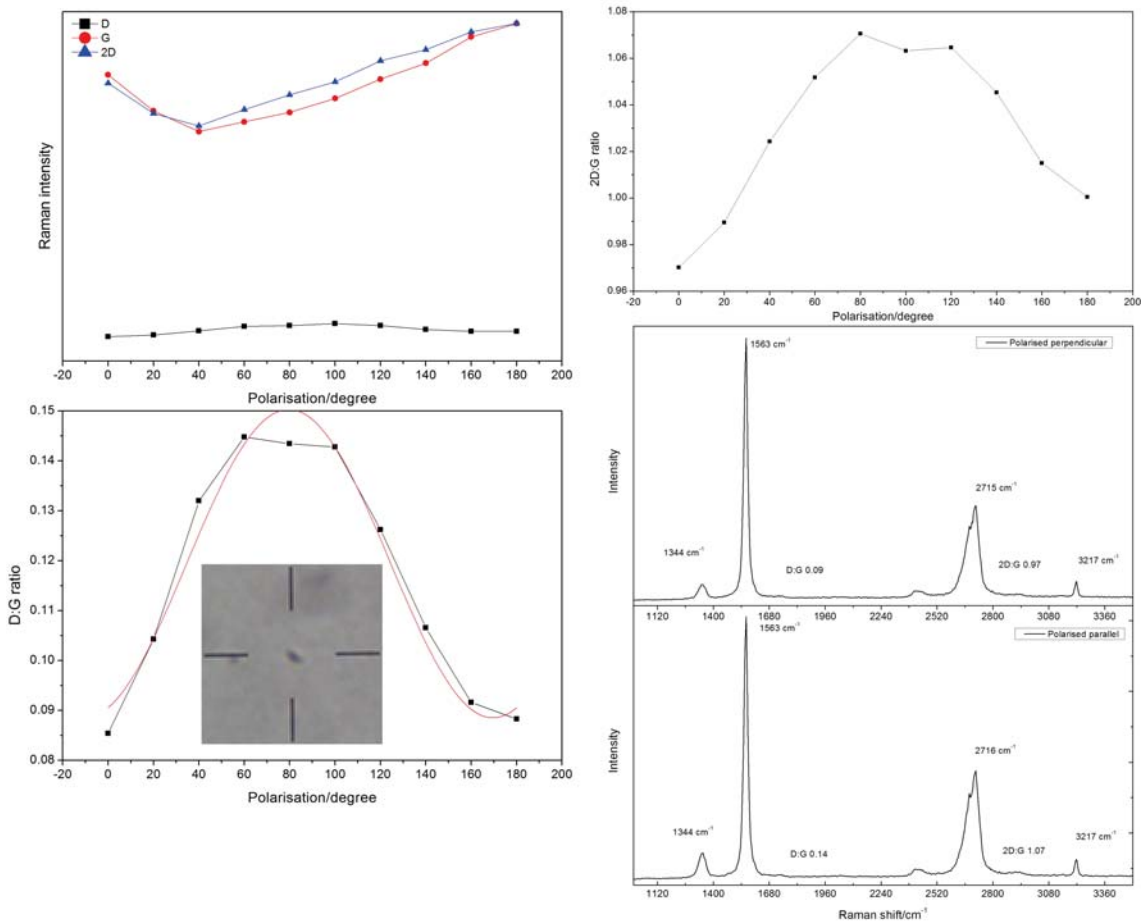

Figure 168: Polarised Raman analysis of 100 nm wet-cut GNR on quartz. Spectra were acquired with 488 nm excitation.

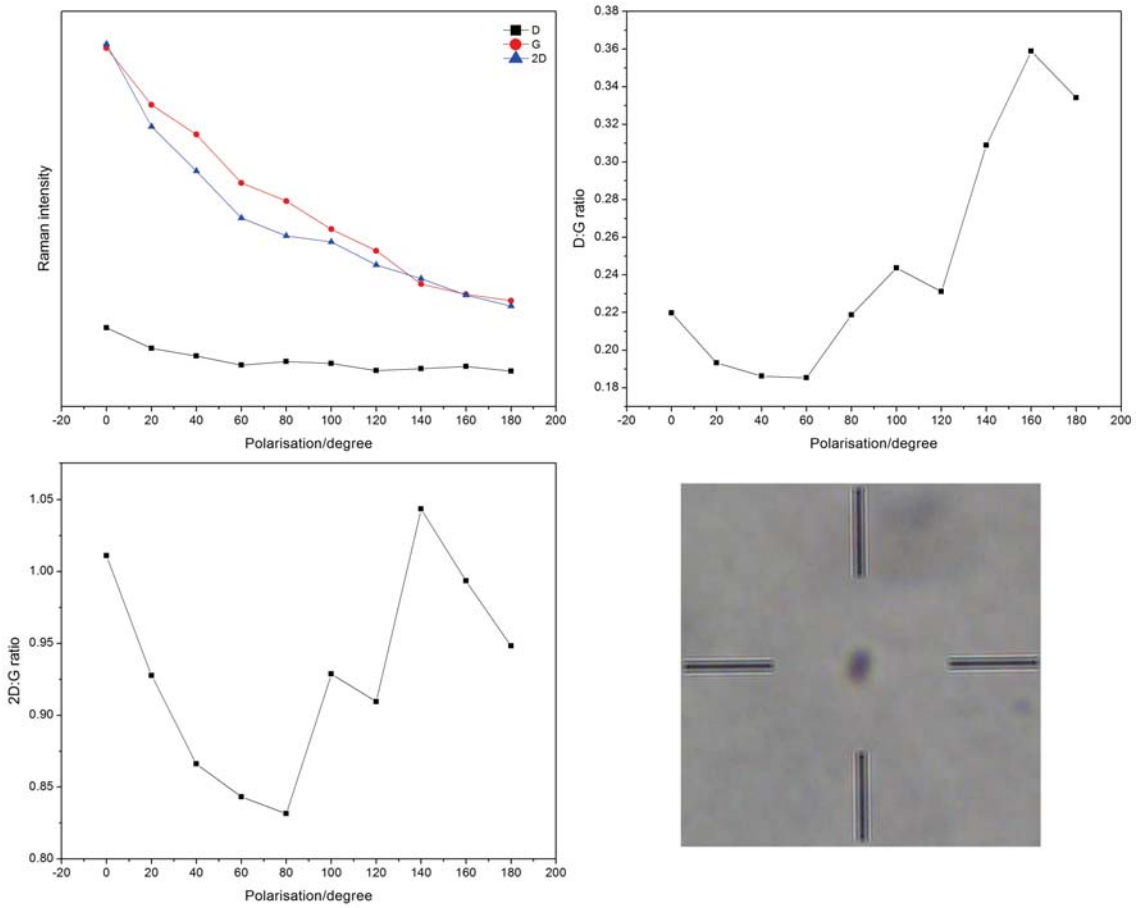

Figure 169: Polarised Raman analysis of 100 nm wet-cut GNR on quartz. Spectra were acquired with 488 nm excitation.

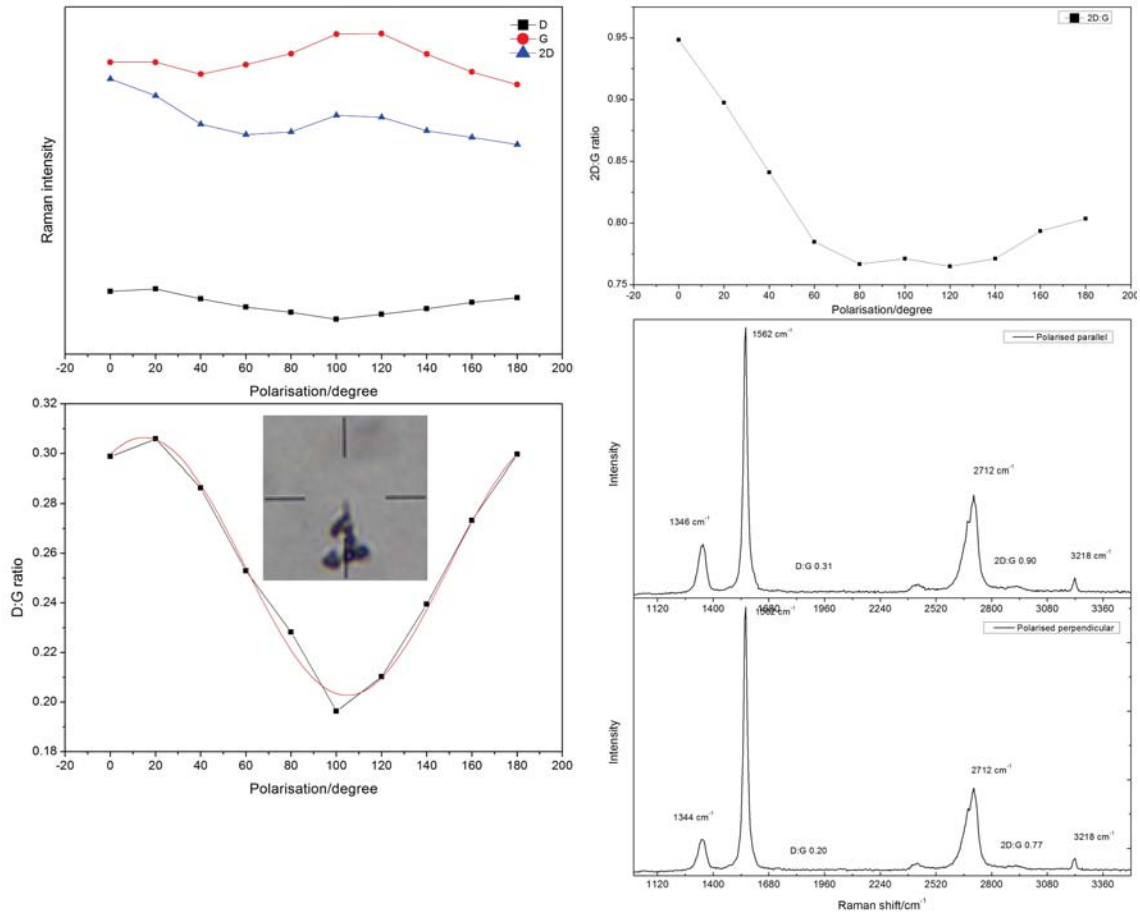

Figure 170: Polarised Raman analysis of 300 nm wet-cut GNR on quartz. Spectra were acquired with 488 nm excitation.

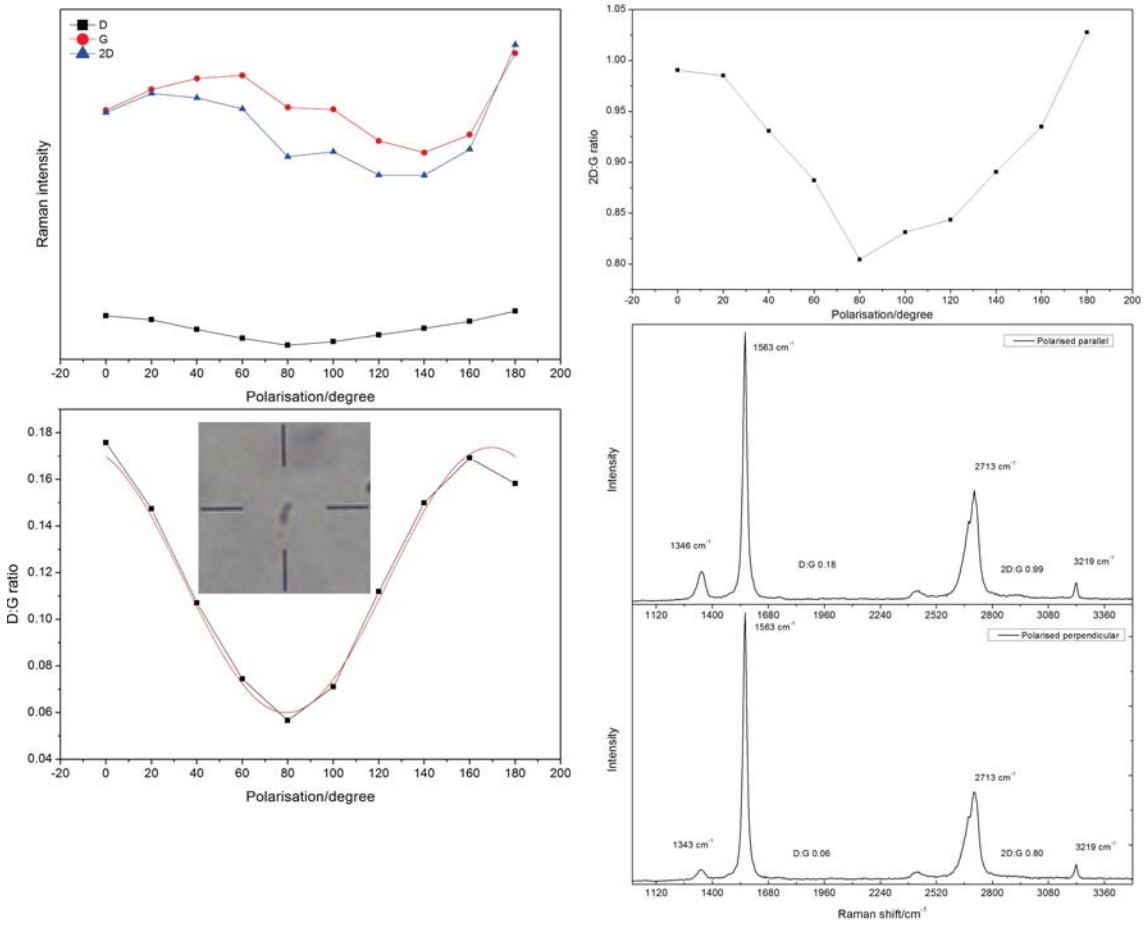

Figure 171: Polarised Raman analysis of 300 nm wet-cut GNR on quartz. Spectra were acquired with 488 nm excitation.

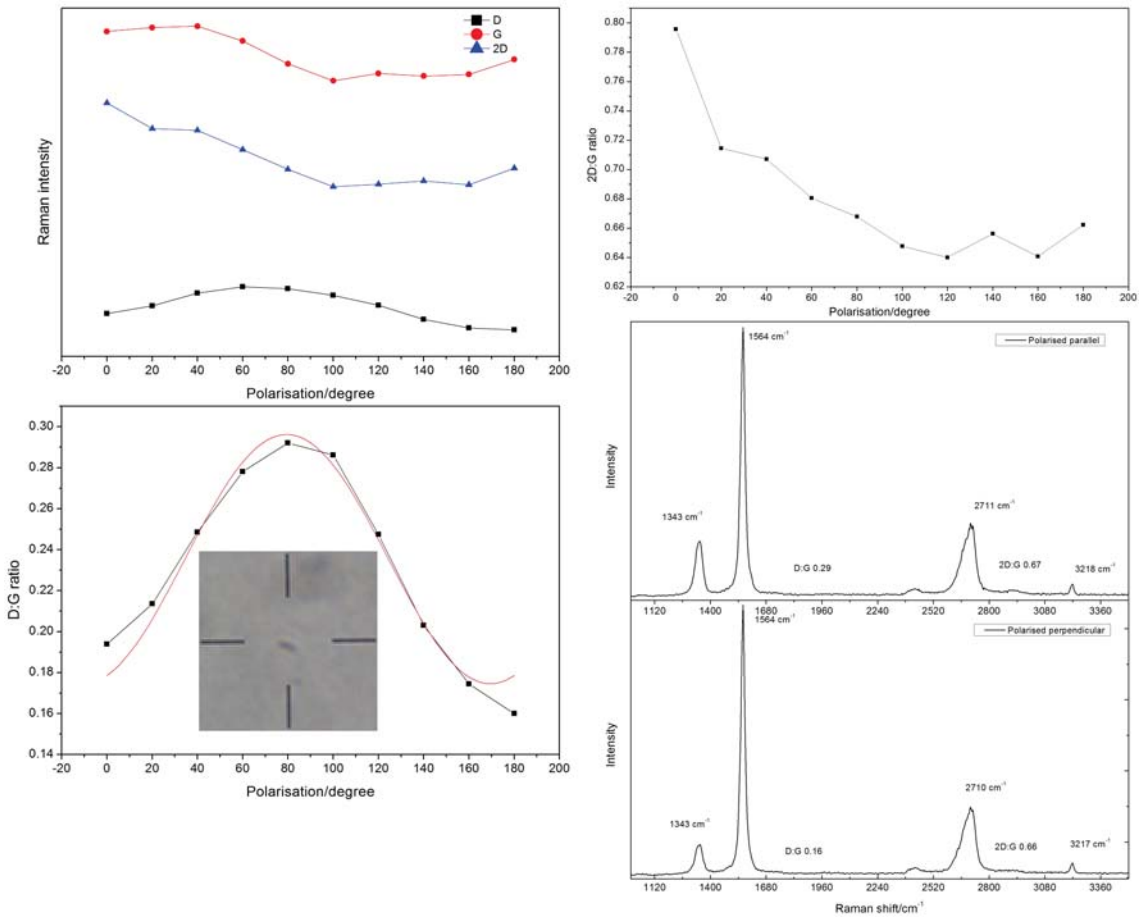

Figure 172: Polarised Raman analysis of 500 nm wet-cut GNR on quartz. Spectra were acquired with 488 nm excitation.

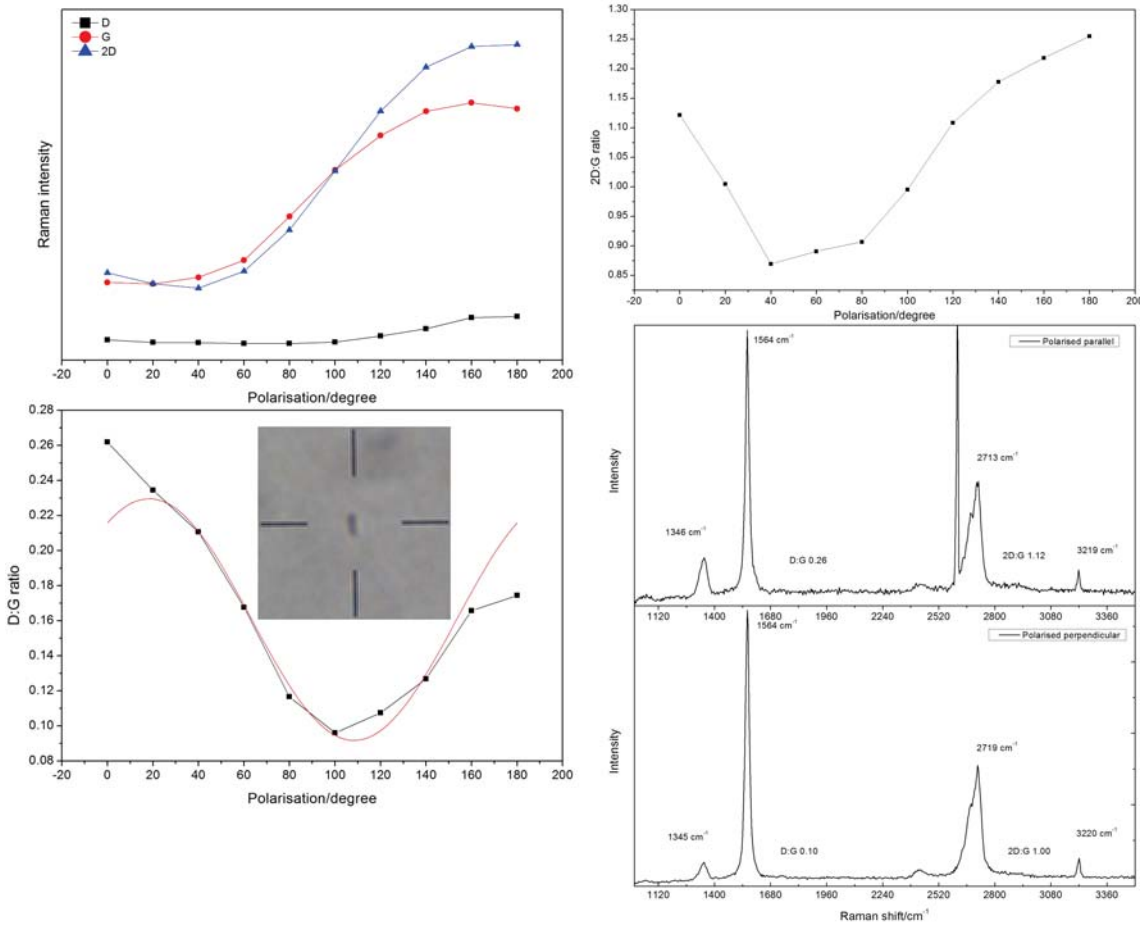

Figure 173: Polarised Raman analysis of 500 nm wet-cut GNR on quartz. Spectra were acquired with 488 nm excitation.

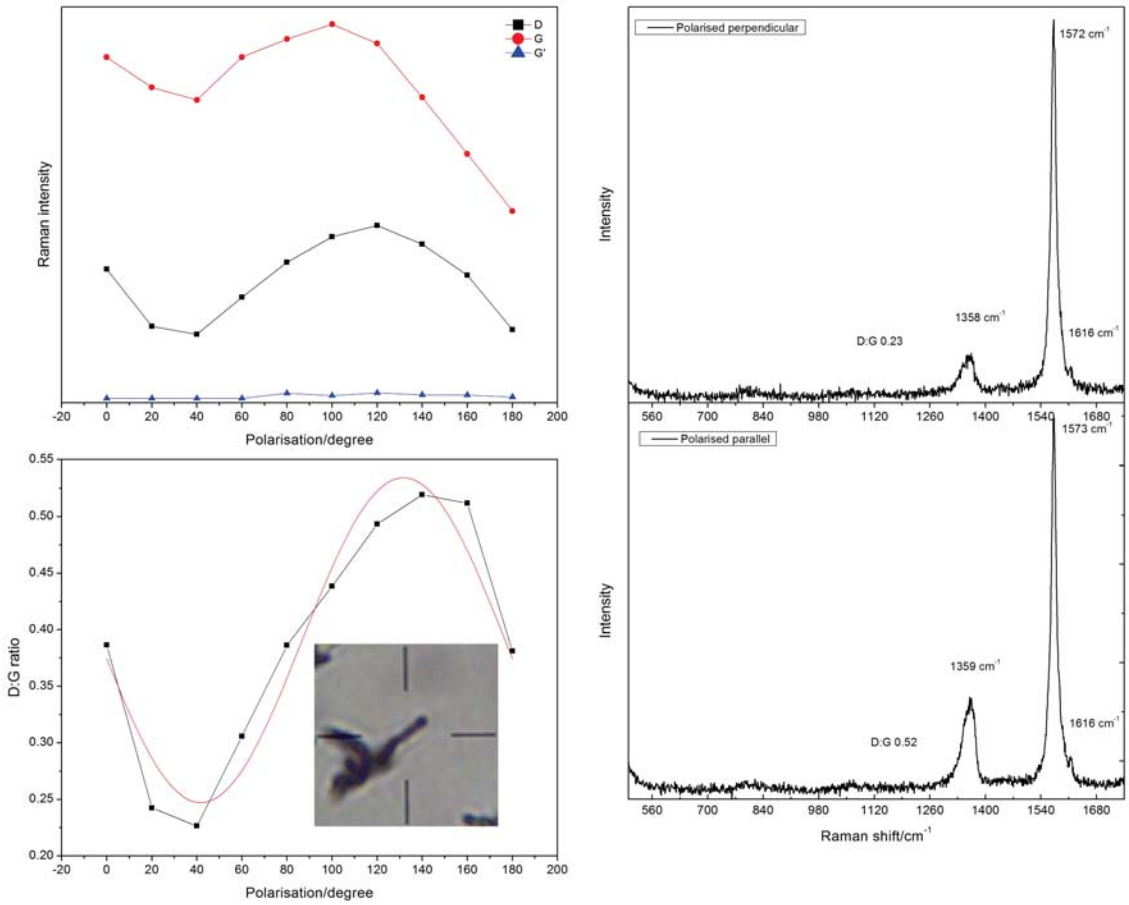

Figure 174: Polarised Raman analysis of 100 nm dry-cut GNR on quartz. Spectra were acquired with 488 nm excitation.

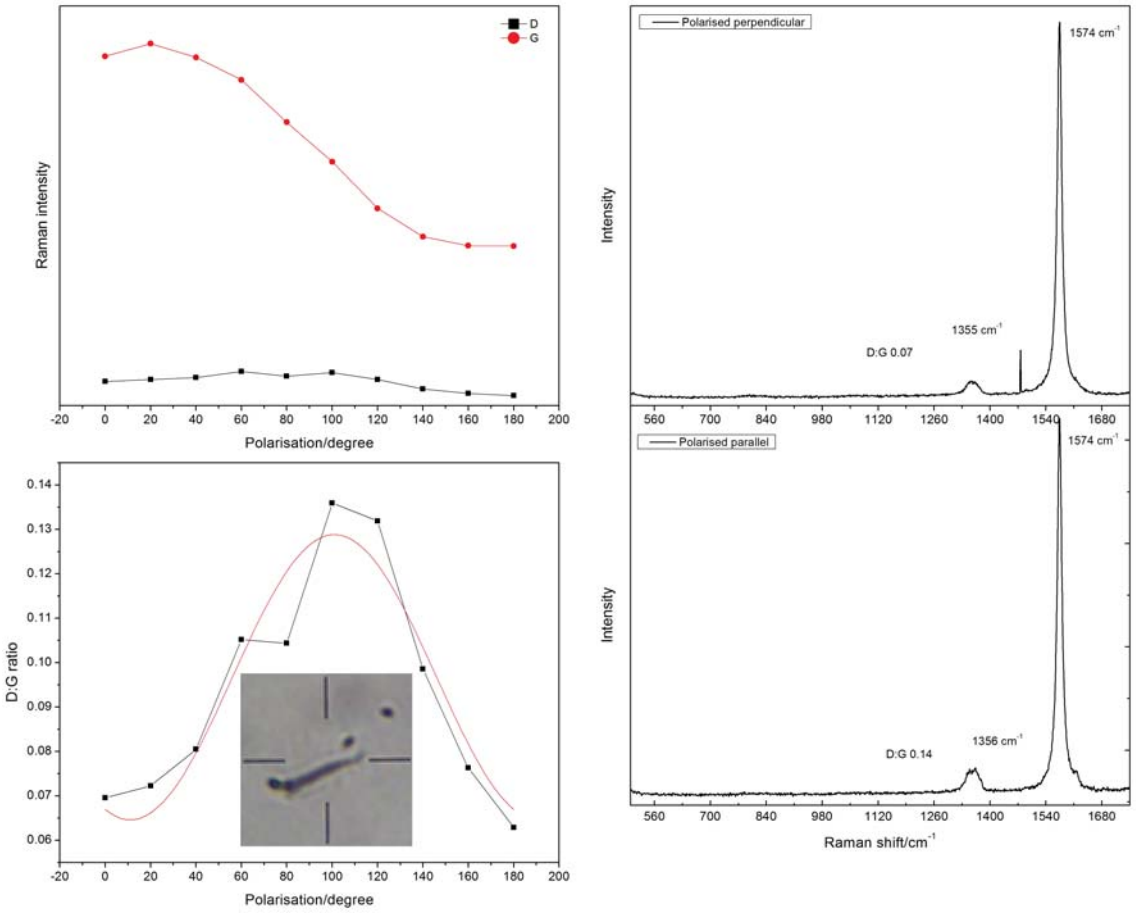

Figure 175: Polarised Raman analysis of 100 nm dry-cut GNR on quartz. Spectra were acquired with 488 nm excitation.

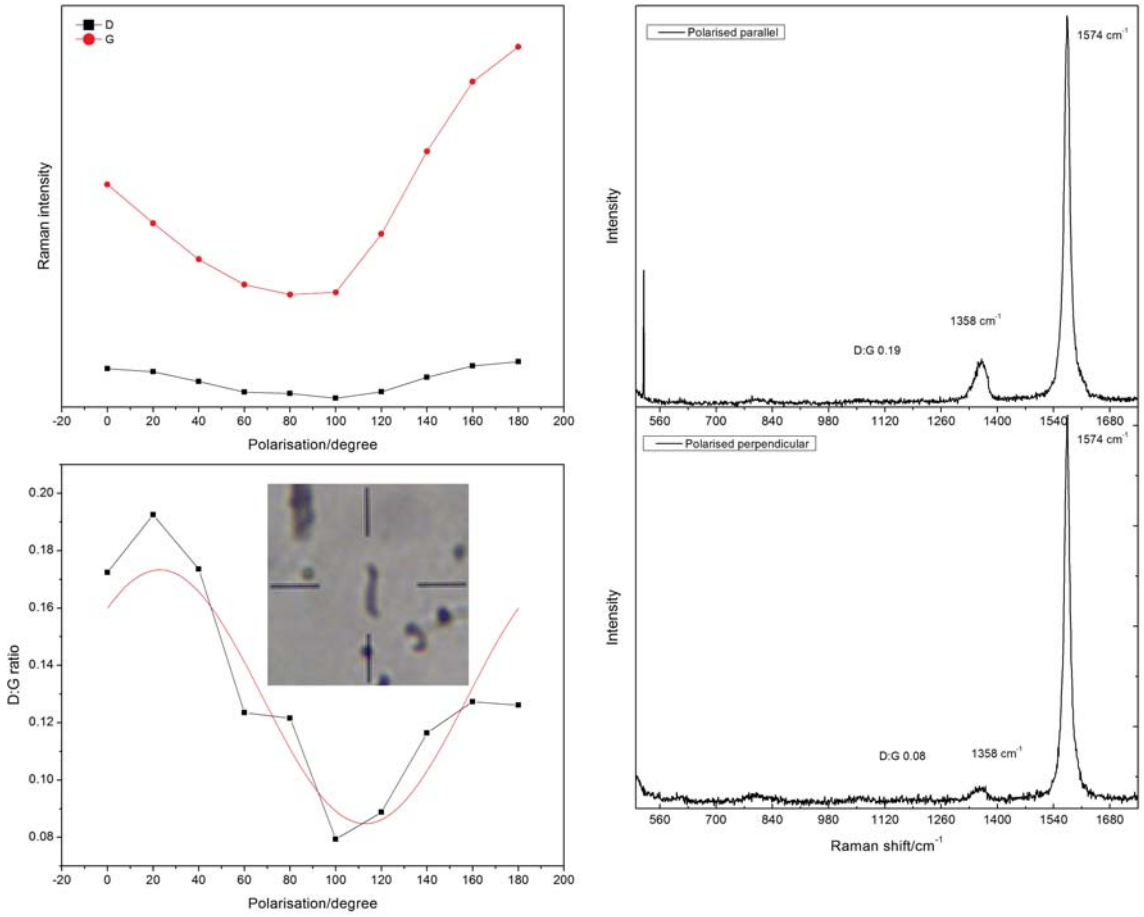

Figure 176: Polarised Raman analysis of 100 nm dry-cut GNR on quartz. Spectra were acquired with 488 nm excitation.

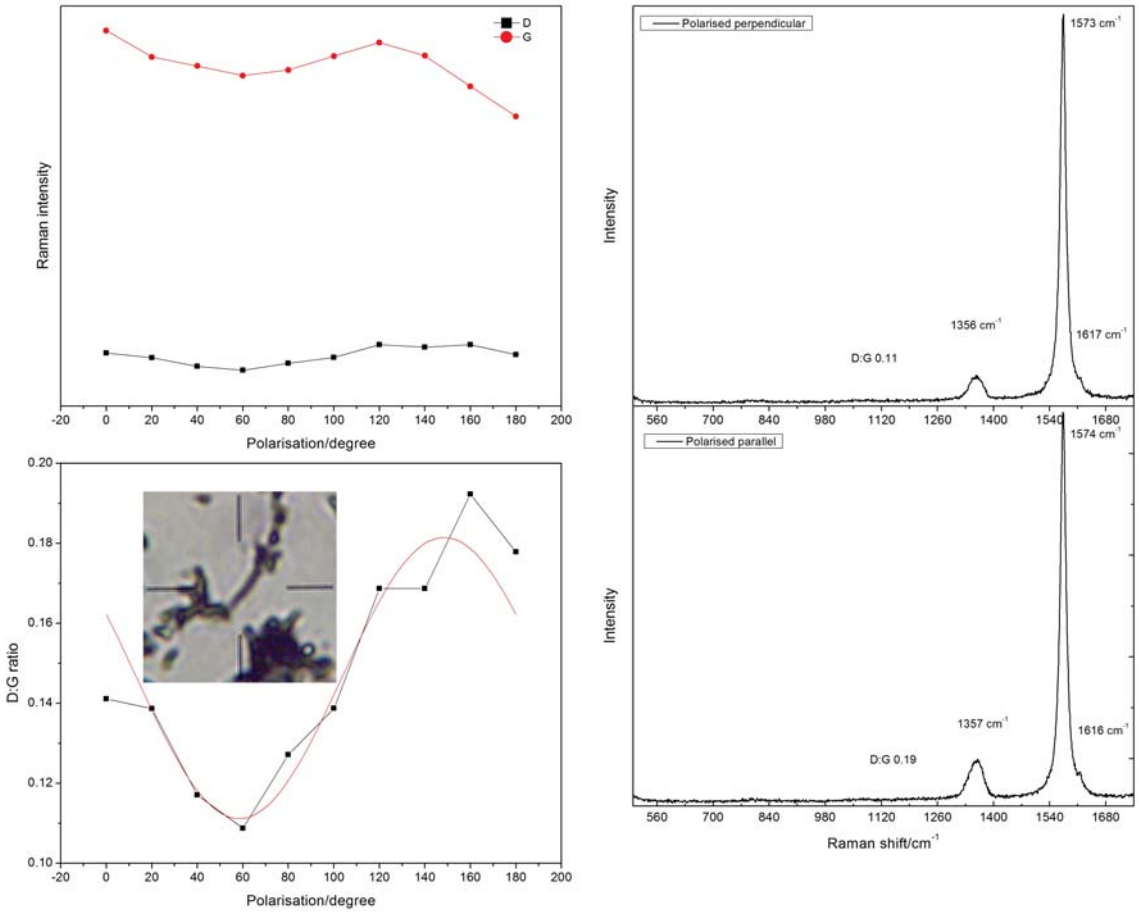

Figure 177: Polarised Raman analysis of 100 nm wet-cut GNR on quartz. Spectra were acquired with 488 nm excitation.

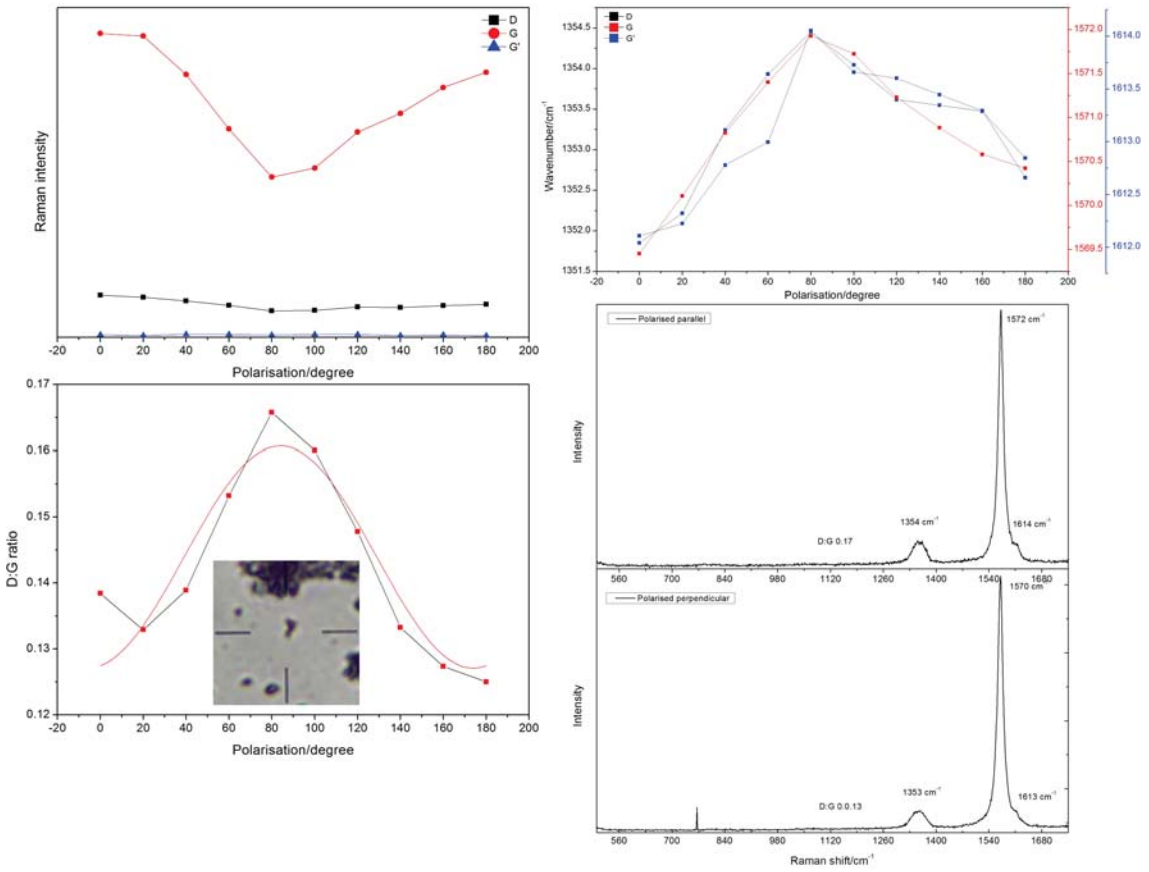

Figure 178: Polarised Raman analysis of 100 nm wet-cut GNR on quartz. Spectra were acquired with 488 nm excitation.

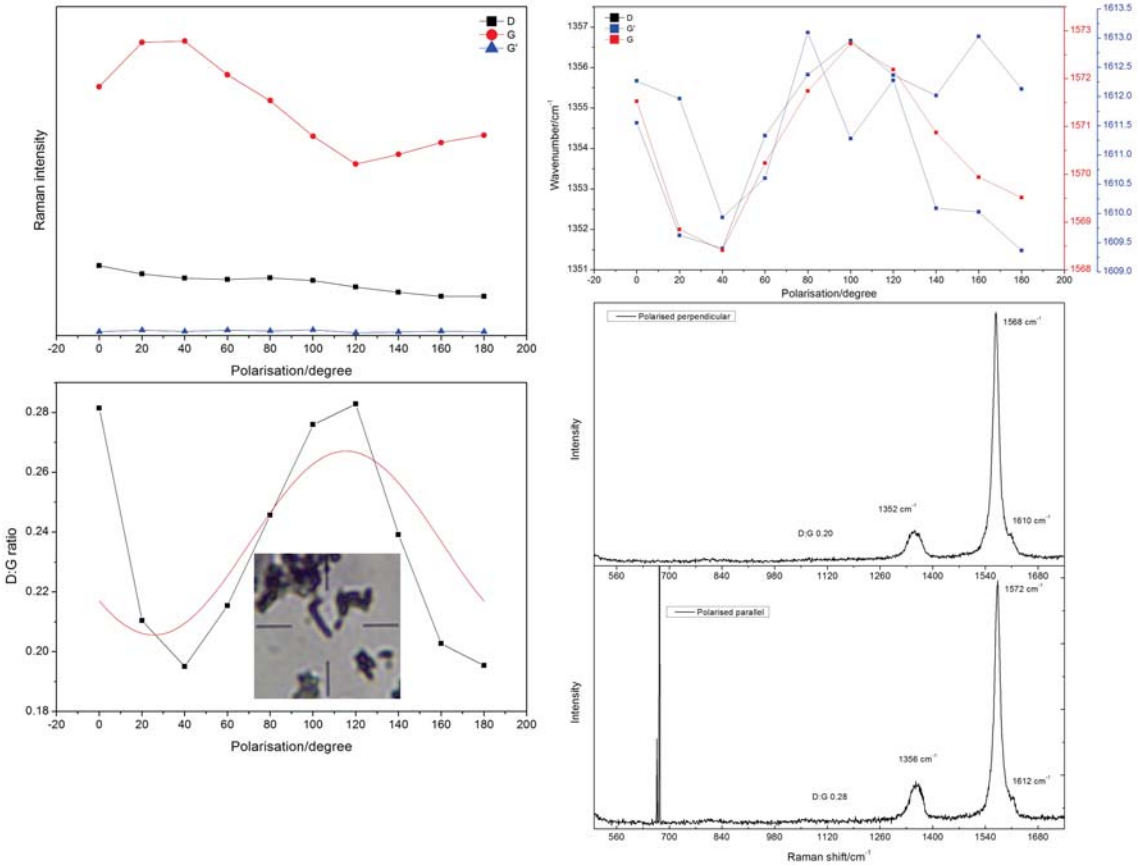

Figure 179: Polarised Raman analysis of 100 nm wet-cut GNR on quartz. Spectra were acquired with 488 nm excitation.

9.3.5 Functionalised GNR

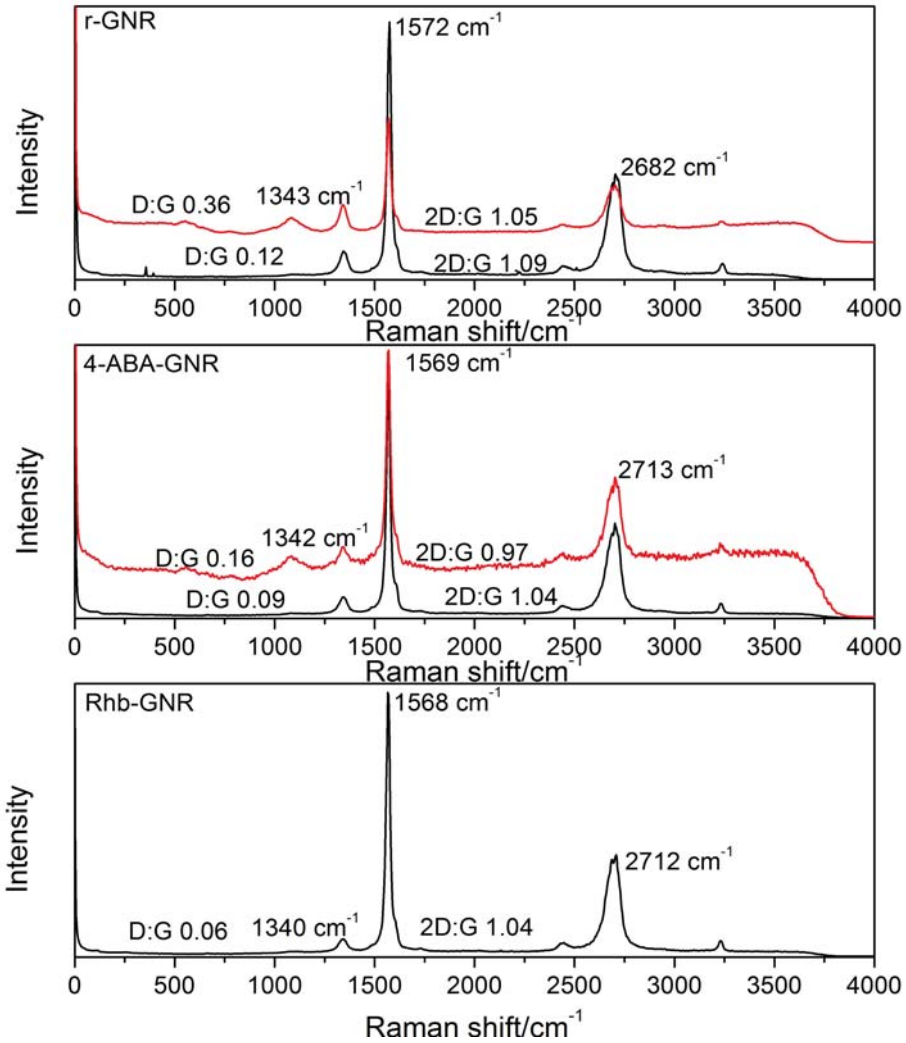

Figure 180: Raman spectra of functionalised 100 nm GNRs acquired with 532 nm excitation.

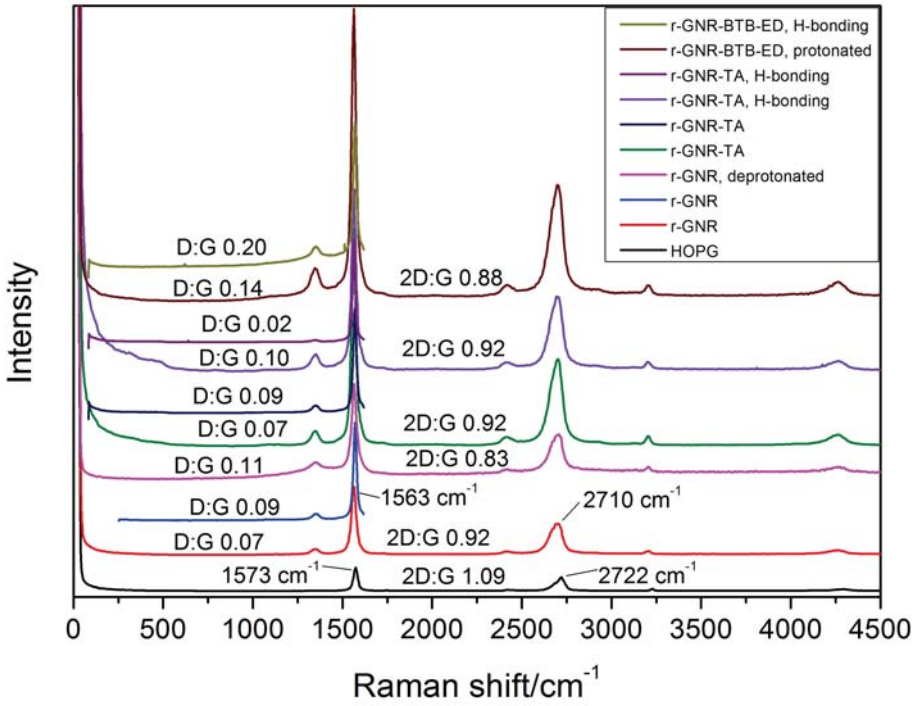

Figure 181: Raman spectra of some of the functionalised 20 nm GNR samples used in the Far-IR measurements at the synchrotron (see Chapter 5.2.5 of the main text). Spectra were acquired with 488 nm excitation.

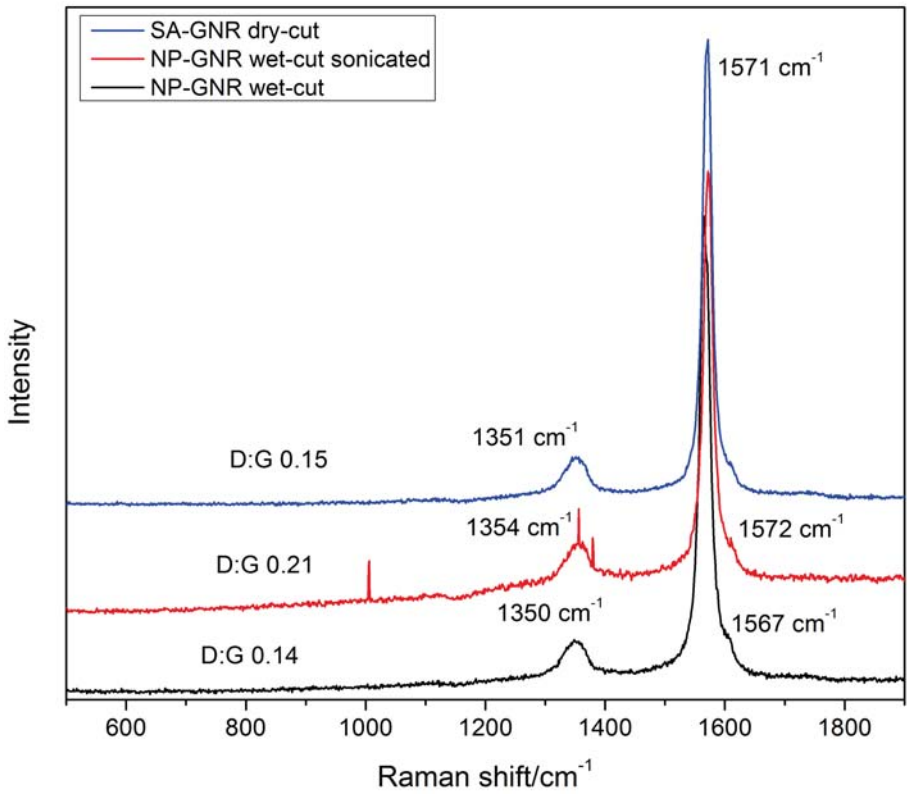

Figure 182: Raman spectra of modified 20 nm GNR samples. Spectra were acquired with 488 nm excitation.

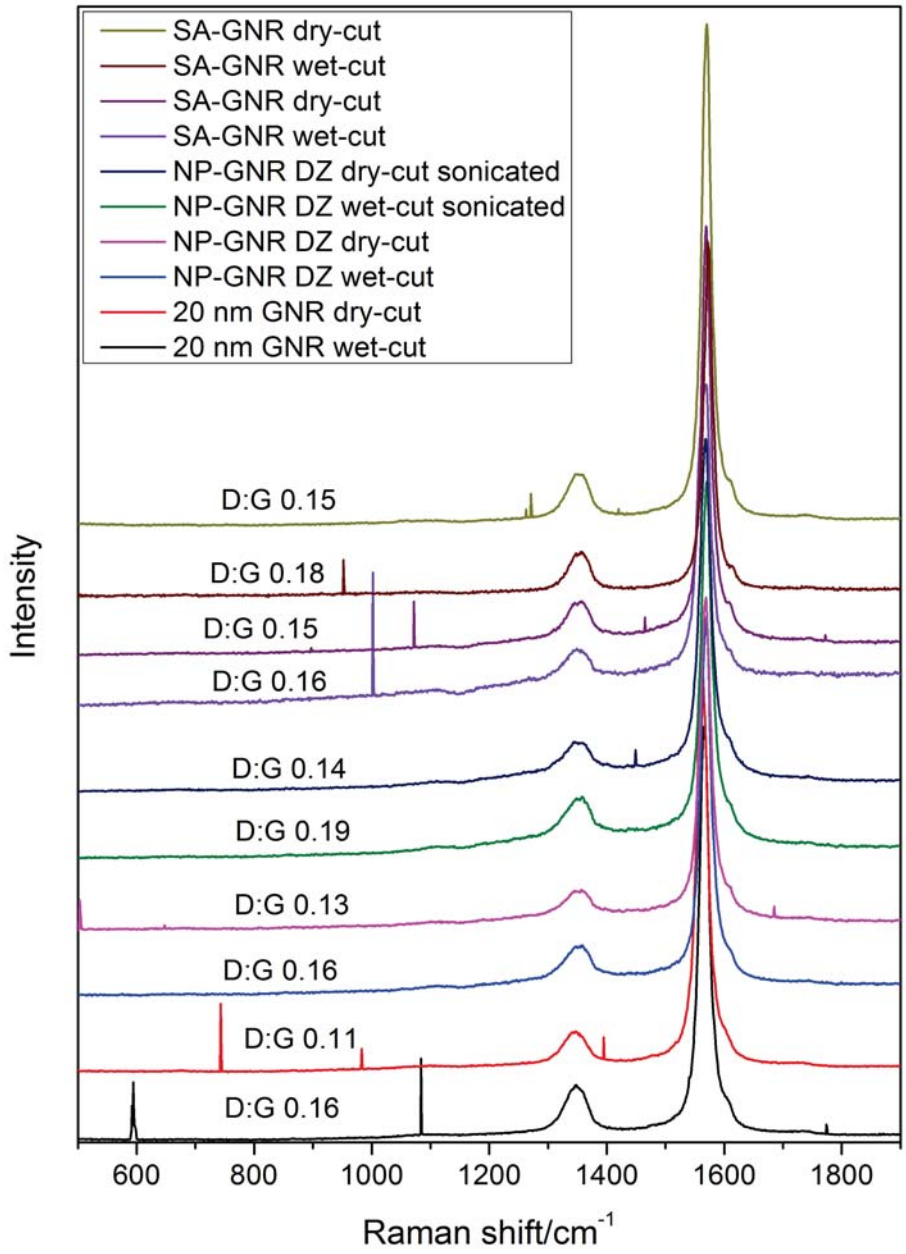

Figure 183: Raman spectra of modified 20 nm GNR samples. Spectra were acquired with 488 nm excitation.

9.4 Additional FTIR data

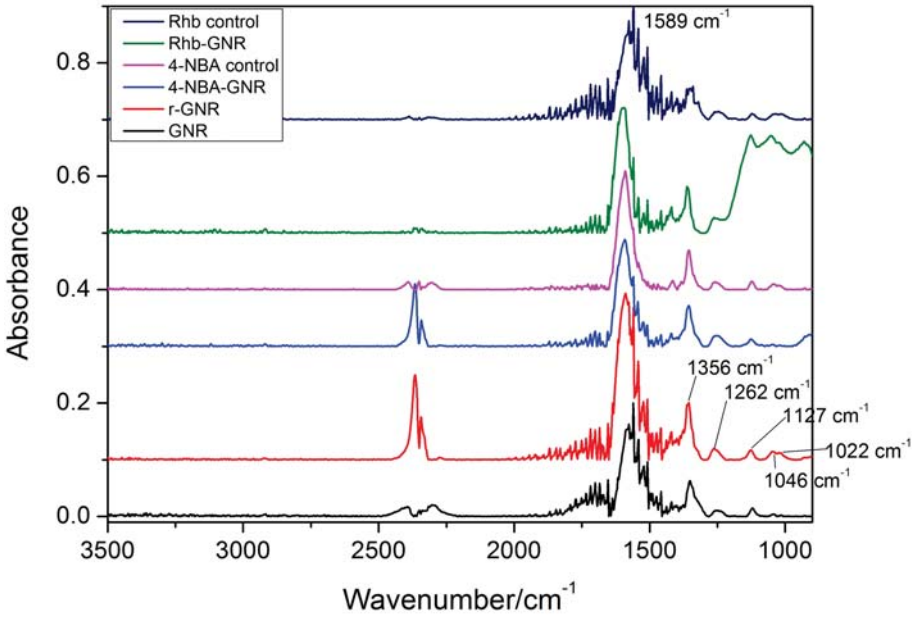

Figure 184: FTIR microscope spectra of modified 50 nm GNR samples. The spectra were taken in reflectance mode and were Kramers-Kronig transformed and baseline corrected.

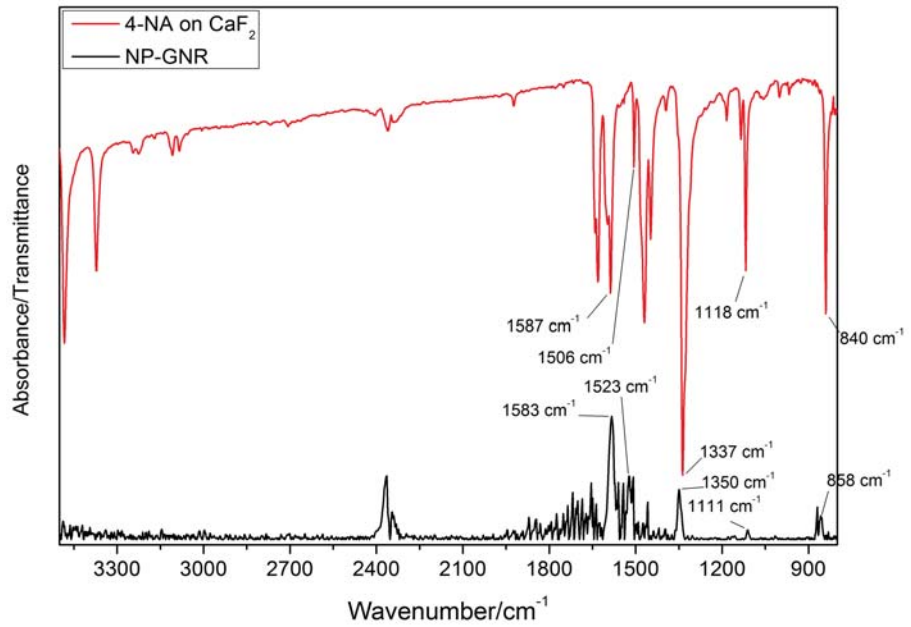

Figure 185: FTIR microscope spectra of 4-nitroaniline taken in transmission mode and 20 nm NP-GNR taken in reflectance mode. The reflectance spectrum was Kramers-Kronig transformed and baseline corrected.

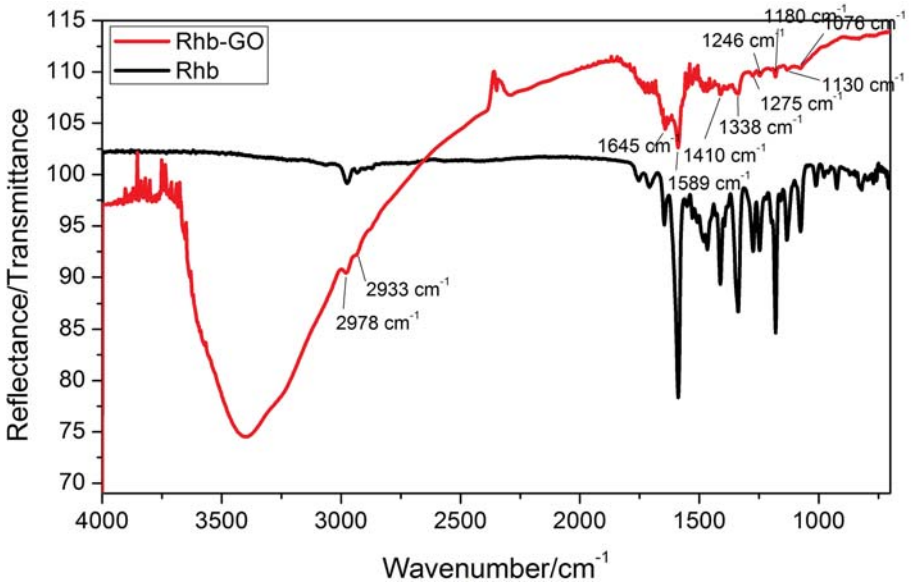

Figure 186: FTIR microscope spectra of Rhodamine B taken in transmission mode and RhB-GO taken in reflectance mode.

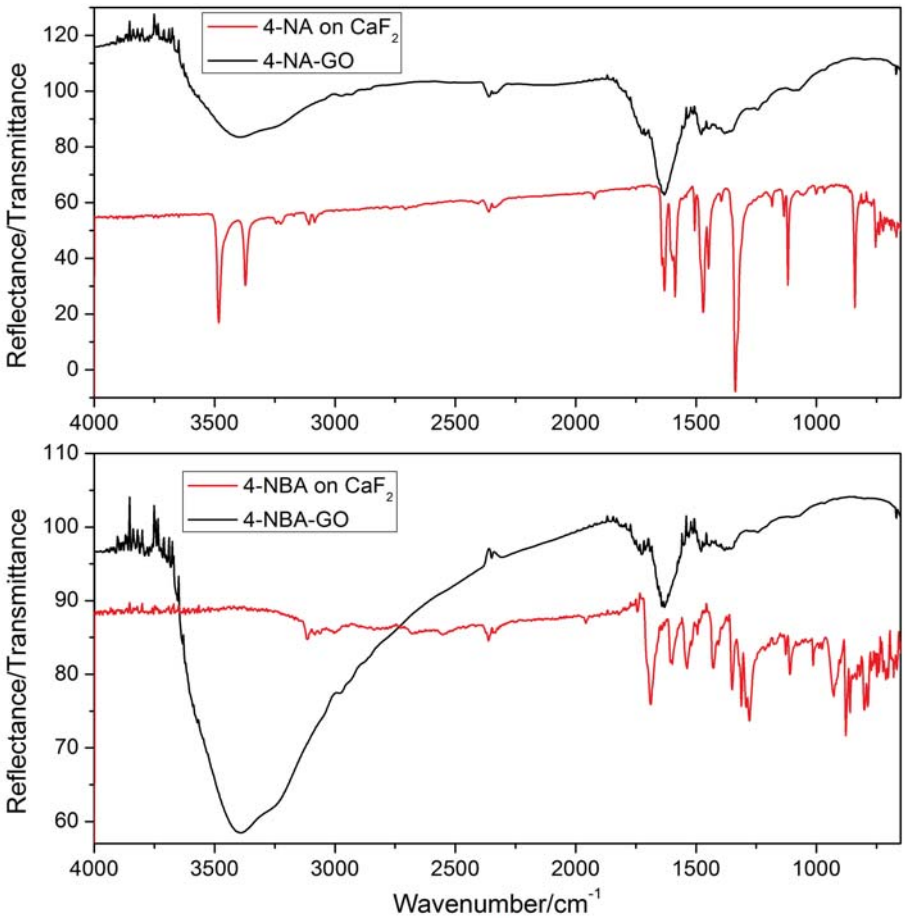

Figure 187: FTIR microscope spectra of 4-NA and 4-NBA taken in transmission mode, and 4-NA-GO and 4-NBA-GO taken in reflectance mode.

It is useful to determine what proportion of edge functional groups to graphene carbon ratio is necessary for the edge groups to become visible in the IR. This was done by mixing solutions of ribbons with solutions of SA of decreasing concentration. By monitoring the strength of the SA peaks in the IR spectrum as the concentration of SA is gradually decreased, an estimate of the proportion of functionalised COOH groups can be made. However, this requires that both the initial GNR concentration be known and the mixing of ribbons and SA be uniform and remain uniform upon drying. Unfortunately, both of these requirements were found to be quite unrealistic; the weight of the cut ribbons was below the limits of the (five-figure) balance ($< \mu g$), and the SA appeared to separate from the ribbons upon drying and form crystals. Nevertheless, the acquired spectra still make for some useful and interesting comparisons (figure 188). This figure compares the spectra of SA-GNR and SA on a CaF2 substrate. There are some immediately apparent differences between the spectra, particularly in the region 1000-1300 cm^{-1}. The bands at 1010 (C-H bend), 1035 (SO_3 stretch) and 1126 cm^{-1} (SO_3 stretch) of SA-GNR are well-matched to SA (and the literature[157]), but some of the other bands are shifted in wavenumber. Figure 188 also compares the spectra of SA on CaF_2 and GNR mixed with 10^{-2} M SA. Interestingly, there are also noticeable differences between these spectra, though SA should be in the same form in both samples (i.e. crystalline and not covalently attached to GNR). It is possible that these differences arise due to the different modes of acquisition (reflectance for SA with GNR, transmission for SA on CaF_2.

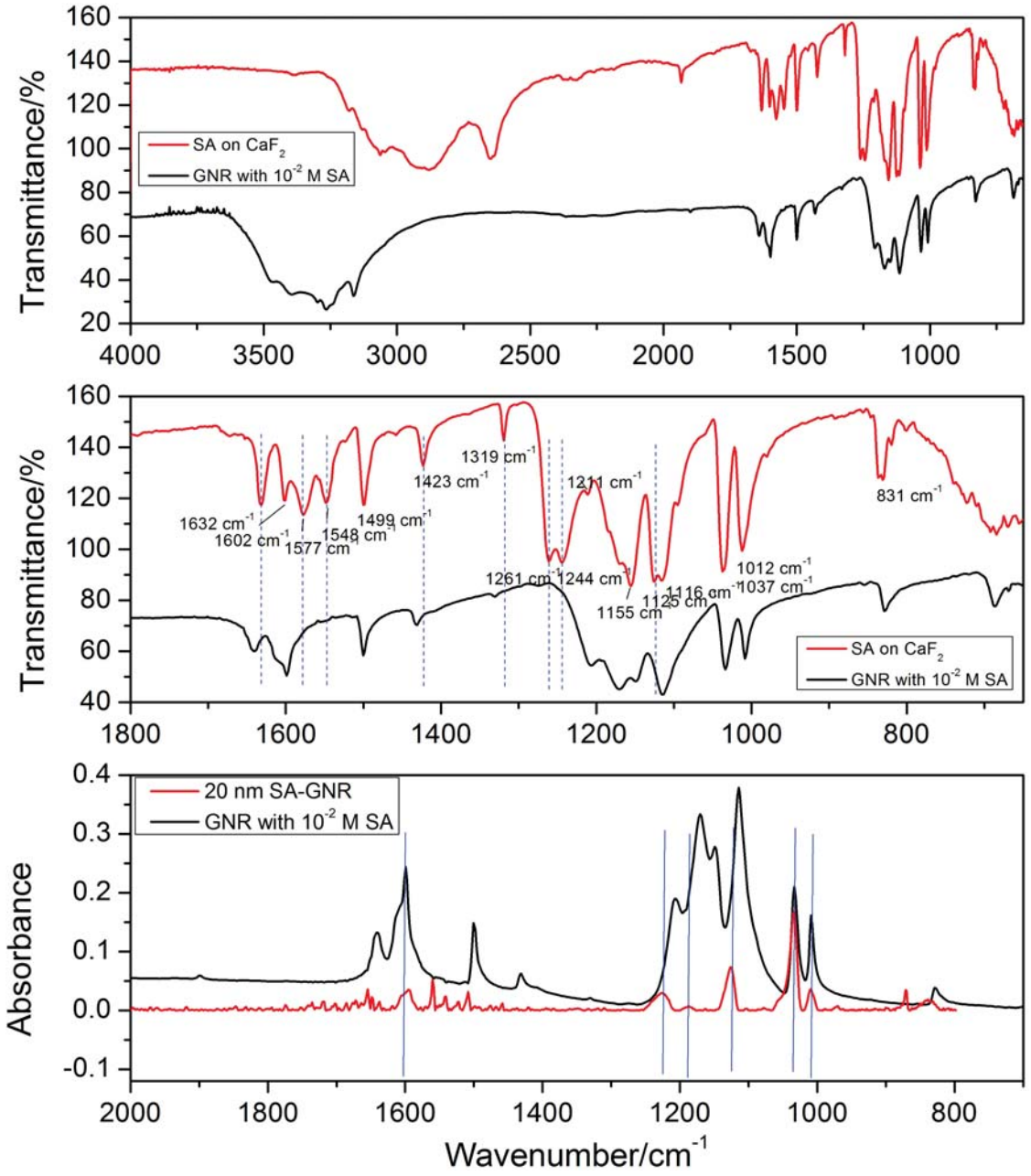

Figure 188: FTIR microscope spectra of SA, GNR with SA and SA-GNR.

9.5 Additional Far-IR data

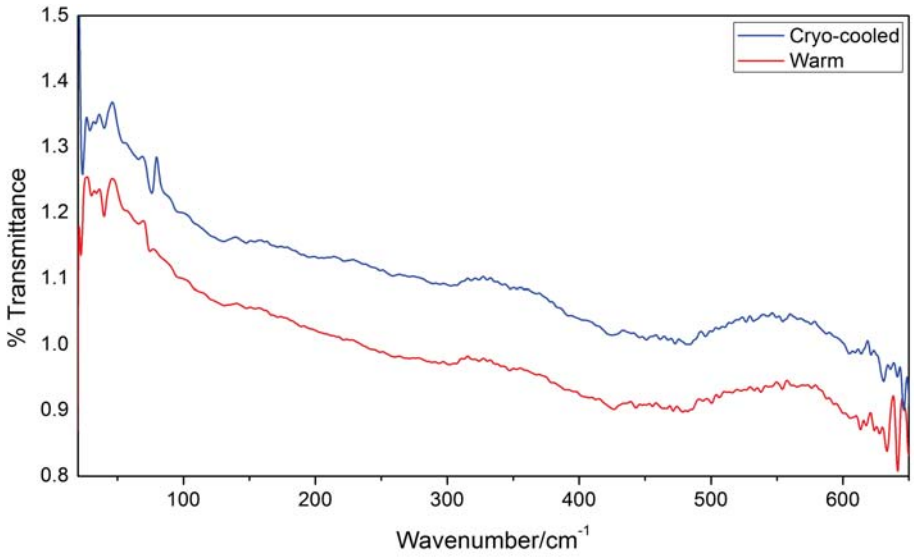

Figure 189: Far-IR spectra of 20 nm r-GNR-TMA-4-NA with urea, taken in transmission mode.

9.6 Additional SERS data

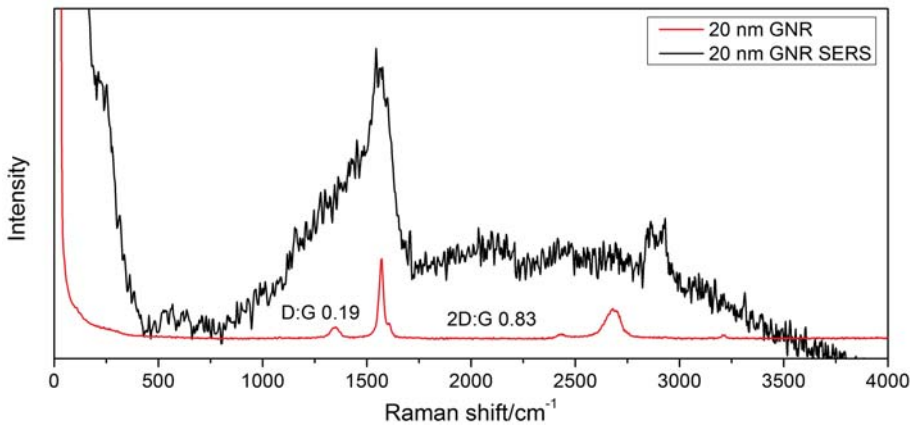

Figure 190: Raman and SERS spectra of 20 nm GNRs on a superhydrophobic Ag substrate. Spectra were acquired with 532 nm excitation.

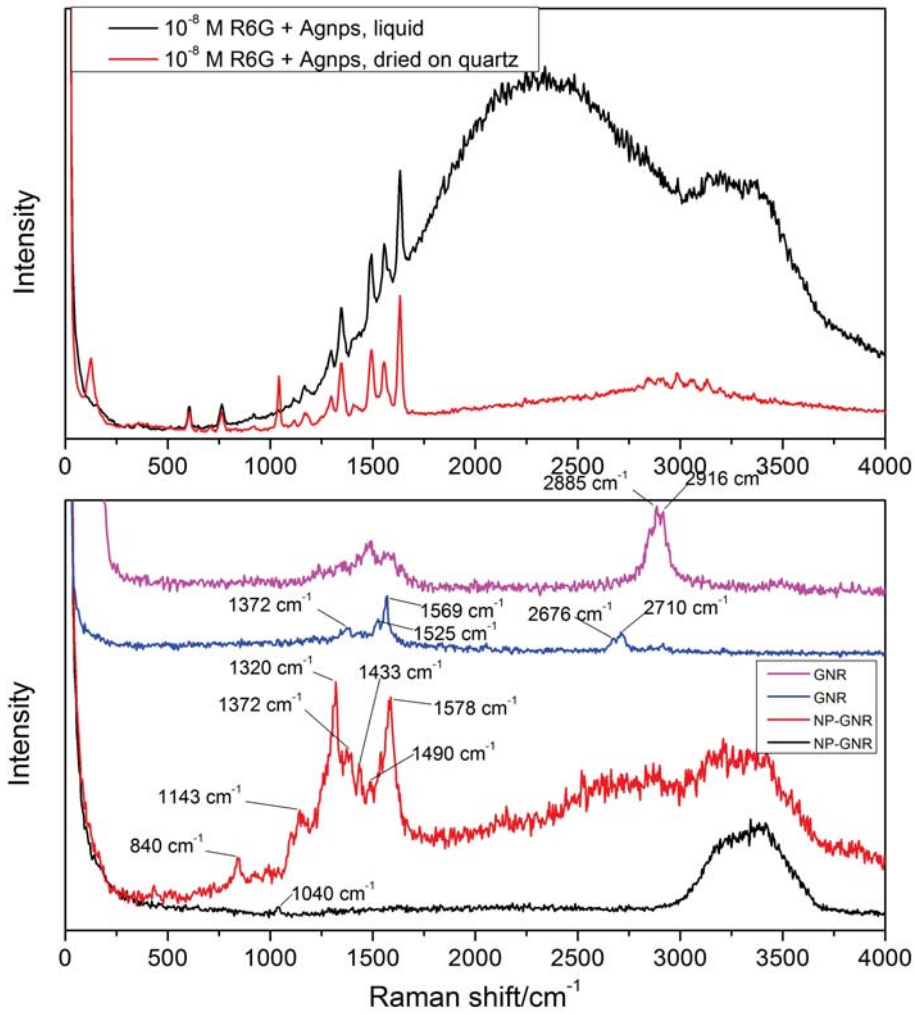

Figure 191: SERS spectra of Rhodamine 6G (top) and 20 nm GNRs (bottom), unmodified and modified with nitrophenyl groups. Spectra were acquired with 488 nm excitation.

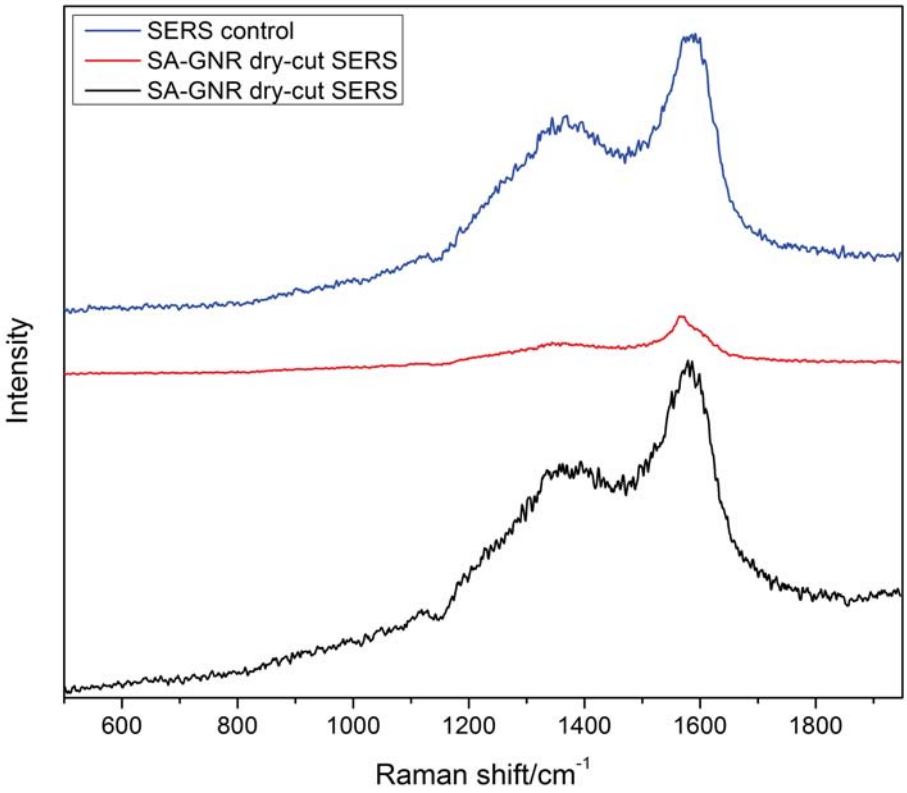

Figure 192: SERS spectra of modified 20 nm GNR samples. Spectra were acquired with 488 nm excitation.